ELECTRONIC TRANSPORT IN GRAPHENE: 2D MATERIALS, COMPOSITES, AND 3D PRINTED STRUCTURES

Jonathan Harry Gosling

Thesis submitted to the University of Nottingham for the degree of
Doctor of Philosophy

School of Physics and Astronomy
The University of Nottingham
August 2022

Abstract

In this thesis, the charge-carrier mobility in graphene, limited by multiple sources of electron scattering, is studied under the framework of the Boltzmann transport equation using the Born approximation for scattering potentials. Two congruent methods are explored: deterministic discontinuous Galerkin, and stochastic Direct Simulation Monte Carlo, to solve the full Boltzmann equation. Such temporal simulations, showcasing the transient dynamics from thermal equilibrium to a new steady-state under electrostatic perturbation, reveal the profound effects of the Joule heating capabilities of graphene, where the electrons behave as an electron gas with weak external lattice coupling. Mobility curves reveal the nature of electronic transport with changing electron population, and under varying physical parameters. As modelled for impurity dominated graphene, we find a "universal" connection between the carrier mobility and variation of conductivity with carrier population, applicable for both pristine graphene and graphene heterostructures. Ultimately, such universality relies on universality at the Dirac point. When thermally excited phonons and charge carriers become important, the behaviour around the Dirac point should be carefully considered. We show how thermal effects on the low-energy electron distributions affect the width of the total resistivity curve with respect to variations of carrier density, and how this affects the measured mobility and it's temperature dependence. Twisting between constituent layers of hexagonal lattices alters the periodic lattice potential, forming secondary Dirac points and band gaps within the low-energy spectrum of a single graphene layer. We show how this can limit conductivity with and without external lattice perturbations. We find intriguing features, such as negative differential conductance, at electron energies around the secondary Dirac points, due to Bloch oscillating electrons. 3D printing provides a potential solution for scalable and efficient manufacturing of 2D materials and heterostructures. Flakes deposited via inkjet printing form percolating networks. Results reveal how the macroscopic electrical properties, characterised by the hopping and tunnelling between individual flakes, are strongly influenced by the distribution of flakes and by complex meandering electron trajectories, which traverse multiple printed layers.

Publications

- "Universal mobility characteristics of graphene originating from charge scattering by ionised impurities". J. H. Gosling, et al. *Communications Physics* **4** (2021): 30.

- "Inter-flake quantum transport of electrons and holes in inkjet-printed graphene devices". F. Wang and J. H. Gosling, et al. *Advanced Functional Materials* **31.5** (2021): 2007478.

- "Graphene FETs with high and low mobilities have universal temperature -dependent properties". J. H. Gosling, et al. (in preparation).

Conferences

- "Quantum Tunneling of Charge Carriers in 3D Printed Graphene Functional Devices". MRS Fall Meeting and Exhibit 2021, Boston, Massachusetts (in-person presentation).

I have been fortunate to work on a project with great breadth, which has led me to work with many fantastic people. Most of all, I would like to thank my supervisor, Professor Mark Fromhold, for facilitating all of these opportunities, sharing your wealth of knowledge and providing incredible support throughout.

Special thanks to Dr Lyudmila Turyanska for superb guidance and allowing me to realise that I'm not too bad at baking.

Dr Oleg Makarovskiy, thank you for fantastic discussions about all things graphene and for all of your help, providing me with crucial experimental results used throughout this work.

Dr Mark Greenaway, thank you for sharing your wisdom. For all of the discussions in our meetings and catch ups, which we always manage to overrun. Through the inevitably many research challenges faced, the help that you have provided in tackling them has been incredibly influential on the outcomes of my research.

Thank you Professor Laurence Eaves for enlightening discussions, valuable ideas and for making manuscript edits *somewhat* fun with all of the personable, often humorous comments.

Thank you to everyone who has worked with me on the 'Enabling Next Generation Additive Manufacturing' programme grant: Richard Hague, Chris Tuck, Ricky Wildman and everyone else, for whom the list is almost endless. A particular thank you to Dr Feiran Wang for endless enthusiasm and, of course, for all of the collaborative work.

To collaborators not aforementioned, particularly Amalia Patanè, Nathan Cottam, Gustavo Trindade, Alexander Balanov, Zakhar Kudrynskyi, Graham Rance, Sergey Morozov, Evgenii Vdovin and Yurii Khanin, thank you for all of your help and inputs.

Also, thank you to everyone who has supported me throughout my PhD. Particularly my family, mum and dad, and the C19 office of past and present (Chris, Peter, Michael, Rosy, Hannah, Logan, Kosit, Yijia, Ali, Kate, Nandha, Monty) for your consistent support and just enough time away from the physics.

List of Abbreviations

BG	Bloch-Gruneisen
BTE	Boltzmann Transport Equation
BZ	Brillouin Zone
CFL	Courant–Friedrichs–Lewy
CVD	Chemical Vapour Deposition
DFT	Density Functional Theory
DG	Discontinuous Galerkin
DoS	(energy) Density of States
EP	Equipartition
FD	Fermi-Dirac
FET	Field-Effect Transistor
FLG	Few Layer Graphene
FWHM	Full Width at Half Maximum (of resistivity vs carrier density)
LB	Linearised Boltzmann
LHS	Left-Hand-Side
MC	Monte Carlo
PEP	Pauli Exclusion Principle
PF	Packing Factor
QD	Quantum Dot
RHS	Right-Hand-Side
RPA	Random Phase Approximation
SL	Superlattice
SLG	Single Layer Graphene
SNR	Signal to Noise Ratio
TVD	Time Variation Diminishing
UV	Ultraviolet
WKB	Wentzel–Kramers–Brillouin

Contents

Chapter 1

Graphene Structure and Charge Transport

1.1 Introduction

Graphene has exciting electronic properties due to its 2D hexagonal carbon structure. The resulting electronic bands, which give rise to electrons with a linear energy-wavevector dispersion, analogous to zero effective mass, were first studied in 1947 by Wallace [1], and later by DiVincenzo and Mele [2] in 1984. In 2004, Geim and Novoselov were able to effectively demonstrate the transfer of atomically thin graphene from bulk graphite onto a silicon dioxide (SiO_2) substrate using scotch tape [3]. Following this, there has been extensive focus on the manufacture of high quality graphene; mostly via exfoliation [4] and chemical vapour deposition [5]. Given the very small effective mass of graphene near the Dirac point (where the conduction and valence bands meet), the electrons behave as relativistic Dirac fermions with a Fermi velocity of $v \sim 10^6$ ms^{-1}. This large velocity allows for potentially high intrinsic electron mobility, reported to be as large as 20 m^2/Vs for suspended graphene, in the low-field regime [6]. It is known that highly dielectric substrates degrade this mobility by as much as two orders of magnitude [7, 8]. Understanding the origins of electron scattering is vital for a complete understanding of the electronic properties in graphene. Advancements in material manufacturing have brought new possibilities to test the fundamental properties of graphene electronics, with some suspended and protectively encapsulated exfoliated graphene samples reported in the ballistic regime [9, 10]. Heterostructures comprising 2D materials have been demonstrated on a research-scale with a broad range of applications, including broadband photodetection [11–13], LEDs [14, 15], tunnelling field effect transistors [16, 17] and flexible electronics [18]. However, there still exists a need for scalable manufacturing techniques to ensure that such layered 2D materials have a wide commercial impact. Additive manufacturing (3D printing) provides a promising solution. A large amount of progress has been made in the development of material inks comprising dielectric, semiconducting and conducting 2D flakes and nano-particles

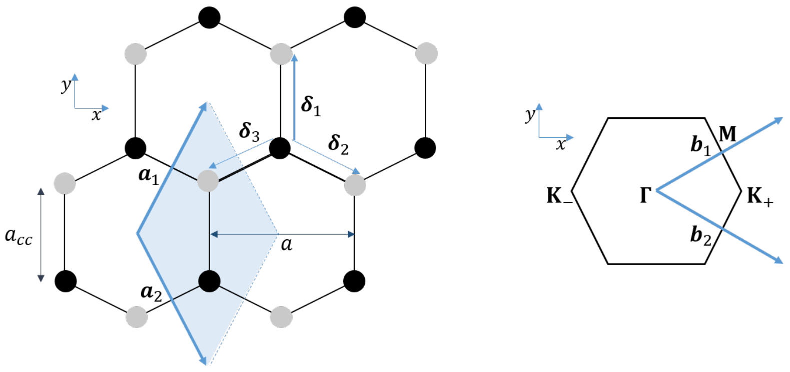

(a) (b)

Figure 1.1: (a) The real-space lattice structure and (b) the first Brillouin zone in k-space. The primitive unit vectors $\mathbf{a}_1$ and $\mathbf{a}_2$, with a magnitude of one lattice constant, $a = 2.46$ Å, make up the unit cell. a_{cc} is the carbon-carbon bond length. Nearest-neighbour vectors are labelled $\delta_1 = \left(0, \frac{a}{\sqrt{3}}\right)$, $\delta_2 = \left(\frac{a}{2}, -\frac{a}{\sqrt{3}}\right)$ and $\delta_3 = \left(-\frac{a}{2}, -\frac{a}{\sqrt{3}}\right)$. The reciprocal lattice vectors $\mathbf{b}_1$ and $\mathbf{b}_2$ define the Brillouin zone, with the high symmetry points $\mathbf{K}_\pm$, $\mathbf{\Gamma}$ and $\mathbf{M}$. Filled black and grey circles are used to distinguish between the two sub-lattices.

[19–26]. However, there is a need for greater understanding of the transport phenomena and structural properties of 3D printed heterostructures.

This introductory chapter outlines the theory that underpins charge carrier scattering in graphene and an overview of the comprehensive subject of transport in discontinuous conductive materials, relevant to inkjet printed structures.

1.2 Electronic Structure of Graphene

1.2.1 Tight-Binding Model

Different hybridization of carbon atoms results in a number of different allotropes with vastly different properties, despite having the same atomic building blocks. Graphene is formed by sp^2 hybridization, whereby an electron is promoted from the 2s orbital into the 2p orbital in order to form an array of sigma bonds in a 2D plane with a separation of 120°. The atoms are therefore arranged in a 2D hexagonal lattice, with the out-of-plane dangling bonds forming a network of π-bonds.

The real-space lattice has a basis of two atoms, which are often referred to as the two sub-lattices. The unit cell, as shown in fig. 1.1a, is defined by two primitive lattice vectors, $\mathbf{a}_1 = \left(\frac{a}{2}, \frac{\sqrt{3}a}{2}\right)$ and $\mathbf{a}_2 = \left(\frac{a}{2}, -\frac{\sqrt{3}a}{2}\right)$, where $a = 2.46$ Å is the lattice constant [27], related to the inter-atomic distance, a_{cc}, by $a = a_{cc}/\sqrt{3}$. The reciprocal lattice vectors are $\mathbf{b}_1 = \left(\frac{2\pi}{a}, \frac{2\pi}{\sqrt{3}a}\right)$ and $\mathbf{b}_2 = \left(\frac{2\pi}{a}, -\frac{2\pi}{\sqrt{3}a}\right)$. This results in the hexagonal first Brillouin zone shown in fig. 1.1b.

In the tight-binding model, the electronic wavefunction of the j^{th} orbital, $\Psi_j(\mathbf{k}, \mathbf{r})$, is given as a superposition of Bloch functions,

$$\Phi_j(\mathbf{k},\mathbf{r}) = \frac{1}{\sqrt{N}} \sum_{i=1}^{N} e^{i\mathbf{k}\cdot\mathbf{R}_{i,j}} \phi_j\left(\mathbf{r} - \mathbf{R}_{i,j}\right), \tag{1.1}$$

where $\mathbf{R}_{i,j}$ is the lattice vector corresponding to the position of the j^{th} atomic orbital within the i^{th} unit cell. This can be applied to the $2\mathrm{p}^{\mathrm{z}}$ orbitals at each atomic site of the two sub-lattices, resulting in a basis of two Bloch functions. We can define a 4 × 4 Hamiltonian, H, in this basis with matrix elements

$$H_{m,n} = \frac{1}{N} \sum_{i=1}^{N} \sum_{j=1}^{N} e^{i\mathbf{k}\cdot(\mathbf{R}_{n,j} - \mathbf{R}_{m,i})} \left\langle \phi_m\left(\mathbf{r} - \mathbf{R}_{m,i}\right) \left| H \right| \phi_n\left(\mathbf{r} - \mathbf{R}_{n,j}\right) \right\rangle \tag{1.2}$$

where m and n can be either of the sublattices A and B. We shall only consider the most dominant terms within the Hamiltonian. These are the terms described by on-site and nearest-neighbour interactions. Therefore, the diagonal matrix elements are given by same-site interactions ($i = j$),

$$H_{AA} \approx \left\langle \phi_A\left(\mathbf{r} - \mathbf{R}_{A,i}\right) \left| H \right| \phi_A\left(\mathbf{r} - \mathbf{R}_{A,i}\right) \right\rangle = \varepsilon_{2p}, \tag{1.3}$$

where $\varepsilon_{2\mathrm{p}}$ is defined as the energy of the $2\mathrm{p}^{\mathrm{z}}$ orbital [28]. The off-diagonal elements, describing inter-sublattice coupling, are given by the nearest neighbour interactions,

$$H_{AB} \approx \frac{1}{N} \sum_{i=1}^{N} \sum_{l=1}^{3} e^{i\mathbf{k}\cdot\boldsymbol{\delta}_l} \left\langle \phi_A\left(\mathbf{r} - \mathbf{R}_{A,i}\right) \left| H \right| \phi_B\left(\mathbf{r} - \mathbf{R}_{B,l}\right) \right\rangle = -\gamma_0 f(\mathbf{k}), \tag{1.4}$$

where we have defined the nearest-neighbour hopping parameter $\gamma_0 = -t = \left\langle \phi_A\left(\mathbf{r} - \mathbf{R}_{A,i}\right) \left| H \right| \phi_B\left(\mathbf{r} - \mathbf{R}_{B,l}\right) \right\rangle$, the function

$$f(\mathbf{k}) = \sum_{l=1}^{3} e^{i\mathbf{k}\cdot\boldsymbol{\delta}_l} = e^{ik_y a/\sqrt{3}} + 2e^{-ik_y a/2\sqrt{3}} \cos\left(k_x a/2\right) \tag{1.5}$$

and the respective positions of the neighbouring atoms $\boldsymbol{\delta}_l = \mathbf{R}_{B,l} - \mathbf{R}_{A,i}$ (shown in fig. 1.1a). Taking the complex conjugates gives $H_{BB} = H^*_{AA} = \varepsilon_{2p}$ and $H_{BA} = H^*_{AB} = -\gamma_0 f^*(\mathbf{k})$, such that

$$H = \begin{pmatrix} \varepsilon_{2p} & -\gamma_0 f(\mathbf{k}) \\ -\gamma_0 f^*(\mathbf{k}) & \varepsilon_{2p} \end{pmatrix}. \tag{1.6}$$

Similarly, an overlap matrix, S, with elements

$$S_{m,n} = \frac{1}{N} \sum_{i=1}^{N} \sum_{j=1}^{N} e^{i\mathbf{k}\cdot(\mathbf{R}_{n,j} - \mathbf{R}_{m,i})} \left\langle \phi_m\left(\mathbf{r} - \mathbf{R}_{m,i}\right) \middle| \phi_n\left(\mathbf{r} - \mathbf{R}_{n,j}\right) \right\rangle \tag{1.7}$$

accounts for non-orthogonality of neighbouring atomic states. Following the same steps as for the Hamiltonian, we find that

$$S = \begin{pmatrix} 1 & s_0 f(\mathbf{k}) \\ s_0 f^*(\mathbf{k}) & 1 \end{pmatrix}, \tag{1.8}$$

where $s_0 = \langle \phi_A(\mathbf{r} - \mathbf{R}_{A,i}) | \phi_B(\mathbf{r} - \mathbf{R}_{B,l}) \rangle$. Solving $H\psi_j = \varepsilon_j S \psi_j$ using

$$\det(H - \varepsilon_j S) = 0, \tag{1.9}$$

gives the two energy bands:

$$\varepsilon_s = \frac{\varepsilon_{2p} + s\gamma_0 |f(\mathbf{k})|}{1 - s s_0 |f(\mathbf{k})|}, \tag{1.10}$$

where $s = \pm 1$ denotes the band indices, conduction and valence bands respectively. We set the energy axis such that $\varepsilon_{2p} = 0$ is the zero-point energy and use the values $\gamma_0 = 3.033\,\mathrm{eV}$ and $s_0 = 0.129$ [27]. The resulting band structure, shown in fig. 1.2a, has a band crossing at the K points with no band gap, from which we name two inequivalent valleys K_- and K_+. In a similar fashion to the band index, s, we will denote the valley index $\zeta = \pm 1$.

Exactly at the valleys (the Dirac point), the wavevector is $\mathbf{K}_\zeta = \zeta(4\pi/3a, 0)$, such that there is no coupling between sublattices, $f(\mathbf{K}_\zeta) = 0$. We can expand about the K points to find the dispersion relation for low energy electrons. Defining a relative momentum $\mathbf{p} = \hbar\mathbf{k} - \hbar\mathbf{K}_\zeta = (p_x, p_y)$ and substituting into eq. (1.5) gives

$$f(\mathbf{k}) \approx -\frac{\sqrt{3}a}{2\hbar}(\zeta p_x - i p_y) \tag{1.11}$$

to first order in momentum, resulting in the Hamiltonian

$$H_\zeta = v \begin{pmatrix} 0 & \zeta p_x - i p_y \\ \zeta p_x + i p_y & 0 \end{pmatrix}, \tag{1.12}$$

where $v = \sqrt{3}a\gamma_0/(2\hbar) \approx 10^6\,\mathrm{ms}^{-1}$ is the "Fermi velocity", often denoted v_F. Throughout this thesis, "v" will be used to denote this constant Fermi velocity, i.e. $v \equiv v_F$. The overlap matrix can be approximated as unitary to first order in momentum and we are left with the energy bands

$$\varepsilon_\pm = s v |\mathbf{p}| \tag{1.13}$$

and corresponding Bloch eigenstates

$$\Phi_\pm = \frac{1}{\sqrt{2A}} \begin{pmatrix} 1 \\ s\zeta e^{i\zeta\varphi} \end{pmatrix} e^{i\mathbf{k}\cdot\mathbf{r}}, \tag{1.14}$$

normalized on the unit cell of area A, where φ is the polar angle of momentum. The Hamiltonian (1.12) is Dirac-like and the resulting band structure (1.13) leads to elec-

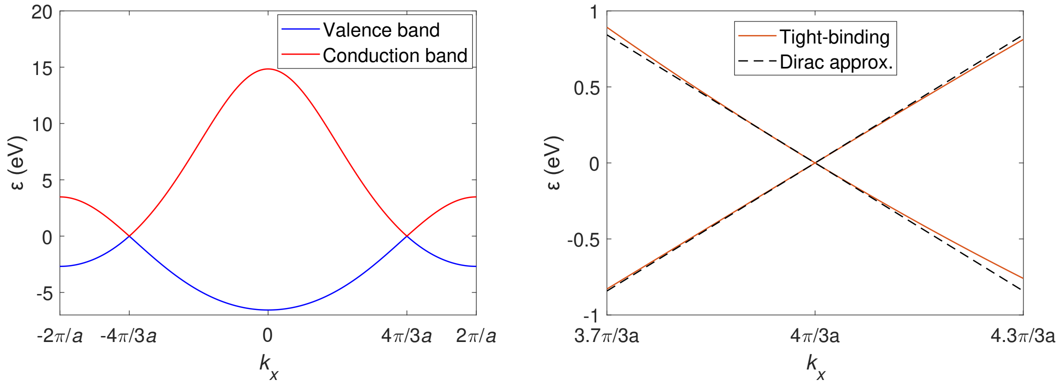

(a) (b)

Figure 1.2: Band structure of single layer graphene in the tight-binding approximation. (a) Variation of the eigenvalues (1.10) for $k_y = 0$. (b) The Dirac eigenvalues (1.13) compared to a magnification of (a) around the Dirac point.

trons with zero effective mass and a constant velocity, v. As shown in fig. 1.2b, the Dirac form of the Hamiltonian is a reasonable approximation to the tight-binding model for low energy electrons ($|\varepsilon| \lesssim 0.25$ eV).

1.2.2 Charge Density and Quantum Capacitance

The linear dispersion relation (1.13), results in a density of states that depends linearly on energy,

$$D(\varepsilon) = \frac{g_s g_v}{2\pi} \frac{|\varepsilon|}{\hbar^2 v^2}, \tag{1.15}$$

where $g_s = 2$ and $g_v = 2$ are the spin and valley degeneracies, respectively. Using the Fermi-Dirac distribution function,

$$f_0(\varepsilon) = \frac{1}{e^{\beta(\varepsilon - \varepsilon_F)} + 1} \tag{1.16}$$

where ε_F is the chemical potential, $\beta = 1/(k_B T)$, and T is the absolute temperature of the graphene sheet, for the probability of occupation of any given state with energy ε, we find the Fermi-Dirac integral form of the charge carrier densities,

$$\begin{aligned} n = \tfrac{g_s g_v}{2\pi} \left(\tfrac{k_B T}{\hbar v}\right)^2 \int_0^\infty \tfrac{\nu}{e^{\nu-\eta}+1} \mathrm{d}\nu = \tfrac{2}{\pi} \left(\tfrac{k_B T}{\hbar v}\right)^2 F_1(\eta) \\ p = \tfrac{g_s g_v}{2\pi} \left(\tfrac{k_B T}{\hbar v}\right)^2 \int_0^\infty \tfrac{\nu}{e^{\nu+\eta}+1} \mathrm{d}\nu = \tfrac{2}{\pi} \left(\tfrac{k_B T}{\hbar v}\right)^2 F_1(-\eta), \end{aligned} \tag{1.17}$$

for electrons in the conduction band, n, and holes in the valence band, p, where F_1 is the first-order complete Fermi-Dirac integral and we have defined the dimensionless variables $\nu = \varepsilon/(k_B T)$ and $\eta = \varepsilon_F/(k_B T)$. These complete functions are related to the polylogarithms, $F_j(x) = -\mathrm{Li}_{j+1}\left[-e^x\right]$, such that

$$n(\varepsilon_F, T) = -\frac{g_s g_v}{2\pi} \left(\frac{k_B T}{\hbar v}\right)^2 \mathrm{Li}_2 \left[-\exp\left(\frac{\varepsilon_F}{k_B T}\right)\right] \tag{1.18}$$

and

$$p(\varepsilon_F, T) = -\frac{g_s g_v}{2\pi}\left(\frac{k_B T}{\hbar v}\right)^2 \mathrm{Li}_2\left[-\exp\left(-\frac{\varepsilon_F}{k_B T}\right)\right]. \tag{1.19}$$

For large chemical potentials, or low temperature, $|\varepsilon_F| \gg k_B T$, the density of electrons (1.18) is

$$n \approx \frac{g_s g_v}{4\pi}\frac{{\varepsilon_F}^2}{\hbar^2 v^2}, \tag{1.20}$$

and the density of holes, $p \to 0$, for $\varepsilon_F > 0$. In the same limit, if $\varepsilon_F < 0$, the density of electrons and holes is reversed due to the symmetry of eqs. (1.18) and (1.19). In the opposing limit, $|\varepsilon_F| \ll k_B T$, the charge density is dominated by thermally excited electron-hole pairs,

$$n(\varepsilon_F = 0, T) = p(\varepsilon_F = 0, T) = \frac{g_s g_v \pi}{24}\left(\frac{k_B T}{\hbar v}\right)^2. \tag{1.21}$$

The chemical potential can be expressed in terms of a channel potential, V_{ch}, $\varepsilon_F = eV_{ch}$, where e is the elementary charge of an electron. Then the quantum capacitance,

$$C_q = \frac{\partial Q_{net}}{\partial V_{ch}}, \tag{1.22}$$

encapsulates the effect of the density of states on the occupancy of states and, therefore, the net sheet charge density Q_{net} in response to a change in the potential energy of the graphene sheet, V_{ch}. The net sheet charge density here is given by $Q_{net} = e(p - n)$. We will also define the total transport charge density, $Q_{tot} = eN_{tot}$, as the total charge contributing to current in an applied electric field, where $N_{tot} = n + p$ is the total carrier density. This will be further discussed in section 2.1. Using eqs. (1.18) and (1.19), the quantum capacitance is

$$C_q = \frac{g_s g_v e^2}{2\pi}\frac{k_B T}{\hbar^2 v^2}\left[\ln\left(2 + 2\cosh\left(\frac{\varepsilon_F}{k_B T}\right)\right)\right]. \tag{1.23}$$

When additional graphene layers are added, the energy bands become parabolic around the K points with a tunable band gap between conduction and valence bands [28]. In bilayer graphene the band gap has been measured as large as 250 meV under large displacement fields [29]. To consider the most general case of a parabolic dispersion relation, we will leave the bandgap, ε_g, arbitrary. The density of states is constant,

$$D = \frac{g_s g_v m^*}{2\pi\hbar^2} \tag{1.24}$$

where m^* is the effective mass. Fixing $\varepsilon = 0$ at the middle of the band gap, we now have the incomplete Fermi-Dirac integrals

$$\begin{aligned} n &= \tfrac{g_s g_v m^*}{2\pi\hbar^2} k_B T \int_{\frac{\varepsilon_g}{2k_B T}}^{\infty} \tfrac{1}{e^{\nu-\eta}+1}\mathrm{d}\nu \\ p &= \tfrac{g_s g_v m^*}{2\pi\hbar^2} k_B T \int_{\frac{\varepsilon_g}{2k_B T}}^{\infty} \tfrac{1}{e^{\nu+\eta}+1}\mathrm{d}\nu, \end{aligned} \tag{1.25}$$

since states residing in the bandgap cannot be occupied. These integrals are evaluated as

$$n = \frac{g_s g_v m^*}{2\pi\hbar^2} k_B T \left[\ln \left(1 + e^{-\frac{\varepsilon_g}{2k_B T} + \eta} \right) \right] \tag{1.26}$$

and

$$p = \frac{g_s g_v m^*}{2\pi\hbar^2} k_B T \left[\ln \left(1 + e^{-\frac{\varepsilon_g}{2k_B T} - \eta} \right) \right]. \tag{1.27}$$

It is important to note that in the limit $\varepsilon_g \to 0$, we retrieve the same form as expected for the complete Fermi-Dirac integral functions:

$$\begin{array}{c} n = -\frac{g_s g_v m^*}{2\pi\hbar^2} k_B T \mathrm{Li}_1 \left(-e^{\eta} \right) \\ p = -\frac{g_s g_v m^*}{2\pi\hbar^2} k_B T \mathrm{Li}_1 \left(-e^{-\eta} \right) \end{array}. \tag{1.28}$$

1.3 Fermi's Golden Rule

The influence of external perturbations to the lattice potential is to 'scatter' electrons between the different eigenstates of eq. (1.14). Fermi's golden rule gives the transition rates between such states. This is an important tool that allows us to understand macroscopic properties, such as the mobility, of the many-body ensemble based upon the quantum mechanics that governs the individual transitions.

Possible causes of such perturbations will be discussed in sections 2.3.2 and 2.4. For now, we can consider two types: constant in time, and harmonically time-varying. An example of the former is a static charged impurity, whilst the latter could be a harmonically oscillating phonon.

The Hamiltonian now includes this perturbation, $U(t)$, as

$$H = H_0 + U(t), \tag{1.29}$$

where H_0 is the unperturbed Hamiltonian of the lattice (1.12), with corresponding eigenstates (1.14). The golden rule is derived using time-dependant perturbation theory. We describe the time-dependence of the eigenstates using the Schrödinger equation in the Dirac picture,

$$i\hbar \frac{\partial}{\partial t} |\Psi(t)\rangle = U_I(t) |\Psi(t)\rangle \tag{1.30}$$

where $U_I(t) = e^{iH_0 t/\hbar} U(t) e^{-iH_0 t/\hbar}$. We denote the initial electron state $|\Psi(t = t_0)\rangle = |i\rangle$, which corresponds to some Bloch eigenstate Φ_i of H_0, with eigenenergy ε_i. Considering electrons near the Dirac point, ε_i and Φ_i are given by eqs. (1.13) and (1.14) respectively.

From eq. (1.30), the wavefunction at time t, $\Psi(t)$, is given by

$$|\Psi(t)\rangle = |i\rangle + \frac{1}{i\hbar} \int_{t_0}^{t} \mathrm{d}t' U_I(t') |i\rangle \tag{1.31}$$

to first order in the perturbation, U. We assume a harmonically time varying perturbation with an adiabatic amplitude such that the states of the initial Hamiltonian, H_0, are exact in the limit $t \to -\infty$,

$$U(t) = e^{\eta t} U \left(e^{-i\omega t} + e^{i\omega t}\right). \tag{1.32}$$

We will later take the limit $\eta \to 0^+$, describing a harmonically oscillating potential with constant amplitude. Taking the overlap of eq. (1.31) with some 'final' state $|f\rangle$ and evaluating the integral in the limit $t_0 \to -\infty$,

$$\langle f|\Psi(t)\rangle = \langle f|U|i\rangle \left[\frac{e^{i(\varepsilon_f-\varepsilon_i-\hbar\omega)t/\hbar}e^{\eta t}}{\varepsilon_i-\varepsilon_f+\hbar\omega+i\hbar\eta} + \frac{e^{i(\varepsilon_f-\varepsilon_i+\hbar\omega)t/\hbar}e^{\eta t}}{\varepsilon_i-\varepsilon_f-\hbar\omega+i\hbar\eta}\right] \tag{1.33}$$

gives the probability amplitude of finding the electron in the state $|f\rangle$ at time t. The transition rate of electrons from the initial to the final state is given by the rate of change of the probability of occupation of the final state due to the harmonic perturbation $U(t)$ made on the initial states in the adiabatic limit ($\eta \to 0^+$),

$$S_{i\to f} = \lim\nolimits_{\eta\to 0^+} \frac{\mathrm{d}}{\mathrm{d}t} \left|\langle f|\Psi(t)\rangle\right|^2 = \frac{2\pi}{\hbar} \left|U_{fi}\right|^2 \left[\delta\left(\varepsilon_i-\varepsilon_f+\hbar\omega\right) + \delta\left(\varepsilon_i-\varepsilon_f-\hbar\omega\right)\right] \tag{1.34}$$

where $U_{fi} = \langle f|U|i\rangle$ and we have used the identity $\delta(x) = \frac{1}{\pi}\lim_{\eta\to 0^+}\frac{\eta}{x^2+\eta^2}$. The two terms in eq. (1.34) represent two separate events: absorption and emission into the oscillating modes of the potential.

For a static potential, the transitions are elastic: the initial and final electron states have equal energy. This can be seen by setting the frequency of oscillation, ω, to 0. In this case,

$$S_{i\to f} = \frac{2\pi}{\hbar}|U_{fi}|^2\delta(\varepsilon_f-\varepsilon_i). \tag{1.35}$$

From here onwards, we will label the states with respect to their wavevector, i.e. $S_{\mathbf{k}\to\mathbf{k}'}$ is the transition rate of electrons from an initial state with wavevector $\mathbf{k}$ to a final state with wavevector $\mathbf{k}'$. In general, the perturbation, $U(t)$, does not depend on the orientation of the wavevector, φ, so the matrix element is

$$U_{\mathbf{k}'\mathbf{k}} = \frac{1}{2A}\langle\mathbf{k}'|\,U\,|\mathbf{k}\rangle\, e^{i(\mathbf{k}'-\mathbf{k})\cdot\mathbf{R}}\left(1+ss'e^{i\zeta\theta_{\mathbf{k},\mathbf{k}'}}\right) \tag{1.36}$$

for intra-valley scattering ($\zeta' = \zeta$), using eq. (1.14) for the eigenstates relative to the position of the source of the potential, $\mathbf{R}$. In eq. (1.36), $|\mathbf{k}\rangle = \exp(i\mathbf{k}\cdot\mathbf{r})$, $\theta_{\mathbf{k},\mathbf{k}'} = \varphi_{\mathbf{k}}-\varphi_{\mathbf{k}'}$ is the angle between $\mathbf{k}$ and $\mathbf{k}'$, and $ss' = \pm 1$ for intra- and inter-band transitions respectively. This simply results in taking the 2D Fourier transform of the perturbation,

$$\tilde{U} = \langle\mathbf{k}'|\,U\,|\mathbf{k}\rangle = \int U(\mathbf{r})e^{-i\mathbf{q}\cdot\mathbf{r}}\mathrm{d}\mathbf{r} \tag{1.37}$$

where we have defined $\mathbf{q} = \mathbf{k}'-\mathbf{k}$.

Considering a sample of finite area, A, in the 2D graphene plane, there can be a number of scatterers available to cause transitions, such that the total perturbation is a sum over the N individual perturbations at positions $\mathbf{R}_i$, $U(\mathbf{r}) = \sum_{i=1}^{N} u(\mathbf{r} - \mathbf{R}_i)$. For randomly distributed scatterers of the same type, we can simply accumulate the transition rates, since $|\mathrm{FT}[U(\mathbf{r})]|^2 = \left|\sum_{i=1}^{N} \mathrm{FT}[u(\mathbf{r} - \mathbf{R}_i)]\right|^2 \approx N\,|\mathrm{FT}[u(\mathbf{r})]|^2$. We will consider the effects of correlated distributions in section 3.4. For random distributions, we define a function, Δ, which encapsulates the number of scatterers available for the allowed transitions, such that

$$S_{\mathbf{k}\to\mathbf{k}'} = \frac{\pi}{A^2\hbar}|\tilde{u}(q)|^2(1 + ss'\cos\theta_{\mathbf{k},\mathbf{k}'})\Delta_{\mathbf{k}\to\mathbf{k}'}. \tag{1.38}$$

For inelastic scattering

$$\Delta^{inel}_{\mathbf{k}\to\mathbf{k}'} = N\delta(\varepsilon(\mathbf{k}') - \varepsilon(\mathbf{k})), \tag{1.39}$$

and for elastic scattering

$$\Delta^{el}_{\mathbf{k}\to\mathbf{k}'}(\omega) = N(\omega)\delta(\varepsilon(s',\mathbf{k}')-\varepsilon(s,\mathbf{k})-\hbar\omega)+(N(\omega)+1)\delta(\varepsilon(s',\mathbf{k}')-\varepsilon(s,\mathbf{k})+\hbar\omega), \tag{1.40}$$

where $N(\omega)$ is the number of harmonically oscillating scatterers of frequency ω, given by the Bose-Einstein distribution function

$$N(\omega) = \frac{1}{e^{\beta\hbar\omega} - 1}. \tag{1.41}$$

Note that for the emission process, the number of scatterers, $N(\omega) + 1$, encapsulates both the phonon occupation of $N(\omega)$ available to induce scattering (stimulated emission) and the ability of an electron itself to emit into the phonon mode of frequency ω (spontaneous emission).

1.4 Boltzmann Transport and Drude Conductivity

When the averaged distance between scattering events, l_s, is much smaller than the device length, the electron momenta is dephased and transport is diffusive. In this case, the Drude model is employed to describe the conductivity in terms of scattering of classical-like particles from their classically accelerated trajectories. The Boltzmann transport equation (BTE) can be used to determine the evolution of the distribution function, $f(\mathbf{x}, \mathbf{k})$, using kinetic theory. The two parts that govern the electron trajectory, free drift and instantaneous transitions, are described separately, such that the evolution is given by three terms:

$$\frac{\partial f(t,\mathbf{x},\mathbf{k})}{\partial t} + \mathbf{v}\cdot\nabla_{\mathbf{x}} f(t,\mathbf{x},\mathbf{k}) + \frac{1}{\hbar}\mathbf{F}\cdot\nabla_{\mathbf{k}} f(t,\mathbf{x},\mathbf{k}) = \left(\frac{\partial f(t,\mathbf{x},\mathbf{k})}{\partial t}\right)_{coll}. \tag{1.42}$$

The second term on the left hand side of eq. (1.42) describes the real-space diffusive motion of particles, and the third term is the acceleration of particles due to some electromagnetic force, $\mathbf{F}$; these two terms are the free drift part. The right hand side, the 'collision term', is given by

$$\begin{aligned}\left(\frac{\partial f(t,\mathbf{x},\mathbf{k})}{\partial t}\right)_{coll} = \sum_{\mathbf{k}'} \big[& S_{\mathbf{k}'\to\mathbf{k}} f(t,\mathbf{x},\mathbf{k}')(1-f(t,\mathbf{x},\mathbf{k})) \\ & - S_{\mathbf{k}\to\mathbf{k}'} f(t,\mathbf{x},\mathbf{k})(1-f(t,\mathbf{x},\mathbf{k}'))\big],\end{aligned} \tag{1.43}$$

where the two terms describe opposing transitions, maintaining a detailed balance. In the case of spatial homogeneity, we can use the homogenised Boltzmann equation,

$$\frac{\partial f(t,\mathbf{k})}{\partial t} + \frac{1}{\hbar}\mathbf{F}\cdot\nabla_{\mathbf{k}} f(t,\mathbf{k}) = \left(\frac{\partial f(t,\mathbf{k})}{\partial t}\right)_{coll}, \tag{1.44}$$

where we eliminate the real spatial coordinates and only consider the trajectory of electrons in reciprocal (k) space. Given a steady-state solution to eq. (1.44), $f(\mathbf{k})$, we can calculate the current density

$$\mathbf{J} = e\frac{g_s g_v}{(2\pi)^2}\frac{1}{\hbar}\int f(\mathbf{k})\nabla_{\mathbf{k}}\varepsilon(\mathbf{k})\mathrm{d}\mathbf{k} = e\frac{g_s g_v}{(2\pi)^2}\int \mathrm{d}\theta \int k\mathrm{d}k f(\mathbf{k})\mathbf{v} \tag{1.45}$$

where $\mathbf{v} = v(\cos\theta\hat{\mathbf{x}} + \sin\theta\hat{\mathbf{y}})$.

Using eq. (1.38), the total rate at which electrons, of wavevector $\mathbf{k}$, are scattered is given by the sum over all possible final states $\mathbf{k}'$,

$$\Gamma(\mathbf{k}) = \sum_{\mathbf{k}'} S_{\mathbf{k}\to\mathbf{k}'} \approx \frac{A}{(2\pi)^2}\int S_{\mathbf{k}\to\mathbf{k}'}\mathrm{d}\mathbf{k}', \tag{1.46}$$

where $(2\pi)^2/A$ is the reciprocal space area between states.

The collisional relaxation time, $\tau_c = 1/\Gamma$, gives the mean free time between collisions. Within the Drude model for the diffusive conductivity, the motion of the individual electrons between individual scatter events is assumed to be ballistic, and the events are assumed to occur instantaneously. To get the measurable relaxation time, the effect of the transition on the change in the electrons trajectory should be considered. The weighted mean free time, which we call the single-electron momentum relaxation time, τ_e, where

$$\frac{1}{\tau_e(\mathbf{k})} = \sum_{\mathbf{k}'} S_{\mathbf{k}\to\mathbf{k}'}(1-\cos\theta_{\mathbf{k},\mathbf{k}'}) \approx \frac{A}{(2\pi)^2}\int S_{\mathbf{k}\to\mathbf{k}'}(1-\cos\theta_{\mathbf{k},\mathbf{k}'})\mathrm{d}\mathbf{k}', \tag{1.47}$$

takes into account the relative effect of the angle of scattering, $\theta_{\mathbf{k},\mathbf{k}'}$, on the change in momentum.

The homogenised Boltzmann eq. (1.44), is highly nonlinear. To find analytical solutions, it is generally linearised by assuming a linear shift in the distribution function, proportional to the momentum relaxation time and of first order in the applied field [30], $f = f_0 - e\tau\mathbf{E}\cdot\mathbf{v}\frac{\partial f_0}{\partial\varepsilon}$, where f_0 is the Fermi-Dirac distribution function (1.16). The derivation of the perturbed distribution function will be discussed in more detail in section 3.2. Using eq. (1.45), the conductivity is thus

$$\sigma = \frac{e^2 v^2}{2} \int_{-\infty}^{\infty} \mathrm{d}\varepsilon D(\varepsilon) \tau(\varepsilon) \left(-\frac{\partial f_0}{\partial \varepsilon} \right). \tag{1.48}$$

The momentum relaxation time, τ, is calculated in reference [31] using the BTE (eq. (1.44)),

$$\frac{1}{\tau(\mathbf{k})} \approx \frac{A}{(2\pi)^2} \int S_{\mathbf{k}\to\mathbf{k}'} (1 - \cos\theta_{\mathbf{k},\mathbf{k}'}) \frac{1 - f_0(\mathbf{k}')}{1 - f_0(\mathbf{k})} \mathrm{d}\mathbf{k}'. \tag{1.49}$$

Equation (1.49) is the single electron momentum relaxation rate, eq. (1.47), modified by the occupation of electrons in the states $\mathbf{k}$ and $\mathbf{k}'$ to account for the electron ensemble. In the case of elastic scattering, $\mathbf{k} = \mathbf{k}'$, eqs. (1.47) and (1.49) are equivalent. In the case of inelastic scattering, eq. (1.49) conserves the detailed balance, dependant upon the relative occupation of states at $\mathbf{k}$ and $\mathbf{k}'$.

For finite temperatures, it is useful to exploit the symmetry between conduction and valence bands. Given that $f_0(-\varepsilon, \varepsilon_F) = 1 - f_0(\varepsilon, -\varepsilon_F)$, and the transition rates, $S_{\mathbf{k}\to\mathbf{k}'}$, only depend on $|\varepsilon|$ in general, we can split eq. (1.48) into two terms:

$$\sigma = \frac{e^2 v^2}{2} \int_0^{\infty} \mathrm{d}\varepsilon D(\varepsilon) \left[\tau(\varepsilon, \varepsilon_F) \left(-\frac{\partial f(\varepsilon, \varepsilon_F)}{\partial \varepsilon} \right) + \tau(\varepsilon, -\varepsilon_F) \left(-\frac{\partial f(\varepsilon, -\varepsilon_F)}{\partial \varepsilon} \right) \right], \tag{1.50}$$

where the first term is the contribution from electrons and the second is the contribution from holes.

We can rewrite eq. (1.48), in terms of the ensemble averaged momentum relaxation rate, $\langle \tau \rangle$,

$$\sigma = \frac{e^2}{\pi \hbar^2} \langle \tau \rangle \int \mathrm{d}\varepsilon f_0(\varepsilon), \tag{1.51}$$

where

$$\langle \tau \rangle = \frac{\int \varepsilon \tau(\varepsilon) \left(-\frac{\partial f_0}{\partial \varepsilon} \right) \mathrm{d}\varepsilon}{\int \varepsilon \left(-\frac{\partial f_0}{\partial \varepsilon} \right) \mathrm{d}\varepsilon}. \tag{1.52}$$

In the degenerate, low temperature regime, the Fermi-Dirac distribution (1.16) is a Heaviside step function, $\vartheta(\varepsilon_F - \varepsilon(\mathbf{k}))$, and the derivative is a delta function, $\delta(\varepsilon_F - \varepsilon(\mathbf{k}))$. Consequently, in the limit $T \to 0$, the ensemble average is given by the value at the Fermi level, $\langle \tau \rangle = \tau(\varepsilon_F)$. Using eq. (1.20) for the carrier density, we find the mobility

$$\mu = \frac{\sigma}{ne} \approx \frac{e v^2 \tau(\varepsilon_F)}{\varepsilon_F}. \tag{1.53}$$

1.5 Charge Transport in Localised Systems

A system with strong disorder results in localised electronic states. Anderson localisation can occur in lattice structures in the presence of a large number of impurities or defects. In granular materials, there is a structural localisation of states within the grains and, in general, an absence of states in the surrounding medium. Localised states also appear in disordered organic (polymer) conductors.

1.5.1 Hopping Conductivity

To conduct, electrons need to be able to move between localised states via a tunnelling or hopping process. In granular conductors, the dynamics is usually assumed to depend entirely on such processes and the effect of scattering within the granules is assumed to be negligible. The rate of thermally assisted hopping from site i with energy ε_i to site j with energy ε_j can be described by the Miller-Abrahams expression [32, 33],

$$\gamma_{ij} = \gamma_0 e^{-\alpha R_{ij}} \begin{cases} e^{-(\varepsilon_j - \varepsilon_i)/k_B T} & \text{for } \varepsilon_j > \varepsilon_i \\ 1 & \text{for } \varepsilon_j \leq \varepsilon_i \end{cases}, \tag{1.54}$$

where: γ_0 is a constant, describing the attempt frequency and is related to the strength of phonon coupling; α is the tunnel constant, also known as the inverse localisation radius; R_{ij} is the distance between sites i and j; and T is the temperature.

The conductivity depends directly on the hopping rate and is often used in the simplified form of the Arrhenius equation

$$\sigma_{Arrhenius} \propto e^{-\alpha r} e^{-E_c/k_B T}, \tag{1.55}$$

where r is the hopping distance and E_c is the activation energy required to charge a neighbouring state. This expression is used widely in the literature to fit and predict the conductivity of granular conductors, such as nano-crystal arrays [34–36]. Typically hopping is considered to be nearest-neighbour only, since conductivity is exponentially suppressed relative to the distance between sites. However, for small temperatures, the exponential suppression relative to $E_c/k_B T$ becomes important. This means that it can become energetically favourable for an electron to hop further to a site of similar energy. In this case, the distance, r, in eq. (1.55) becomes temperature dependent [34].

Such variable range hopping is often described by

$$\sigma_{VRH} \propto \exp\left[-\left(T_0/T\right)^{1/\beta}\right], \tag{1.56}$$

where β is some exponent depending on the details of the system, such as the dimensionality, and T_0 is a constant depending on the energy density of states/sites and the tunnel constant, α. Mott showed that $\beta = 4$ for a 3D system, assuming a constant density of states around the Fermi level [33, 37]. The same expression with $\beta = 4$ was also derived using a percolation method by Ambegaokar et al. in the presence of energetic and spatial disorder [38]. Equation (1.56) has been found to agree well with the conductivity measured in amorphous germanium at $T < 300$ K [39, 40] and ordered defect compound $\mathrm{CuIn_3Te_5}$ at $T < 210$ K [41].

1.5.2 Field-Effect in Discontinuous and Disordered Media

To model the field-effect in a discontinuous, thin (2D) film, Adkins et al. proposed a model based on the capacitative charging energy required to place a charge on the grains and the detailed balance of relative occupation between grains [42]. Assuming a maximum of one charge per grain, standard Boltzmann statistics are used to determine the probability of any one grain being positively charged (a hole), negatively charged (an electron) or uncharged,

$$\begin{aligned} p_+ &= \exp\left(-\mu_{eff}/k_BT\right) \big/ \left[\exp\left(E_c/k_BT\right) + 2\cosh\left(\mu_{eff}/k_BT\right)\right] \\ p_- &= \exp\left(\mu_{eff}/k_BT\right) \big/ \left[\exp\left(E_c/k_BT\right) + 2\cosh\left(\mu_{eff}/k_BT\right)\right] \\ p_0 &= \exp\left(E_c/k_BT\right) \big/ \left[\exp\left(E_c/k_BT\right) + 2\cosh\left(\mu_{eff}/k_BT\right)\right], \end{aligned} \tag{1.57}$$

respectively, where E_c is the charging energy between flakes and μ_{eff} is an effective chemical potential of the granular system which promotes the charging of grains and is controlled by the gate voltage, V_g, via $CV_g = N(p_- - p_+)$ where C is the areal capacitance density between the gate and the bulk film and N is the areal density of grains. The conductivity depends on the relative occupation of grains, since electrons can only transport into unoccupied states,

$$\sigma_{Adkins} \propto p_0(p_- + p_+). \tag{1.58}$$

Assuming $E_c \gg k_BT$ (a necessary condition for the Adkins model, since multiple charging is neglected) and $\mu_{eff} = 0$, eq. (1.58) has the same form as the Arrhenius equation (1.55). As discussed in [42], this model is derived assuming a granular film which is ordered in both the charging energy between any two grains and their distance apart. The introduction of disorder can cause trapped states, time dependence, frustration and non-ergodicity.

Highly disordered systems exhibiting Anderson localisation or composed of granular structures can display glassy behaviour out of equilibrium [43, 44]. A particular feature of such electron glasses is the anomolous field effect, as observed in granular metal films [45–48]. Unlike the ordinary field effect, where changing the gate voltage causes an increase or decrease in conductivity, depending on the relative change in carrier density, in the anomolous field effect any change in gate voltage results in an increase of conductivity if the electron glass has already equilibrated at the initial gate voltage. This is a feature of the slow response of the electron glass to external perturbation. If a long enough time is left between each measurement, thus allowing the electron glass to reach equilibrium at each gate voltage, the normal field effect can be retrieved, as demonstrated in two-dip experiments [49, 50].

Chapter 2

Electron Scattering in Graphene and Numerical Methods

2.1 Thermal Equilibrium Calculations of Charge Carrier Population in Gated Graphene

We model the effects of gating the graphene sheet with a potential, V_g, over a capacitance, C_d, on the charge carrier population. We anticipate this carrier population to be sensitive to the temperature around the Dirac point, since electrons can easily be excited into the conduction band from the valence band, creating electron-hole pairs, due to the zero-band gap.

Semiconductors have an associated ‘quantum capacitance’, due to the finite density of states. For graphene, we derived this in section 1.2.2. This quantum capacitance can force a voltage drop at the graphene plane compared to what would be expected for a metallic parallel plate capacitor, thus reducing the number of excited carriers. We explore this effect first before considering the simpler parallel plate capacitor model.

2.1.1 Quantum Capacitance Model

Here we model a basic field-effect transistor (FET) consisting of a single gate electrode, separated from the graphene plane via a dielectric medium of capacitance C_d, as shown in fig. 2.1a. A current is passed through the graphene channel by the source and drain electrodes, controlled by the drain-source potential, V_{ds}. The carrier density is controlled by the potential difference across the source and gate electrodes, V_g. We consider diffusive transport with a constant electric field, $E = V_{ds}/L$, across the channel of length L. Applying Kirchoff’s voltage law to the circuit diagram in fig. 2.1b, where we have defined the direction of V_g such that positive V_g corresponds to a positive channel potential, results in the self-consistent equation for the channel potential

$$V_{ch} = \frac{C_d}{C_d + \alpha C_q}(V_g + V(x)) \tag{2.1}$$

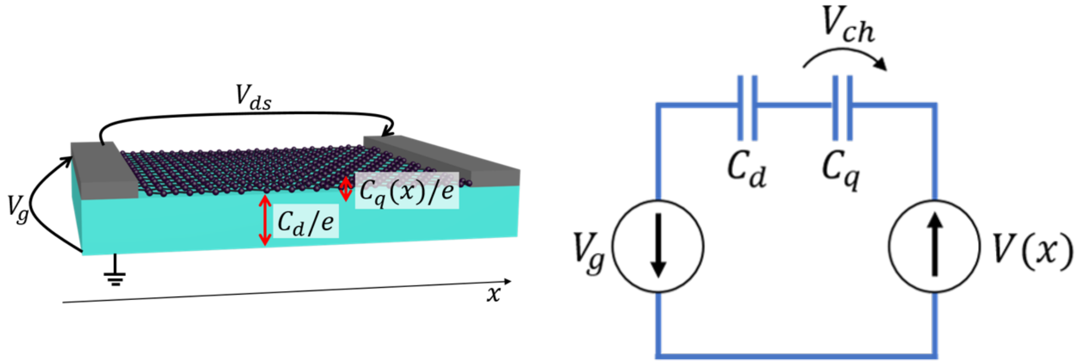

(a) (b)

Figure 2.1: (a) Diagram showing graphene FET. Graphene sheet forms a conducting channel between two electrodes with potential difference V_{ds}. A gate voltage, V_g, is applied over the dielectric gate material. The applied voltages, V_g and V_{ds}, are compensated by a potential difference over the dielectric capacitance, C_d, and the quantum capacitance, C_q. (b) Circuit diagram for FET in figure (a) at position x along the channel length. A gate voltage V_g is applied; the capacitance, C_d, is known for a given dielectric medium between the gate electrode and the graphene plane; and the potential dropped across the channel, $V(x)$, is assumed to increase linearly from 0, at $x = 0$, to V_{ds}, at $x = L$. Kirchoff's law, along with an expression for the quantum capacitance, C_q, can be used to determine the potential, V_{ch}, that controls the chemical potential.

which determines the chemical potential, $\varepsilon_F = eV_{ch}$, where $V(x)$ is the value of the potential at position x along the channel, in the direction of the field, due to the drain-source potential gradient. In eq. (2.1), α is defined as the capacitance weighting factor,

$$Q_{net} = -\int C_q \mathrm{d}V_{ch} = -\alpha C_q V_{ch}. \tag{2.2}$$

From eq. (1.20), at $T = 0$, $n = (eV_{ch})^2/\pi\hbar^2 v^2$. Substituting this into eqs. (2.1) and (2.2) and solving for the channel potential, V_{ch}, results in

$$N_{tot}(T = 0) = n_G + n_Q \left(1 - \sqrt{1 + 2\frac{n_G}{n_Q}}\right) \tag{2.3}$$

for $V(x) = 0$, where $n_G = C_d|V_g|/e$ is the charge density induced by the gate electrode assuming a single parallel plate capacitor and $n_Q = \frac{\pi}{2}\left(\frac{C_d \hbar v}{e^2}\right)^2$ determines the correction due to the quantum capacitance.

In order to probe the electrical properties of graphene, we need to drive a current through the transistor, thus requiring the application of a drain-source potential difference, V_{ds}, across the in-plane electrodes. This creates an inhomogeneity in the potential, $V(x)$, across the channel. We assume that the potential varies linearly across the channel, $V(x) = V_{ds}x/L$. We can calculate the charge density at points along the channel, $n(x) + p(x)$, and define the total carrier density as the mean, $n + p = L^{-1} \int \mathrm{d}x[n(x) + p(x)]$. Figure 2.2a shows the result of including this drain-

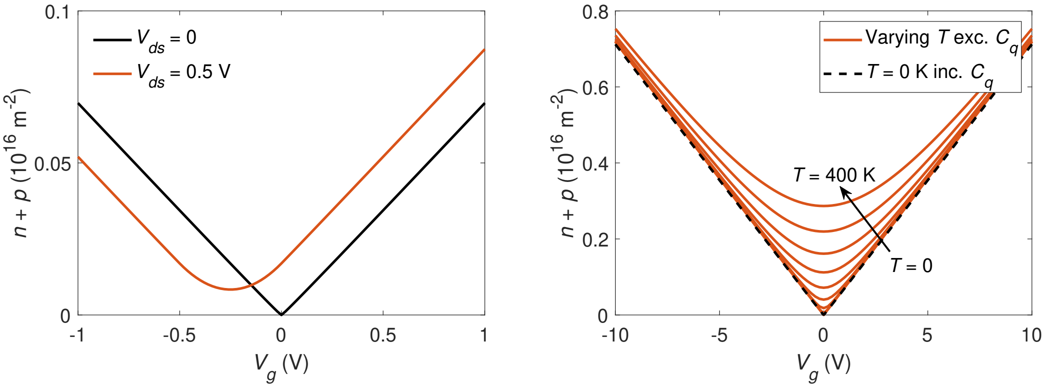

(a) (b)

Figure 2.2: Variation of the total transport carrier density $n + p$ with applied gate voltage, V_g, for $C_d = 1.15 \times 10^{-4}$ Fm^{-2}. (a) Effect of the applied drain-source potential, V_{ds}, on the charge carrier profile, demonstrated here for $T = 0$, calculated using the results of eq. (2.1). (a) Effect of changing the temperature from $T = 0$ to $T = 400$ K in increments of 50 K for $V_{ds} = 0$, calculated excluding (exc.) quantum capacitance using the results of charge conservation with the linear capacitor model, 2.4 (solid orange lines). A comparison of the results including (inc.) quantum capacitance is shown by the black dashed line for $T = 0$ K.

source potential. We see that the total transport charge never reaches 0, due to the inhomogeneity, and the gate voltage of minimum carrier concentration, V_0, is offset by $V_{ds}/2$, the mean of $V(x)$. Such effects have been observed experimentally [51]. However, the effect of drain-source voltage on carrier density is often unimportant, since the applied V_{ds} is usually small compared to the range of gate voltages, V_g. Furthermore, the spatially inhomogeneous residual charge induced by the charged impurity potential, to be demonstrated in section 2.3.1, is much more significant in most devices.

2.1.2 Linear Capacitor Model

We can generally ignore the quantum capacitance, particularly at large gate voltages, where $n_G \gg n_Q$. Neglecting the quantum capacitance and $V(x)$, fig. 2.1b is reduced to a simple parallel plate capacitor with net charge density $|Q_{net}| = C_d|V_g|$. The polarity of the charge, Q_{net}, depends on the direction of the applied gate voltage. By convention, we assume that a positive gate voltage corresponds to a build up of electrons in the graphene layer, i.e. $Q_{net} = -C_d V_g$. To calculate the chemical potential, we equate this gate induced net charge density to the carrier densities, n and p, defined in eqs. (1.18) and (1.19),

$$e(p(\varepsilon_F, T) - n(\varepsilon_F, T)) = -C_d V_g \tag{2.4}$$

thus ensuring conservation of charge density.

For non-zero temperatures we expect, from eq. (1.21), that $N_{tot}(\varepsilon_F = 0, T) = n(\varepsilon_F = 0, T) + p(\varepsilon_F = 0, T) \propto T^2$. Figure 2.2b shows the results of solving eq. (2.4) to calculate the variation of total carrier density with gate voltage and temperature for a gate capacitance of $C_d = 1.15 \times 10^{-4}$ Fm^{-2} (corresponding to a 300 nm layer thickness of SiO$_2$).

Figure 2.2b compares the results for the two calculations, with and without quantum capacitance. Both eqs. (2.1) and (2.4) give $\varepsilon_F = 0$ for $V_g = 0$. Away from this point, we find a minor decrease in the total charge density due to the quantum capacitance of the graphene sheet. The effect of the quantum capacitance is found to be insignificant, validating the approximation of a sheet charge density given by the gate capacitance, n_G. We will choose to use this linear capacitor model for all future calculations, since it is both simpler and more commonly used for experimental fitting.

2.2 Dielectric response: Screening

Screening by the Fermi gas can reduce the effect of external perturbations. This is characterised by a dynamic relative permittivity, $\epsilon_{sc}(\mathbf{q}, \omega)$. In the random phase approximation (RPA), a linear response is assumed; the electrons respond to a linear sum of the external, $\tilde{U}^{ext}$, and induced, $\tilde{U}^{ind}$, potential:

$$\tilde{U}(\mathbf{q}, \omega) = \tilde{U}^{ext}(\mathbf{q}, \omega) + \tilde{U}^{ind}(\mathbf{q}, \omega) = \frac{\tilde{U}^{ext}(\mathbf{q}, \omega)}{\epsilon_{sc}(\mathbf{q}, \omega)}, \tag{2.5}$$

where the potentials are Fourier tranforms with reciprocal space components, $\mathbf{q}$, and frequency of oscillation, ω. The perturbation in the charge density is given in terms of the polarization function, Π,

$$\delta n(\mathbf{q}, \omega) = -\Pi(\mathbf{q}, \omega)\tilde{U}(\mathbf{q}, \omega), \tag{2.6}$$

this results in the induced potential,

$$\tilde{U}^{ind}(\mathbf{q}, \omega) = v_c(q)\delta n(\mathbf{q}, \omega) \tag{2.7}$$

where $v_c(q)$ is the 2D Fourier transform of the coulomb potential [52]. Introducing the variable $\kappa = 4\pi\epsilon_0\epsilon_r$, where ϵ_r is the external dielectric constant (without the addition of free charges),

$$v_c(q) = \frac{2\pi e^2}{\kappa q}. \tag{2.8}$$

Equations (2.5) and (2.7) form a self-consistant set; the solution is a simple geometric series with the result,

$$\epsilon_{sc}(\mathbf{q}, \omega) = 1 + v_c(q)\Pi(\mathbf{q}, \omega). \tag{2.9}$$

The response function is given by the Lindhard function

$$\Pi(q, \omega) = -\frac{g_s g_v}{A} \sum_{\mathbf{k}ss'} \frac{f_{\mathbf{k}s} - f_{\mathbf{k}'s'}}{\hbar\omega + \varepsilon_{\mathbf{k}s} - \varepsilon_{\mathbf{k}'s'} + i\hbar 0_+} \left[\frac{1}{2}\left(1 + ss'\cos\theta_{\mathbf{k},\mathbf{k}'}\right)\right] \tag{2.10}$$

where the term in square brackets results from the angular dependence of the overlap, as in eq. (1.36). For a static potential ($\omega = 0$), summing over bands s and s' and performing the angular integral in eq. (2.10) results in the response function [53]

$$\begin{aligned}\Pi(q, \varepsilon_F, T) = &\frac{2\varepsilon_F}{\pi\hbar^2 v^2} + \frac{q}{4\hbar v} + \frac{4k_B T}{\pi\hbar^2 v^2} + \frac{4k_B T}{\pi\hbar^2 v^2}\ln\left(1 + e^{-\varepsilon_F/k_B T}\right) \\ &- \frac{2}{\pi\hbar^2 v^2}\int_0^{q/2} \mathrm{d}k\sqrt{1 - \left(\frac{2k}{q}\right)^2}\left[\frac{1}{\exp\left(\frac{\hbar v k - \varepsilon_F}{k_B T}\right) + 1} + \frac{1}{\exp\left(\frac{\hbar v k + \varepsilon_F}{k_B T}\right) + 1}\right],\end{aligned} \tag{2.11}$$

where we have assumed that $g_s = g_v = 2$ for graphene. In the long wavelength limit ($q \ll k_F$), the response is well described by the Thomas-Fermi approximation. Since the change in potential energy at any given point, $\delta U(\mathbf{R})$, is equivalent to the apparent change in the chemical potential, $\delta U(\mathbf{R}) = -\delta\varepsilon_F(\mathbf{R})$, one can say that, if the change in potential energy is only slowly varying over space,

$$\Pi_{TF} = \frac{\mathrm{d}n}{\mathrm{d}\varepsilon_F} = \int D(\varepsilon)\frac{\partial f(\varepsilon, \varepsilon_F)}{\partial\varepsilon_F}\mathrm{d}\varepsilon = -\frac{2}{\pi(\hbar v)^2}\int f(\varepsilon, \varepsilon_F)\mathrm{d}\varepsilon. \tag{2.12}$$

This is the Thomas-Fermi approximation of the polarization function. The degeneracy of the distribution at low temperatures can be used to simplify the expression, such that the polarization function is just the density of states at the Fermi-level, $\Pi_{TF}(T = 0) = D(\varepsilon_F)$. Using eq. (1.15) for the polarization, the dielectric screening is

$$\epsilon_{sc}(q)|_{q \ll 2k_F, T=0} \approx 1 + q_s/q, \tag{2.13}$$

where $q_s = 4k_F e^2/(\hbar v\kappa)$ is the Thomas-Fermi wave number.

In the opposing, large energy limit, $q \gg 2k_F$, screening by the conduction band becomes significantly small, such that the polarization function is given only by the polarization of the valence band, $\Pi_{val} = q/4\hbar v$ [54]. In this case, the dielectric screening tends to a constant value,

$$\epsilon_{sc}|_{q \gg 2k_F, T=0} \approx 1 + \frac{\pi r_s}{2}. \tag{2.14}$$

The response function over the full range of wavelengths was calculated by Hwang and Das Sarma [54] using the Lindhard equation (2.10), they found

$$\epsilon_{sc}(q)|_{T=0} = \begin{cases} 1 + q_s/q & \text{for } q \leq 2k_F \\ 1 + r_s\left(\frac{\pi}{2} - \sin^{-1}\left(\frac{2k_F}{q}\right)\right) + \frac{q_s}{q}\left(1 - \frac{1}{2}\sqrt{1 - \frac{4{k_F}^2}{q^2}}\right) & \text{for } q > 2k_F \end{cases} \tag{2.15}$$

where $r_s = e^2/(\hbar v\kappa)$, such that $q_s = 4k_F r_s$. Equation (2.15) returns eqs. (2.13) and (2.14) in the corresponding limits.

In simulations describing the evolution of the distribution function over time, which will be presented in section 2.5, the distribution function can become far from the initial

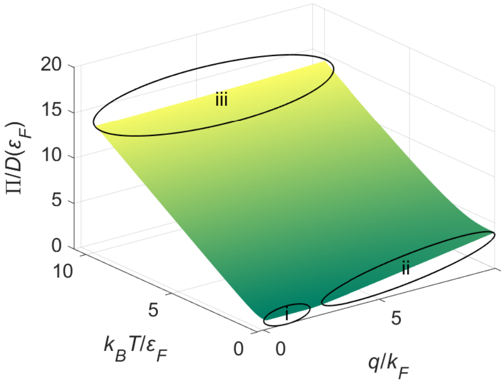

Figure 2.3: Screening polarization response, Π, as a function of temperature, T, and inverse wavelength, q. $D(\varepsilon_F)$ is the density of states at the Fermi energy, ε_F, and k_F is the Fermi wavenumber. (i) $\Pi/D(\varepsilon_F) \approx 1$, (ii) $\Pi/D(\varepsilon_F) \approx \frac{\pi}{8}\frac{q}{k_F}$ and (iii) $\Pi/D(\varepsilon_F) \approx \ln(4)\frac{k_BT}{\varepsilon_F} + \frac{1}{24}\frac{\varepsilon_F}{k_BT}\left(\frac{q}{k_F}\right)^2$ show the three limiting regimes.

Fermi distribution assumed in the derivation of eq. (2.15). However, throughout the time-dependant simulations, the result of the integral in eq. (2.12) does not change, due to conservation of charge. Therefore, since both eqs. (2.13) and (2.14) are independent of the evolution of the distribution function, we define a time-independent two-regime screening function, where Thomas-Fermi screening is assumed for low-energy scattering and the valence electron screening is assumed for high-energy electrons, i.e. we set

$$\epsilon_{sc}(q)|_{T\approx 0} = \begin{cases} 1 + \frac{q_s}{q} & \text{for } q \leq \frac{8}{\pi}k_F \\ 1 + \frac{\pi r_s}{2} & \text{for } q > \frac{8}{\pi}k_F \end{cases}. \tag{2.16}$$

In the high temperature limit, $k_BT \gg \varepsilon_F$, eq. (2.11) is reduced to $\Pi(k_BT \gg \varepsilon_F) \approx 2k_BT\ln(2)/(\pi\hbar^2v^2) + q^2/(12\pi k_BT)$ such that the screening function is

$$\epsilon_{sc}|_{T\gg\varepsilon_F/k_B} \approx 1 + \frac{8\ln(2)e^2k_BT}{\kappa\hbar^2v^2q} + \frac{e^2q}{6\kappa k_BT}. \tag{2.17}$$

Figure 2.3 shows the result of numerical evaluation of eq. (2.11). To summarise, the three analytical limits are given by

$$\begin{aligned} &\text{(i)}\ \Pi(q=0,T=0) = \Pi_{TF}(T=0) = D(\varepsilon_F) = \frac{2\varepsilon_F}{\pi\hbar^2v^2} \\ &\text{(ii)}\ \Pi(q\gg 2k_F,T=0) \approx \Pi_{val} = D(\varepsilon_F)\frac{\pi}{8}\frac{q}{k_F} \\ &\text{(iii)}\ \Pi(q,T\gg\varepsilon_F/k_B) \approx D(\varepsilon_F)\left[\ln(4)\frac{k_BT}{\varepsilon_F} + \frac{1}{24}\frac{\varepsilon_F}{k_BT}\left(\frac{q}{k_F}\right)^2\right]. \end{aligned} \tag{2.18}$$

2.3 Impurities

The presence of any charged impurities of unit charge, e, on/within the substrate material, at distance d from the graphene plane, causes a long-range coulomb potential,

$$u(r) = \frac{e^2}{\kappa\sqrt{r^2+d^2}}, \tag{2.19}$$

before the effects of screening. The integral over the angular part of the 2D Fourier transform results in the integral representation of the zero-*th* order Bessel function,

$$\tilde{u} = \frac{e^2}{\kappa\epsilon_{sc}(q)}\int_0^\infty \frac{2\pi J_0(qr)r\mathrm{d}r}{\sqrt{r^2+d^2}} = \frac{2\pi e^2}{\kappa}\frac{\exp(-qd)}{q\epsilon_{sc}(q)}, \tag{2.20}$$

where we have now added in the k-space screening function, $\varepsilon_{sc}(q)$, from eq. (2.16). The result of integration is as given in reference [55].

2.3.1 Residual Charge

Charged impurities induce a spatially varying potential at the graphene plane, $V_{imp}(\mathbf{r})$, the spatial mean of which we denote $V_{0imp} = \langle V_{imp}(\mathbf{r})\rangle$. This distorts the bands throughout the graphene, as shown schematically in fig. 2.4a. When a potential of V_{0imp} is applied, corresponding to some gate voltage $V_g = V_0$, we mostly cancel this impurity induced potential and achieve the point of minimum carrier density, at which $\varepsilon_F = 0$. However, at this point there still remains spatial fluctuations in the potential, $\delta V_{imp}(\mathbf{r}) = [V_{imp}(\mathbf{r}) - V_{0imp}]$. Quantifying the average fluctuation of the potential about the mean [56, 57],

$$\langle \delta V_{imp}^2\rangle = \langle [V_{imp} - V_{0imp}]^2\rangle = n_{imp}\int \frac{\mathrm{d}^2q}{(2\pi)^2}\,|\tilde{u}(q)|^2 \tag{2.21}$$

and using eq. (2.20),

$$\langle \delta V_{imp}^2\rangle = 2\pi n_{imp}\left(\frac{e^2}{\kappa}\right)^2 C_0(r_s, 4k_F d), \tag{2.22}$$

where n_{imp} is the density of impurities. In eq. (2.22), the function

$$C_0(a,b) = -1 + \frac{4E_1[b]}{(2+\pi a)^2} + \frac{2e^{-b}a}{1+2a} + (1+2ab)e^{2ab}(E_1[2ab] - E_1[b(1+2a)]), \tag{2.23}$$

where $E_1[z]$ represents the exponential integral function [57]. To calculate the extent of the resulting electron-hole puddles, the root mean squared spatial average fluctuation in the impurity potential, $\sqrt{\langle \delta V_{imp}^2\rangle}$, is equated to the spatially averaged shift in the local Dirac point, $\langle \delta\varepsilon_{imp}\rangle$ [57]. A self-consistent equation is obtained for the offset of

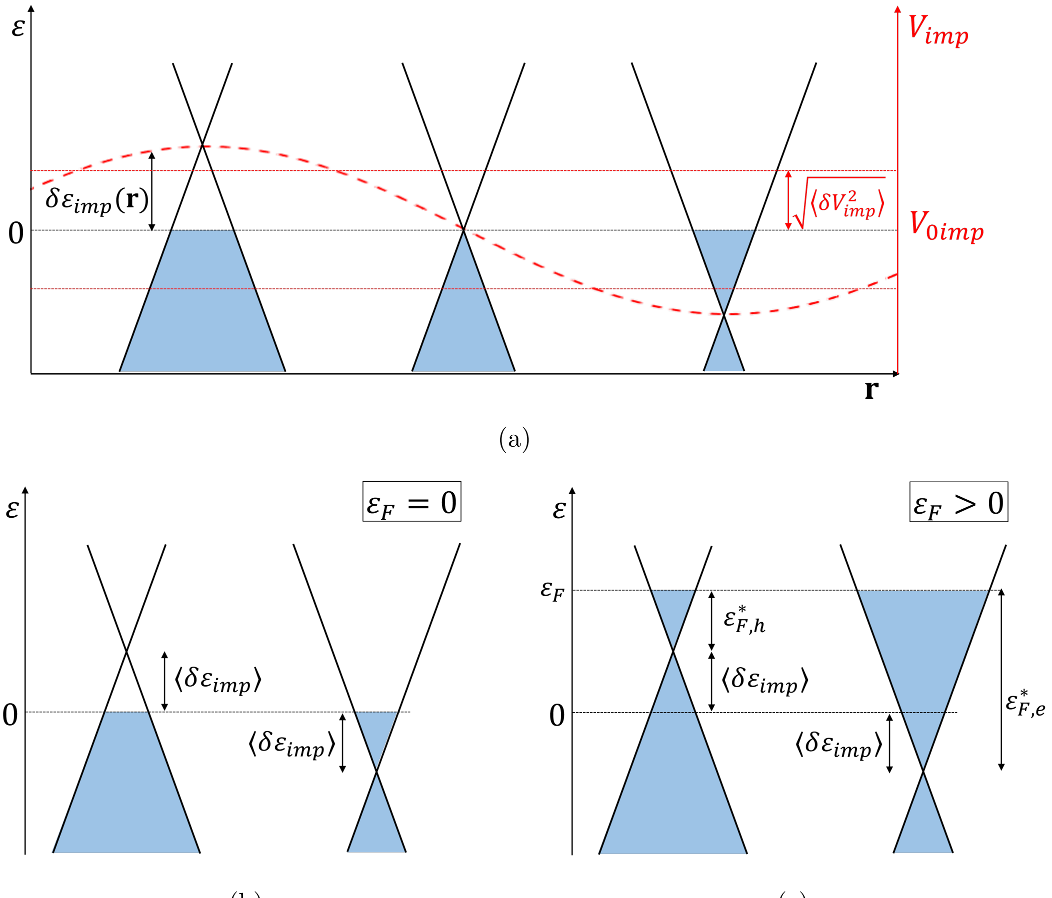

(a)

(b)

(c)

Figure 2.4: (a) Band structure of energy, ε, shown over spatially varying impurity potential, $V_{imp}(\mathbf{r})$, with mean V_{0imp}. The shift of the Dirac point, $\delta\varepsilon_{imp}$, at any position $\mathbf{r}$ is given by $V_{imp}(\mathbf{r}) - V_{0imp}$. $\sqrt{\langle\delta V_{imp}^2\rangle}$ is the root-mean squared of the deviation of $V_{imp}(\mathbf{r})$ from V_{0imp}. (b) and (c) show representative (spatially averaged) electron (right) and hole (left) puddles for chemical potentials of (b) $\varepsilon_F = 0$ and (c) $\varepsilon_F > 0$. As an approximation to model the induced electron and hole puddles, $\sqrt{\langle\delta V_{imp}^2\rangle}$, as shown in (a), can be equated to mean the shift of the Dirac point from $\varepsilon = 0$, $\langle\delta\varepsilon_{imp}\rangle$ [57]. $\varepsilon^*_{F,h}$ and $\varepsilon^*_{F,e}$ denote the quasi-Fermi level in hole and electron puddles, respectively.

the Dirac point, $\langle\delta\varepsilon_{imp}\rangle$,

$$\langle\delta\varepsilon_{imp}\rangle^2 = 2\pi n_{imp}\left(\frac{e^2}{\kappa}\right)^2 C_0(r_s, 4\langle\delta\varepsilon_{imp}\rangle d/\hbar v). \tag{2.24}$$

Due to these inhomogeneities, approximately half of the graphene sheet will experience a potential below the mean (electron puddles), whilst the other half has a potential above the mean (hole puddles). We define a quasi-Fermi level locally in the hole and electron puddles, $\varepsilon^*_{F,h} = \varepsilon_F - \langle\delta\varepsilon_{imp}\rangle$ and $\varepsilon^*_{F,e} = \varepsilon_F + \langle\delta\varepsilon_{imp}\rangle$, respectively. Energetics of the spatially averaged electron-hole puddles are shown schematically in figs. 2.4b and 2.4c.

For simple charge transport calculations, we can assume a homogeneous potential landscape with a chemical potential which varies as calculated via eq. (2.4). To account for the effect of residual charge, we set a minimum limit on the magnitude of the chemical potential of the total system, given by $\langle\delta\varepsilon_{imp}\rangle$. Given ε_F calculated for graphene in the absence of potential inhomogeneity: for $\varepsilon_F < \langle\delta\varepsilon_{imp}\rangle$, the charge density is dominated by residual charge, for $\varepsilon_F \geq \langle\delta\varepsilon_{imp}\rangle$, we assume that the fluctuations are washed out. This sets a hard boundary between the gate induced charge density and the gate-independent residual charge density,

$$N_{tot} = \begin{cases} n(\langle\delta\varepsilon_{imp}\rangle, T) + p(\langle\delta\varepsilon_{imp}\rangle, T) & \text{if } \ \varepsilon_F < \langle\delta\varepsilon_{imp}\rangle \\ n(\varepsilon_F, T) + p(\varepsilon_F, T) & \text{if } \ \varepsilon_F \geq \langle\delta\varepsilon_{imp}\rangle \end{cases}, \tag{2.25}$$

as in ref. [57]. From eq. (1.20), at $T = 0$, the residual carrier density at charge neutrality is

$$n_{res} = \frac{\langle\delta\varepsilon_{imp}\rangle^2}{\pi\hbar^2 v^2}. \tag{2.26}$$

To calculate the $N_{tot}(V_g)$ profile more precisely, with a continuous variation between gate-induced and residual charge dominated regimes, we explicitly include the spatially averaged electron and hole puddles. Therefore eq. (2.4) becomes

$$\frac{1}{2}e\left[p\left(\varepsilon^*_{F,h}, T\right) + p\left(\varepsilon^*_{F,e}, T\right) - n\left(\varepsilon^*_{F,h}, T\right) - n\left(\varepsilon^*_{F,e}, T\right)\right] = -CV_g \tag{2.27}$$

for the net charge density, which can be solved to find the chemical potential, ε_F, and substituted back into

$$N_{tot} = \frac{1}{2}\left[p\left(\varepsilon^*_{F,h}, T\right) + p\left(\varepsilon^*_{F,e}, T\right) + n\left(\varepsilon^*_{F,h}, T\right) + n\left(\varepsilon^*_{F,e}, T\right)\right] \tag{2.28}$$

to calculate the total carrier density. The results of this full calculation are shown in fig. 2.5.

The total residual carrier density at the charge neutrality point, $\varepsilon_F = 0$, is

$$\begin{aligned} N_{tot}(\varepsilon_F = 0, T) &= \frac{1}{2}\left[n(-\delta\varepsilon_{imp}, T) + p(-\delta\varepsilon_{imp}, T) + n(\delta\varepsilon_{imp}, T) + p(\delta\varepsilon_{imp}, T)\right] \\ &= \frac{\langle\delta\varepsilon_{imp}\rangle^2}{\pi\hbar^2 v^2} + \frac{\pi}{3}\left(\frac{k_B T}{\hbar v}\right)^2, \end{aligned} \tag{2.29}$$

where we have made use of eqs. (1.18) and (1.19) and the dilogarithm inversion identity. Remarkably, this is simply the sum of the residual carriers due to local potential fluctuations calculated at $T = 0$, eq. (2.26), and the thermally excited carriers at the Dirac point in the absence of potential fluctuations, $n_{TH} = n(T, \varepsilon^*_F = 0) + p(T, \varepsilon^*_F = 0)$. Therefore, the effects of the impurity-induced residual carrier density and the thermally excited carrier density are additive at the charge neutrality point,

$$n_{NP} = n_{res} + n_{TH}, \tag{2.30}$$

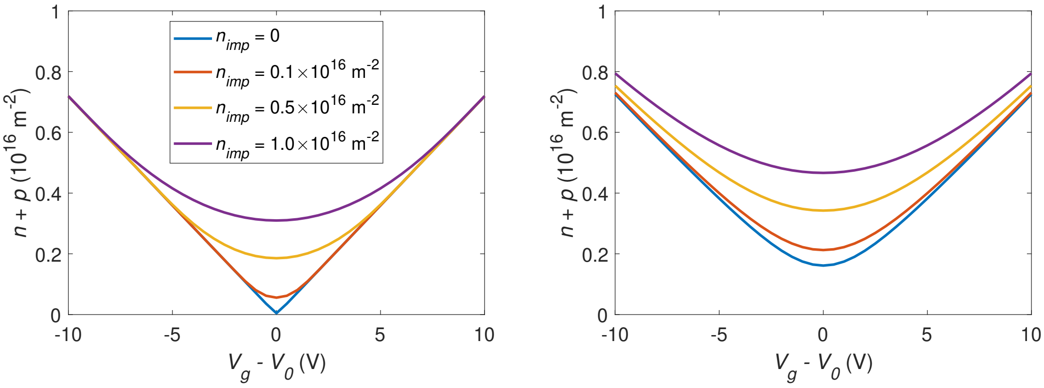

(a) (b)

Figure 2.5: Total transport carrier density variation with gate voltage, V_g, about the offset, V_0, for varying density of impurities, n_{imp}. Carrier densities were calculated using eq. (2.28), accounting for electron and hole puddles. (a) $T = 50$ K. (b) $T = 300$ K. The legend shown in (a) also applies to (b).

where n_{NP} denotes the carrier density at the charge neutrality point ($\varepsilon_F = 0$).

2.3.2 Impurity Scattering

The impurity potential will also result in the deflection and decoherence of electron momenta, as described for a general potential in section 1.3. The transition rate between momentum states, given by eq. (1.38), is

$$S^{imp}_{\mathbf{k}\to\mathbf{k}'} = n_{imp}\frac{\pi}{A\hbar}\left|\frac{2\pi e^2}{\kappa q\epsilon_{sc}(q)}\right|^2 e^{-2qd}(1 + ss'\cos\theta_{\mathbf{k},\mathbf{k}'})\delta(\varepsilon_{\mathbf{k}'} - \varepsilon_{\mathbf{k}}) \tag{2.31}$$

where we have used the result of eq. (2.20). Note that $ss' = 1$ since scattering is assumed to be elastic. Using eq. (1.49), the momentum relaxation time is

$$\frac{1}{\tau(k)} = n_{imp}\pi v r_s^2 k \int_0^{2\pi} \mathrm{d}\theta \sin^2\theta \frac{e^{-2qd}}{(q\epsilon_{sc}(q))^2}. \tag{2.32}$$

For elastic scattering, $q = 2k\sin(\theta_{\mathbf{k},\mathbf{k}'}/2)$.

In the low temperature limit, the ensemble relaxation time is given by the value of the momentum relaxation time, τ, at $k = k_F$. As a result, the Thomas-Fermi screening limit, $q \leq 2k_F$, is always satisfied. This makes sense, as we are approximating that the distribution is highly degenerate, with all electrons residing below the Fermi-level. If we approximate that $d = 0$, we find the analytical solution,

$$\frac{1}{\tau(k_F)} = \frac{n_{imp}\pi v}{16k_F} I(1/2r_s) \tag{2.33}$$

for the momentum relaxation time at the chemical potential, where the function

$$I(x) = \frac{2}{x^4}\left[2\pi x^2 + 24x - 12\pi + \frac{\left(12\pi - 8\pi x^2 - \left(24 - 16x^2\right)\tan^{-1}\left(\frac{x}{\sqrt{1-x^2}}\right)\right)}{\sqrt{1-x^2}}\right]. \tag{2.34}$$

The electrostatic environment for graphene on a $\mathrm{SiO_2}$ substrate is assumed to be described by the bulk 3D properties of neighbouring materials. The external dielectric constant is therefore taken as an average of the dielectric constant in the two mediums that the field permeates ($\mathrm{SiO_2}$ and vacuum) [58], $\epsilon_r \approx 2.5$, thus $r_s \approx 0.8$. Using this value and eq. (2.34), we find $I(1/2r_s) \approx 1.6$.

Using eq. (1.20) for the low temperature carrier density and eq. (1.53), we obtain the low-temperature, linearised Boltzmann result for $d = 0$,

$$\mu_{imp} \approx \frac{20e}{n_{imp}h}, \tag{2.35}$$

as in [57]. The mobility due to ionised impurities is constant, and the conductivity is thus proportional to the carrier density, with a gradient dependent on the density of impurities. We will further explore impurity scattering and the effects of the distance of impurities from the graphene plane in detail in chapter 3. However, from eq. (2.32), it is straightforward to observe qualitatively that for an increased impurity distance, d, the scattering of higher energy electrons (i.e. large q) is suppressed.

It should be noted that we have only considered randomly distributed impurities. If the substrate chemistry is such that impurities are correlated, then above a critical impurity density, the nature of correlations becomes important, as will be shown in section 3.4.

2.3.3 Real-Space Screened Coulomb Potential

Before deriving the form of the 2D screened Coulomb potential, we start by deriving the well-known Yukawa-potential for a 3D screened Coulomb potential for comparison. The Thomas-Fermi approximation for the dielectric screening in 3D is $\epsilon_{3D} = 1 + q_{TF}^2/q^2$, where the Thomas-Fermi wavevector, $q_{TF} = \sqrt{\frac{e^2}{\epsilon_0\epsilon_r}\frac{\partial n}{\partial \varepsilon_F}}$ in 3D [59]. The Fourier transform of the 3D coulomb potential is

$$\tilde{u}_{3D} = \frac{e^2}{\kappa\epsilon_{3D}(q)}\int \mathrm{d}^3r \frac{1}{r} e^{i\mathbf{q}\cdot\mathbf{r}} = \frac{4\pi e^2}{\kappa\epsilon_{3D}(q)q^2}. \tag{2.36}$$

To find the form of the real-space screened potential, we now take the inverse Fourier transform of eq. (2.36),

$$u_{3D}(r) = \frac{1}{(2\pi)^3}\int \mathrm{d}^3q \frac{4\pi e^2}{\kappa(q^2 + q_{TF}^2)} e^{-i\mathbf{q}\cdot\mathbf{r}} = \frac{e^2}{\kappa\pi r}\int_{-\infty}^{\infty} \mathrm{d}q \frac{q}{q^2 + q_{TF}^2}\sin(qr). \tag{2.37}$$

The integrand of eq. (2.37) has two simple poles, $q = iq_{TF}$ and $q = -iq_{TF}$. Evaluating a contour integral over an infinitely large semicircular region in the top (complex positive) half of the complex plane, we find

$$u_{3D}(r) = \frac{e^2}{\kappa r} e^{-q_{TF} r}. \tag{2.38}$$

Considering the k-space form of the 2D coulomb potential (2.20), the inverse Fourier transform is,

$$u_{2D}(r) = \frac{1}{(2\pi)^2} \int \mathrm{d}^2 q \frac{2\pi e^2}{\kappa(q + q_s)} e^{-qd} e^{-i\mathbf{q}\cdot\mathbf{r}} = \frac{e^2}{\kappa} \int_0^\infty \mathrm{d}q \frac{e^{-qd}}{q + q_s} q J_0(qr). \tag{2.39}$$

The Laplace transform of the Bessel part is [55],

$$\mathcal{L}_1(s) = \int_0^\infty J_0(qr) e^{-qs} \mathrm{d}q = \frac{1}{\sqrt{r^2 + s^2}}. \tag{2.40}$$

The inverse Laplace transform of the preceding factor of the integrand can be evaluated as

$$\mathcal{L}_2^{-1}(s) = \lim_{R\to\infty} \frac{1}{2\pi i} \int_{-iR}^{iR} \frac{q e^{-qd}}{q + q_s} e^{qs} \mathrm{d}q. \tag{2.41}$$

Evaluating the relevant contour integral, semicircle over the left (real negative) of the complex plane, we find that

$$\mathcal{L}_2^{-1}(s) = \begin{cases} -q_s e^{-q_s(s-d)} + \delta(s-d) & \text{for } s - d \geq 0 \\ 0 & \text{for } s - d < 0 \end{cases}. \tag{2.42}$$

Integrating over eqs. (2.40) and (2.42),

$$u_{2D}(r) = \frac{e^2}{\kappa} \int_d^\infty \mathrm{d}s \left[-q_s \frac{e^{-q_s(s-d)}}{\sqrt{r^2 + s^2}} + \frac{\delta(s-d)}{\sqrt{r^2 + s^2}} \right]. \tag{2.43}$$

The resulting real-space screened 2D coulomb potential is

$$u_{2D}(r) = \frac{e^2}{\kappa\sqrt{r^2 + d^2}} - \frac{e^2 q_s}{\kappa} \mathcal{F}(q_s)\{r, d\} \tag{2.44}$$

where $\mathcal{F}(q_s)\{r, d\}$ is the Laplace transform,

$$\mathcal{F}(q_s)\{r, d\} = \int_0^\infty \frac{e^{-q_s u}}{\sqrt{r^2 + (u + d)^2}} \mathrm{d}u. \tag{2.45}$$

Therefore, a 3D electron gas modifies the Coulomb potential by a multiplicative factor, $e^{-q_{TF} r}$, whilst a 2D electron gas modifies the Coulomb potential by the additive term, $\frac{e^2 q_s}{\kappa} \mathcal{F}(q_s)\{r, d\}$. The form of eqs. (2.38) and (2.44) are compared in fig. 2.6 for given values of the screening wavevectors, $q_{sc} = q_{TF} = q_s$.

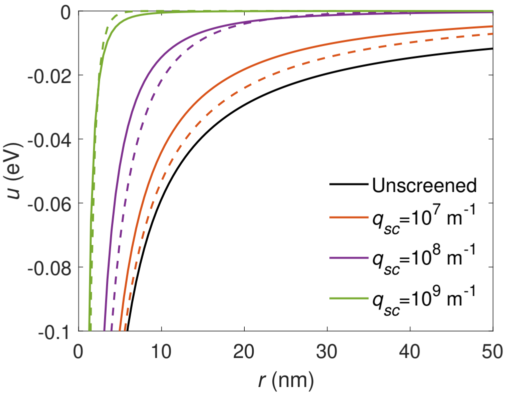

Figure 2.6: Potential, $u(r)$, for attractive impurity, screened by a 2D (solid lines) and a 3D (dashed lines) electron gas with screening wavevector, $q_{sc} = q_s = q_{TF}$. For the 2D electron gas, we have assumed that $d = 0$.

2.4 Further Scattering Mechanisms

2.4.1 Point Defects

Defects to the lattice chemistry will disrupt the band structure over a small area. Such scatterers will be considered as short-range potentials, only effective over a small region containing the defect. This 'region' can be characterised as a finite spatial limit, R,

$$u(r) = \begin{cases} U_0 & \text{for} \quad r \leq R \\ 0 & \text{for} \quad r > R \end{cases}. \tag{2.46}$$

The integral over the angular part of the 2D Fourier transform results in the integral representation of the zero-*th* order Bessel function,

$$\tilde{u} = 2\pi \frac{U_0}{\epsilon_{sc}} \int_0^R J_0(qr) r \mathrm{d}r = \pi R^2 \frac{U_0}{\epsilon_{sc}} \left(\frac{2J_1(qR)}{qR} \right), \tag{2.47}$$

where we have included the screening effect of the 2D carriers, ϵ_{sc}. Considering point defects ($R \to 0$), we find the limit

$$\lim_{qR \to 0} \left(\frac{2J_1(qR)}{qR} \right) = \lim_{qR \to 0} (\mathrm{sinc}(qR)) = 1, \tag{2.48}$$

such that $\tilde{u} \sim \pi R^2 U_0 / \epsilon_{sc}$. This gives an effective cross-section of scattering, $A_{sr} = \pi R^2$. Consequently, the transition rate, given by eq. (1.38), is

$$S^{sr}_{\mathbf{k} \to \mathbf{k}'} = n_{sr} \frac{\pi}{A\hbar} \left| \frac{A_{sr} U_0}{\epsilon_{sc}(q)} \right|^2 (1 + ss' \cos\theta_{\mathbf{k},\mathbf{k}'}) \delta(\varepsilon_{\mathbf{k}'} - \varepsilon_{\mathbf{k}}) \tag{2.49}$$

for a density of n_{sr} defects. We assume defect scattering to be elastic: $ss' = 1$ and $q = 2k\sin(\theta_{\mathbf{k},\mathbf{k}'}/2)$. Using eq. (1.49), the momentum relaxation time is

$$\frac{1}{\tau_{sr}(k)} = n_{sr}\frac{\left(A_{sr}U_0\right)^2}{4\pi\hbar}\frac{k}{\hbar v}\int_0^{2\pi}\mathrm{d}\theta\left(1-\cos^2\theta\right)\frac{1}{\epsilon_{sc}(q)} = \frac{n_{sr}\left(A_{sr}U_0\right)^2 k}{4\pi\hbar^2 v}F(2r_s), \tag{2.50}$$

where the function

$$F(x) = \frac{1}{8x}\left[\frac{64x^4\left(-4+5x^2\right)}{\sqrt{x^2-1}}\left(\pi - 2\tan^{-1}\left(\frac{1}{\sqrt{x^2-1}}\right)\right)\right.$$
$$\left. + \left(8\pi x + 96\pi x^3 - 320\pi x^5 + 16x^2\left(-7+40x^2\right) + 2\left(1+\frac{40}{3}x^2\right) - 2\right)\right]. \tag{2.51}$$

Using eqs. (1.20) and (1.53) for the low temperature carrier density and mobility respectively, the mobility due to short range scatters is inversely proportional to the carrier density, n,

$$\mu_{sr} \approx \frac{100}{7}\frac{\hbar v^2 e}{\left(A_{sr}U_0\right)^2 n_{sr}}n^{-1}. \tag{2.52}$$

This means that the conductivity limited by short range scattering potentials, $\sigma_{sr} = ne\mu_{sr}$, is a constant, determined only by the density of defects and the strength of the potential that they generate.

2.4.2 Strong Defects and Mid-Gap States

For strongly interacting defect potentials, it is necessary to go beyond the Born approximation. Various forms of charge-neutral "resonant" impurities and defects, such as vacancies, adatoms and adsorbates, create mid-gap states [60–62]. The presence of such mid-gap states has been confirmed and characterised by density functional theory (DFT) calculations [63]. Extended calculations of the interaction Hamiltonian [60, 64, 65] lead to the relaxation rate

$$\frac{1}{\tau_{res}(\varepsilon)} = \frac{\pi n_{res} D_{res}^2}{2\varepsilon\hbar}\left(\ln\left(\varepsilon/D_{res}\right)\right)^{-2} \tag{2.53}$$

in the limit of a large defect potential, $U \to \infty$, and assuming that $\varepsilon < D_{res}$, where $D_{res} = \sqrt{\sqrt{3}\pi\gamma_0} \approx 6$ eV and n_{res} is the number of resonant scatterers per carbon atom. The resulting resonant impurity limited mobility is

$$\mu_{res} = \frac{2ev^2\hbar}{\pi n_{res} D_{res}^2}\left(\ln\left(\frac{\hbar v\sqrt{\pi n}}{D_{res}}\right)\right)^2. \tag{2.54}$$

Although eq. (2.54) decreases with increasing carrier density (since $\varepsilon_F < D_{res}$), the logarithmic decrease is not as strong as the inverse relationship found for weak scattering, eq. (2.52). Therefore, such scattering can be difficult to distinguish from that of charged impurity scattering with a weak defect scattering from conductivity measurements alone [61].

2.4.3 Acoustic Phonons

Acoustic phonons, of wavevector $\mathbf{k}_a$, couple to the lattice through the 'deformation potential', $U(\mathbf{r}) = D_{ac}e(\mathbf{r})$, proportional to the strain, $e(\mathbf{r})$, with a constant of proportionality, $D_{ac} \approx 25$eV [66]. The deformation potential constant, D_{ac}, is reported with a large range of experimentally calculated values [6, 66, 67]. Assuming harmonic phonon oscillations, described by the atomic displacement

$$s(\mathbf{r},t) = \sqrt{\frac{2\hbar}{A\rho_m\omega(k_a)}}\cos(\mathbf{k}_a \cdot \mathbf{r} - \omega(k_a)t), \tag{2.55}$$

the deformation potential is

$$u(\mathbf{r},t) = u_{abs}(\mathbf{r},t) + u_{em}(\mathbf{r},t) = i\sqrt{\frac{\hbar k_a}{2A\rho_m v_s}}D_{ac}\left(e^{i\mathbf{k}_a\cdot\mathbf{r}}e^{-i\omega(k_a)t} - e^{-i\mathbf{k}_a\cdot\mathbf{r}}e^{i\omega(k_a)t}\right) \tag{2.56}$$

where $\rho_m = 7.6 \times 10^{-7}$ kgm^{-2} is the graphene mass density, $v_s \approx 2.6 \times 10^4$ ms^{-1} is the speed of sound in graphene [66] and we have assumed a linear vibrational dispersion relation $\omega_q = v_s k_a$, strictly valid for long wavelengths ($q \ll \pi/a$). The amplitude of oscillation in eq. (2.55) is found by equating the total energy of oscillation to the single phonon quantum, $\hbar\omega(k_a)$ [59]. For the absorption term, the Fourier transform

$$\tilde{u}_{abs} = i\sqrt{\frac{\hbar k_a}{2A\rho_m v_s}}D_{ac}e^{-i\omega(k_a)t}\int e^{i\mathbf{k}_a\cdot\mathbf{r}}e^{-i\mathbf{q}\cdot\mathbf{r}}\mathrm{d}\mathbf{r} \tag{2.57}$$

is simply the Dirac-delta function, requiring that wavevectors sum to zero, $\mathbf{k}_a = \mathbf{q}$. The case is similar for emission, with $\mathbf{k}_a = -\mathbf{q}$. In both cases, the magnitude of the phonon wavevector is equivalent to magnitude of the change in electron wavevector $k_a = q = |\mathbf{k}' - \mathbf{k}|$. The transition rate, including both absorption and emission, is

$$S^{ac}_{\mathbf{k}\to\mathbf{k}'} = \frac{\pi q}{2A\rho_m v_s}D^2_{ac}\left(1 + \cos\theta_{\mathbf{k},\mathbf{k}'}\right)\left(2N(q)+1\right)\delta(\varepsilon_{\mathbf{k}'} - \varepsilon_{\mathbf{k}}). \tag{2.58}$$

In deriving eq. (2.58), we made the quasi-elastic approximation, $\hbar\omega(q) = 0$. This is a useful simplification to make, especially when it comes to the computational methods, since the dynamic dependence of the change in energy on the initial and final wavevectors can be ignored. The approximation is strictly valid for $\hbar\omega(q) \ll \varepsilon_F$, which is the case since $v_s \ll v$.

Using eq. (1.49), the resulting total relaxation time is

$$\frac{1}{\tau_{ac}(\varepsilon)} = \frac{D_{ac}^2}{8\pi\rho_m v_s(\hbar v)^2}\varepsilon\int_0^{2\pi} \mathrm{d}\theta \frac{q\sin^2\theta}{1-f(\varepsilon)}\big[(N_q+1)\left(1-f(\varepsilon-\hbar\omega_q)\right) + N_q\left(1-f(\varepsilon+\hbar\omega_q)\right)\big]. \tag{2.59}$$

In the equipartition regime, $T \gg T_{BG} = \hbar v_s 2k_F/k_B$, the phonon occupation is $N_q \approx k_BT/\hbar\omega_q$ and scattering is dominated by stimulated emission and absorption events. Equation (2.59) simplifies to $\tau_{ac}(\varepsilon) \approx 4\rho_m v_s^2\hbar^3 v^2/k_BTD_{ac}^2\varepsilon$, and using eq. (1.50), we find that the equipartition conductivity is

$$\sigma_{EP} = \frac{4e^2\rho_m v_s^2\hbar v^2}{\pi D_{ac}^2}(k_BT)^{-1}, \tag{2.60}$$

independent of n and inversely proportional to T. A comparison between eq. (2.60) and the full, numerically integrated acoustic conductivity from eq. (2.59) is shown in fig. 2.7a, where we calculated the chemical potential, $\varepsilon_F(V_g)$ using eq. (2.4). The EP conductivity, eq. (2.60), agrees with the full calculation in the limit of large T and small V_g. Using eq. (2.60), the mobility limited by acoustic phonons in the equipartition regime,

$$\mu_{EP} = \frac{4e\hbar v^2\rho_m v_s^2}{\pi k_BTD_{ac}^2}(n+p)^{-1}, \tag{2.61}$$

is inversely proportional to the carrier density, similar to short-range defects (2.52), and also inversely proportional to temperature.

In the opposing, Bloch-Gruneisen, limit, $T \ll T_{BG}$, the relaxation rate was calculated in ref. [68]: $\tau(\varepsilon_F) = (2\pi\hbar^3 v_s^5\rho_m\varepsilon_F)/(4!\zeta(4)D_{ac}^2 v(k_BT)^4)$. Given that we are in a low temperature regime, $T \ll T_{BG} \ll \varepsilon_F/k_B$, we can use eq. (1.53), to find that the conductivity is

$$\sigma_{BG} = \frac{2\pi^{3/2}e^2\rho_m v_s^5\hbar^4 v^2}{4!\zeta(4)D_{ac}^2}[n_{T=0}]^{3/2}(k_BT)^{-4}. \tag{2.62}$$

From eq. (2.62), we can see that $\sigma_{BG} \propto n^{3/2}T^{-4}$. A comparison between eq. (2.62) and the full, numerically calculated acoustic conductivity is shown in fig. 2.7b, the two calculations agree in the limit of small T and large V_g.

From fig. 2.7a, it can be seen that the EP approximation, eq. (2.60), is valid at room temperature over a reasonable range of applied gate voltages.

2.4.4 Optical Phonons

Calculations of the finite momentum coupling to in-plane optical phonon modes about the $\mathbf{\Gamma}$ point have been carried out in ref. [31]. We shall summarise and use the results here. DFT was used to determine the eigenvectors of the phonon modes, and the perturbation in the presence of mixing of modes. For intraband longitudinal and

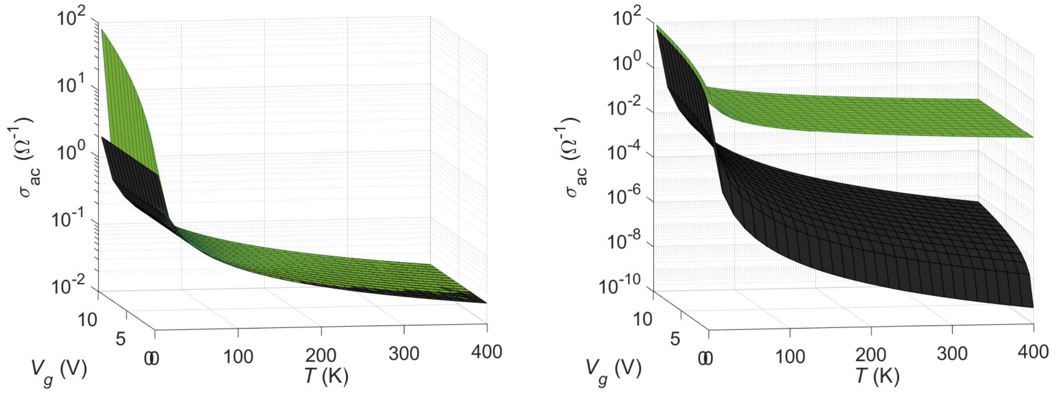

(a) (b)

Figure 2.7: Conductivity due to acoustic phonon scattering, using the deformation potential approximation, as a function of applied gate voltage, V_g, and temperature, T, (green). (a) Comparison to the EP approximation eq. (2.60) (black). (b) Comparison to BG approximation eq. (2.62) (black).

transverse optical scattering, the transition rates in the small momentum limit are

$$S^{LO}_{\mathbf{k}\rightarrow\mathbf{k}'} = \frac{\pi}{A\rho_m\omega_O}\beta_O^2\left(1 - ss'\cos\left(\varphi_{\mathbf{k}'} + \varphi_{\mathbf{k}} - 2\varphi_{\mathbf{q}}\right)\right)\Delta^{el}_{\mathbf{k}\rightarrow\mathbf{k}'}(\omega_O) \tag{2.63}$$

and

$$S^{TO}_{\mathbf{k}\rightarrow\mathbf{k}'} = \frac{\pi}{A\rho_m\omega_O}\beta_O^2\left(1 + ss'\cos\left(\varphi_{\mathbf{k}'} + \varphi_{\mathbf{k}} - 2\varphi_{\mathbf{q}}\right)\right)\Delta^{el}_{\mathbf{k}\rightarrow\mathbf{k}'}(\omega_K). \tag{2.64}$$

The total transition rate due to optical phonons,

$$S^{O}_{\mathbf{k}\rightarrow\mathbf{k}'} = \frac{2\pi\beta_O^2}{A\rho_m\omega_O}\Delta^{el}_{\mathbf{k}\rightarrow\mathbf{k}'}(\omega_O), \tag{2.65}$$

is independent of the angular distribution. Given that the angular dependence from longitudinal and transverse modes cancel out, the total transition rate is the same for both intra- and inter- band scattering by Γ optical phonons.

Phonons at the K point cause intervalley scattering in which an electron scatters by the reciprocal lattice vector, K, to an inequivalent valley. As noted in reference [31], the DFT calculations for the phonon dispersion and corresponding matrix elements were performed in [69]. The result is

$$S^{K}_{\mathbf{k}\rightarrow\mathbf{k}'} = \frac{2\pi}{A\rho_m\omega_K}\beta_K^2\left(1 - ss'\cos\theta_{\mathbf{k},\mathbf{k}'}\right)\Delta^{el}_{\mathbf{k}\rightarrow\mathbf{k}'}(\omega_K) \tag{2.66}$$

The ‘gauge field’, β, terms are physical parameters representing the phonon coupling strength, calculated to be $\beta_O \approx 10$ eV/Å and $\beta_K \approx 3.5$ eV/Å [67]. The resonant optical modes in graphene are near dispersionless, such that we can assume them to be of constant energy, independent of the electron transition, with values of $\hbar\omega_O \approx 165$ meV for both transverse and longitudinal modes and $\hbar\omega_K \approx 124$ meV [67].

The sum of longitudinal and transverse optical phonons around the Γ point results in the relaxation time

$$\begin{aligned}\frac{1}{\tau_O(\varepsilon)} = \frac{\beta_O^2}{\rho_m \omega_O (\hbar v)^2} \Bigg[& N(\omega_O)\,|\varepsilon + \hbar\omega_O|\,\frac{1 - f(\varepsilon + \hbar\omega_O)}{1 - f(\varepsilon)} \\ & + (N(\omega_O) + 1)\,|\varepsilon - \hbar\omega_O|\,\frac{1 - f(\varepsilon - \hbar\omega_O)}{1 - f(\varepsilon)} \Bigg].\end{aligned} \tag{2.67}$$

Similarly, for phonons at the K point,

$$\begin{aligned}\frac{1}{\tau_K(\varepsilon)} = \frac{\beta_K^2}{\rho_m \omega_K (\hbar v)^2} \Bigg[& \frac{3}{2} N(\omega_K)\,|\varepsilon + \hbar\omega_K|\,\frac{1 - f(\varepsilon + \hbar\omega_K)}{1 - f(\varepsilon)} \\ & + (N(\omega_K) + 1) \left(|\varepsilon - \hbar\omega_K| + \frac{1}{2}(\varepsilon - \hbar\omega_K) \right) \frac{1 - f(\varepsilon - \hbar\omega_K)}{1 - f(\varepsilon)} \Bigg].\end{aligned} \tag{2.68}$$

In calculating eq. (2.68), we have taken care that, for electron emission, $ss' = -1$ (interband) in eq. (2.66) if $\hbar\omega > \varepsilon$ and $ss' = +1$ (intraband) otherwise. Taking the low temperature limit, $T \to 0$, using eq. (1.53),

$$\sigma_O|_{T\approx 0} \approx \frac{e^2 \rho_m \omega_O v^2 \sqrt{n_{T=0}}}{\sqrt{\pi}\beta_O^2} \left[\left| \sqrt{\pi n_{T=0}} + \frac{\omega_O}{v} \right| + \left| \sqrt{\pi n_{T=0}} - \frac{\omega_O}{v} \right| \right]^{-1} \sinh\left(\frac{\hbar\omega_O}{k_B T} \right) \tag{2.69}$$

and

$$\begin{aligned}\sigma_K|_{T\approx 0} \approx & \frac{e^2 \rho_m \omega_K v^2 \sqrt{n_{T=0}}}{\sqrt{\pi}\beta_K^2} \sinh\left(\frac{\hbar\omega_K}{k_B T} \right) \\ & \times \left[\frac{3}{2} \left| \sqrt{\pi n_{T=0}} + \frac{\omega_K}{v} \right| + \left| \sqrt{\pi n_{T=0}} - \frac{\omega_K}{v} \right| + \frac{1}{2} \left(\sqrt{\pi n_{T=0}} - \frac{\omega_K}{v} \right) \right]^{-1}.\end{aligned} \tag{2.70}$$

Figure 2.8 shows the calculated resistivity of the two optical phonon modes using the full relaxation times (eqs. (2.67) and (2.68)) and eq. (1.50). The result of eqs. (2.69) and (2.70) are also shown at $V_g = 20$ V in fig. 2.8.

The $(1 - f_0(\varepsilon_F - \hbar\omega))$ terms in eqs. (2.67) and (2.68) highly suppress the scattering by emission, since, for most temperatures considered, the distribution at $\varepsilon = \varepsilon_F - \hbar\omega$ will be approximately full. However, the shift of the distribution function under an applied field will make more low-energy states available for electrons to scatter in to. The full time-dependant simulations described in section 2.5 will overcome any oversimplifications that are present in eqs. (2.67) and (2.68).

2.4.5 Substrate Polar Phonons

Optical phonons in neighbouring polar substrate materials, such as hBN or SiO$_2$, create fluctuating electric fields; electrons in the graphene plane then couple to the modes of the polarization field. The perturbation to the Hamiltonian is characterised by the

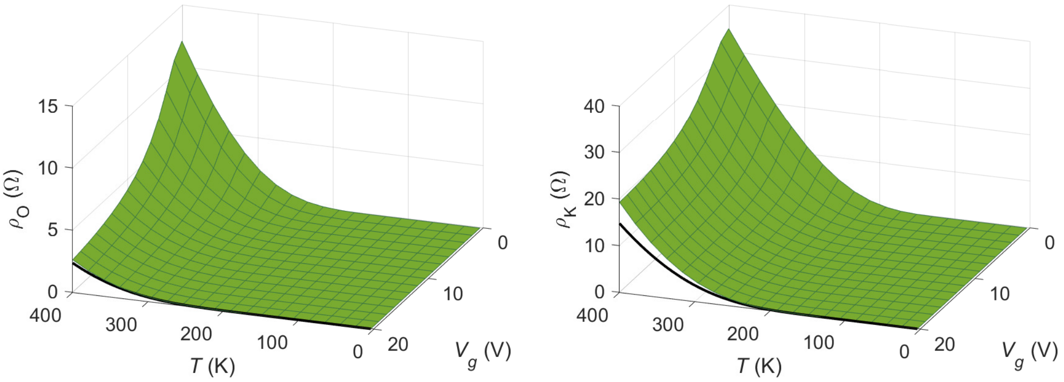

(a) (b)

Figure 2.8: Resistivity due to (a) Γ- and (b) K- optical phonon scattering, as a function of applied gate voltage, V_g, and temperature, T, compared to the low temperature approximations, eqs. (2.69) and (2.70), at $V_g = 20$ V (black line).

substrate dielectric response,

$$u(\mathbf{r},t) = eF\frac{e^{-k_o z}}{i\sqrt{k_o}}\left(e^{i\mathbf{k}_o\cdot\mathbf{r}}e^{-i\omega_{so}t} - e^{-i\mathbf{k}_o\cdot\mathbf{r}}e^{i\omega_{so}t}\right), \tag{2.71}$$

for surface optical modes of frequency ω_{so}, where z is the normal distance to the substrate surface and F is the Fröhlich coupling parameter [70]:

$$F = \left[\left(\frac{1}{\epsilon(\infty)+1} - \frac{1}{\epsilon(0)+1}\right)\frac{\hbar\omega_{so}}{2A\epsilon_0}\right]^{1/2}, \tag{2.72}$$

where $\epsilon(0)$ and $\epsilon(\infty)$ are the static and high frequency dielectric constants respectively. When taking the overlap, we maintain the 2D Fourier transform by restricting the z-extent of the wavefunction to an impulse, $\delta(z - d_{spp})$, at the distance of the graphene plane from the substrate, d_{spp}. As for acoustic phonons, the spatial Fourier transform from the overlap results in $k_o = q$ and the resulting transition rate is

$$S^{spp}_{\mathbf{k}\to\mathbf{k}'} = F^2 e^2 \frac{\pi}{\hbar}\left(\frac{e^{-2qd_{spp}}}{q\epsilon_{sc}(q)^2}\right)\left(1 + ss'\cos\theta_{\mathbf{k},\mathbf{k}'}\right)\Delta^{inel}_{\mathbf{k}\to\mathbf{k}'}. \tag{2.73}$$

For a SiO$_2$ substrate, $\epsilon(0) = 2.5$ and $\epsilon(\infty) = 3.9$, $d_{spp} \approx 0.4$ nm and there are two dominating, near dispersionless, surface modes of energy $\hbar\omega_{so} \approx 56$ meV and $\hbar\omega_{so} \approx 140$ meV [71].

We write the momentum relaxation rate as a sum of the absorption and emission parts

$$\frac{1}{\tau_{spp}} = \frac{1}{\tau_{spp,abs}} + \frac{1}{\tau_{spp,em}} \tag{2.74}$$

where

$$\frac{1}{\tau_{spp,abs}(\varepsilon)} = \frac{Ae^2F^2}{4\pi\hbar(\hbar v)^2} N(\omega_{so}) \left|\varepsilon + \hbar\omega_{so}\right| \frac{1 - f(\varepsilon + \hbar\omega_{so})}{1 - f(\varepsilon)} \int_0^{2\pi} \mathrm{d}\theta \sin^2\theta \frac{e^{-2q_{\theta+}d_{spp}}}{q_{\theta+}\epsilon_{sc}(q_{\theta+})}, \tag{2.75}$$

$$\begin{aligned}\frac{1}{\tau_{spp,em}(\varepsilon)} = \frac{Ae^2F^2}{4\pi\hbar(\hbar v)^2} \Bigg[& (N(\omega_{so}) + 1) \left|\varepsilon - \hbar\omega_{so}\right| \frac{1 - f(\varepsilon - \hbar\omega_{so})}{1 - f(\varepsilon)} \\ & \times \left(\vartheta\left(\varepsilon - \hbar\omega_{so}\right) \int_0^{2\pi} \mathrm{d}\theta \frac{e^{-2q_{\theta-}d_{spp}}}{q_{\theta-}\epsilon_{sc}(q_{\theta-})} \sin^2\theta \right. \\ & \left. + \vartheta\left(-\varepsilon + \hbar\omega_{so}\right) \int_0^{2\pi} \mathrm{d}\theta \frac{e^{-2q_{\theta i}d_{spp}}}{q_{\theta i}\epsilon_{sc}(q_{\theta i})} \left(1 - \cos\theta\right)^2 \right) \Bigg],\end{aligned} \tag{2.76}$$

$q_{\theta\pm}^2 = [2(\varepsilon^2 \pm \varepsilon\hbar\omega_{so})(1 - \cos\theta) + \hbar^2\omega^2]/(\hbar v)^2$ is the reciprocal scattering length for intraband absorption and emission, respectively, and $q_{\theta i}^2 = [2(\varepsilon^2 - \varepsilon\hbar\omega_{so})(1 + \cos\theta) + \hbar^2\omega^2]/(\hbar v)^2$ for interband emission.

2.5 Computational Methods

In the models shown in this section, we make a number of simplifying assumptions: (1) homogeneity in real-space throughout the device, this can later be extended to consider transport between real-space cells, where inhomogeneity can exist on the scale of the cell size; (2) high chemical potential, such that only intraband scattering is present, $ss' = 1$; (3) valleys are assumed to have equivalent distributions. We will explore two methods to model transport given a uniform applied electric field, $\mathbf{E}$, and multiple sources of electron scattering: Direct Simulation Monte Carlo and discontinuous Galerkin. Later, in section 3.1, we will expand upon these methods to allow us to relax assumption (2) and model inter-band transitions.

2.5.1 Direct Simulation Monte Carlo (MC)

A rectangular grid is used to discretise the 2D k-space into a set of values over a range $[-k_x^{max}, k_x^{max}] \times [-k_y^{max}, k_y^{max}]$, chosen such that the distribution, $f(t, \mathbf{k})$, at the boundary and beyond is negligibly small throughout the simulation. Each k-space coordinate $(k_x(i), k_y(j))$ defines a cell, C_{ij}. We simulate N_p electrons on this grid, assumed to be representative of the entire ensemble of real electrons that would be present in the device. These simulated electrons are distributed onto the grid, with each simulated electron holding the same statistical weight in comparison to the real electron distribution. Therefore, the Pauli exclusion principle (PEP) is accounted for by setting a maximum number of electrons allowed in each cell, N_{ij}^{max}. Using the same reasoning as in [72],

$$N_{ij}^{max} = \frac{2}{(2\pi)^2} \Omega_{ij} \frac{N_p}{n}, \tag{2.77}$$

since $0 \leq f \leq 1$, where $\Omega_{ij} = \int_{C_{ij}} \mathrm{d}\mathbf{k}$ is the k-space area of the cell C_{ij} and n is the real-space density of electrons given by eq. (1.18) with $g_v = 1$ (only one simulated valley). Initially, the electrons are distributed according to the Fermi-Dirac distribution (1.16). This equates to assuming that the system is initially in equilibrium with the thermal bath of the environment and has some chemical potential, ε_F, which sets the density of real electrons, n, and, therefore, the maximum number of simulated electrons in each cell, N_{ij}^{max}. The simulated distribution in each cell is given by $f_{ij} = N_{ij}/N_{ij}^{max}$.

The free-flight trajectories are determined by assuming uniform acceleration by the applied electric field, $\mathbf{E}$, over the short times between scattering, Δt. Integrating over the rate of change in electron momentum, equated to the electrostatic force gives

$$\Delta\mathbf{k} = -\frac{e\mathbf{E}}{\hbar}\Delta t. \tag{2.78}$$

Upon updating the wavevector of each electron, the grid is also shifted according to eq. (2.78) to ensure that the number of electrons in each cell remains constant. This procedure, which is well described in ref. [73], ensures that distribution doesn't become unphysical (ensures that $f \leq 1$) due to inhomogeneities in the flux between cell boundaries.

Using the total transition rates, $\Gamma(\mathbf{k})$, for each scatterer, we can use a stochastic approach to model the evolution of the system to a steady-state solution of the Boltzmann equation (1.44). The duration of free flight, between any two collisions, for a single electron is given by [74]

$$\Delta t = -\frac{1}{\Gamma_{tot}}\ln\varrho_1 \tag{2.79}$$

where ϱ_1 is a randomly generated number from a uniform distribution between 0 and 1 and $\Gamma_{tot} = \sum_i \Gamma_i$ is the sum of total transition rates over each individual scatter rate, Γ_i. At the end of free drift, the scatterer encountered by the electron is chosen based on the relative total scattering rates. A randomly selected value, ϱ_2, is compared to the accumulative sum of the individual total scatter rates, Γ_i.

Generally, to consider a large distribution of electrons, an energy-dependant self-scattering term is included, such that all electrons free drift for the same length of time over each iteration. In essence, this means that Γ_{tot} is the same for each electron, whilst the self-scattering, $\Gamma_s = \Gamma_{tot} - \sum_i \Gamma_i(\varepsilon)$, differs, as shown in fig. 2.9. If self-scattering is chosen as the scatterer at the end of free drift, the electron remains in its current state. For our simulations, we find that, since having to calculate the values of Γ_i for each electron to determine the scatterer encountered, it is beneficial to allow the electrons to free drift independently and neglect the large amount of self-scatters that would otherwise have to be considered.

The state after scattering, $\mathbf{k}'$, is then selected by consideration of the transition rate, $S_{\mathbf{k}\to\mathbf{k}'}$, to different k-states. The magnitude, k, after scattering is given by the energy conserving terms (1.39) and (1.40). The probability of the change in polar angle

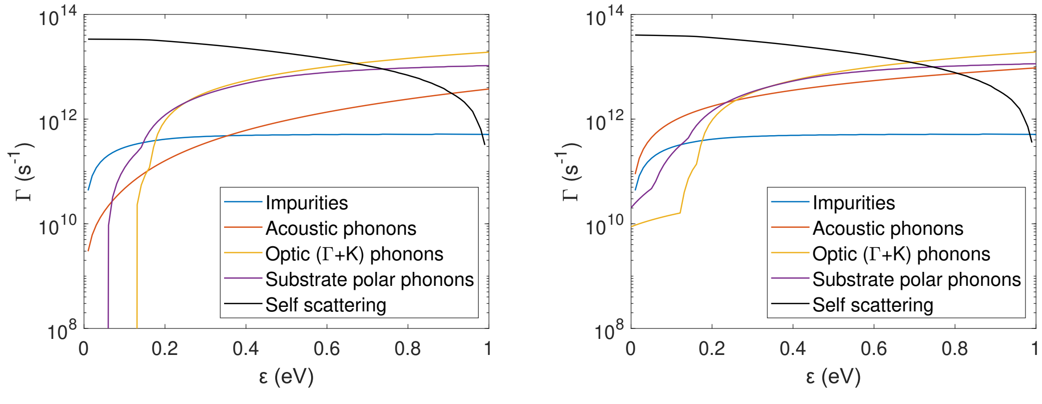

(a) (b)

Figure 2.9: Total scatter rates, $\Gamma(\varepsilon)$, over a range of electron energies, ε, for the different sources of scattering. We have used the following parameters: density of impurities, $n_{imp} = 0.5 \times 10^{15}$ m^{-2}; impurity distance, $d_{imp} = 0.4$ nm; substrate distance, $d_{spp} = 0.4$ nm; chemical potential, $\varepsilon_F = 0.3$ eV. (a) Temperature, $T = 10$ K. (b) Temperature, $T = 300$ K. In both cases we have approximated low temperature screening, eq. (2.16).

of the wavevector being between θ and $\theta + \mathrm{d}\theta$ is given by

$$P(\theta_c)\mathrm{d}\theta = \frac{\mathrm{d}\theta S_{\mathbf{k}\to\mathbf{k}'}(\theta_c)}{\int_0^{2\pi} S_{\mathbf{k}\to\mathbf{k}'}(\theta_c)\mathrm{d}\theta}. \tag{2.80}$$

Another uniformly generated random number, ϱ_3, is selected to represent a point on the probability distribution, corresponding to the angle, θ_c, such that

$$\varrho_3 = \frac{\int_0^{\theta_c} S_{\mathbf{k}\to\mathbf{k}'}(\theta_c)\mathrm{d}\theta}{\int_0^{2\pi} S_{\mathbf{k}\to\mathbf{k}'}(\theta_c)\mathrm{d}\theta}. \tag{2.81}$$

The simplest angular dependence of scattering comes from the overlap of the pseudospinor part of the Bloch states. This corresponds to the $(1 + \cos\theta)$ term in eq. (2.49) for short-range defects, for example. Using eq. (2.81), the change in angle, θ_c, is thus found by solving

$$\varrho_3 = \frac{1}{2\pi}\left(\theta_c + \sin\theta_c\right). \tag{2.82}$$

Solving such equations using symbolic equation solvers can be inefficient. Therefore, it is found to be beneficial to discretise θ into an array and selecting θ_c by comparing the relative probabilities to ϱ_3 in a similar manner to selecting the scatterer encountered at the end of free drift.

The cell, C'_{ij}, that the electron scatters to can now be determined, and the distribution, f'_{ij}, has to be considered. A rejection technique is used to determine whether the chosen transition can occur based on the PEP. It follows the form of the ‘collision term’, eq. (1.43), in the BTE: a random number ϱ_4 is chosen such that, if $\varrho_4 < 1 - f'_{ij}$ the transition is accepted, else it is rejected.

The simulated distribution function is continuously updated after every scatter event to ensure the PEP is always satisfied. Macroscopic quantities, such as total velocity and energy, are recorded at designated time steps. An outline of the algorithm used is shown in fig. 2.10.

Using eq. (1.46) and the calculated transition rates from sections 2.3.2 and 2.4, the scatter rates are:

$$\Gamma^{O}(\varepsilon) = \frac{\beta_O^2}{\hbar^2 v^2 \rho_m \omega_O} \left[(\varepsilon - \hbar\omega_O)\left(N_{\omega_O} + 1\right) \vartheta\left(\varepsilon - \hbar\omega_O\right) + (\varepsilon + \hbar\omega_O) N_{\omega_O} \right] \tag{2.83}$$

for Γ-optical phonons, where the Heaviside function, $\vartheta\left(\varepsilon - \hbar\omega_O\right)$, ensures that only emission events for which the electron is left in the conduction band are allowed; for K-optical phonons,

$$\Gamma^{K}(\varepsilon) = \frac{\beta_K^2}{\hbar^2 v^2 \rho_m \omega_K} \left[(\varepsilon - \hbar\omega_K)\left(N_{\omega_K} + 1\right) \vartheta\left(\varepsilon - \hbar\omega_K\right) + (\varepsilon + \hbar\omega_K) N_{\omega_K} \right]. \tag{2.84}$$

The expressions for impurity, short-range, acoustic phonon, and substrate polar phonon scattering are more involved and are therefore integrated numerically. An example of the total scatter rates over the range of considered electron energies are shown in fig. 2.9. For low temperatures (fig. 2.9a), optic phonon and substrate phonon scattering is effectively switched off at low electron energies due to the lack of absorption ($N(\omega) \approx 0$) and inability to emit into the valence band.

2.5.2 Discontinuous Galerkin (DG)

In the DG scheme, the Boltzmann equation is integrated using time variation diminishing (TVD) Runge-Kutta [75] on a finite element grid in which the flux between grid elements is carefully considered. For a hyperbolic set of differential equations, the TVD conditions are used to prevent the formation of spurious oscillations. The conditions are such that the total spatial variation of the distribution function, f, between cells does not increase over time. The temporal integration is performed with a time step chosen to satisfy the CFL condition for a convergent solution [76]; 1 fs is used as standard.

In order to exploit the rotational symmetry of the electron energy in k-space, a polar coordinate system is used, discretised over a circular grid, as shown in fig. 2.11. In a similar manner to the MC method, the size of the grid is chosen such that the distribution outside of the considered domain is negligible. We label the N_c cells C_α and, instead of considering single particle trajectories from $\mathbf{k}$ to $\mathbf{k}'$, we consider the flux from cell C_α to C_β. The result is N_c coupled Boltzmann equations with a constant, piece-wise distribution function, $f_\alpha(t)$, in each cell. The prescription of the DG method used is well outlined in [77], here we will look at the key points.

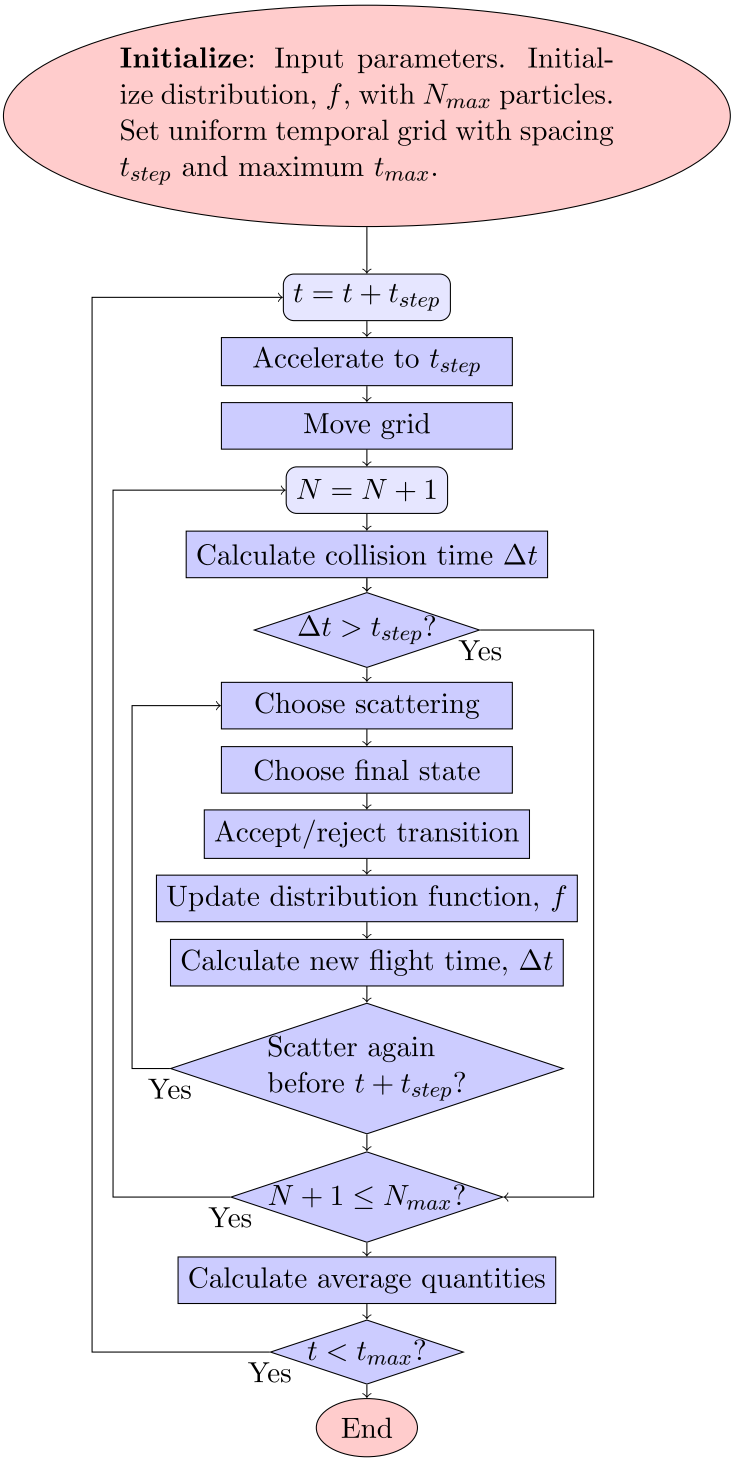

Figure 2.10: Flow chart of Monte Carlo (MC) algorithm for diffusive electron transport that obeys the Pauli exclusion principle (PEP).

Integrating over each cell, the Boltzmann equation for cell C_α becomes

$$\begin{aligned}\Omega_\alpha \frac{\mathrm{d}f_\alpha(t)}{\mathrm{d}t} =& \frac{e}{\hbar}\mathbf{E}\cdot\int_{C_\alpha} \nabla_{\mathbf{k}} f(t,\mathbf{k})\mathrm{d}\mathbf{k} \\ &+ \frac{A}{(2\pi)^2}\sum_{\beta=1}^{N_c}\Big[A^{\beta,\alpha} f_\beta(t)\left(1-f_\alpha(t)\right) - A^{\alpha,\beta} f_\alpha(t)\left(1-f_\beta(t)\right)\Big]\end{aligned} \tag{2.85}$$

where $\Omega_\alpha = \int_{C_\alpha} \mathrm{d}\mathbf{k}$ and

$$A^{\alpha,\beta} = \int_{C_\alpha}\left(\int_{C_\beta} S_{\mathbf{k}\to\mathbf{k}'}\mathrm{d}\mathbf{k}'\right)\mathrm{d}\mathbf{k}. \tag{2.86}$$

The first term on the right hand side of eq. (2.85), the drift-term, requires knowledge of the values of $f(t,\mathbf{k})$ on the boundaries of each cell. Each cell, defined by radius k_n and angle θ_m, has boundary distribution values at half integer values of n and m, as shown in fig. 2.11. The boundary coordinates are uniformly spaced and labelled $k_{-1/2} = 0 < k_{1/2} < k_{3/2} < \cdots < k_{N+1/2} = k_{max}$ and $\theta_{-1/2} = 0 < \theta_{1/2} < \theta_{3/2} < \cdots < \theta_{M+1/2} = 2\pi$. For an electric field in the x-direction, $\mathbf{E} = E\hat{\mathbf{\imath}}$, the drift-term evaluates to

$$\begin{aligned}\mathbf{E}\cdot\int_{C_\alpha}\nabla_{\mathbf{k}} f(t,\mathbf{k})\mathrm{d}\mathbf{k} =& E\Big[\left(k_{n+1/2}f_{n+1/2,m} - k_{n-1/2}f_{n-1/2,m}\right)\left(\sin\theta_{m+1/2} - \sin\theta_{m-1/2}\right) \\ &- \left(\sin\theta_{m+1/2}f_{n,m+1/2} - \sin\theta_{m-1/2}f_{n,m-1/2}\right)\left(k_{n+1/2} - k_{n-1/2}\right)\Big].\end{aligned} \tag{2.87}$$

The boundary values are estimated using a Taylor expansion, taking into account the direction of flux by defining a ‘wind velocity’, $a = -\mathbf{E}\cdot\mathbf{n}$, where $\mathbf{n}$ is the unit vector normal to the boundary in the direction away from the cell. For the boundaries of constant k,

$$f_{n+1/2,m} \approx \begin{cases} f_{n,m} + \frac{\Delta k_n}{2}\partial_k f_{n,m} & \text{for } a > 0 \\ f_{n+1,m} - \frac{\Delta k_{n+1}}{2}\partial_k f_{n+1,m} & \text{for } a < 0 \end{cases} \tag{2.88}$$

where $\Delta k_n = k_{n+1/2} - k_{n-1/2}$ and the derivatives, $\partial_k f_{n,m}$, can be approximated using a minmod slope limiter, to ensure the TVD conditions are satisfied [78]. The minmod limited gradients are defined as

$$f'_{n,m} = \mathrm{minmod}\left(\frac{f_{n,m} - f_{n-1,m}}{k_n - k_{n-1}}, \frac{f_{n+1,m} - f_{n,m}}{k_{n+1} - k_n}\right), \tag{2.89}$$

where the minmod function is

$$\mathrm{minmod}(a,b) = \frac{1}{2}\left(\mathrm{sgn}(a) + \mathrm{sgn}(b)\right)\min\left(|a|, |b|\right). \tag{2.90}$$

Exactly the same procedure is followed for the boundaries of constant θ.

The second term on the right hand side of eq. (2.85), the collision term, requires the

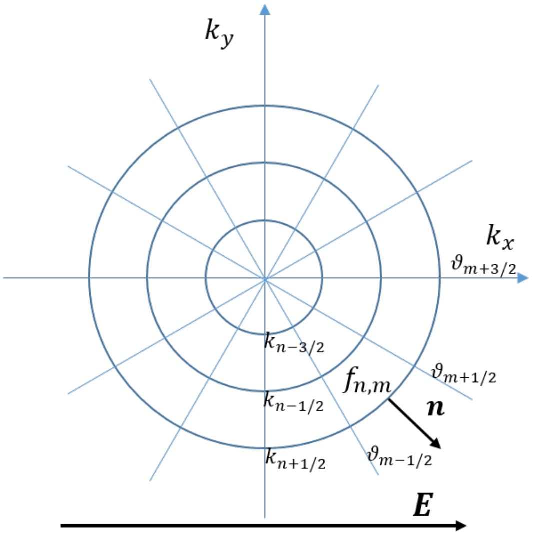

Figure 2.11: Diagram of the radial discretisation of k-space used in the DG simulation. $f_{n,m}$ is the occupation of cell $C_{n,m}$, where the labels n, m and α can be used interchangeably, the values of k and θ at the boundaries are denoted by half integer indices, $\mathbf{n}$ is the unit vector normal to any given boundary and $\mathbf{E}$ shows the direction of the applied electric field.

evaluation of the integrals (2.86), which are constant throughout the simulation, for each given cell. For each cell C_α and each scatterer, the summation over all cells, C_β, is reduced to a sum over two sets (absorption and emission), at fixed k, by consideration of the energy conserving limits (1.39) and (1.40) of the transition rates. For intrinsic phonons, this can be evaluated analytically, whereas the values for substrate polar phonons, impurities and short-range defects are evaluated numerically in quadrature.

At each time step, we calculate the simulated charge density,

$$n_{sim}(t) = \frac{2g_v}{(2\pi)^2} \int f(t, \mathbf{k}) \mathrm{d}\mathbf{k} = \frac{2g_v}{(2\pi)^2} \sum_\alpha f_\alpha(t) \Omega_\alpha, \tag{2.91}$$

mean velocity,

$$\langle \mathbf{v}(t) \rangle = \frac{2g_v}{(2\pi)^2 n_{sim}} \frac{1}{\hbar} \int f(t, \mathbf{k}) \nabla_{\mathbf{k}} \varepsilon(\mathbf{k}) \mathrm{d}\mathbf{k} = \frac{2g_v}{(2\pi)^2 n_{sim}} v \sum_\alpha f_\alpha \frac{\mathbf{k}_\alpha}{k_\alpha} \Omega_\alpha, \tag{2.92}$$

and mean energy,

$$\langle \varepsilon(t) \rangle = \frac{2g_v}{(2\pi)^2 n_{sim}} \int f(t, \mathbf{k}) \varepsilon(\mathbf{k}) \mathrm{d}\mathbf{k} = \frac{2g_v}{(2\pi)^2 n_{sim}} \hbar v \sum_\alpha f_\alpha k_\alpha \Omega_\alpha. \tag{2.93}$$

Charge conservation means that the charge density (2.91) should be constant throughout the simulation. This is used as a test to make sure that flux through cells is balanced and the domain size is reasonable.

2.5.3 Preliminary Results

The results shown are obtained using both the MC and DG methods, along with all of the scattering mechanisms shown in sections 2.3.2 and 2.4, except for short-range scattering. Therefore, we have assumed pristine, non-defective monolayer graphene on a $\mathrm{SiO_2}$ substrate. The physical parameters used are the same as were used to demonstrate the scatter rates, Γ, in fig. 2.9a: density of impurities, $n_{imp} = 0.5 \times 10^{15}$ m^{-2}; impurity distance, $d_{imp} = 0.4$ nm; substrate distance, $d_{spp} = 0.4$ nm, and temperature, $T = 10$ K.

In both the MC and DG simulations, the drift velocity is calculated as the mean velocity in the direction of the applied electric field, $v_d = \langle v_x \rangle$ for a field in the x-direction. The mobility is calculated from this drift velocity, $\mu = v_d/E$.

Figure 2.12 shows comparisons of the two methods over the course of the simulation. These results were achieved on a grid of $k_{max} = 1.5\,\mathrm{nm}^{-1}$, partitioned as $\{k \times \theta\} = \{140 \times 100\}$ for DG and $k_{max} = 2\,\mathrm{nm}^{-1}$, partitioned as $\{k_x \times k_y\} = \{150 \times 150\}$ for MC. In the MC simulations we use 5×10^4 particles. The DG and MC methods provide congruent results for both the electron drift velocity (average velocity in the direction of the applied electric field), v_d, and average energy, $\langle \varepsilon \rangle$, over all times t.

Using the DG method, we investigate the effect of the electric field on the mobility. For small fields, we expect mobility to be independent of the applied field, where $v_d \propto E$. The low-field dynamics are described in detail in section 3.2. The results of varying applied electric field on the mobility and drift velocity are shown in fig. 2.13. For the electronic scattering used here, the mobility converges for electric fields $E < 10^3\mathrm{V/m}$, as shown in fig. 2.13a. Figure 2.13b shows that the drift velocity tends toward a constant value, limited by the single electron speed ($v = 10^6$ ms^{-1}), in the high field regime such that $\mu \propto 1/E$ for very large ($> 10^6$ V/m) electric fields. Similar saturation points (10^6 V/m) have been observed in graphene field effect transistors [7].

2.5.4 Discussion

It clear from fig. 2.12 that the MC and DG methods give equivalent results, as was been shown previously in ref. [73]. This provides two methods to choose from when solving the Boltzmann equation for broad distributions with multiple sources of scattering.

The DG method has an advantage over MC in that statistical noise is absent. In MC simulations, this problem increases at low fields. For low driving electric fields, the SNR is reduced due to the small drift velocities resulting in the stochastic scattering becoming the dominant term the Boltzmann equation. This noise can only be decreased by increasing the number of simulated particles, vastly increasing computational time.

However, MC provides flexibility to include additional effects, acting on the individual electrons throughout simulation. It could have potential advantages when considering spatial inhomogeneity. For this case, one can discretise real space into N_r real-space cells. Although, the computational cost should be considered. The simula-

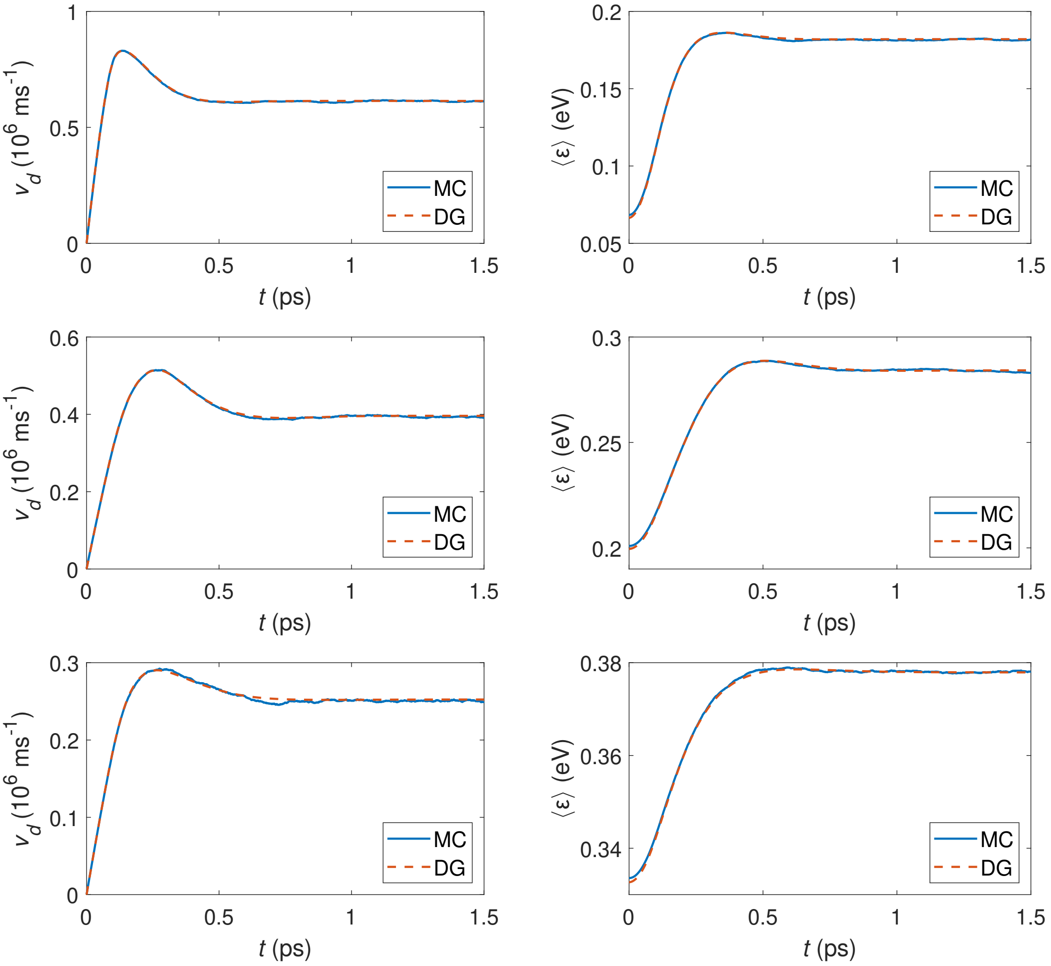

Figure 2.12: Variation of drift velocity (left-most plots), v_d, and mean electron energy (right-most plots), $\langle\varepsilon\rangle$, with time, t. The plots show comparisons of the results from both MC and DG methods for chemical potentials of 0.1 eV, 0.3 eV and 0.5 eV from top to bottom for a field of $E = 10^6\,\mathrm{V/m}$. Physical parameters used: density of impurities, $n_{imp} = 0.5 \times 10^{15}\ \mathrm{m}^{-2}$; impurity distance, $d_{imp} = 0.4$ nm; substrate distance, $d_{spp} = 0.4$ nm; temperature, $T = 10$ K.

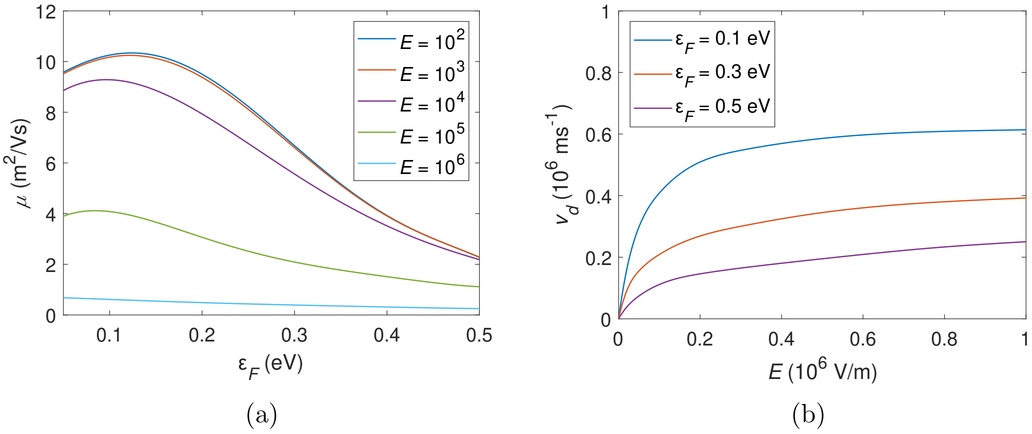

(a) (b)

Figure 2.13: (a) Mobility, μ, variation with chemical potential, ε_F, for a number of different applied electric field strengths, E (in V/m). (b) Drift velocity, v_d, as a function of applied electric field strength, E, for different values of the chemical potential, ε_F. The DG method was used to calculate the results. Physical parameters used: density of impurities, $n_{imp} = 0.5 \times 10^{15}$ m^{-2}; impurity distance, $d_{imp} = 0.4$ nm; substrate distance, $d_{spp} = 0.4$ nm; temperature, $T = 10$ K.

tion time, t_{sim}, is increased by more than $N_r \times t_{sim}$, due to running N_r homogeneous simulations and then redistributing the particles throughout the real space cells after each time step. In chapter 4, we will employ and adapt the MC method for transport in superlattice structures, where the energy band structure is significantly perturbed from the isotropic conical structure and, within each time step, we can simulate both electron scattering and tunnelling between subbands.

Chapter 3

Modelling of Conductivity in Pristine Graphene

3.1 Simulating Inter-Band Scattering

At high temperatures and small chemical potentials, there exists both holes in the valence band and electrons in the conduction band. If there are no inelastic scattering events, then the two bands can be treated independently. However, if inelastic phonon scattering is present, then the bands are coupled and interband scattering should be carefully considered.

The linearised Boltzmann method, eq. (1.50), can be used to find the conductivity based upon the rates $S_{\mathbf{k}\to\mathbf{k}'}$ of electron scattering between any two states $\mathbf{k}$ and $\mathbf{k}'$, where there exists no discrimination between the bands of the initial and final states (i.e. $s = \pm 1$ and $s' = \pm 1$ independently). However, in simplifying the problem to the LB method, we lose information on the momentum distribution of electrons and holes. Here we show how the methods described previously, in section 2.5, for simulating an electron distribution can be extended to a coupled electron-hole distribution. We will then use these simulations to investigate the effect of phonon scattering on the electron-hole dynamics.

First, it is useful to define the distribution function of the electrons and holes separately, $f_e(\mathbf{k}) = f(s = +1, \mathbf{k})$ and $f_h(\mathbf{k}) = 1 - f(s = -1, \mathbf{k})$ respectively, within k-space where $s = \pm 1$ denotes the band index ($\varepsilon = s\hbar v k$).

The DG method treats the full distribution function in energy space according to eq. (2.85). Therefore, we can easily extend the method to model the electron distribution over negative energy values ($s = -1$). In the scattering term (second term on RHS of eq. (2.85)), it should be taken care that the band indices (s) are included when computing the scattering coefficients, $A^{\alpha,\beta}$, from eq. (2.86). For the drift term (first term on RHS of eq. (2.85)), it is most convenient to calculate separately for electrons and holes i.e. $df_{\text{drift},e} = \mathbf{E}\cdot\int_{C_\alpha}\nabla_{\mathbf{k}} f_e(t,\mathbf{k})\mathrm{d}\mathbf{k}$ and $df_{\text{drift},h} = -\mathbf{E}\cdot\int_{C_\alpha}\nabla_{\mathbf{k}} f_h(t,\mathbf{k})\mathrm{d}\mathbf{k}$, using eq. (2.87). This also ensures symmetry in the TVD conditions for electrons and holes.

The total drift term over all energy space is then

$$df_{\text{drift}}(s,\mathbf{k}) = \begin{cases} df_{\text{drift},e}(\mathbf{k}) & \text{for } s=+1 \\ -df_{\text{drift},h}(\mathbf{k}) & \text{for } s=-1 \end{cases}. \tag{3.1}$$

In the MC simulations we model the distinct hole and electron distributions, f_e and f_h. The algorithm for the hole distribution, f_h, follows that of the electron distribution outlined in section 2.5.1, where $E \to -E$ due to the changed polarity of the charge carriers. The total scatter rates, Γ, for holes are found as in eq. (1.46) using the electron scatter rates $S_{\mathbf{k}\to\mathbf{k}'}$, except we sum over all *initial* electron states, $\mathbf{k}$, rather than *final* states, $\mathbf{k}'$, since the initial state of the electron corresponds to the final state of the hole. We also have to be sure to include the band indices, s i.e. $\varepsilon(k) \to -\varepsilon(k)$. Then, upon calculating the total scatter rates for holes, we find that they are equivalent to the electron scattering rates with respect to the k-coordinates. Therefore, we have two simultaneous independent identical algorithms moving the electrons and holes in their respective k-space grids. However, upon scattering, we now have to consider the possibility for interband transport, thus coupling the two otherwise independent algorithms.

The interband transitions consist of emission and absorption. We will first address emission. This is simply incorporated into the electron scattering. Including the band index of the final state, s', in the calculation, the total scatter rates of electrons in the conduction band by Γ- and K-optical phonons (eqs. (2.83) and (2.84)) become

$$\Gamma^O(\varepsilon) = \frac{\beta_O^2}{\hbar^2 v^2 \rho_m \omega_O}\left[\frac{\varepsilon - \hbar\omega_O}{s'}\left(N_{\omega_O}+1\right) + \left(\varepsilon + \hbar\omega_O\right) N_{\omega_O}\right] \tag{3.2}$$

and

$$\Gamma^K(\varepsilon) = \frac{\beta_K^2}{\hbar^2 v^2 \rho_m \omega_K}\left[\frac{\varepsilon - \hbar\omega_K}{s'}\left(N_{\omega_K}+1\right) + \left(\varepsilon + \hbar\omega_K\right) N_{\omega_K}\right]. \tag{3.3}$$

If the electron scatters via emission and the final state, k', is in the valence band ($s' = -1$), then a hole from the corresponding cell in the valence band, specifically the closest hole to the final state, and the scattered electron are both removed from the simulation.

Since we are simulating valence holes and conduction electrons, there are no simulated particles that can represent electron absorption into the conduction band. Instead, we need to input a reasonable number of new particles (electron/hole pairs) representing absorption from the continuum of available electron states (i.e. empty hole states) in the valence band at each time step within the simulation. For each cell, C_{ij}, in the valence band with $k < \omega/v$, we find cells in the conduction band that are coupled via absorption, $C_{i'j'}$. This means finding the cells with k-space coordinates such that $|k' - \hbar\omega + k| < \delta k/2$, where $k' = \sqrt{k_x(i')^2 + k_y(j')^2}$ and $k = \sqrt{k_x(i)^2 + k_y(j)^2}$ correspond to the k-space coordinates of the cell in the conduction and valence band respectively, and δk is the width of each cell. For each pair of coupled cells, we calculate

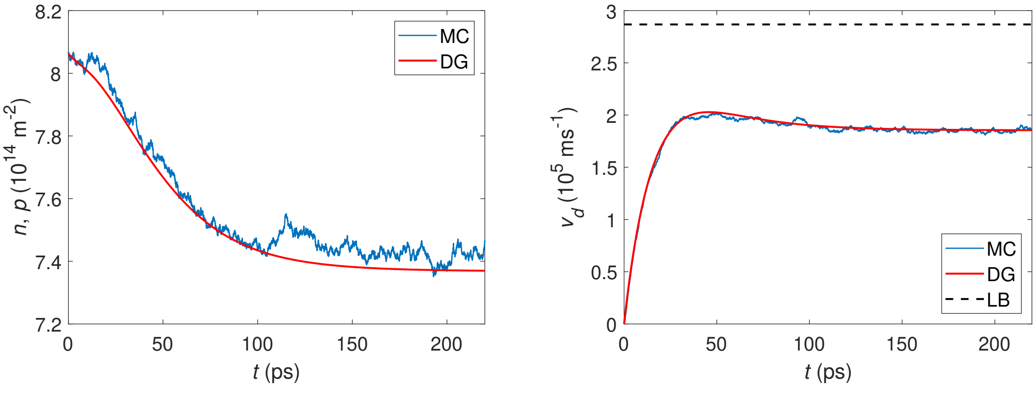

(a) (b)

Figure 3.1: (a) Electron and hole carrier densities, n and p, and (b) drift velocity, v_d, as a function of time, calculated for K and Γ- optical phonon scattering with zero chemical potential, $\varepsilon_F = 0$, temperature, $T = 300$ K, and an electric field of strength $E = 10^3$ V/m using both MC and DG methods. The black dashed line in figure (b) shows the value of v_d calculated using the linearised Boltzmann (LB) method.

the flux between them using the incremental scatter rates

$$\Gamma^O_{\text{abs}}(\varepsilon) = \frac{\beta_O^2}{2\pi\hbar^2 v^2 \rho_m \omega_O} \left(\varepsilon + \hbar\omega_O\right) N_{\omega_O} \Delta\theta \tag{3.4}$$

and

$$\Gamma^K_{\text{abs}}(\varepsilon, \theta_{k,k'}) = \frac{\beta_K^2}{2\pi\hbar^2 v^2 \rho_m \omega_K} \left(\varepsilon + \hbar\omega_K\right) N_{\omega_K} (1 + \cos\theta_{k,k'})\Delta\theta, \tag{3.5}$$

where $\Delta\theta$ is the angular extent of the coupled cell in the conduction band, which is approximately 2π divided by the number of coupled cells, and $\theta_{k,k'}$ is the angle between cells C_{ij} and $C_{i'j'}$. The time between each absorption event is calculated as in eq. (2.79), except the scatter rate is adjusted by the occupation, since we are generating the flux from the simulated distribution function rather than individually simulated particles,

$$\Delta t = -\frac{1}{\Gamma_{\text{abs}} \left(1 - f_h(k)\right)\left(1 - f_e(k)\right)} \ln\varrho \tag{3.6}$$

where $0 < \varrho < 1$ is a randomly generated number. For each absorption event, a hole and an electron are randomly generated within cells C_{ij} and $C_{i'j'}$ respectively.

In this subsection, the interband simulations were performed using k-space grids with an extent $k_{max} = 0.5$ nm^{-1}, partitioned as $k \times \theta = 200 \times 140$ for DG simulations and $k_x \times k_y = 200 \times 200$ for MC simulations. The total number of particles (electrons and holes) used in the MC simulations is 5×10^4.

Figure 3.1 shows the results of both methods when simulating scattering by optical (K and Γ) phonons only with no doping ($\varepsilon_F = 0$) at room temperature ($T = 300$ K) and with an applied electric field strength of $E = 10^3$ V/m. Firstly, we note that the two methods successfully provide congruent results. Figure 3.2 shows the number of interband scatter events by both emission and absorption in 10 ps intervals from the

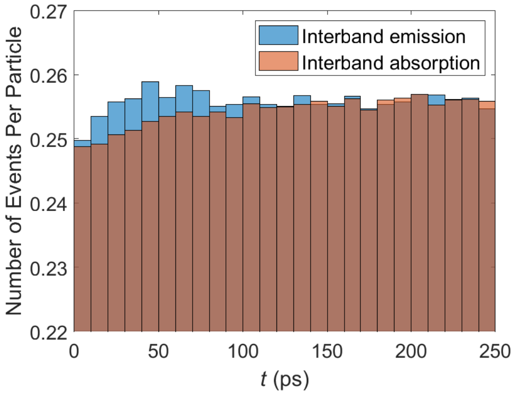

Figure 3.2: Number of interband scattering events per particle in a 10 ps interval via Γ and K optical phonon emission and absorption over time, t, simulated using the MC method. Chemical potential, $\varepsilon_F = 0$, temperature, $T = 300$ K, and electric field, $E = 10^3$ V/m.

MC simulation. Initially, as the distribution is perturbed, the rate of electron emission is larger than absorption. At later times, the emission and absorption rates equilibrate and reach a detailed balance. This results in a net decrease in the carrier density initially (fig. 3.1a), with phonon emission causing electrons in the conduction band to fill available states in the valence band as the distributions are shifted under the applied field.

Using the relaxation times, eqs. (2.67) and (2.68), we also calculated the the conductivity, σ, using the linearised Boltzmann (LB) method, eq. (1.50). The drift velocity is then calculated as $v_d = \sigma E/(e(n+p))$ where, for $\varepsilon_F = 0$, n and p are given by eq. (1.21). Figure 3.1b shows the results of MC and DG simulations compared to the LB result for the carrier drift velocity, v_d. We find that the simulated results of the full Boltzmann equation give a smaller value of drift velocity than the LB method. This is likely due to the increased availability of lower energy states for electron emission as the distribution spreads out in k-space causing an increase in scattering which is not captured in eqs. (2.67) and (2.68) due to the rigid $1 - f_0$ terms, as described in section 2.4.4. We note, however, that the drift velocity is of the same order as calculated using the LB method and the change in the carrier density is less than 10%. Therefore, the LB method still provides a reasonable approximation of the behaviour of inelastic scattering, even around the charge neutrality point, $\varepsilon_F = 0$.

When elastic scattering dominates over inelastic scattering, the steady-state characteristics converge towards the LB approximation. To demonstrate this, we include a simple characteristic unscreened ($\epsilon_{sc} = 0$) short-range defect elastic scattering potential with transition rate given by eq. (2.49). Using the LB method, the mobility for such scattering is

$$\mu = \frac{4e\hbar v^2}{n_{sr} A_{sr} U_0 \pi (n+p)}, \tag{3.7}$$

where n_{sr} is the density of defects, A_{sr} is the effective cross-sectional area of defect

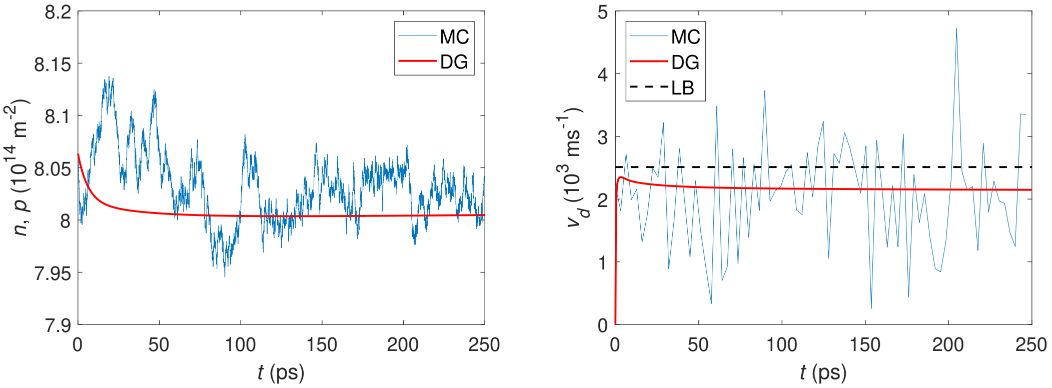

(a) (b)

Figure 3.3: (a) Electron and hole carrier densities, n and p, and (b) drift velocity, v_d, as a function of time, calculated using both MC and DG methods including K and Γ-optical phonon scattering and an unscreened short-range defect scattering potential of strength $n_{sr}(A_{sr}U_0)^2 = 0.21$ nm^{2}eV^2. The chemical potential, $\varepsilon_F = 0$, temperature, $T = 300$ K, and electric field strength, $E = 10^3$ V/m. The black dashed line in figure (b) shows the value of v_d calculated using the linearised Boltzmann (LB) method.

scattering and U_0 is the potential perturbation caused by the defects. Figure 3.3 shows the time-varying carrier densities, n and p, and drift velocity ($v_d = \mu E$) when including defect scattering of strength $n_{sr}A_{sr}U_0 = 0.21$ nm^{2}eV^2.

Stochastic simulation of defect scattering, combined with the reduced drift velocity, v_d, results in a smaller signal-to-noise ratio (SNR) for the MC results in fig. 3.3b compared to fig. 3.1b, where only phonon scattering is included. This SNR can be increased by increasing the number of simulated particles within the MC simulation.

3.2 Joule Heating

The conductivity described by the linearised Boltzmann approximation, eq. (1.48), assumes that the distribution function, expanded as powers of the applied field, is dominated by the zero-th and first order terms. This is generally the case for small electric field strengths, where the shift in the distribution function is linear with respect to the field strength, as long as the distribution is constrained by elastic scattering. If the electron gas momenta are not constrained by elastic scattering, then the electron energy can continue to increase under the applied fields such that the higher order terms become significant. This phenomenon, known as ‘Joule heating’, has been observed previously, e.g. in metals [79].

Here, we will expand the Boltzmann equation up to second order, using the momentum relaxation time approximation, and compare the results with full numerical solutions of the BTE using the DG and MC methods.

The momentum relaxation time, eq. (1.49), gives the time constant over which a perturbed, coherent distribution of electrons is completely dephased by scattering to a distribution with zero net momentum. The momentum relaxation time approximation approximates the collision term, eq. (1.43), in the BTE as

$$\left(\frac{\partial f(t,\mathbf{k})}{\partial t}\right)_{coll} \approx -\frac{f(t,\mathbf{k})-\bar{f}(t,k)}{\tau(k)} \tag{3.8}$$

where $\bar{f}$ represents the angular average of the function f [30]. Substituting this into the BTE, eq. (1.44), we have

$$\frac{\partial f(t,\mathbf{k})}{\partial t} + \frac{1}{\hbar}\mathbf{F}\cdot\nabla_{\mathbf{k}} f(t,\mathbf{k}) = -\frac{f(t,\mathbf{k})-\bar{f}(t,k)}{\tau(k)}. \tag{3.9}$$

We expand the time-dependant distribution function as a linear sum, $f(t,\mathbf{k}) = f_0(t,\mathbf{k}) + f_1(t,\mathbf{k}) + f_2(t,\mathbf{k})\cdots$, of terms with varying field dependencies: $f_n \propto E^n$. The zero-th order term, f_0, is the unperturbed Fermi-Dirac equilibrium distribution, $f_0(k) = [\exp(\varepsilon(k)/k_BT)+1]^{-1}$.

Expanding the BTE to first order in the applied field strength,

$$\frac{\partial f_1(t,\mathbf{k})}{\partial t} + \frac{\mathbf{F}}{\hbar}\cdot\nabla_{\mathbf{k}} f_0(k) = -\frac{f_1(t,\mathbf{k})-\bar{f}_1(t,k)}{\tau(k)}, \tag{3.10}$$

since $f_0(k)$ is time independent and symmetric i.e. $\partial f_0/\partial t = 0$ and $f_0 = \bar{f}_0$. From eq. (3.10), we can see that the solution for $f_1(t,\mathbf{k})$ will be asymmetric in $\mathbf{k}$ with respect to the direction of the field, $\mathbf{F}$. This can be understood physically, since the first order perturbation, f_1, is proportional to the applied field, which drives the electron motion such that states with momentum opposing the field direction (negative $\mathbf{F}\cdot\mathbf{k}$) have an increasing distribution (positive f_1) whilst those with momentum in the field direction (positive $\mathbf{F}\cdot\mathbf{k}$) have an decreasing distribution (negative f_1) and charge conservation requires that the magnitude of change in the distribution be equivalent for positive and negative $\mathbf{F}\cdot\mathbf{k}$. Therefore, the angular average disappears, $\bar{f}_1(t,k) = 0$. Solving eq. (3.10) for the first order correction,

$$f_1(t,\mathbf{k}) = -\tau(k)\frac{\mathbf{F}}{\hbar}\cdot\nabla_{\mathbf{k}} f_0(k)\left(1-e^{-t/\tau(k)}\right). \tag{3.11}$$

In the long time limit ($t \gg \tau$), we find the steady state solution,

$$f_1(t\to\infty,\mathbf{k}) = -\tau(k)\frac{\mathbf{F}}{\hbar}\cdot\nabla_{\mathbf{k}} f_0(k), \tag{3.12}$$

for which $\partial f_1(t,\mathbf{k})/\partial t = 0$, and thus $\partial f(t,\mathbf{k})/\partial t = 0$ to first order. In section 1.4, we used the first order steady state solution, $f(\mathrm{k}) = f_0(k) + f_1(t\to\infty,\mathbf{k})$, to calculate the linearised Boltzmann mobility, eq. (1.53).

Expanding to second order, we find

$$\frac{\partial f_2(t,\mathbf{k})}{\partial t} + \frac{\mathbf{F}}{\hbar}\cdot\nabla_{\mathbf{k}} f_1(t,\mathbf{k}) = -\frac{f_2(t,\mathbf{k})-\bar{f}_2(t,k)}{\tau(k)}, \tag{3.13}$$

where we have used eq. (3.10) to cancel out the first order terms. Approximating f_1 in the long time limit,

$$\frac{\partial f_2(t,\mathbf{k})}{\partial t} \approx \frac{\tau}{\hbar^2}\left(\mathbf{F}\cdot\nabla_{\mathbf{k}}\right)^2 f_0(k) - \frac{f_2(t,\mathbf{k}) - \bar{f}_2(t,k)}{\tau(k)}. \tag{3.14}$$

Taking the angular average of eq. (3.14) and integrating with respect to time,

$$\bar{f}_2(t,k) \approx \frac{t\tau(k)}{\hbar^2}\left\langle \left(\mathbf{F}\cdot\nabla_{\mathbf{k}}\right)^2 f_0(k)\right\rangle_\theta \tag{3.15}$$

is the angular average of the second order perturbation in the long time limit ($t \gg \tau$), where we have also used $\langle \ldots \rangle_\theta$ to represent the angular average. Firstly, we note that $\bar{f}_2$ is proportional to time. This means that, to second order in the applied field, there is no steady state solution. Secondly, since the energy of electrons depends only on the magnitude of the momentum and not the orientation, the average energy of electrons in the distribution depends only on the angular average of the distribution,

$$\langle\varepsilon\rangle(t) = \frac{1}{n}\int \mathrm{d}\varepsilon\, \varepsilon D(\varepsilon)\left(\bar{f}_0(\varepsilon) + \bar{f}_2(t,\varepsilon)\right). \tag{3.16}$$

The integral over $\bar{f}_0(\varepsilon)$ gives the time-independent initial average energy as given by the Fermi-Dirac distribution which, for graphene at $T = 0$, is $\langle\varepsilon\rangle(t = 0) = 2\varepsilon_F/3$. Using eq. (3.15), the average energy of electrons increases linearly with time in the long time limit,

$$\delta\langle\varepsilon\rangle(t) = \langle\varepsilon\rangle(t) - \langle\varepsilon\rangle(t=0) \approx \frac{t}{\hbar^2 n}\int \mathrm{d}\varepsilon\, \varepsilon D(\varepsilon)\tau(\varepsilon)\left\langle \left(\mathbf{F}\cdot\nabla_{\mathbf{k}}\right)^2 f_0(k)\right\rangle_\theta. \tag{3.17}$$

To check the validity of the second order expansion, we will compare eq. (3.17) to results using the numerical calculations of the MC simulations as outlined in section 2.5.1.

In 2D, the angular average of the second order perturbation, eq. (3.15), is

$$\begin{aligned}\bar{f}_2(t,k) &= \frac{t\tau(k)e^2E^2}{\hbar^2}\frac{1}{2\pi}\int_0^{2\pi}\mathrm{d}\theta\,\frac{\partial^2}{\partial k_x^2} f_0(k_x(\theta),k_y(\theta)) \\ &= -\frac{t\tau(k)e^2E^2}{\hbar^2}\left[\frac{\delta(k_F-k)}{k} + \frac{k}{2}\frac{\partial}{\partial k}\left(\frac{\delta(k_F-k)}{k}\right)\right],\end{aligned} \tag{3.18}$$

where we have assumed that the field is in the x-direction, $\mathbf{E} = E\hat{\mathbf{\imath}}$.

For the purpose of comparing the analytical 2nd order approximation to the Monte Carlo simulations, we will consider a simple case of isotropic elastic scattering with an energy-independent relaxation time. Then, the total scatter rate, Γ, (eq. (1.46)) used in the MC simulation is related to the momentum relaxation time (eq. (1.49)) by

$$\Gamma = \frac{1}{\tau}\frac{2\pi}{\int_0^{2\pi}(1-\cos\theta)} = \frac{1}{\tau}. \tag{3.19}$$

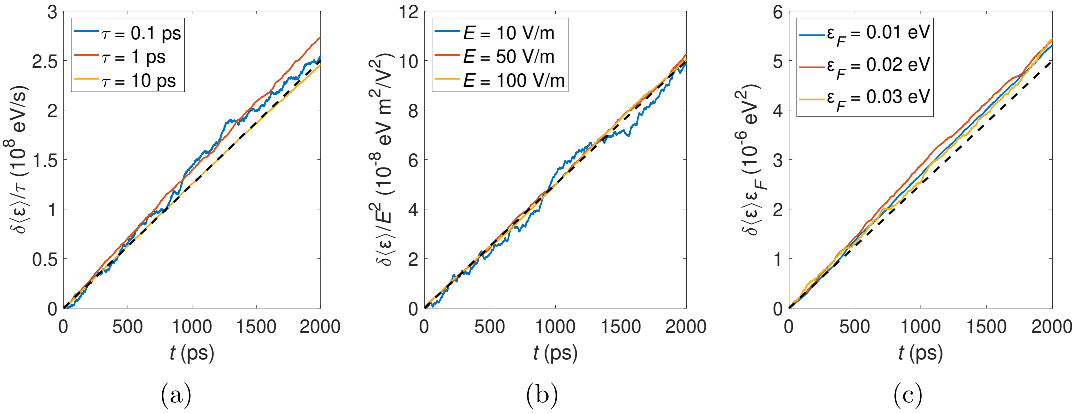

(a) (b) (c)

Figure 3.4: Monte Carlo results for the change of average electron energy, $\delta\langle\varepsilon\rangle$, with time t, for varying parameters: (a) relaxation time, τ, (b) electric field strength, E, and (c) chemical potential, ε_F. In each case, $\delta\langle\varepsilon\rangle$ is scaled by the parameter being varied such that the same temporal dependence remains the same for ease of comparison. The black dashed line shows the results of eq. (3.20). We have set $\tau = 1$ ps, $E = 50$ V/m, $\varepsilon_F = 0.02$ eV as standard.

In 2D graphene, the density of states is $D(\varepsilon) = g_s g_v \varepsilon / 2\pi\hbar^2 v^2$ and carrier density, $n = D(\varepsilon_F)\varepsilon_F/2$ (see eqs. (1.15) and (1.20)). Using eq. (3.18), eq. (3.17), describing the time-varying change in the average electron energy, becomes

$$\delta\langle\varepsilon\rangle = -\frac{t\tau e^2 E^2}{\hbar^2}\frac{2}{\varepsilon_F^2}(\hbar^2 v^2)\int \mathrm{d}\varepsilon\, \varepsilon^2 \left[\frac{\delta(\varepsilon_F - \varepsilon)}{\varepsilon} + \frac{\varepsilon}{2}\frac{\partial}{\partial\varepsilon}\left(\frac{\delta(\varepsilon_F - \varepsilon)}{\varepsilon}\right)\right] = \frac{t\tau e^2 E^2 v^2}{\varepsilon_F}. \tag{3.20}$$

The results of the time-varying averaged energy from MC simulations are compared to eq. (3.20) in fig. 3.4 under varying parameters: relaxation time, τ; electric field strength, E; and chemical potential, ε_F.

If the momentum relaxation time, τ, is energy-dependent then the mean change in electron energy due to an applied field depends only on the value at the Fermi energy, i.e.

$$\delta\langle\varepsilon\rangle = \frac{t\tau(\varepsilon_F)e^2 E^2 v^2}{\varepsilon_F}, \tag{3.21}$$

in the limit $T = 0$.

3.2.1 Including Inelastic Scattering

We have found that, when scattering is purely elastic, it is not possible to reach a steady-state within the BTE. Physically, this means that an electric field applied to an electron distribution causes the electrons to continually gain energy according to eq. (3.17). In order to find physical steady-state, equilibrium solutions of the electron distribution in an electric field, we need to consider inelastic scattering. Inelastic scattering by phonon emission will remove energy from hot electrons that have been accelerated by the field to the phonon energy.

Here we model graphene with elastic impurity scattering (section 2.3.2) and inelastic

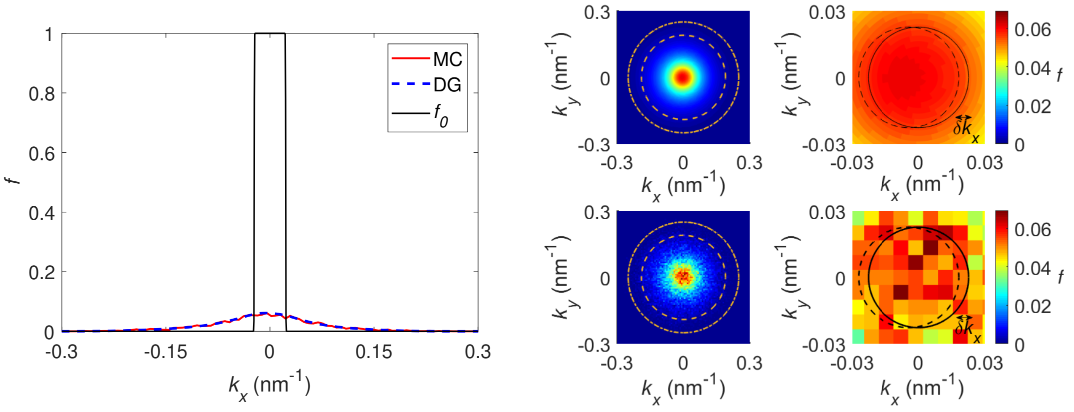

(a) (b)

Figure 3.5: Steady-state distribution of electron momenta calculated for a small impurity density, $n_{imp} = 0.025 \times 10^{16}$ m^{-2}, at a distance $d_{imp} = 1$ nm and chemical potential, $\varepsilon_F = \langle \delta\varepsilon_{imp} \rangle = 0.015$ eV. (a) Cross-section of the distribution at $k_y = 0$ calculated using MC (solid red line) and DG (dashed blue line) compared to the initial Fermi-Dirac distribution, f_0. (b) Steady-state distribution shown in the full 2D k-space calculated using DG method (top) and MC method (bottom). Solid black circle represents the initial Fermi circle, of radius k_F, dashed black circle shows a linear shift of the Fermi circle by $\delta k_x = eE\tau(\varepsilon_F)/\hbar$, orange dashed circle represents the K-phonon level, and the orange dashed-dotted circle represents the Γ-phonon level. Note that the right-hand plots show the centre of the left-hand plots. The colour scale corresponds to both left- and- right hand plots.

Γ- and K-optic phonon scattering (section 2.4.4) to investigate how Joule heating could affect the mobility compared to the mobility calculated using the linearised Boltzmann (LB) steady-state solution, eq. (1.53).

For small impurity densities, i.e. highly pure graphene, the mean chemical potential at charge neutrality can also be small. When the chemical potential is much smaller than the phonon energy, Joule heating will have a stronger effect on the electrons, since inelastic scattering is only effective once the electrons are accelerated to the phonon energy.

To demonstrate this, we consider a small impurity density, $n_{imp} = 0.025 \times 10^{16}$ m^{-2}. We take the chemical potential to be at the limit set by residual carriers at charge neutrality, $\langle \delta\varepsilon_{imp} \rangle$, as given by eq. (2.24). From the initial Fermi-Dirac distribution, f_0, at $t = 0$, we achieve a non-degenerate, dilute electron gas in the long-time, steady-state limit as shown in fig. 3.5a. The point at which the steady-state is realised is determined by the phonon energy, as shown in fig. 3.5b. Once the carriers reach the phonon limit, they relax their energy resulting in an equilibrium ensemble distribution.

Figure 3.6 shows the results of simulation for $n_{imp} = 0.025 \times 10^{16}$ m^{-2} (corresponding to fig. 3.5). For small times, the simulated drift velocity agrees well with the result calculated from the LB formalism as the distribution is initially shifted from thermal equilibrium. However, as the distribution spreads in k-space and the second order term, eq. (3.15), becomes more dominant, the mean velocity decreases. Steady state is

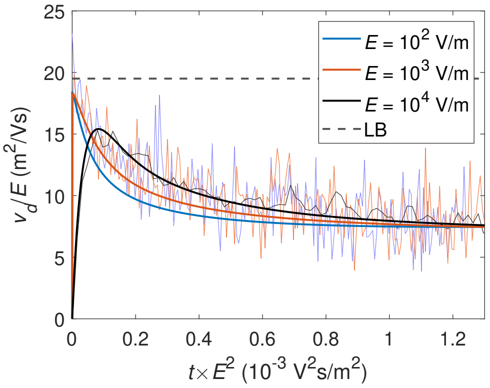

Figure 3.6: Variation of drift velocity, v_d, with time, t, calculated for a range of applied electric field strengths, E, using the DG method (bold solid lines) and MC method (fine solid lines). The time-independent LB result is shown by the dashed black line. The impurity density used is, $n_{imp} = 0.025 \times 10^{16}$ m^{-2}, at a distance $d_{imp} = 1$ nm and with a chemical potential, $\varepsilon_F = \langle \delta\varepsilon_{imp} \rangle = 0.015$ eV.

realised once the carrier energy approaches the optical phonon energy.

For larger chemical potentials, the maximum electron energy at thermal equilibrium may already be close to the phonon energy at $t = 0$. For large impurity densities, the spatial fluctuation, $\delta\varepsilon_{imp}$, in the impurity potential is large and so the mean carrier energy will always be large. Figure 3.7a shows the steady-state distribution function for a large impurity density, $n_{imp} = 10 \times 10^{16}$ m^{-2} calculated using the DG method, and compared to the thermal thermal equilibrium distribution, f_0. In this case, the deviation of the final distribution from the initial distribution, f_0, is much smaller than in the previous case (fig. 3.5a) where the chemical potential was smaller. Since the perturbation to the distribution is smaller, it can be expected that the effect of the second order term, eq. (3.15), will be smaller and the first order correction, eq. (3.12), may be dominant at all times. In fig. 3.7b, we see that this is the case: the drift velocity agrees with the linearised Boltzmann result for the 1st order steady state solution, eq. (1.53).

3.2.2 Energy Relaxation By Acoustic Phonons

Acoustic phonons with dispersion $\hbar\omega_q = \hbar v_s q$ can also dissipate the energy of the system. We will now include inelastic acoustic phonon scattering in the MC simulations to see how effective they may be in suppressing the effects of Joule heating. In the low temperature limit, $T \to 0$, scattering occurs only via emission with transition rate

$$S^{ac}_{\mathbf{k}\to\mathbf{k}'} = \frac{\pi q}{2A\rho_m v_s} D^2_{ac} \left(1 + \cos\theta_{\mathbf{k},\mathbf{k}'}\right) \delta(\varepsilon_{\mathbf{k}'} - \varepsilon_{\mathbf{k}} + \hbar\omega_q). \tag{3.22}$$

Unlike in eq. (2.58), we have not omitted the phonon energy, $\hbar\omega_q$, from the delta function since we are no longer making the quasi-elastic approximation. Given the linear phonon dispersion, $\hbar\omega_q = \hbar v_s q$ where $q = |\mathbf{k}' - \mathbf{k}|$, energy conservation, as

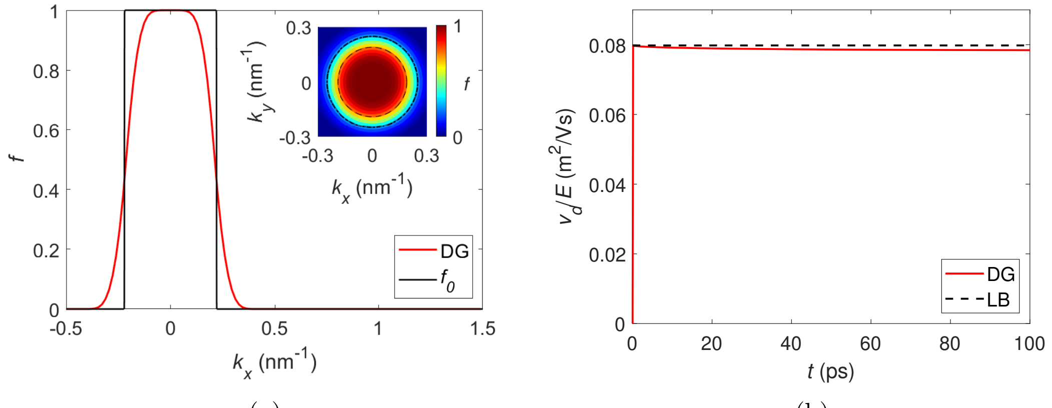

(a) (b)

Figure 3.7: (a) Cross-section, at $k_y = 0$, of the steady-state distribution of electron momenta calculated for a large impurity density, $n_{imp} = 10 \times 10^{16}$ m^{-2}, at a distance $d_{imp} = 1$ nm and chemical potential, $\varepsilon_F = \langle \delta\varepsilon_{imp} \rangle = 0.15$ eV calculated using the DG method (solid red line). The solid black line shows the initial Fermi-Dirac distribution, f_0. Inset shows the steady-state distribution in the full 2D k-space where the black dashed circle represents the K-phonon level, and the black dashed-dotted circle represents the Γ-phonon level. (b) Variation of drift velocity, v_d, with time, t, calculated for electric field strength, $E = 10^4$ V/m, using the DG method. Dashed line shows the result of the linearised Boltzmann method.

enforced by the delta function in eq. (3.22), imposes a constraint on k':

$$v\alpha - v + v_s\sqrt{\alpha^2 + 1 - 2\alpha\cos\theta_{\mathbf{k},\mathbf{k}'}} = 0 \tag{3.23}$$

where $k' = \alpha(\theta_{\mathbf{k},\mathbf{k}'})k$. Therefore, the momentum after scattering, $\hbar k'$, is proportional to the initial momentum, k, but the constant of proportionality, α, is dependent on the angle of scattering, $\theta_{\mathbf{k},\mathbf{k}'}$, and is given by the solution of eq. (3.23). Figure 3.8 shows a schematic example of all possible scattering states via acoustic emission for one initial energy state. Forward scattering ($\theta_{\mathbf{k},\mathbf{k}'} = 0$) is elastic: $k' = k$ and the phonon energy is $\hbar\omega_q = 0$. The maximum phonon emission energy occurs for backscattering ($\theta_{\mathbf{k},\mathbf{k}'} = \pi$): $k' = \frac{v - v_s}{v + v_s}k \approx 0.95k$ and $\hbar\omega_q = \frac{2v_s}{v+v_s}\hbar v k \approx 0.05\hbar v k$. Using the transition rate between single states, eq. (3.22), the total scatter rate of an electron with momentum $\hbar k$ for the MC simulations is

$$\Gamma^{ac}(k) = \frac{D_{ac}^2 v}{8\pi\hbar v \rho_m v_s^2} k^2 \int_0^{2\pi} \mathrm{d}\theta\, \alpha(\theta)\left[1 - \alpha(\theta)\right](1 + \cos\theta)\,. \tag{3.24}$$

Figure 3.9 shows the increase in mean electron energy with time for varying electric fields both with and without the inclusion of inelastic acoustic phonons. We note that the MC simulations over estimate the effect of acoustic phonons in removing energy from the system. This is best seen for $E = 10$ V/m in fig. 3.9, where the average energy decreases with time when acoustic phonons are included. This is an unphysical result which occurs due to the discrete cell spacing used to describe the distribution. Electrons

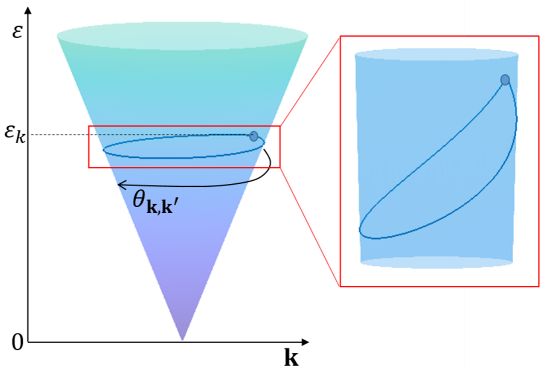

Figure 3.8: Schematic diagram showing the conical energy-wavevector, $\varepsilon(\mathbf{k})$, dispersion in graphene with possible scattering states (blue line) from an initial energy state (blue dot) of energy ε_k via acoustic emission. The angle of scattering is denoted $\theta_{\mathbf{k},\mathbf{k}'}$.

are able to emit energy values from a continuous range, between $0 < \hbar\omega_q < 0.05\hbar vk$, such that emission of low-energy phonons can allow an electron to move into a lower energy state within its current cell of occupation. In all other cases, the energy increase from thermal equilibrium follows eq. (3.21) at small times, before tending towards the steady-state at larger times. Despite the limitations of the MC method for modelling such low energy inelastic scattering, our calculations show that the hot electron effect is significant for electric fields at least as low as ∼100 V/m, comparable to commonly used experimental values, even with elastic scattering from acoustic phonons.

We suspect that at small electric fields ($< 10^2$ V/m), the acoustic phonon scattering may allow the distribution to reach steady state before the optical phonon limit. However, for larger electric fields, the rate of energy increase due to the applied field exceeds the rate of energy dissipation in acoustic phonons, thus requiring the optical phonon modes to achieve steady-state. We note that this hot-electron phenomenon is particularly prominent in graphene, due to its relatively high-energy optical phonons and weak electron-acoustic phonon scattering. As presented in 2.4.3, acoustic phonon scattering in graphene is most often approximated as elastic (the “quasi-elastic” approximation) because the phonon energy $\hbar\omega_q$ only corresponds to a very small change in electron energy ($\lesssim 5\%$), since $v \gg v_s$.

3.3 Scaling Laws in Impurity-Dominated Graphene

Various theoretical models have been proposed to explain the effect of impurities on carrier mobility in SLG. It is commonly accepted that μ is inversely proportional to the impurity density, n_{imp}, and independent of carrier density (eq. (2.35)) [57, 58]. Scattering by charge-neutral point defects can also affect μ, which is typically inversely proportional to the carrier density (eq. (2.52)), making it the dominant scattering mechanism at large carrier densities. The 2D nature of SLG means that it is sensitive to the surrounding environment, in particular the presence and position of the charged

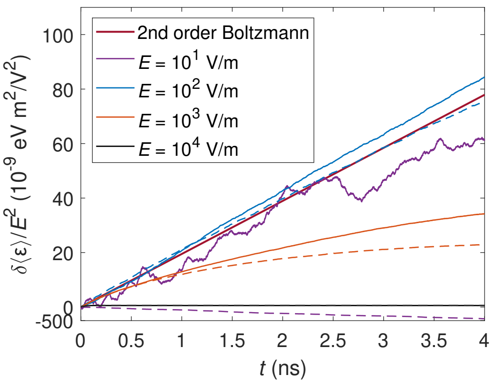

Figure 3.9: MC results for the change of average energy, $\delta\langle\varepsilon\rangle$, with time, t, calculated for a range of applied electric field strengths, E, with and without inelastic acoustic phonon scattering (dashed and solid lines, respectively). The 2nd order BTE result, eq. (3.21), is shown by the solid red line. The impurity density used is, $n_{imp} = 0.025 \times 10^{16}$ m^{-2}, at a distance $d_{imp} = 1$ nm and with a chemical potential, $\varepsilon_F = \langle\delta\varepsilon_{imp}\rangle = 0.015$ eV.

impurities. However, there is still limited understanding of the effect that the standoff distance, d, of the impurities from the graphene plane has on the carrier mobility, and other transport parameters. Additional complications arise in graphene-based heterostructures where SLG is sandwiched between two other materials with the same or different dimensionality (3D bulk, 2D layers and/or 0D quantum dots [80–83]).

We will begin by deriving a simple phenomenological analytical equation. Following this we will use the DG method to perform numerical k-space simulations of carrier transport over a range of experimentally relevant gate-induced doping levels, which we compare to results using the simplified linearised Boltzmann formalism. We find that the shape of the conductivity curve over a wide range of carrier densities demonstrates that the mobility increases inversely as the conductance peak narrows. The calculations are supported by analysing experimental results obtained on both pristine (fig. 3.10a) and surface-decorated (fig. 3.10b) graphene devices, we find this inverse scaling to be universal throughout the devices presented.

3.3.1 Theoretical Model

We consider graphene sheets with charged impurities at a distance, d_{imp}, from the graphene plane and optical phonons with energy, $\hbar\omega$ (fig. 3.10a). We model the effect of these two scattering mechanisms on the following electrical properties of graphene: the full-width-half-maximum (FWHM) carrier concentration (δn) of resistivity, mobility (μ), conductivity (σ) and resistivity (ρ) at the Dirac point (ρ_{max}) (fig. 3.11). The minimum conductivity, σ_{min}, in impurity-dominated graphene is generally restricted by residual charge and temperature (section 2.3.1). Here, we will assume that $T = 0$, before discussing the effect of non-zero temperatures in section 3.9. In the samples with high residual charge, localised ‘puddles’ of electrons and holes are formed. The

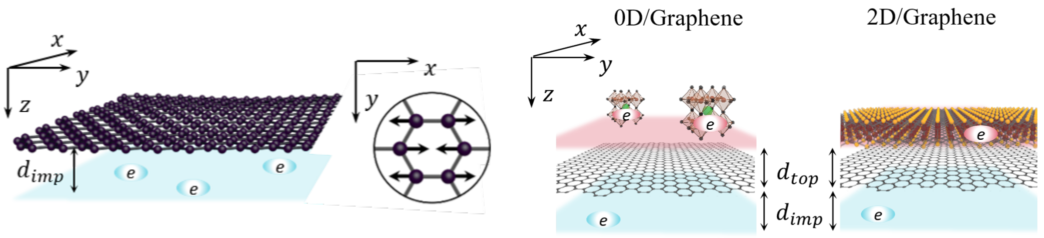

(a) (b)

Figure 3.10: (a) Schematic diagram showing the impurity position, d_{imp}, with respect to the graphene sheet and a pictorial representation of spatio-temporal (angular frequency ω) phonon oscillations over one unit cell. (b) Schematic diagram showing the position of impurities (d_{imp}) and surface-charges (d_{top}), due to 0D structures (e.g. perovskites) and 2D structures (e.g. InSe), with respect to the graphene sheet.

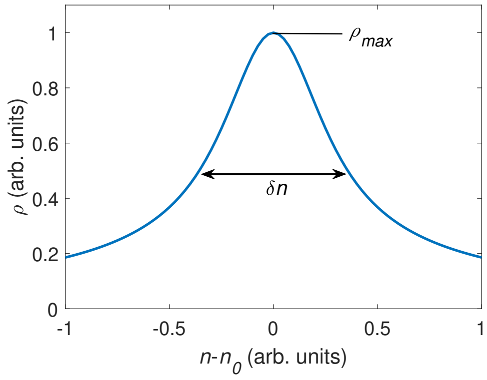

Figure 3.11: Exemplar, idealised curve of resistivity, ρ, against carrier density, n, showing the full-width-half-maximum (FWHM), δn. The maximum resistivity, ρ_{max} corresponds to $n = n_0$.

electrons and holes play equal roles in determining the graphene conductivity with no scattering at the borders between the n- and p-type graphene areas due to the Klein paradox [84]. Only in highly clean, usually suspended, graphene at low temperatures, can the Dirac point, $n = 0$, be probed. Even in this ballistic regime, there remains a finite conductance [9, 85–87].

An analytical expression is derived simply by assuming that away from the Dirac point, where the mobility is measured, conductivity increases linearly with carrier density. In this case, the resistivity at half maximum is $\rho_{1/2}^{-1} = 1/(n_{1/2}e\mu_{1/2}) = 2\rho_{max}^{-1}$ where $\rho_{max} = 1/\sigma_{min}$ and $n_{1/2}$ and $\mu_{1/2}$ are the carrier density and mobility at the half maximum, respectively. Assuming that the mobility is constant, independent of carrier density, then the mobility at the half maximum gives the mobility at all n, $\mu_{1/2} = \mu$. Considering both types of carriers (electrons and holes), the full-width-half-maximum (FWHM), δn, is $2n_{1/2}$, thus,

$$\mu \approx \mu_{1/2} = \frac{4}{e\rho_{max}}\frac{1}{\delta n}. \tag{3.25}$$

To explain the observed $\mu(\delta n)$ and $\mu(V_g)$ curves in more detail, we use the Boltzmann transport method for diffusive scattering. Specifically we use the DG method (section 2.5.2) for the impurity scattering. We perform the DG calculations using an initial Fermi-distribution of low finite temperature, $T = 20$ K, to avoid discontinuities over the discretised k-space. Therefore, one might not expect phonons to have a significant effect on the transport properties compared to that of scattering by impurities [88]. However, for low carrier densities, carriers can be accelerated to high energies (~ 100 meV) resulting in a 'hot electron' distribution due to the Joule heating phenomena described in section 3.2. In this case, inelastic optical phonon scattering becomes important in relaxing the energy of the carriers. In our calculations we set the phonon occupation to $N = 0$, such that only spontaneous emission occurs since we are considering only the low temperature regime ($T \approx 0$).

For all numerical simulations, we apply an electric field, $E = 10^4$ V/m (0.1 V drop across a 10 µm-long SLG), corresponding to a regime of low-field mobility, where μ is independent of the applied electric field strength (see fig. 3.6). For comparison, we also calculate the mobility using the LB formalism, eq. (1.53), with the momentum relaxation time for impurity scattering, calculated by evaluating eq. (2.32) numerically.

We assume that the residual charge density of electron-hole puddles at the Dirac point defines the limit of the minimum conductivity throughout. Here, we assume that the transition from the residual charge dominated minimum carrier concentration to the linearly V_g -dependent concentration occurs when the gate-induced charged density, $n(V_g - V_0)$, is equal to the residual charge density, $n_{NP} = n_{res}$, where V_0 is the position of the Dirac point and n_{res} is given by eq. (2.26). Since we are assuming randomly distributed, unipolar impurities, we can make the assumption that $n_{imp} = n_0$ due to the requirement of charge neutrality, where $n_0 = n(V_0)$ is the doping carrier density.

Figure 3.12a shows the calculated dependence of μ on n for $n > n_{NP}$. With increasing n, we observe an initial increase of μ. This is followed by a peak and a monotonic decrease of μ at large n. This dependence arises from the competition between scattering by long-range Coulombic impurities and short-range defects. Short-range defect scattering is found to be dominant at large n, as expected from comparison of the momentum relaxation time for short-range defects, $\tau_{sr} \sim n^{-1/2}$, calculated using the Born approximation, and long-range impurities, $\tau_{imp} \sim n^{1/2}$. Beyond the Born approximation, for sufficiently strong defect scattering, the exponent of n in the momentum relaxation time, τ_{sr}, can increase towards that of long-range impurity scattering, as shown in section 2.4.2. The dependence of mobility on carrier concentration, $\mu(n)$, is affected by the density of impurities, n_0, and by their distance from the graphene plane, d_{imp}. Hence, both δn and the mobility depend on n_0 and d_{imp}. As shown in fig. 3.12b, the mobility increases as d_{imp} is increased. Furthermore, for low impurity densities, and thus small residual charge densities, the mobility given by the DG simulations differs from that obtained from the LB calculations due to Joule heating effects, whereas the two methods give μ values that converge at higher impurity densities.

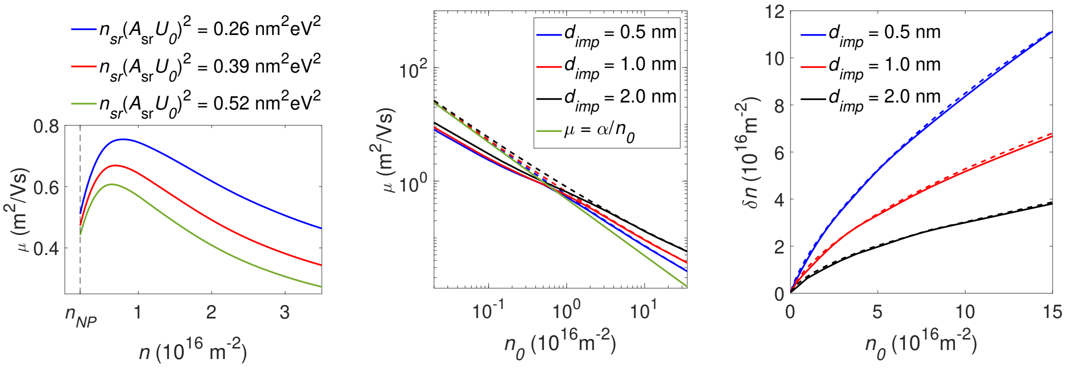

(a) (b) (c)

Figure 3.12: (a) Mobility, μ, calculated using the Discontinuous Galerkin (DG) method as a function of gate-induced carrier density, n, beyond the minimum carrier density, n_{NP} (vertical dashed line), for varying short-range scattering strengths. The impurity density is $n_0 = 0.6 \times 10^{16}$ m^{-2}. (b) Mobility, μ, calculated as a function of impurity density, n_0, for several stand-off distances, d_{imp}. Dashed curves are calculated using the linearised Boltzmann (LB) approximation, using eq. (1.53). The solid green curve, where $\alpha = 20e/h$, shows eq. (2.35) (corresponding to the LB result in the limit $d_{imp} = 0$) as given in [57]. (c) Dependence of FWHM, δn, on impurity density, n_0, for different stand-off distances: $d_{imp} = 0.5$ nm (blue curves), 1.0 nm (red curves), 2.0 nm (black curves).

Our calculations demonstrate that the linewidth, δn, of the $\rho(V_g)$ curve broadens with decreasing d_{imp} and increasing impurity density, n_0 (fig. 3.12c). Suggesting a key link between the FWHM, δn, and the strength of the impurity potential.

3.3.2 Comparison to Experimental Devices

In this study, we analysed the data recorded in previous work on graphene devices fabricated using single-layer graphene placed on 300 nm thick SiO$_2$/Si or on a few monolayer thick hBN/SiO$_2$/Si substrates with a bottom gate electrode. We used two device geometries: a 2-terminal diode and a Hall bar. Results obtained for the following devices are analysed in this work: pristine exfoliated single-layer graphene [89]; pristine CVD-grown single-layer graphene (Graphenea and Graphene Supermarket) [90]; graphene covered by a thin (from 5 nm to 50 nm) layer of exfoliated InSe [90]; graphene covered by a layer of inorganic perovskite CsPbI$_3$ nanocrystals [91]; graphene covered by a layer of colloidal PbS quantum dots [92].

We apply our analysis to the above experimental results reported previously for over 20 devices fabricated using exfoliated and CVD-grown graphene, and for heterostructures incorporating 2D (InSe, hBN) or 0D (colloidal QDs, inorganic perovskites) layers.

There exists large experimental uncertainty in the value of the impurity density, n_0, due to the uncertainty in it's origin: we will see later, in section 3.4, that many impurity configurations can lead to the same n_0. However, in examining the mobility, we can eliminate n_0 by combining the results of figs. 3.12b and 3.12c and using the carrier density fluctuations, δn, as a more direct probe of the nature, and specifically the scattering strength, of underlying potentials. The carrier mobility decreases with increasing δn (fig. 3.13a), with the broadening of δn being larger for smaller d_{imp} at a given value of mobility. Measurements from graphene devices are in good agreement with the results of our DG simulations with $d_{imp} = 2$ nm. We note that our fit (fig. 3.13a) uses δn calculated from $\rho_{1/2}$ (resistivity/conductivity at half maximum), rather than n_0 extracted from the gate voltage at which $\sigma(V_g) = \sigma_{min}$. By using eq. (3.25) and assuming a universal minimum conductivity for pristine graphene, $\sigma_{min} \approx 4e^2/h$ [93], we obtain a simple inverse power law for mobility, which provides excellent agreement with experimental data from a range of devices (see section 3.3.3),

$$\mu \approx \frac{16e}{h} \frac{1}{\delta n}. \tag{3.26}$$

Recently, the decoration of graphene devices with other low-dimensional materials, such as 0D (colloidal PbS quantum dots [94] or CsPbI$_3$ perovskite [95]) and 2D (InSe flakes) [96] materials has been used to functionalise these devices, e.g. for photon sensing [95–97]. The properties of the graphene heterostructures are greatly affected by both the unintentional presence of charged impurities in the vicinity of graphene (as described above by d_{imp}) and those deliberately introduced by the top layer (d_{top}) in graphene heterostructures (fig. 3.10b), which we model as a distribution of impurities at an effective distance, d_{eff}. We note that in surface-decorated graphene devices, the distance between the graphene plane and the top layer can be controlled, for example by introducing a dielectric layer such as hBN, thus providing a tool for tailoring the electrical properties.

The relationship between mobility and the gate-voltage offset is $\mu \propto 1/n_0$ for most pristine devices (eq. (2.35)). However, for devices with high densities of correlated unipolar charges [98, 99] or uncorrelated bipolar charges, [92] spatial correlation between charges must be considered, as will be shown in section 3.4. This is particularly important when the dopants are mobile and able to adopt low energy, correlated configurations. Such effects were recently demonstrated for quantum dot-decorated graphene and validated using Monte Carlo simulations [92, 99]. Despite the different $\mu(n_0)$ characteristics of decorated and pristine graphene, remarkably we find that both types of device exhibit the "universal" scaling behaviour shown in fig. 3.13b.

Different surface-decorated devices follow a common trend observed in pristine graphene. In particular, the experimental results for the InSe, perovskite and PbS decorated SLG are best fitted by DG calculations when $d_{eff} = 1$ nm. Therefore, we find that the relationship between μ and δn is consistent throughout all of the devices, as can be expected from the analytical expression given in eq. (3.26), with modifications to only the effective distance of the impurities. Flexibility to modify composition and/or geometry of a heterostructure offers opportunities to tune the distribution and stand-off distance of ionised impurities, hence changing d_{eff} and providing a tool to

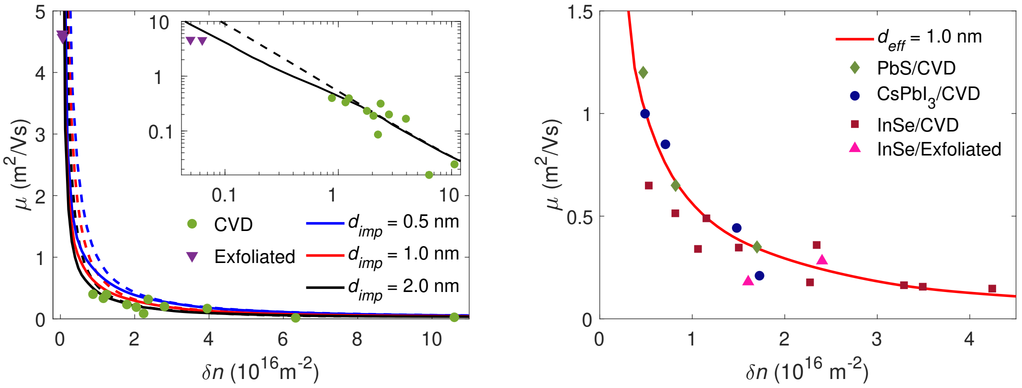

(a) (b)

Figure 3.13: (a) Calculated mobility, μ, versus FWHM, δn, curves (dashed and solid curves) compared to data from pristine graphene samples grown by CVD (filled circles) or exfoliated (filled triangles). The dashed lines are obtained from eq. (1.53), the solid lines are obtained using the DG simulations. (b) Relationship between mobility, μ, and the FWHM, δn, obtained using the DG simulations, taking $d_{eff} = 1.0$ nm. In surface decorated devices the effective impurity distance, d_{eff}, describes the combined effect of charges below (d_{imp}) and above (d_{top}) the graphene layer. Compared to data from multiple modified graphene samples (data points for each sample type are labelled as shown in the inset legend).

control transport properties of these devices. We note, that our model is valid for all devices where the position of ionised impurities is not affected by V_g. In rare cases, at high V_g, the ionisation of donor impurities can be affected by the applied gate voltage [90, 100] and the corresponding change in the impurity distribution, n_{imp} and d_{imp}, would need to be accounted for.

3.3.3 Key Transport Parameter Relations

The model developed allows us to link together three key transport parameters of SLG devices: μ, n_0 and δn, from which it is possible to predict the $\sigma(V_g)$ behaviour. We now look to extract some simple, phenomenological-based analytical expressions to relate these transport parameters into an easy-to-use set.

Figure 3.14a shows that the minimum conductivity for all pristine graphene samples is around the quantum limit, $\sigma_{min} \sim 4e^2/h$, with no correlation to the doping density, n_0. As a result, the simple analytical expression (3.26) provides a good fit (fig. 3.14b). For the surface modified devices measured in this study, the average maximum conductivity is found to be slightly larger than in the pristine SLG devices (fig. 3.14c). This is likely due to the increased amount of residual charge, as modelled by the the smaller effective distance. If we approximate $\sigma_{min} \approx 5e^2/h$, we find that $\mu \approx 20e/h\delta n$ for modified graphene (see fig. 3.14d). This result suggests that the characteristic carrier density fluctuation determined from the FWHM, δn, of the $R(V_g)$ dependence can be used to estimate the mobility of a wide range of graphene devices in a way that

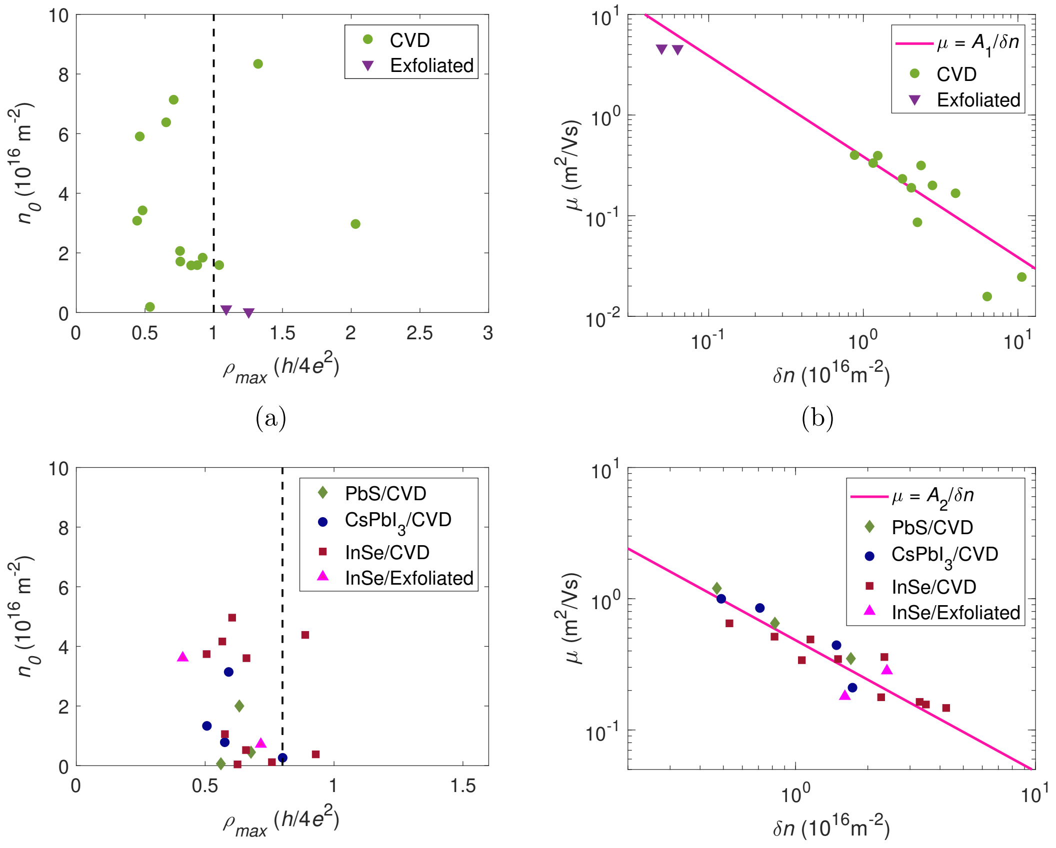

(a) (b)

(c) (d)

Figure 3.14: Values of the maximum resistivity, ρ_{max}, measured for (a) pristine graphene and (c) surface modified graphene with different levels of doping, n_0. Variation of the mobility, μ, with the carrier density fluctuation, δn, measured for (b) pristine graphene and (d) surface modified graphene. Magenta curve shows the analysis using the inverse power law, eq. (3.25), where $A_1 = 16e/h$ and $A_2 = 20e/h$.

is strikingly similar to the phenomenological relation defined for impurity density, i.e. $\mu = \alpha/n_0$ (eq. (2.35)).

From fig. 3.15a, we see that eq. (2.35), with $n_{imp} = n_0$, is reasonable for $\mu(n_0)$,

$$\mu \approx \frac{20e}{h}\frac{1}{n_0}. \tag{3.27}$$

Equating eqs. (3.26) and (3.27), we find that $\delta n \approx \frac{4}{5}n_0$, which is a reasonable approximation over the range of data considered here, as shown in fig. 3.15b.

We note that the results of $\mu(n_0)$ and $\delta n(n_0)$ (fig. 3.15) are more scattered, with larger variance, than the results of $\mu(\delta n)$ (fig. 3.14). As described in section 3.3.2, this is likely due to the fact that there are many different configurations of charged impurities that can lead to the same value of the doping density, n_0. The assumption that $n_0 = n_{imp}$ only corresponds to the simplest case of uniform randomly distributed unipolar impurities. However, by eliminating n_0, we find the "universal" behaviour of

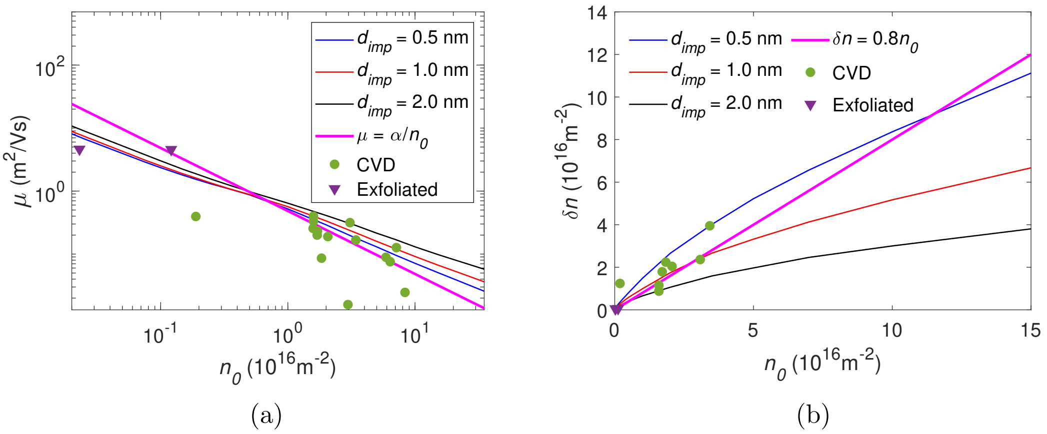

Figure 3.15: (a) Mobility, μ, calculated as a function of dopant density, n_0, for several stand-off distances, d_{imp}. The solid magenta curve is given by eq. (3.27) (i.e. $\alpha = 20e^2/h$). The results are compared to data from pristine graphene samples. (b) Dependence of δn, on impurity density n_0 for several stand-off distances compared to the phenomenological relation, $\delta n = \frac{4}{5}n_0$. The results are compared to data from pristine graphene samples.

$\mu(\delta n)$ as presented in fig. 3.13.

To summarise, the key analytical relations for transport measurements of graphene on SiO_2, or substrates with a similar dielectric constant, useful for fast experimental analysis are:

- $\mu \approx \frac{20e}{h}\frac{1}{n_0}$
- $\mu \approx \frac{16e}{h}\frac{1}{\delta n}$
- $\rho_{max} \approx h/4e^2$
- $\delta n \approx \frac{4}{5}n_0$

Overall, our model of $\mu(\delta n)$, which considers the effect of impurity scattering to be dominant on mobility, describes well all examined types of graphene: high mobility exfoliated graphene and low-mobility CVD-grown graphene.

3.4 Correlated Impurities

Here we consider the effect of spatial correlations between charged impurities on the total impurity induced potential and the impact that this has on the mobility and self-consistently calculated residual charge density. For the calculations of mobility, we use the linearised Boltzmann approximation. We consider two new scenarios: (A) spatially correlated unipolar impurities, (B) spatially correlated bipolar impurities; further expanding the random distributions derived in section 2.3 and used in section 3.3.

For N_j correlated scatterers at positions $\mathbf{R}_j$, we retain the full summation over individual scattering centre positions. In this case, the transition rate, eq. (1.38), becomes

$$S_{\mathbf{k}\to\mathbf{k}'} = \frac{\pi}{A^2\hbar}\left|\sum_{j=1}^{N_j} e^{-i\mathbf{q}\cdot\mathbf{R}_j}\right|^2 |\tilde{u}(q)|^2 (1+\cos\theta_{\mathbf{k},\mathbf{k}'})\delta_{k'k} \tag{3.28}$$

in the case of elastic scattering, where $\delta_{k'k} = \delta(\varepsilon(k') - \varepsilon(k))$. Using eq. (2.20), the Fourier transform of the single charged impurity potential, we find

$$S_{\mathbf{k}\to\mathbf{k}'} = \frac{\pi}{A^2\hbar}\left|\frac{2\pi e^2}{\kappa q \epsilon_{sc}(q)}\right|^2 \left|\sum_{j=1}^{N_{(-)}} e^{-i\mathbf{q}\cdot\mathbf{R}_j} - \sum_{k=1}^{N_{(+)}} e^{-i\mathbf{q}\cdot\mathbf{R}_k}\right|^2 e^{-2qd}(1+\cos\theta_{\mathbf{k},\mathbf{k}'})\delta_{k'k} \tag{3.29}$$

where $N_{(-)}$ and $N_{(+)}$ are the number of negatively and positively charged impurities, respectively. Using eq. (1.49), the momentum relaxation time is

$$\frac{1}{\tau(k_F)} = \pi v r_s^2 k_F \int d\theta \frac{\sin^2\theta}{(2k_F\sin(\theta/2)+q_s)^2}\frac{S_f(2k_F\sin(\theta/2))}{A}e^{-4k_F\sin(\theta/2)d}, \tag{3.30}$$

where we identify the structure factor

$$S_f(q) = \left|\sum_{j=1}^{N_{(-)}} e^{-i\mathbf{q}\cdot\mathbf{R}_j} - \sum_{k=1}^{N_{(+)}} e^{-i\mathbf{q}\cdot\mathbf{R}_k}\right|^2 \tag{3.31}$$

which depends on the spatial distribution of impurities.

Conserving the full spatially dependant potential in the calculation of the residual charge fluctuations, eq. (2.21), gives

$$\langle\delta\varepsilon_{imp}\rangle^2 = \int \frac{d^2q}{(2\pi)^2}\left|\frac{2\pi e^2 e^{-qd}}{\kappa q \epsilon_{sc}(q)}\right|^2 S_f(q) = 2\pi\left(\frac{e^2}{\kappa}\right)^2 \int_0^\infty q dq \frac{e^{-2qd}}{(q\epsilon_{sc}(q))^2} S_f(q), \tag{3.32}$$

from which we find the residual charge, $n_{NP} = \langle\delta\varepsilon_{imp}\rangle^2/(\pi\hbar^2v^2)$ at the point of minimum conductivity.

In the limit of randomly distributed impurities, $S_f \approx N_- + N_+ = N_{imp}$, and we retrieve the results derived in section 2.3.

3.4.1 Unipolar

Correlations of the $N_{(\pm)}$ unipolar impurities can be expected due to positioning the charges in a lattice network, or due to doping with mobile unipolar charges which can move into low energy, highly correlated configurations. We characterise this correlation by a minimum allowed distance between any two impurities, r_0. For a given r_0 there exists a maximum density of impurities, $n_{max} = 1/(\pi r_0^2)$, constrained by the minimum separation, r_0, between the impurities.

The structure factor, eq. (3.31), for unipolar impurities is

$$S_f(\mathbf{q}) = \sum_{j=1}^{N_{(\pm)}} \sum_{k=1}^{N_{(\pm)}} e^{-i\mathbf{q}\cdot(\mathbf{R}_j - \mathbf{R}_k)} = N_{(\pm)} + \sum_{j=1}^{N_{(\pm)}} \sum_{k\neq j} e^{-i\mathbf{q}\cdot(\mathbf{R}_j - \mathbf{R}_k)}. \tag{3.33}$$

We approximate the structure factor by averaging over the possible distribution of positions, $\mathbf{R}_{j,k}$,

$$S_f(q) \approx N_{(\pm)} + N_{(\pm)}(N_{(\pm)} - 1)\langle e^{iqr\cos\theta}\rangle \tag{3.34}$$

where $\langle ... \rangle$ represents the ensemble average, $r_0 < r < L$ is the distance and between the vectors $\mathbf{R}_j$ and $\mathbf{R}_k$ of any two impurities, L is the maximum distance between any two impurities (i.e. roughly the device size) and θ is the angle between $\mathbf{q}$ and $\mathbf{R}_j - \mathbf{R}_k$.

The ensemble average of the exponential phase difference between impurities is found by assuming a uniform probability distribution of impurity-impurity distances between r_0 and L,

$$\left\langle e^{iqr\cos\theta} \right\rangle \approx \frac{\int_0^{2\pi} \mathrm{d}\theta \int_{r_0}^{L} r\mathrm{d}r e^{iqr\cos\theta}}{A - \pi r_0^2} = \frac{2\pi \left(LJ_1(qL) - r_0 J_1(qr_0)\right)}{A - \pi r_0^2} \tag{3.35}$$

where $A = \pi L^2$ is the device area and $J_1(x)$ is the Bessel function of the first kind. In the limit of a large sample size, $L \to \infty$,

$$\left\langle e^{iqr\cos\theta} \right\rangle \approx -\frac{2\pi}{qA} r_0 J_1(qr_0), \tag{3.36}$$

such that the structure factor is given by

$$S_f(q) \approx N_{(\pm)} \left(1 - 2\pi n_{(\pm)} r_0^2 \frac{J_1(qr_0)}{qr_0}\right), \tag{3.37}$$

assuming that $N_{(\pm)} \gg 1$. There are two important limits:

$$\frac{J_1(qr_0)}{qr_0} \to \begin{cases} 1/2 & \text{when } \ qr_0 \to 0 \\ 0 & \text{when } \ qr_0 \to \infty \end{cases}. \tag{3.38}$$

When $r_0 = 0$, we retrieve $S_f(q) = N_{(\pm)}$ as for the random case.

We note that the same result as eq. (3.37) can be achieved by the structure factor formulation given in Refs. [98, 101] using the pair distribution function,

$$g(\mathbf{r}) = \begin{cases} 0 & \text{for } \ r \leq r_0 \\ 1 & \text{for } \ r > r_0 \end{cases}, \tag{3.39}$$

which describes the relative density of impurities at position $\mathbf{r}$ from any given impurity.

Subbing eq. (3.37) into eq. (3.30), results in

$$\begin{aligned}\frac{1}{\tau(k_F)} = n_{(\pm)}\pi v r_s^2 k_F \int \mathrm{d}\theta \Bigg[& \frac{\sin^2\theta}{\left(2k_F\sin^2(\theta/2)+q_s\right)^2} e^{-4k_F d\sin(\theta/2)} \\ & \times \left(1 - 2\pi n_{(\pm)} r_0^2 \frac{J_1\left(2k_F\sin(\theta/2)r_0\right)}{2k_F\sin(\theta/2)r_0}\right)\Bigg]\end{aligned} \tag{3.40}$$

for the momentum relaxation rate. Whilst subbing eq. (3.37) into eq. (3.32), we find

$$\begin{aligned}\delta k_{imp}^2 = 2\pi\left(\frac{e^2}{\hbar v\kappa}\right)^2 n_{(\pm)}\Bigg[& C_0(r_s, 4\delta k_{imp}d) - 2\pi n_{(\pm)} r_0 \Bigg(\int_0^{2\delta k_{imp}} \mathrm{d}q \frac{e^{-2qd}}{(q+q_s)^2} J_1(qr_0) \\ & + \frac{4}{(2+\pi r_s)^2}\int_{2\delta k_{imp}}^{\infty} \mathrm{d}q \frac{e^{-2qd}}{q^2} J_1(qr_0)\Bigg)\Bigg],\end{aligned} \tag{3.41}$$

where we have defined $\delta k_{imp} = \langle\delta\varepsilon_{imp}\rangle/\hbar v$, the mean fluctuation in the quasi-Fermi wavevector due to the impurity potential. Equation (3.41) can be solved self-consistently using an iterative process with input wavevector calculated from the random case, eq. (2.24).

We will now investigate the effect of changing the correlation length. Here, we consider the case of $d = 1$ nm for varying impurity densities, $0.02 \times 10^{16}\mathrm{m}^{-2} \leq n_{(\pm)} \leq 20 \times 10^{16}\mathrm{m}^{-2}$.

Figures 3.16a and 3.16b show the calculated variation of charge density, n_{NP}, and mobility, $\mu(n_{NP})$, at the Dirac point. From this we calculate the maximum resistivity, $\rho_{max} = (1/n_{NP}e\mu(n_{NP}))$ (fig. 3.16c). We see that, as correlation is increased, the effect of the electrostatic field is reduced. As a result, the residual charge decreases (fig. 3.16a) and mobility increases (fig. 3.16b). The increase in mobility is stronger than the decrease in residual charge such that the resistivity at the Dirac point, $\rho_{max} = 1/(n_{NP}e\mu(n_{NP}))$, decreases with increasing correlation (fig. 3.16c). For low impurity densities, $n_{(\pm)}$, and small correlation lengths, r_0, the results are the same as the random case; for small densities, the correlated configurations will be indistinguishable from random configurations.

Figures 3.17a and 3.17b show the variation of mobility and resulting resistivity with carrier density, between the minimum carrier concentration, n_{NP}, and the density corresponding to the FWHM, $n_{1/2}$, for an impurity density of $n_{(\pm)} = 2 \times 10^{16}$ m^{-2}. We see that, when correlations are strong, the mobility begins to decrease with increasing carrier concentration due to an increase in scattering at high energy as a direct result of the structure factor.

Figure 3.18a shows the variation of FWHM, δn, with doping level, $n_0 = n_{(\pm)}$. There exists a maximum value of δn for a given correlation length, as can be understood by the results of fig. 3.16, where we see that the effects of the field are reversed as $n_0 = n_{(\pm)}$ increases. Figure 3.18b shows the relationship between mobility, μ, (calculated at the

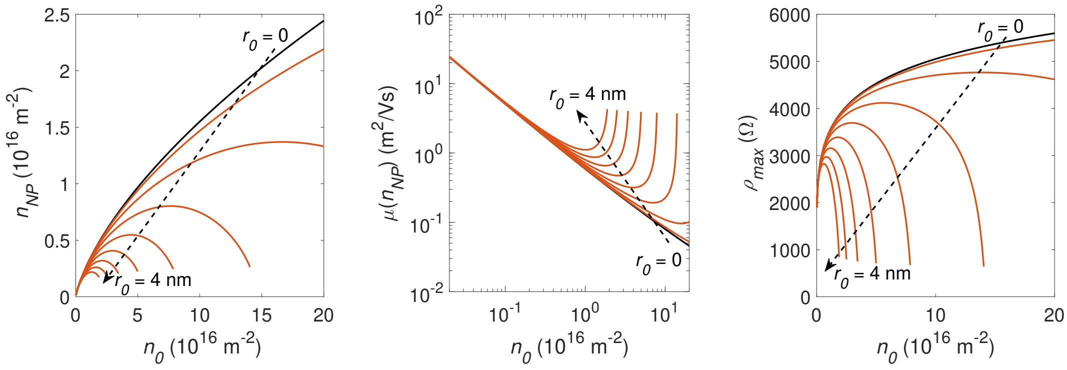

(a) (b) (c)

Figure 3.16: Calculated variations of (a) residual charge, n_{NP}, (b) mobility at n_{NP}, $\mu(n_{NP})$, (c) maximum resistivity, ρ_{max}, for varying $n_0 = n_{(\pm)}$. Results show a number of correlation lengths, r_0, in 0.5 nm increments. We have set a stand-off distance of $d = 1$ nm.

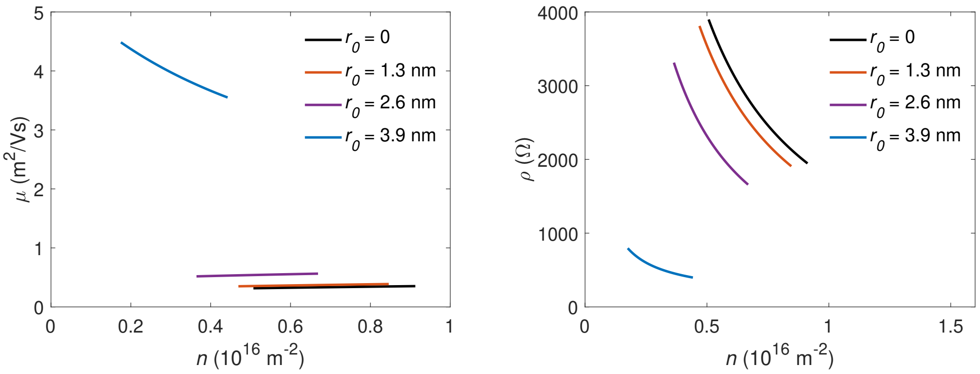

(a) (b)

Figure 3.17: (a) mobility and (b) resistivity as a function of carrier concentration, n, for a number of correlation lengths, r_0, from the neutrality carrier density, $n = n_{NP}$, to the carrier density at the resistivity half-maximum, $n = n_{1/2}$. The impurity density is $n_{(\pm)} = 2 \times 10^{16}$ m^{-2}. We have set a stand-off distance of $d = 1$ nm.

half maximum, $n_{1/2}$), and the FWHM, δn. As the correlations begin to flatten the field, the mobility varies from the $\mu(\delta n)$ curve for the random case (black line). From eq. (3.25), we can see that this is due to the large decrease in ρ_{max} for large $n_0 = n_{(\pm)}$, as shown in fig. 3.16c.

3.4.2 Bipolar

Here we consider a fixed random distribution of $N_{(-)}$ negatively charged impurities, and explore the effects of adding $N_{(+)}$ positively charged impurities. As in reference [92], we assume that each positive impurity added will become correlated to a negative impurity to reduce the overall electrostatic potential energy of the sample. We define r_{max} as the maximum radius between a given negative impurity and a corresponding

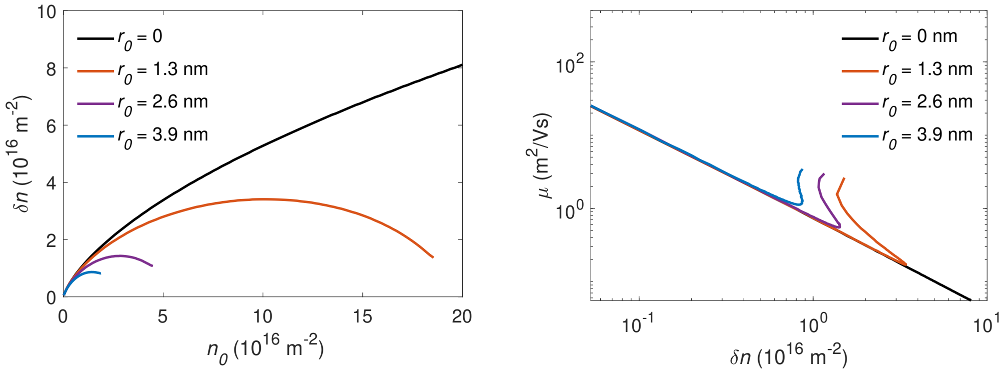

(a) (b)

Figure 3.18: (a) FWHM, δn as a function of $n_0 = n_{(\pm)}$ and (b) mobility, μ, as a function of FWHM, δn, calculated for a number of correlation lengths, r_0. We have set a stand-off distance of $d = 1$ nm.

correlated positive impurity. The structure factor is

$$\begin{aligned} S_f(\mathbf{q}) = &\sum_{j=1}^{N_{(-)}}\sum_{k=1}^{N_{(-)}} e^{i\mathbf{q}\cdot(\mathbf{R}_{-,j}-\mathbf{R}_{-,k})} + \sum_{j=1}^{N_{(+)}}\sum_{k=1}^{N_{(+)}} e^{i\mathbf{q}\cdot(\mathbf{R}_{+,j}-\mathbf{R}_{+,k})} \\ &- \sum_{j=1}^{N_{(-)}}\sum_{k=1}^{N_{(+)}} e^{i\mathbf{q}\cdot(\mathbf{R}_{-,j}-\mathbf{R}_{+,k})} - \sum_{j=1}^{N_{(+)}}\sum_{k=1}^{N_{(-)}} e^{i\mathbf{q}\cdot(\mathbf{R}_{+,j}-\mathbf{R}_{-,k})}, \end{aligned} \tag{3.42}$$

where $\mathbf{R}_{-,j}$ represents the position of the j^{th} negative impurity. As for the random case, the first two double summations of eq. (3.42) give $N_{(-)} + N_{(+)}$, since the negative distribution, and thus the positive distribution, are random so only the $j = k$ terms contribute and all other terms average to zero. However, we now also need to consider the $j = k$ terms in the third and fourth double summation in eq. (3.42), since the j^{th} positive impurity is correlated to the j^{th} negative impurity. Thus we find that

$$S_f(q) = N_{(-)} + N_{(+)} - \sum_{k=1}^{N_{(+)}} e^{i\mathbf{q}\cdot(\mathbf{R}_{-,k}-\mathbf{R}_{+,k})} - \sum_{j=1}^{N_{(+)}} e^{i\mathbf{q}\cdot(\mathbf{R}_{+,j}-\mathbf{R}_{-,j})}. \tag{3.43}$$

Using the same approach as in section 3.4.1, we approximate

$$\sum_{k=1}^{N_{(+)}} e^{i\mathbf{q}\cdot(\mathbf{R}_{-,k}-\mathbf{R}_{+,k})} = \sum_{j=1}^{N_{(+)}} e^{i\mathbf{q}\cdot(\mathbf{R}_{+,j}-\mathbf{R}_{-,j})} \approx N_{(+)} \left\langle e^{iqr\cos\theta} \right\rangle \tag{3.44}$$

where $0 < r < r_{max}$ is the distance between the vectors $\mathbf{R}_{+,j}$ and $\mathbf{R}_{-,j}$ of the correlated impurities, and θ is the angle between $\mathbf{q}$ and $\mathbf{R}_{+,j} - \mathbf{R}_{-,j}$. The ensemble average of the contribution from correlated impurities is found by evaluating the Hankel transform,

$$\left\langle e^{iqr\cos\theta} \right\rangle \approx \frac{2\pi \int_0^{r_{max}} r\mathrm{d}r J_0(qr)}{\pi r_{max}^2} = 2\frac{J_1(qr_{max})}{qr_{max}}. \tag{3.45}$$

Therefore, the total structure factor is

$$S_f(q) \approx N_{(-)} + N_{(+)} - 4N_{(+)}\frac{J_1(qr_{max})}{qr_{max}}. \tag{3.46}$$

Making use of the limits shown earlier (eq. (3.38)), we can see that when $r_{max} \to 0$, $S_f(q) = N_{(-)} - N_{(+)}$, i.e. we return a random distribution of $N_{(-)} - N_{(+)}$ negative impurities, since the positive impurities are perfectly aligned with the negative impurities such to cancel the field of $N_{(+)}$ negative impurities exactly. Whereas, in the limit $r_{max} \to \infty$, $S_f(q) = N_{(-)} + N_{(+)}$, i.e. we return the case of a random distribution of $N_{(-)} + N_{(+)}$ impurities.

Subbing eq. (3.46) into eq. (3.30), results in

$$\begin{aligned}\frac{1}{\tau(k_F)} = \pi v r_s^2 k_F \int \mathrm{d}\theta \Bigg[&\frac{\sin^2\theta}{(2k_F\sin(\theta/2) + q_s)^2} e^{-4k_F d\sin(\theta/2)} \\ &\times \left((n_{(-)} + n_{(+)}) - 4n_{(+)}\frac{J_1\left(2k_F\sin(\theta/2)r_{max}\right)}{2k_F\sin(\theta/2)r_{max}} \right) \Bigg]\end{aligned} \tag{3.47}$$

for the momentum relaxation rate. Whilst subbing eq. (3.46) into eq. (3.32), obtains

$$\begin{aligned}\delta k_{imp}^2 = 2\pi \left(\frac{e^2}{\hbar v \kappa}\right)^2 \Bigg[&(n_{(-)} + n_{(+)})C_0(r_s, 4k_{imp}d) \\ &- 4n_{(+)}\left(\int_0^{2\delta k_{imp}} \mathrm{d}q \frac{qe^{-2qd}}{(q+q_s)^2}\frac{J_1(qr_{max})}{qr_{max}} \right. \\ &\left. + \frac{4}{(2+\pi r_s)^2}\int_{2\delta k_{imp}}^{\infty} \mathrm{d}q \frac{e^{-2qd}}{q}\frac{J_1(qr_{max})}{qr_{max}} \right) \Bigg]\end{aligned} \tag{3.48}$$

for the mean deviation of the quasi-Fermi level from zero at the minimum conductivity. As for eq. (3.41), this can be solved iteratively.

We will now investigate the effect of changing the correlation length. Here, we consider the case of $d = 1$ nm for a fixed density of 'negative' impurities, $n_{(-)}$, and add 'positive' impurities of varying density, $n_{(+)}$.

From fig. 3.19, we see that, at $r_{max} = 0$, the system behaves as if it contains $n_{(-)} - n_{(+)}$ randomly distributed unipolar impurities, due to perfect cancellation of the N_+ charges. As r_{max} increases, we observe transition to a point where the system behaves as if it contains $n_{(-)} + n_{(+)}$ randomly distributed unipolar impurities, except for offset of the Dirac point, which is always defined as $n_0 = n_{(-)} - n_{(+)}$. As a result, we get a reflection of the unipolar random case about $n_0 = n_{(-)}$ as $r_{max} \to \infty$. The expected scale of r_{max}, about which this transition occurs can be calculated as the mean distance between the randomly distributed negative impurities, $\langle r_{(-)} \rangle \approx \sqrt{\pi/n_{(-)}}$.

In fig. 3.20b, we eliminate n_0 by plotting $\mu(\delta n)$. We see behaviour that can be anticipated from the results of fig. 3.19. That is that when $r_{max} = 0$ and when $r_{max} \to \infty$ the behaviour is of randomly distributed unipolar impurities, in terms of $\mu(\delta n)$. In

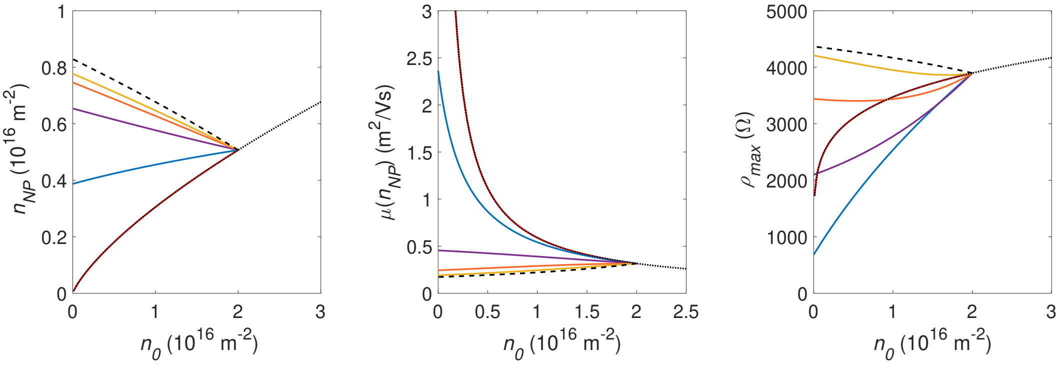

(a) (b) (c)

Figure 3.19: Calculated variations of (a) residual charge, n_{NP}, (b) mobility at n_{NP}, $\mu(n_{NP})$, (c) maximum resistivity, ρ_{max}, for varying $n_0 = n_{(-)} - n_{(+)}$ where we have fixed $n_{(-)} = 2 \times 10^{16}$ m^{-2}. Red- $r_{max} = 0$, blue- $r_{max} = 5$ nm, purple- $r_{max} = 10$ nm, salmon- $r_{max} = 15$ nm, yellow- $r_{max} = 20$ nm. The dotted black line was calculated for a random distribution of unipolar impurities ($S_f = N_{(\pm)} = An_0$). The dashed line was calculated for a random distribution with both polarities of impurity ($S_f = N_{(-)} + N_{(+)}$). We have set a stand-off distance of $d = 1$ nm.

between these two limits, we observe a period of transition.

3.4.3 Summary

For a given doping density, n_0, if impurities are unipolar, spatial correlations can lead to increased mobility. While, if both negatively and positively charged impurities exist, the mobility may be decreased relative to the expectation by the perceived impurity density, n_0.

In both cases, the mobility for a given δn appears to be increased relative to that of a random distribution due to the effect of the smoothing of the electrostatic potential on the carrier dynamics at the charge neutrality point. However, the extent of deviation is limited by the maximum correlation for a given impurity density, as shown in fig. 3.21. Figure 3.21 shows the results of $\mu(\delta n)$ for a number of different impurity configurations (taken from sections 3.3 (random), 3.4.1 (unipolar correlated) and 3.4.2 (bipolar correlated)).

We note that the measurements of QD doped graphene (fig. 3.13b) seems to show no obvious deviations from the observed "universal" trend in $\mu(\delta n)$ even when correlations between impurities/dopants are expected [92, 99].

3.4.4 Classical Real-Space Monte Carlo

In references [92] and [99], a real-space Monte Carlo simulation was used to model the effect of impurity/QD dopant correlations. Their Monte Carlo model used a phenomenologically modified Coulomb potential for a randomly generated, correlated distribution of electrons to simulate the deterministic trajectory of electrons. Here we

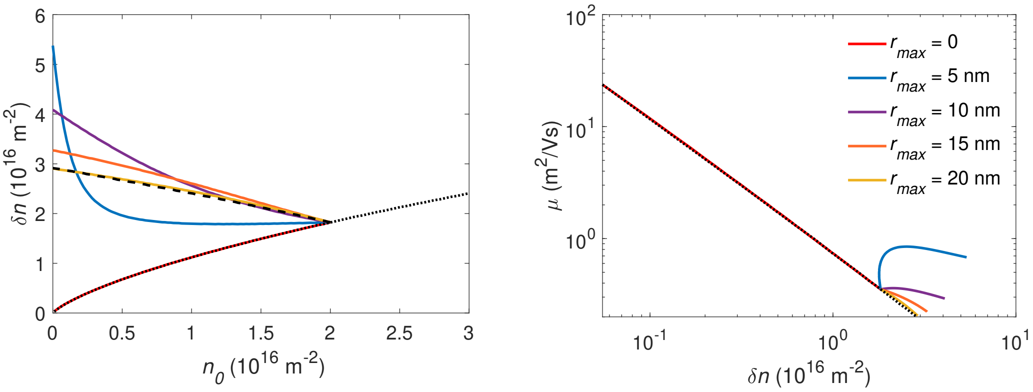

(a) (b)

Figure 3.20: (a) FWHM, δn as a function of $n_0 = n_{(-)} - n_{(+)}$ and (b) mobility, μ, as a function of FWHM, δn. We have fixed $n_{(-)} = 2 \times 10^{16}$ m^{-2}. Red- $r_{max} = 0$, blue- $r_{max} = 5$ nm, purple- $r_{max} = 10$ nm, salmon- $r_{max} = 15$ nm, yellow- $r_{max} = 20$ nm. The black dotted line was calculated for a random distribution, as in (A), for just one type of impurity ($S_f = N_{(\pm)} = An_0$). The black dashed line was calculated for a random distribution, as in (A), with both types of impurity ($S_f = N_{(-)} + N_{(+)}$). We have set a stand-off distance of $d = 1$ nm.

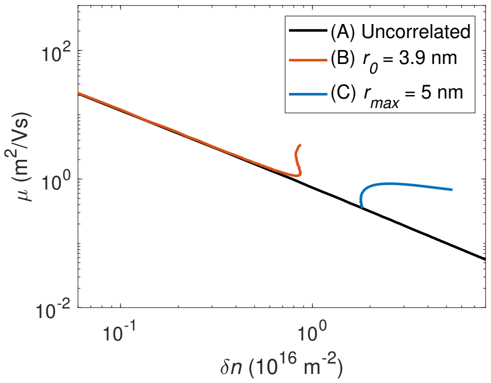

Figure 3.21: Mobility, μ, as a function of FWHM, δn, for $d = 1$ nm. The legend shows the type of distribution of impurities considered ((A) random - sections 2.3 and 3.3.1, (B) unipolar - section 3.4.1, (C) bipolar - section 3.4.2) and the relevant correlation length.

will look at employing the modified potential, as described in [92], to model a classical single-electron trajectory and compare the results to those obtained in sections 3.4.1 and 3.4.2.

The potential of a single charged impurity at distance, r, is given by [92]

$$u(r) = u_C(r)u_q(r)u_{sc}(r), \tag{3.49}$$

where $u_C(r)$ is the classical Coulomb potential, $u_q(r)$ is the quantum correction to the classical potential, and $u_{sc}(r)$ is the screening correction. The quantum correction, $u_q(r) = \mathrm{erf}(r/\lambda_q)$ where $\mathrm{erf}(x)$ is the error function and λ_q is a fitting parameter [92, 102]. The screening correction is approximated to be of the Yukawa form (2.38), $u_{sc}(r) = \exp(-r/\lambda_{sc})$, where the screening length, $\lambda_{sc} = \hbar v/(8\ln(2)r_s k_B T)$ is taken as the high-temperature limit [53].

A grid is generated and the total field, generated by the simulated distribution of charged impurities, is calculated at the centre of each cell on the grid, according to eq. (3.49). The size of the cells is chosen in accordance with the chosen time step, such that an electron is only able to move to one of the surrounding 8 cells in one time step, given the velocity, $v = 10^6$ ms^{-1}. Typically, the cell size is chosen to be 1 nm with a time step of 1 fs. Electrons are input with a wavevector chosen randomly from the Fermi-Dirac distribution with $k_F = \sqrt{\pi n_{(-)}}$. Once an electron completes the length of the channel (chosen to be 2 μm here), it is reinserted with a new randomly selected input wavevector. The details of the algorithm are shown in fig. 3.22.

The maximum time, t_{max}, is chosen such that the mean energy and velocity have converged, within the constraints imposed by statistical noise. The velocity is averaged over the final time steps to find the drift velocity, v_d, from which we calculate the mobility, $\mu = v_d/E$.

For a random unipolar impurity density $n_{(-)} = 2\times10^{16}$ m^{-2} at a distance, $d = 1$ nm, calculated using the linearised Boltzmann formalism (used in sections 3.4.1 and 3.4.2), we find $\mu \approx 0.3$ m^2/Vs. From this, we calibrate the quantum correction to the impurity potential and find $\lambda_q = 11$ nm.

Figure 3.23a shows the fluctuation of the total impurity potential about the mean $(U - \bar{U})$, for increasing minimum distance between unipolar impurities, r_0. As r_0 increases, the fluctuations in the potential are reduced, thus carrier mobility increases, as shown in fig. 3.23b, in agreement with the results from section 3.4.1.

Figure 3.24a shows the total impurity potential, U, from a random and a correlated distribution of bipolar charges. Correlations between the negative and positive impurities result in a decrease in the fluctuations of the field due to the cancellation of the potential from oppositely charged impurities. In fig. 3.24b, the results of mobility obtained from the classical Monte Carlo, for varying r_{max}, are compared to the results of section 3.4.2.

It is clear from figs. 3.23b and 3.24b, that the classical single electron trajectory ap-

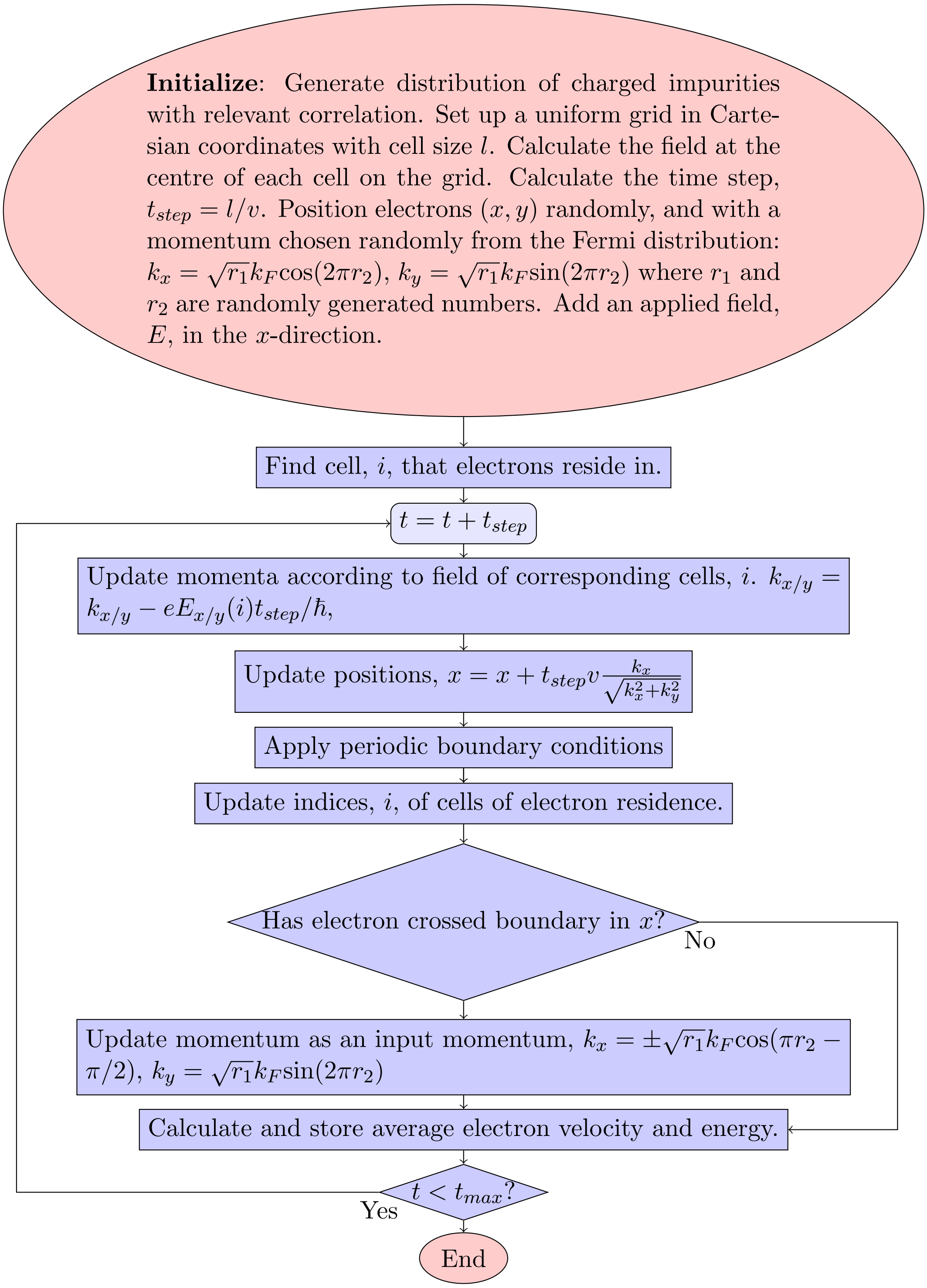

Figure 3.22: Flow chart of a simple algorithm for electron trajectories through an impurity potential with a defined input and output.

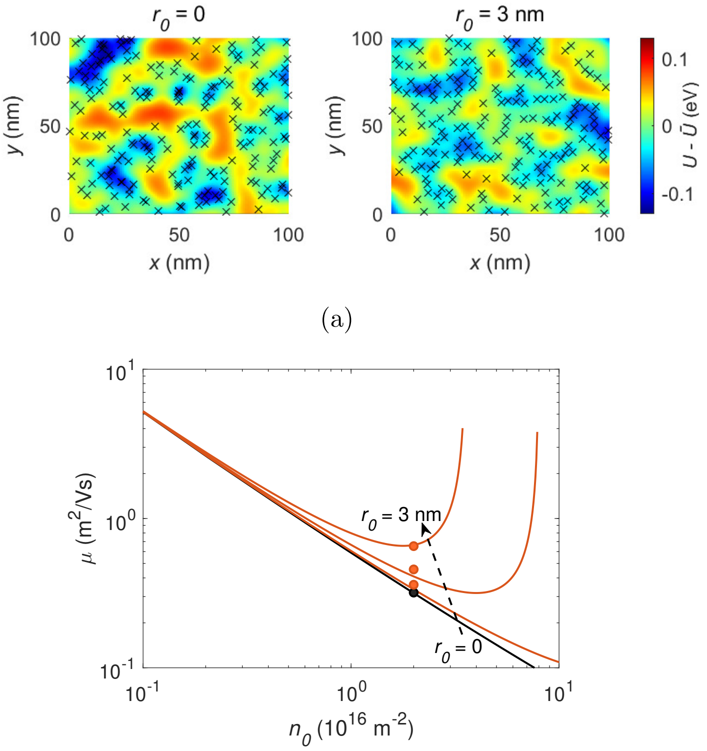

(a)

(b)

Figure 3.23: (a) Variation of potential, $U(x, y)$, about the mean, $\bar{U}$, for unipolar impurities (black crosses) of density $n_{(-)} = 2 \times 10^{16}$ m^{-2} with $r_0 = 0$ nm (random) and $r_0 = 3$ nm. (b) Variation of mobility, μ, with impurity density, $n_0 = n_{(-)}$, for a number of correlation lengths, r_0, in 1 nm increments. Solid lines are the results of the linearised Boltzmann method (section 3.4.1), filled circles show the results of the phenomenological real-space Monte Carlo for $n_0 = 2 \times 10^{16}$ m^{-2}.

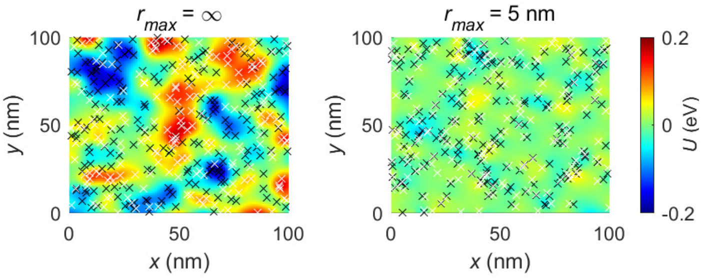

(a)

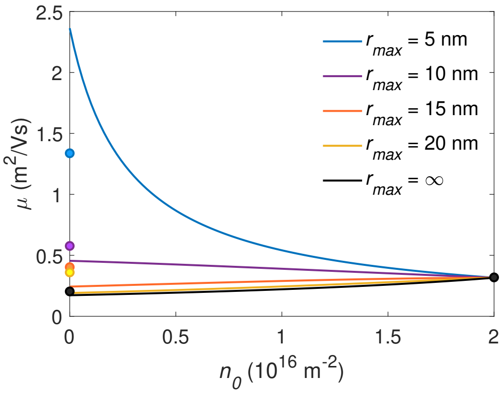

(b)

Figure 3.24: (a) Variation of potential, $U(x, y)$, for bipolar impurities (black crosses-negative, white crosses- positive) of densities $n_{(-)} = n_{(+)} = 2{\times}10^{16}$ m^{-2} with $r_{max} = \infty$ (random) and $r_{max} = 5$ nm. (b) Variation of mobility, μ, with impurity charge density, $n_0 = n_{(-)} - n_{(+)}$, for a number of correlation lengths, r_{max}, where we have fixed the density of negative impurities, $n_{(-)} = 2 \times 10^{16}$ m^{-2}. Solid lines are the results of the linearised Boltzmann method (section 3.4.2), filled circles show the results of the phenomenological real-space Monte Carlo for $n_{(+)} = 0$ and $n_{(+)} = 2 \times 10^{16}$ m^{-2}.

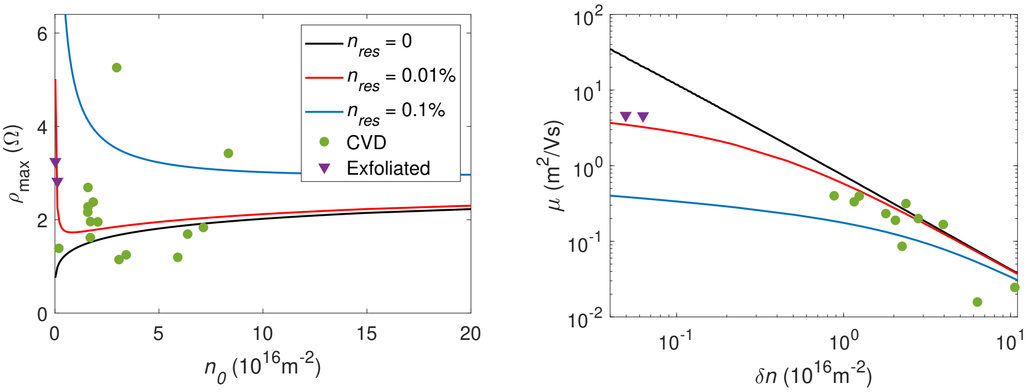

(a) (b)

Figure 3.25: (a) Maximum resistivity, ρ_{max}, as a function of dopant density, n_0, and (b) Mobility, μ, as a function of the FWHM of resistivity, δn. Solid lines show results using the LB approximation for a combination of scattering by random unipolar impurities, with a stand-off distance $d_{imp} = 1$ nm, and charge-netural resonant impurities. n_{res} shows the number of charge neutral impurities (vacancies, adatoms) as a percentage of the number of carbon atoms. Results are compared to data from pristine graphene samples grown by CVD (filled circles) or exfoliated (filled triangles).

proach qualitatively captures the results of the Boltzmann equation. Therefore, it could be used to predict and explain the characteristics of more complex impurity configurations. In particular, it could provide intuition, and possibly a quantitative analysis, of the electron-hole asymmetry believed to arise from the difference in scattering strength between attractive and repulsive potentials [103, 104], which is not present in the result of the Born approximation (2.31).

3.5 Charge-neutral Impurities

As shown in section 2.4, the scattering rate from weak point defects and even phonons is typically proportional to electron energy. Therefore, they do not usually restrict the acceleration of low energy charge carriers, at the Dirac point. However, for neutral resonant impurities, the momentum relaxation time has a weaker dependence on energy. This means that the potential remains effective at scattering electrons even at low energies, approaching the Dirac point.

Figure 3.25a shows the effect of such impurities on the maximum resistivity. At low dopant densities, the charge neutral defects remain effective, and can even become the dominant source of scattering, causing an increase in the maximum resistivity on top of the charged impurity scattering. This potentially explains the large spread of measured values, with little correlation to the charged doping density, n_0. The increased ρ_{max} due to neutral resonant impurities results in a decreased mobility at fixed δn, as shown in fig. 3.25b.

3.6 Universal Temperature-Dependent Properties

The temperature dependence of electron transport in single layer graphene (SLG) field-effect transistors (FETs) is unusual, e.g. a relatively large electron mobility, $\mu \approx 1$ m^2/Vs, was found to have relatively little change over a wide range of temperatures (4K $< T <$ 300 K) [3] compared to conventional semiconductors. Most experimental studies of graphene FETs have focused on high mobility exfoliated graphene ($\mu >$ 10 m^2/Vs) either suspended [85] or encapsulated in hexagonal boron nitride (hBN) [10, 105]. They revealed a significant decrease of mobility at high temperatures due to phonon scattering [105]. They also indicated that a large number of different mechanisms, namely charged impurity scattering, sample edge scattering [10, 105], scattering on graphene bubbles [105] and acoustic and optical phonon scattering [106] can affect the carrier mobility in different temperature ranges. These studies have also demonstrated that the temperature dependence of the conductivity, $\sigma(T)$, of SLG can vary between a linear/superlinear increase to a marked decrease with increasing temperature [85, 107]. The nature of this temperature dependence of conductivity and mobility is sensitive to both the applied gate voltage and the type of SLG material, as different types of scattering are observed in exfoliated graphene compared to CVD-grown layers, and other types of SLG e.g. graphene grown on SiC, and multilayer graphene [85, 107–110].

There have been a number of theoretical models to investigate the scattering processes responsible for electron transport in SLG, and the way in which they depend on temperature and carrier concentration [57, 68, 111, 112]. There appears to be no obvious universal behaviour of $\sigma(T)$ and $\mu(T)$. Moreover, additional factors arise from the significant role of ballistic transport in small size ($\sim$ 10 μm) high mobility SLG devices; these ballistic effects can be observed up to room temperature [10, 113, 114].

In section 3.3, we showed that the mobility at the half maximum of the resistivity is given by $\mu_{1/2} = 4/(e\delta n\rho_{max})$. Since ρ_{max} appears uncorrelated to the impurity density, we found a simple inverse relation $\mu \propto 1/\delta n$ describing the mobility across a broad range of SLG devices (fig. 3.14). Here we inspect the deviation from this simple trend within any given graphene device under variation of the temperature.

In this study, we analyse the results from 6 different SLG FETs, which can be divided into 3 groups according to their mobility and manufacturing technique. The high mobility devices Exf1 and Exf2 ($\mu >$ 20 m^2/Vs at $T <$ 10 K) were fabricated using dry transfer of single layer graphene encapsulated between two hBN layers and dry-transfer onto a Si/SiO$_2$ substrate [10, 105, 113, 115]. The lower mobility exfoliated devices Exf3 and Exf4 ($1 < \mu < 2$ m^2/Vs at $T <$ 10 K) were fabricated using exfoliated SLG and conventional wet-transfer of graphene onto Si/SiO$_2$ [116] but without use of additional protective layers of hBN or other materials. The lowest mobility devices CVD1 and CVD2 ($\mu <$ 1 m^2/Vs) were fabricated using commercial CVD-hBN film heterostructures mounted on Si/SiO$_2$ wafers. CVD2 was fabricated by capping half of the graphene layer of CVD1 with a thin ($\sim$ 1 μm) layer of exfoliated monocrystalline

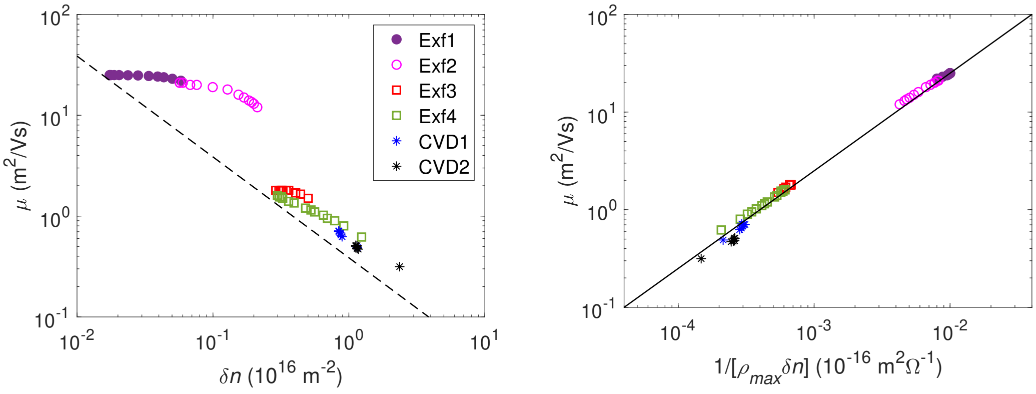

(a) (b)

Figure 3.26: (a) Field-effect mobility, μ, as function of δn for each device over a wide range of temperatures. Black lines show the results of $\mu = 16e/(h\delta n)$ (dashed line). (b) Suggested universal dependence of the graphene mobility, $\mu = 4/(e\rho_{max}\delta n)$ shown for all devices and temperatures.

InSe using the technique described in ref. [90]. The InSe layer is known to affect the carrier density and mobility of the adjacent graphene layer [90]. Further details of all devices can be found in appendix A. See ref. [117] for acknowledgements to those responsible for the fabrication of the 6 devices and for providing the experimental measurements on the 6 devices, shown throughout sections 3.6 to 3.9.

Figure 3.26a shows the results of the relationship between mobility, μ, and FWHM, δn. Notably, the low mobility samples appear to largely maintain the inverse relationship under varying temperatures. However, the high mobility (Exf1 and Exf2) samples display a more stable mobility with varying δn. The reason for this is that, when considering the temperature dependence, the assumption of a constant (or uncorrelated) maximum resistivity is only valid for the low mobility samples, where ρ_{max} is almost independent of temperature (see fig. 3.34a). For exfoliated graphene, the temperature dependence of ρ_{max} is significant. We note that, for Exf2, at large δn, corresponding to high temperature, the inverse relationship is established. This is because $\rho_{max}(T)$ stabilises, likely due to increased phonon scattering compensating for the increased thermally excited carrier density.

As shown in fig. 3.26b, the mobility calculated using eq. (3.25) provides excellent agreement with the field-effect mobility calculated using conventional methods: namely the linearisation of $\sigma(V_g)$ [107] and the value of mobility at the maximum of $d\sigma/dV_g$. Equation (3.25) can be used to calculate the mobility from the measured $\rho(V_g)$ curve of a graphene FET from ρ_{max} and δn. This way of calculating the field-effect mobility, requires measurements of $\rho(V_g)$ at just 3 points (the "3-point method"): one at $\rho(V_g) = \rho_{max}$ and two at the FWHM points, with $\rho(V_g) = \rho_{max}/2$. This 3-point method provides a better defined estimate of the field-effect mobility in the vicinity of the Dirac point, $|n| < \delta n/2$, compared to the method of linearisation of $\sigma(V_g)$. In particular, it is well defined even if $\sigma(V_g)$ has a nonlinear dependence, as for the case of strong short range

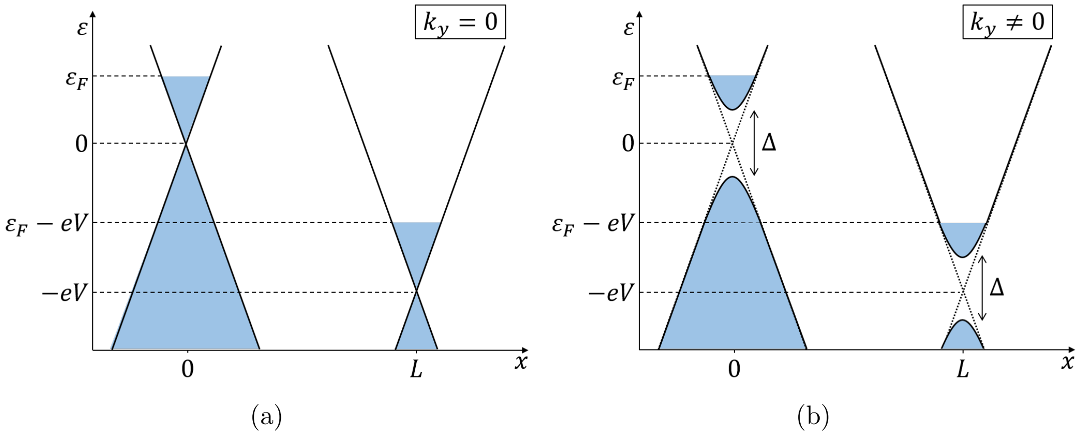

Figure 3.27: Cross-sections of the energy, ε, band structure diagrams for an applied potential difference, V, over a distance L in the x-direction. The chemical potential is denoted ε_F. (a) Cross-section at $k_y = 0$, i.e. electrons have no momentum component perpendicular to the direction of the potential difference. (b) $k_y \neq 0$, i.e. electrons have a finite momentum component perpendicular to the direction of the potential difference. The energy gap is $\Delta = 2\hbar v\,|k_y|$.

scattering or ballistic transport.

3.7 Beyond Diffusive: Charge Transport in High Quality Graphene

3.7.1 Ballistic Transport

Here we analyse the ballistic conductivity using the standard Landauer formula. A potential difference, V, is applied between two regions, as shown in fig. 3.27a. At $T = 0$, the distribution of electrons in the bands is sharp and right-going electrons on the LHS, with energy $\varepsilon_F - eV < \varepsilon < \varepsilon_F$, are able to accelerate into the available states in the RHS. The Landauer formula for charge transport is,

$$\mathbf{J} = \frac{g_s g_v e}{(2\pi)^2} \int \mathrm{d}\mathbf{k}\, \mathbf{v}_g \mathcal{T} \left[f(k, \varepsilon_F) - f(k, \varepsilon_F - eV) \right], \tag{3.50}$$

where $\mathbf{v}_g(\mathbf{k}) = v\mathbf{k}/k$ is the group velocity, $\mathcal{T}(\mathbf{k})$ is the transmission coefficient, and $f(k, \varepsilon_F)$ is the Fermi-Dirac distribution function.

For large chemical potentials, $\varepsilon_F > eV$, at $T = 0$, all transport will be in the conduction band. In this case, eq. (3.50) becomes

$$J(\varepsilon_F > eV, T = 0) = \frac{g_s g_v e}{(2\pi)^2} \frac{v}{(\hbar v)^2} \int_{-\pi/2}^{\pi/2} \mathrm{d}\theta \cos(\theta) \int_{\varepsilon_F - eV}^{\varepsilon_F} \mathrm{d}\varepsilon\, \varepsilon \tag{3.51}$$

for ideal transmission ($\mathcal{T} = 1$), where we have assumed the potential difference to be in the x direction. Evaluating eq. (3.51) and using $J = \sigma V/L$, where L is the length over which there exists the potential difference, we find that

$$\sigma(\varepsilon_F > eV) = L\frac{2g_sg_se^2v}{(2\pi\hbar v)^2}\left(\varepsilon_F - \frac{1}{2}eV\right). \tag{3.52}$$

Significantly, the conductivity is found to be proportional to the length. This is expected for ballistic transport, where the 'quantum' conductance becomes independent of length over which the ballistic transport occurs. We also find that $\sigma \propto \varepsilon_F$. Therefore, the conductivity is sublinear with applied gate voltage, $\sigma \propto V_g^{1/2}$.

Considering both conduction and valence bands, the current density is $J = J_k(\varepsilon_+) + J_k(\varepsilon_-)$, where

$$J_k(\varepsilon_\pm) = \frac{g_sg_ve}{(2\pi)^2}v\int_{-\infty}^{\infty}\mathrm{d}k_y\int_0^{\infty}\mathrm{d}k_x\frac{k_x}{k}\mathcal{T}\left[f(\varepsilon_\pm,\varepsilon_F) - f(\varepsilon_\pm,\varepsilon_F - eV)\right] \tag{3.53}$$

and $\varepsilon_\pm = \pm\hbar v\sqrt{k_x^2 + k_y^2}$ are the energies of electrons in the conduction and valence bands, respectively, on the left-hand-side of figs. 3.27a and 3.27b. The band structure of graphene is cononical with zero band gap. However, for ballistic transport in the x-direction, electron momentum in the y-direction, k_y, must be conserved. The energy of electrons in the right band is given by $\varepsilon_{\pm,R} = \pm\hbar v\sqrt{k_{x,R}^2 + k_{y,R}^2} - eV$. Since the momentum in the y-direction and total energy are conserved (i.e. $k_{y,R} = k_y$ and $\varepsilon_{\pm,R} = \varepsilon_\pm$), we find a constraint, $|\varepsilon_\pm + eV| > \hbar v|k_y|$, on the allowed energies of electrons in the left band that are able to transport into the right band. This momentum and energy conservation manifests itself as a gap in the available states for non-zero k_y (see fig. 3.27b), $\Delta = 2\hbar v|k_y|$. Therefore, one should modify eq. (3.53) to impose this constraint,

$$\begin{aligned} J_k(\varepsilon_\pm) = \pm\frac{g_sg_ve}{(2\pi)^2}v\int_{-\infty}^{\infty}\mathrm{d}k_y\int_0^{\infty}\mathrm{d}k_x\frac{k_x}{k}\mathcal{T}\left[f(\varepsilon_\pm,\varepsilon_F) - f(\varepsilon_\pm,\varepsilon_F - eV)\right]& \\ \times H\left(|\varepsilon_\pm + eV| - \hbar v|k_y|\right).& \end{aligned} \tag{3.54}$$

Since the energy constraint and the distribution functions depend explicitly on energy, it is convenient to substitute k_x for energy. However, after doing so, the two variables of integration, k_y and ε, will not be independent. Therefore, one will have to take care when changing the limits of integration: the maximum value of $\hbar v k_y$ is given by the maximum value of ε. Making the substitution, the total current density is

$$J = \frac{g_sg_ve}{(2\pi)^2}\frac{1}{\hbar}\int_{-\infty}^{\infty}\mathrm{d}k_y\int_{-\infty}^{\infty}\mathrm{d}\varepsilon\mathcal{T}F(\varepsilon,k_y)H\left(|\varepsilon + eV| - \hbar v|k_y|\right) \tag{3.55}$$

where

$$F(\varepsilon,k_y) = \left[f(\varepsilon(k_y),\varepsilon_F) - f(\varepsilon(k_y),\varepsilon_F - eV)\right] \tag{3.56}$$

determines the availability of states. Imposing the energy and k_y conserving Heaviside function on the range of integration,

$$
\begin{aligned}
J = \frac{g_s g_v e}{(2\pi)^2}\frac{1}{\hbar}\Bigg[&\int_{-\infty}^{\infty}\mathrm{d}k_y\int_{\frac{\Delta}{2}}^{\infty}\mathrm{d}\varepsilon\mathcal{T}F(\varepsilon,k_y)\\
&+\int_{-\frac{eV}{2\hbar v}}^{\frac{eV}{2\hbar v}}\mathrm{d}k_y\int_{-eV+\frac{\Delta}{2}}^{-\frac{\Delta}{2}}\mathrm{d}\varepsilon\mathcal{T}F(\varepsilon,k_y)\\
&+\int_{-\infty}^{\infty}\mathrm{d}k_y\int_{-\infty}^{-eV-\frac{\Delta}{2}}\mathrm{d}\varepsilon\mathcal{T}F(\varepsilon,k_y)\Bigg].
\end{aligned}
\tag{3.57}
$$

The first, second and third terms in eq. (3.57) describe current from transport intraband in the conduction band, interband and intraband in the valence band, respectively. For $T = 0$, the difference of the distribution functions, $F(\varepsilon) = H(\varepsilon_F - \varepsilon) - H(\varepsilon_F - eV - \varepsilon)$, simply acts to restrict the energy range to the interval $\varepsilon_F - eV < \varepsilon < \varepsilon_F$. Let us first evaluate each of the double integrals in eq. (3.57) separately for the case of completely ideal transport ($\mathcal{T} = 1$) and a positive chemical potential, $\varepsilon_F > 0$, before collating the results to find the total current.

The first term is

$$
J_1 = \frac{g_s g_v e}{(2\pi)^2}\frac{1}{\hbar}\int_{-\frac{\varepsilon_F}{\hbar v}}^{\frac{\varepsilon_F}{\hbar v}}\mathrm{d}k_y\int_{\max(\frac{\Delta}{2},\varepsilon_F-eV)}^{\varepsilon_F}\mathrm{d}\varepsilon. \tag{3.58}
$$

The lower energy limit, $\max(\frac{\Delta}{2},\varepsilon_F - eV) = \max(\hbar v|k_y|,\varepsilon_F - eV)$, is $\Delta/2$ for $\hbar v|k_y| > \varepsilon_F - eV$ and $\varepsilon_F - eV$ for $\hbar v|k_y| < \varepsilon_F - eV$. Therefore, for $\varepsilon_F < eV$,

$$
J_1 = \frac{g_s g_v e}{(2\pi)^2}\frac{2}{\hbar}\int_0^{\frac{\varepsilon_F}{\hbar v}}\mathrm{d}k_y\int_{\hbar v k_y}^{\varepsilon_F}\mathrm{d}\varepsilon = \frac{g_s g_v e}{(2\pi)^2}\frac{\varepsilon_F^2}{\hbar^2 v}, \tag{3.59}
$$

whilst, for $\varepsilon_F > eV$,

$$
\begin{aligned}
J_1 &= \frac{g_s g_v e}{(2\pi)^2}\frac{2}{\hbar}\left[\int_0^{\frac{\varepsilon_F-eV}{\hbar v}}\mathrm{d}k_y\int_{\varepsilon_f-eV}^{\varepsilon_F}\mathrm{d}\varepsilon + \int_{\frac{\varepsilon_F-eV}{\hbar v}}^{\frac{\varepsilon_F}{\hbar v}}\mathrm{d}k_y\int_{\hbar v k_y}^{\varepsilon_F}\mathrm{d}\varepsilon\right]\\
&= \frac{g_s g_v e}{(2\pi)^2}\frac{1}{\hbar^2 v}\left(2\varepsilon_F eV - (eV)^2\right).
\end{aligned}
\tag{3.60}
$$

The second term does not contribute for $\varepsilon_F > eV$, since all transport will be in the conduction band. However, for $\varepsilon_F < eV$,

$$
J_2 = \frac{g_s g_v e}{(2\pi)^2}\frac{2}{\hbar}\int_0^{\min(\frac{eV}{2\hbar v},\frac{eV-\varepsilon_F}{\hbar v})}\mathrm{d}k_y\int_{\max(-eV+\frac{\Delta}{2},\varepsilon_F-eV)}^{-\frac{\Delta}{2}}\mathrm{d}\varepsilon. \tag{3.61}
$$

For $eV < 2\varepsilon_F$, $\min(\frac{eV}{2\hbar v},\frac{eV-\varepsilon_F}{\hbar v}) = \frac{eV-\varepsilon_F}{\hbar v}$ and $\max(-eV + \frac{\Delta}{2}, \varepsilon_F - eV) = \varepsilon_F - eV$ for all k_y. Therefore, for $eV/2 < \varepsilon_F < eV$,

$$J_2 = \frac{g_s g_v e}{(2\pi)^2} \frac{2}{\hbar} \int_0^{\frac{eV-\varepsilon_F}{\hbar v}} \mathrm{d}k_y \int_{\varepsilon_F - eV}^{-\hbar v k_y} \mathrm{d}\varepsilon = \frac{g_s g_v e}{(2\pi)^2} \frac{1}{\hbar^2 v} \left(\varepsilon_F - eV\right)^2, \tag{3.62}$$

For $\varepsilon_F < eV/2$, $\min(\frac{eV}{2\hbar v}, \frac{eV-\varepsilon_F}{\hbar v}) = \frac{eV}{2\hbar v}$, and $\max(-eV + \frac{\Delta}{2}, \varepsilon_F - eV)$ varies over k_y,

$$\begin{aligned} J_2 &= \frac{g_s g_v e}{(2\pi)^2} \frac{2}{\hbar} \left[\int_0^{\frac{\varepsilon_F}{\hbar v}} \mathrm{d}k_y \int_{\varepsilon_F - eV}^{-\hbar v k_y} \mathrm{d}\varepsilon + \int_{\frac{\varepsilon_F}{\hbar v}}^{\frac{eV}{2\hbar v}} \mathrm{d}k_y \int_{-eV+\hbar v k_y}^{-\hbar v k_y} \mathrm{d}\varepsilon \right] \\ &= \frac{g_s g_v e}{(2\pi)^2} \frac{1}{\hbar^2 v} \left(\frac{1}{2}(eV)^2 - \varepsilon_F^2 \right). \end{aligned} \tag{3.63}$$

Finally, the third term does not contribute for $\varepsilon_F > 0$, $J_3 = 0$.

Summing the results for the intra- and inter- band components, J_1 and J_2, the total conductivity is

$$\sigma = L \frac{g_s g_v e}{(2\pi)^2 \hbar^2 v} \times \begin{cases} \frac{1}{2} e^2 V & \text{if } |\varepsilon_F| < \frac{eV}{2} \\ \varepsilon_F^2 / V + \left(|\varepsilon_F| - eV\right)^2 / V & \text{if } \frac{eV}{2} \leq |\varepsilon_F| \leq eV \\ 2e|\varepsilon_F| - e^2 V & \text{if } |\varepsilon_F| > eV \end{cases}, \tag{3.64}$$

where we have made use of the symmetry in the chemical potential ($\varepsilon_F \to -\varepsilon_F$) in eq. (3.50) when transport switches from electrons to holes.

Zener tunnelling describes the process of electron tunnelling through an energy gap. Using the WKB approximation, the tunnel coefficient is $\mathcal{T}_Z = \exp\left(-\pi m \Delta^2 L / (4\hbar p e V)\right)$, where Δ is typically the size of the band gap [118, 119]. For graphene, the band gap is zero and the relativistic Dirac electrons are able to tunnel almost unimpeded, without reflection; this is Klein tunneling [84]. However, tunnelling by Dirac electrons in graphene with finite k_y is similar to that of massive zener electrons where $\Delta = 2\hbar v k_y$, $\mathcal{T}_{ZK} = \exp\left(-\pi \Delta^2 L / (4\hbar v e V)\right)$ [120–123]. For interband tunneling, where the electrons have to penetrate the forbidden energy gap, Δ, the transmission coefficient is given by the Zener-Klein coefficient, $\mathcal{T}_{ZK}$. Therefore, eq. (3.64) is strictly the limiting case for $V/L \to \infty$. The interband part corresponds only to the second term in eq. (3.57), such that

$$\begin{aligned} J = \frac{g_s g_v e}{(2\pi)^2} \frac{1}{\hbar} \Bigg[&\int_{-\infty}^{\infty} \mathrm{d}k_y \int_{\frac{\Delta}{2}}^{\infty} \mathrm{d}\varepsilon F(\varepsilon, k_y) \\ &+ \int_{-\frac{eV}{2\hbar v}}^{\frac{eV}{2\hbar v}} \mathrm{d}k_y \mathcal{T}_{ZK}(k_y) \int_{-eV+\frac{\Delta}{2}}^{-\frac{\Delta}{2}} \mathrm{d}\varepsilon F(\varepsilon, k_y) \\ &+ \int_{-\infty}^{\infty} \mathrm{d}k_y \int_{-\infty}^{-eV-\frac{\Delta}{2}} \mathrm{d}\varepsilon F(\varepsilon, k_y) \Bigg]. \end{aligned} \tag{3.65}$$

For $T = 0$, eq. (3.65), can be evaluated analytically following the same process as in deriving eq. (3.64). This has been done in ref. [123]. We find that, as expected,

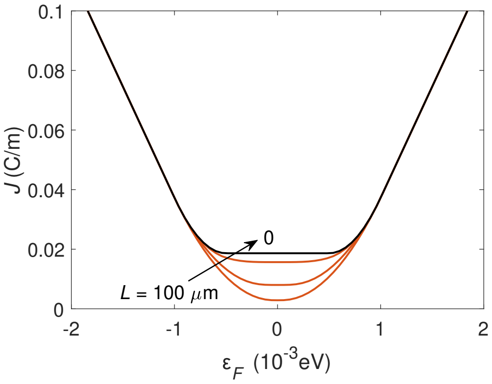

Figure 3.28: Current density, J, as a function of chemical potential, ε_F, for ballistic transport in graphene using the Landauer formula and WKB approximation of Zener-Klein tunnelling. The red lines show results for varying finite channel lengths, $L = 100$, 10, 1 μm, as calculated in reference [123]. The black line shows the result of eq. (3.64), the limit of $L \to 0$. The potential difference is V = 1 meV.

Zener-Klein tunneling suppresses the current for $|\varepsilon_F| < eV$, where most transport is interband, whilst converging toward eq. (3.64) in the limit $L/V \to 0$, as shown in fig. 3.28.

For non-zero temperature, we can integrate eq. (3.65) numerically. Figure 3.29 shows the results for varying temperature. There is an increase in the current around the Dirac point with increasing temperature, as expected by the increasing carrier density. Comparing figs. 3.29a and 3.29b, the temperature dependence of conductivity around the Dirac point is weaker when the applied potential difference, V, is larger. This is because, when the applied potential difference is large, the transport window, eV, shown in fig. 3.27, is large, such that the window of transport by thermally excited electrons, k_BT, is less significant ($k_BT \ll eV$). For sufficiently large chemical potentials, $|\varepsilon_F| \gg (k_BT, eV)$, the difference in occupation between left and right contacts is approximately 0 around $\varepsilon < \Delta/2$ over most momentum states, k_y. Therefore we can write the current density eq. (3.50) as

$$\begin{aligned} J(|\varepsilon_F| \gg k_BT, eV) &\approx \frac{g_s g_v e}{(2\pi)^2} \frac{v}{(\hbar v)^2} \int_{-\pi/2}^{\pi/2} \mathrm{d}\theta \cos(\theta) \int_0^\infty \mathrm{d}\varepsilon\, \varepsilon \left[f(\varepsilon, \varepsilon_F) - f(\varepsilon, \varepsilon_F - eV) \right] \\ &= \frac{qv}{\pi} \left[n(\varepsilon_F, T) - n(\varepsilon_F - eV, T) \right]. \end{aligned} \tag{3.66}$$

As shown in section 1.2.2, in the limit $|\varepsilon_F| \gg k_BT$, $n(\varepsilon_F) \to g_s g_v \varepsilon_F^2/(4\pi\hbar^2 v^2)$. Then eq. (3.66) returns eq. (3.51), derived strictly for $T = 0$ and with ideal transmission, and the current at all temperatures converge at large $|\varepsilon_F|$, as shown in fig. 3.29. However, from eq. (2.4), we find that the chemical potential decreases with increasing temperature for a given gate voltage, V_g. This can be understood qualitatively: the energy density of states is proportional to energy, meaning that, as electrons are thermally excited into higher energy states, the chemical potential is relaxed due to the increased availability

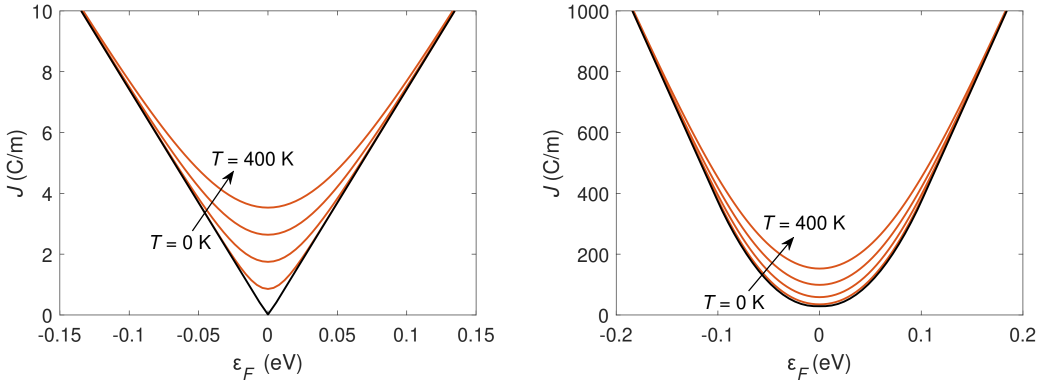

(a) (b)

Figure 3.29: Current density, J, as a function of chemical potential, ε_F, for ballistic transport in graphene using the Landauer formula and WKB approximation of Zener-Klein tunnelling. The red lines show results for varying finite temperatures ($T = 100$, 200, 300, 400 K) calculated by numerical integration of eq. (3.65), the black line shows the result for $T = 0$ K. The length is $L = 1$ µm. (a) Potential difference, V = 1 meV. (b) V = 0.1 eV.

of states at higher energy. As a result, the conductivity is found to decrease with increasing temperature for large gate voltages, even in ballistic devices, as shown in fig. 3.30, an effect often attributed to phonon scattering.

When the potential difference is applied between contact leads, the leads themselves impose boundary conditions on the wavefunctions within the graphene sheet. In this case, the transmission coefficient is limited by these boundary conditions. Calculations of the boundary effects have been done in references [9, 124]. In ref. [124], they found that, in the limit of a sufficiently wide device ($W/L \to \infty$), the minimum conductivity (corresponding to $\varepsilon_F = 0$) is given by $4e^2/\pi h$. In ref. [9], the same method was used to find that $\sigma = e^2 L\varepsilon_F/h\hbar v$ for large sufficiently large values of the chemical potential, ε_F.

If we are able to neglect such constraints imposed at the boundaries, in a 4-terminal Hall bar measurement for example [9], then we can assume $\mathcal{T} = 1$ for intraband transport and $\mathcal{T} = \mathcal{T}_{ZK}$ for interband transport. Figure 3.31a shows the results from a 4-terminal measurement of conductance for Exf1, at varying temperatures. Figure fig. 3.31b shows the total transport carrier density, N_{tot}, calculated as in section 2.1.2. To see how the 'mobility' varies with gate voltage, we divide the experimental conductance by the calculated total carrier charge density, as shown in fig. 3.31c. At small temperatures, there is large uncertainty in the value of N_{tot} around the Dirac point, due to possible spatial fluctuations in the local quasi-Fermi level. Since we assume complete spatial homoegeneity ($\delta\varepsilon_{imp} = 0$), the mobility is ill-defined at low temperatures and small V_g, where $N_{tot} \to 0$. Also, quantum conductance around $N_{tot} = 0$ will result in an undefined 'mobility'. However, at higher temperatures, the results displayed in fig. 3.31c are much less susceptible to uncertainty in $\delta\varepsilon_{imp}$, since the carrier density is

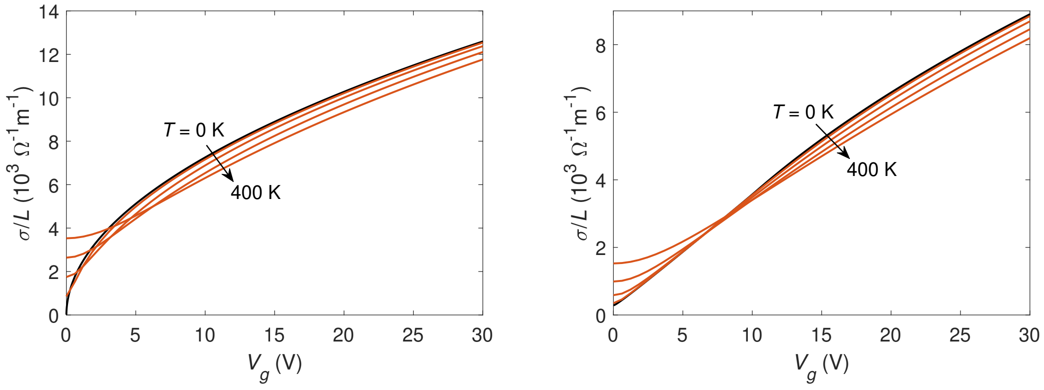

(a) (b)

Figure 3.30: Conductivity, σ, as a function of gate voltage, V_g, for ballistic transport in graphene using the Landauer formula and WKB approximation of Zener-Klein tunnelling. The red lines show results for varying finite temperatures ($T = 100$, 200, 300, 400 K), the black line shows the result for $T = 0$ K. We have calculated the conductivity as $\sigma/L = J/V$, where current density J, is calculated by numerical integration of eq. (3.65). The chemical potential for each gate voltage is found by eq. (2.4), where we assume the capacitance, $C_d/e = 7 \times 10^{14}$ m^{-2}V^{-1}. The length is $L = 1$ µm. (a) Potential difference, $V = 1$ meV. (b) $V = 0.1$ eV.

dominated by thermally excited carriers.

Typically, such Hall measurements are performed using a constant current [10, 113]. Therefore, the potential difference changes as the device resistance changes. This means that V in eq. (3.65) is a function of ε_F. Here, we investigate how changes in the applied potential could explain the mobility drop around the Dirac point shown in fig. 3.31c. In fig. 3.32 we have estimated the potential dropped over the ballistic region as $V = I_B R$, where R is the resistance measured experimentally, for some constant value of current, I_B, over the ballistic region. We assume the transport channel length to be $L = 4$ µm and width $W = 0.4$ µm, close to the device dimensions (see appendix A and table A.1). As V increases, the conductivity (and therefore mobility) around the Dirac point decreases sharply, converging toward the measured values. This is due to the increasing range of energies where the valence band on the LHS and the conduction band on the RHS of fig. 3.27 are in energetic alignment. This means that more electrons, with $k_y \neq 0$, are tunnelling through the inter-band energy gap, Δ, and their transmission coefficient is suppressed by Zener-Klein tunneling. The applied potential is largest at the Dirac point, whilst the chemical potential here is smallest, such that the ratio between the number of states undergoing interband transport compared to those undergoing intraband transport is at a maximum and, therefore, suppression by Zener-Klein tunnelling is also maximum.

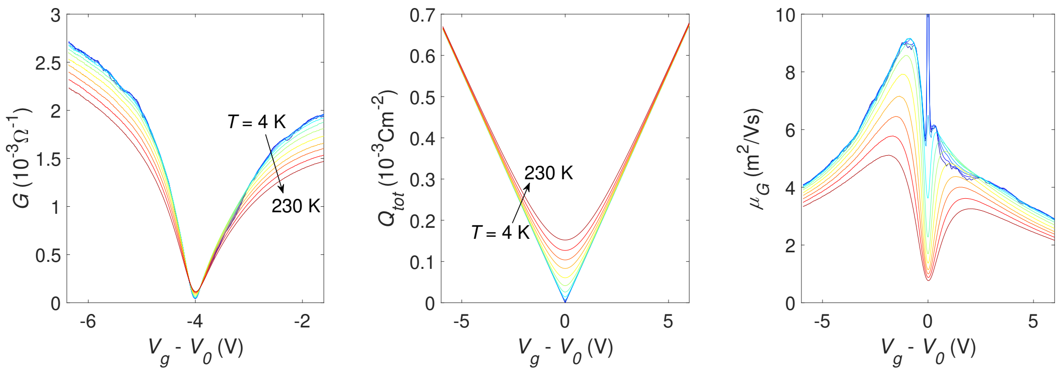

(a) (b) (c)

Figure 3.31: (a) Measured conductance, G, of Exf1 as a function of applied gate voltage, $V_g - V_0$, where $V_0 \approx -0.08$ V is the offset of the Dirac point, for varying temperature T. (b) Total transport carrier charge density, $Q_{tot} = eN_{tot}$, as a function of applied gate voltage, $V_g - V_0$, calculated using eq. (2.4) for varying temperature, T. (c) Effective mobility, $\mu_G = G/Q_{tot}$, of Exf1 as a function of gate voltage, $V_g - V_0$, for varying temperatures.

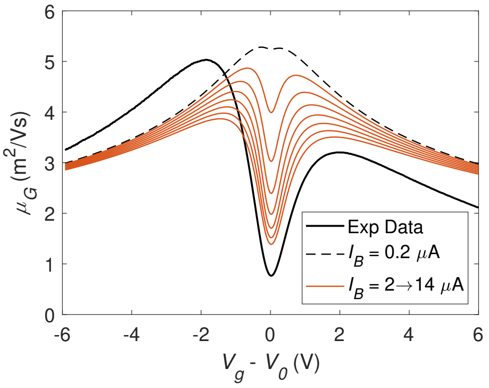

Figure 3.32: Effective mobility, $\mu_G = G/eN_{tot}$, as a function of gate voltage, $V_g - V_0$, for $T = 230$ K, where G is the conductance and N_{tot} is the total carrier density. The solid black line shows the results from the experimentally measured conductance of Exf1. The black dashed line and solid red lines show the results from the calculated conductance assuming ballistic transport (eq. (3.65)). The potential difference input into the ballistic calculations (eq. (3.65)) is be $V = I_B R$, where R is the experimentally measured resistance of Exf1. The black dashed line shows the results for $I_B = 0.2$ µA. The solid red lines show the results for increasing the assumed potential dropped over the ballistic region by increasing the assumed current 2 µA $< I_B <$ 14 µA in increments of 2 µA. Note μ_G is the ratio of conductance to carrier charge density. To compare to the experimental mobility, μ_G should be multiplied by the experimentally measured aspect ratio ($L/W = 4$ in this case).

3.7.2 Note on Hydrodynamic Transport

Recently, it has been shown that the hydrodynamic regime, characterised by the viscous flow of charge carriers, can be realised in graphene [125, 126]. Such viscous flow occurs when the momentum-conserving electron-electron scattering length l_{ee} is less than both the momentum changing, diffusive scattering lengths and the sample length. In this case, the conductivity is given by

$$\sigma_v = LW\frac{\varepsilon_F e^2}{\hbar^2 v 4 l_{ee}}, \tag{3.67}$$

where W is the width. At a given temperature, less than the chemical potential ($k_BT < \varepsilon_F$), l_{ee} is a constant with respect to the chemical potential [127]. In this regime, the conductivity of hydrodynamic flow, eq. (3.67), has the same form as for ballistic transport, eq. (3.52), with respect to any doping. At larger temperature, $k_BT > \varepsilon_F$, the electron-electron scattering length is proportional to the chemical potential [127], such that the hydrodynamic conductivity tends toward a constant with respect to the gating level.

3.8 Temperature-Dependent Diffusive Transport

In section 3.3, we showed that the electronic properties of graphene deposited on a substrate can mostly be explained by the scattering of carriers by charged impurities at low temperatures. At high temperatures, inelastic phonon scattering is activated and can have a significant effect on the total scattering relaxation time of the charge carriers. Furthermore, the thermal broadening of the distribution function affects the relaxation time of inelastic events, leading to a temperature dependence of impurity scattering [53, 111]. Here, we perform calculations of the effect of temperature on the conductivity of graphene due to substrate effects involving charged impurities and substrate polar phonons, as well as the intrinsic acoustic and optical phonons of graphene. Specifically, we want to inspect the effect of the non-zero perpendicular distance of the substrate on the effectiveness of scattering at different energies. This will be important when we try to understand the behaviour of the FWHM of resistivity at varying temperatures in section 3.9.

Since we are interested in examining both the low and high temperature regimes, we need to use the full LB equation (eq. (1.50)), including the temperature dependant Fermi distribution function. Similarly, by using eq. (2.11), we also maintain the temperature dependence of the electron distribution in the polarization function for screening by the electron gas. Since we are considering a broad range of chemical potential energies and temperatures, for completeness we include scattering by: both the transverse and longitudinal optical phonons of graphene around the Γ and K points; acoustic phonons; polar phonons in the substrate layer. The momentum relaxation time, τ, for each of the scattering mechanisms is evaluated using the expressions derived in section 2.3.2 for charged impurities and throughout section 2.4 for phonons. Then, the conductivity is calculated by integrating eq. (1.50) numerically for both hole ($\varepsilon_F^* = \varepsilon_{F,h}^*$) and electron ($\varepsilon_F^* = \varepsilon_{F,e}^*$) puddle regions.

Figure 3.33a shows the variation of impurity-limited conductivity with gate voltage and temperature for two impurity densities, $n_{imp} = 1 \times 10^{15}$ m^{-2} and $n_{imp} = 1 \times 10^{16}$ m^{-2}, where we have approximated $d_{imp} = 0$ for ease of comparison to the analytical results of [57] obtained at $T = 0$. Unlike phonon scattering, impurity scattering is intrinsically temperature independent. However, the conductivity is affected by the temperature dependence of carrier density (see fig. 2.2b). There is also a weak temperature dependence, notable at large gate voltages, due to the effect of thermal broadening of the Fermi-Dirac distribution of electron occupation on screening, energy of occupied states, and the chemical potential.

Figure 3.33b shows the results of conductivity including scattering by substrate polar phonons and intrinsic phonons, where we have assumed that $d_{imp} = 1$ nm. The finite distances of charged impurities and the polarization field generated by substrate phonons from the graphene plane, d_{imp} and d_{spp}, result in the suppression of scattering as the electron energy, and therefore the reciprocal space scattering length, q, increase. This exponential increase in the relaxation times, eqs. (2.32) and (2.74), arises from the interaction between the 2D electronic wavefunctions with the 3D spatially varying electric fields. This suppression of scattering at high energies leads to an increasing mobility with gate voltage (fig. 3.33c) and a superlinear dependence of the conductivity on gate voltage.

Figure 3.33b shows that the resistivity decreases with increasing temperature at low gate voltage due to the increased carrier density involving thermally excited electron-hole pairs. However, as the gate voltage and hence the carrier energy is increased, fewer electron-hole pairs are created by thermal excitation and phonon scattering becomes dominant. Therefore, since the phonon scattering rate increases with increasing temperature, due to increased phonon occupancy and availability of electronic states, the resistivity increases with increasing temperature at high gate voltages.

3.9 Analytical Model of T-Dependent Transport Parameters

Equation (3.25) provides a good fit to the measured temperature-dependent mobility (see fig. 3.26b). To model $\mu(T)$ in more detail, we first consider the effect of temperature on ρ_{max} and δn. Since δn represents an uncertainty in the carrier density near the Dirac point and ρ_{max} is directly related to δn, they both involve temperature-induced broadening described by the Fermi-Dirac (FD) function. The minimum carrier density at the neutrality (Dirac) point is $n_{NP} = n_{res} + n_{TH}$, as determined by eq. (2.29), where n_{res} is the sheet density of the residual carriers due to spatial variations of the potential landscape and $n_{TH} = (\pi/3)(k_B T/\hbar v)^2$ is the density of thermally activated

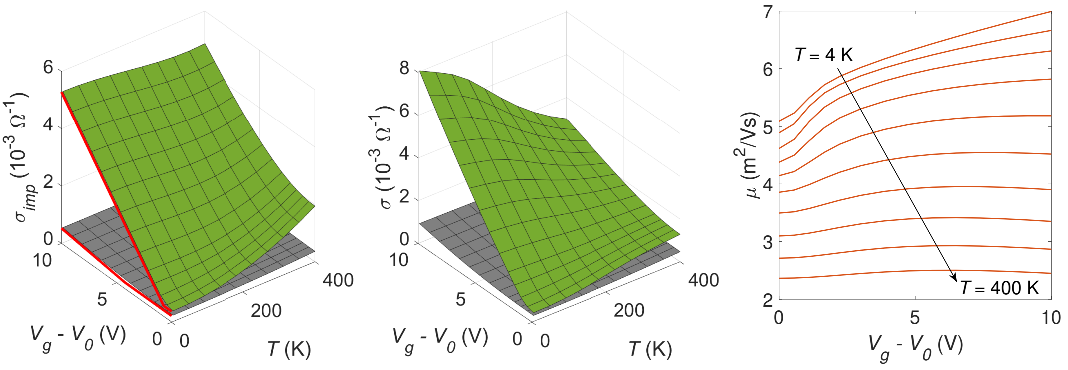

(a) (b) (c)

Figure 3.33: (a) Impurity-limited conductivity, σ_{imp}, assuming an impurity distance of $d_{imp} = 0$, as a function of applied gate voltage, $V_g - V_0$, and temperature, T, for graphene on SiO$_2$. Red lines show results of ref [57], i.e. using the analytical expressions (2.35) and (2.25). (b) Total conductivity, σ, as a function of applied gate voltage, $V_g - V_0$, and temperature, T, for graphene on SiO$_2$, calculated assuming scattering by charged impurities, polar substrate optical phonons, and intrinsic acoustic and optical phonons. The impurity distance is assumed to be $d_{imp} = 1$ nm. In both (a) and (b) we show results for two impurity densities: $n_{imp} = 10^{15}$ m^{-2} (green) and $n_{imp} = 10^{16}$ m^{-2} (grey). (c) Mobility, μ, for varying gate voltage, $V_g - V_0$, for temperatures between 4 K and 400 K. The mobility is obtained here from the conductivity in (b) as $\mu = \sigma/(eN_{tot})$ where N_{tot} is the total carrier density, given by eq. (2.28). The temperature is varied in steps of equal intervals, and is shown by the black lines in (b).

electron-hole pairs. Therefore

$$\rho_{max} = \frac{1}{(e\mu_0 n_{NP})} = \frac{1}{e\mu_0(n_{res} + n_{TH}(T))}, \tag{3.68}$$

where μ_0 is the mobility at the neutrality point. Since the relaxation rate of phonon scattering is proportional to electron energy (see section 2.4), the effect of phonon scattering is expected to be relatively weak around the Dirac point [88]. Therefore, we make the approximation that μ_0 is temperature-independent. As shown in fig. 3.34a, eq. (3.68) provides a good fit to the measured values of $\rho_{max}(T)$ for all six devices using μ_0 and n_{res} as fitting parameters. The average deviation from the data is less than 10% for all fits[1]. The values of these fitting parameters for each sample are shown as a plot of μ_0 versus n_{res} in fig. 3.34b. Their values are consistent with those obtained from eqs. (2.26) and (2.35), as presented in [57], for graphene on SiO$_2$ with impurity-to-graphene distances, d_{imp}, within a range of 0.3 nm $\lesssim d_{imp} \lesssim$ 1 nm (see grey shaded region in fig. 3.34b).

---

[1] Method of least squares used to find optimal values, n_{res} and μ. For CVD1, the optimal solution is unphysical, $n_{res} \to \infty$ and $\mu \to 0$. We restricted $n_{res} < 2.5 \times 10^{16}$ m^{-2}, where we find that the optimal solution fits within the bounds of 0.3 nm $\lesssim d_{imp} \lesssim 1$ (grey shaded region in fig. 3.34a) and remains well within a 10% deviation of the data.

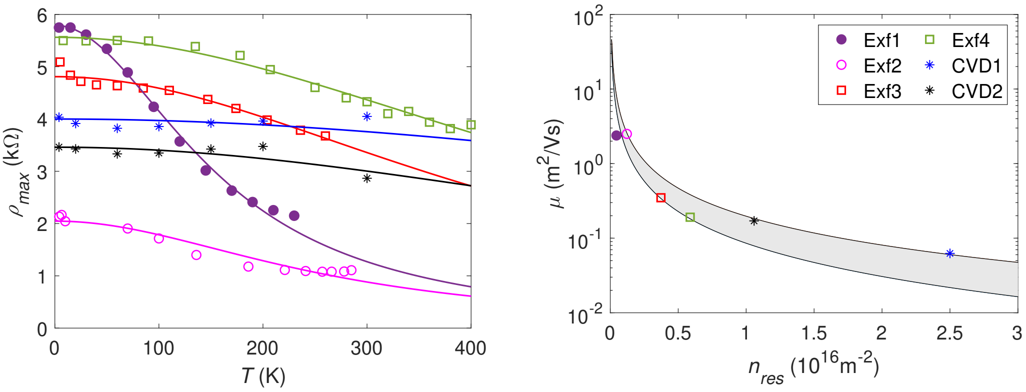

(a) (b)

Figure 3.34: (a) Maximum resistivity, ρ_{max}, as function of temperature for all 6 devices as shown by the data points, see legend in (b). The solid lines are determined using eq. (3.68). (b) The parameters μ_0, mobility at charge neutrality, and n_{res}, residual carrier density at charge neutrality, used in (a) for each device are compared to the model reported in ref. [57] within a range of impurity stand-off distances, 0.3 nm $\lesssim d_{imp} \lesssim$ 1 nm (grey shaded region).

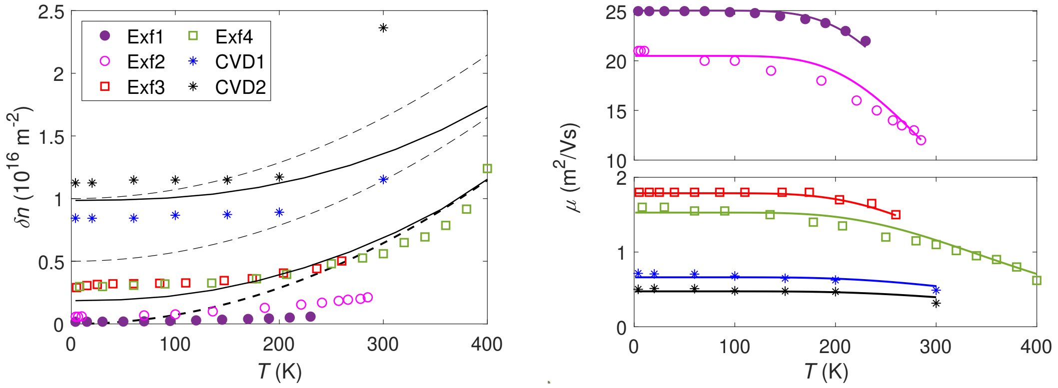

(a) (b)

Figure 3.35: (a) Temperature dependence of the carrier concentration at the FWHM of resistivity, δn. The data points are the measured $\delta n(T)$ dependences for the 6 devices; dashed lines: fits using the Fermi-Dirac model with $\delta n = 4(n_{res} + n_{TH})$ for impurity induced carrier densities, $n_{res} = 0$, 1.25×10^{15} and 2.5×10^{15} m^{-2}, and where $n_{TH} \propto T^2$ is the thermally excited carrier density; solid lines: fits using conductivity calculations including substrate impurities and phonons, see section 3.8. (b) Mobility, μ, calculated at the half maximum resistivity using eq. (3.72) as a function of temperature for all devices (solid lines), compared to the measured mobility (data points).

Substituting eq. (3.68) into eq. (3.25) we obtain the following expression:

$$\delta n = 4n_{NP}(\mu_0/\mu), \tag{3.69}$$

where μ is the mobility defined by eq. (3.25), i.e. at the half-maximum point of the resistivity. This expression indicates that δn is proportional to the total carrier density at the neutrality point and is modulated by the ratio of the mobility at the neutrality point to that at the half maximum. Assuming that the mobility is constant, $\mu_0 = \mu$, eq. (3.69) becomes $\delta n(T) = 4n_{NP}(T)$. The resulting T-dependence of δn is shown by the dashed lines in fig. 3.35a for different values of n_{res} given in the figure caption. For the low mobility devices, we find that the effect of residual charge is particularly important, resulting in the non-zero δn at low temperatures where $\delta n \approx 4n_{res}$. For the hypothetical case when $n_{res} = 0$ (no charged impurities, no e-h puddles, etc.), the FWHM would be dependant only on the thermally excited carrier density, $n_{TH} \propto T^2$, and has no fitting parameters (see the bold dashed line in fig. 3.35a starting from the $\delta n = T = 0$ origin). This simple model provides good qualitative agreement with the measured $\delta n(T)$ for the low mobility devices and at low temperatures, $T < 100$ K. However, at high temperature we find a weaker increase in $\delta n(T)$ than the one predicted by the relation $\delta n(T) = 4n_{NP}(T)$. This suggests that the electron mobility may vary significantly in the vicinity of the Dirac point, where $|n| < \delta n/2$, i.e. $\mu_0/\mu < 1$ in eq. (3.69). By modelling the substrate scattering effects (charged impurities and substrate phonons) at a finite distance from the graphene plane, we find that $\mu_0/\mu < 1$ (see fig. 3.33c). The results for δn calculated from fig. 3.33b, where the effects of charged impurities and phonons on mobility variations were modelled, are included in fig. 3.35a as solid lines, which are in better agreement with the measurements.

The measurements of the high mobility devices, in particular Exf1, reveal a weak $\delta n(T)$ dependence (fig. 3.35a), suggesting an even stronger relative decrease of mobility close to the Dirac point. This mobility dip at the Dirac point can be seen directly in fig. 3.31c. Our initial assumption of a gate-voltage independent mobility cannot be applied to the high mobility devices (> 10 m^2/Vs) in the vicinity of the Dirac point. Unfortunately, experimental measurements of the Hall carrier concentration and mobility have a large uncertainty at gate voltages close to the Dirac point where $|n| < \delta n/2$, due to the presence of both electron and hole carriers. Given the very weak impurity scattering, we are unable to attribute this dependence of mobility on carrier density to substrate scattering effects in the high mobility samples. Also, in section 3.1, we saw that the effect of interband scattering at $\varepsilon_F = 0$ only has a weak effect on the thermally excited carrier density. However, it is also known that high mobility quasi-ballistic devices are sensitive to the detailed electrostatics within the device and can be non-ohmic [123, 128]. Therefore, changes in the applied bias voltage dropped across the ballistic transport regions of high mobility devices can result in changes to the measured resistivity as shown in section 3.7.1.

Since we have established that the mobility calculated at the half-maximum of the charge density given by eq. (3.25) agrees closely with the measured mobility, we can use a linearised Boltzmann model to describe the temperature dependence of the mobility, $\mu(T)$. For simplicity, we consider a single relaxation time, τ_{op}, to model the optical phonon scattering, which has both a temperature and energy dependence given by

$$\begin{aligned}\frac{1}{\tau_{op}(\varepsilon,T)} \propto \Bigg[&N(\omega,T)\,|\varepsilon+\hbar\omega|\,\frac{1-f(\varepsilon+\hbar\omega,T)}{1-f(\varepsilon,T)}\\ &+(N(\omega,T)+1)\,|\varepsilon-\hbar\omega|\,\frac{1-f(\varepsilon-\hbar\omega,T)}{1-f(\varepsilon,T)}\Bigg],\end{aligned} \tag{3.70}$$

where $N(\omega,T)$ is the phonon occupation. For simplicity, we also use an energy of $\hbar\omega = 100$ meV for the high energy optical phonon modes in graphene [31, 71]. This gives an onset of phonon occupation around $T \approx 200$ K, in qualitative agreement with the measured decrease of mobility shown in fig. 3.35b. This approximates to the range of weakly dispersed, higher energy phonon modes of graphene. We make the approximation of eq. (1.53), $\mu \approx ev^2\tau(\varepsilon_F)/\varepsilon_F$, which is exact in the limit $T \to 0$. For $\varepsilon_F < \hbar\omega$, the mobility is then given by

$$\frac{1}{\mu} = \frac{1}{\mu_c} + \frac{D_{op}\sqrt{\delta n/2}}{\sinh\left(\frac{\hbar\omega}{k_BT}\right)}. \tag{3.71}$$

Here we have assumed that the carrier density $n \propto \varepsilon_F^2$ (strictly true in the limit $\varepsilon_F \gg k_BT$), and μ_c is the mobility in the low temperature limit. In eq. (3.71), D_{op} is a constant related to the optical phonon gauge field coupling strength, β_{op}, given by $D_{op} = 2\beta_{op}2\pi^{1/2}/(ev^3\rho_m)$, where ρ_m is the mass density of graphene. Substituting eq. (3.69) for δn into eq. (3.71) and solving the resulting self-consistent equation we obtain the following relation

$$\mu/\mu_0 = D_{op}^2\frac{\mu_c^2}{2}\frac{n_{NP}(T)}{\sinh^2\left(\frac{\hbar\omega}{k_BT}\right)}\left[1-\sqrt{1+\frac{2\sinh^2\left(\frac{\hbar\omega}{k_BT}\right)}{D_{op}^2\mu_c\mu_0 n_{NP}(T)}}\right]^2. \tag{3.72}$$

We have determined the values of n_{res} and μ_0 for each device from the measured ρ_{max} using eq. (3.68), see fig. 3.34. The typical value of the gauge field strength for optical phonons is $\beta_{op} \approx 12$ eV/Å [31], which gives an estimate $D_{op} \approx 1\times10^{-8}$ Vs/m. We find that a value of $D_{op} = 3\times10^{-8}$ Vs/m provides a good fit for the high mobility exfoliated graphene on hBN, while $D_{op} = 1\times10^{-7}$ Vs/m fits the lower mobility exfoliated graphene on SiO_2 and the lowest mobility CVD devices, see fig. 3.35b. These values of D_{op} are larger than the estimated value deduced from the single optical gauge field strength since, for simplicity, we use a single energy, 100 meV, for the optical phonon modes and a single average scattering rate. We note that a discrepancy exists between the values of D_{op} for the different types of graphene device. Differences between the environment of the different graphene samples, the surrounding materials, and even distances to the substrates, will affect the details of polar and remote optical phonon scattering in each sample. Stronger substrate phonon scattering in the graphene on SiO_2 which arises from the weaker screening and a lower onset energy [71] likely results in differing fitting parameters, D_{op}. In high mobility samples, the chemical potential is likely to be small even around the half maximum resistivity point. This will lead to a large additional carrier concentration from thermal excitation on top of the gate induced carrier concentration. Therefore, in addition to any differences in electrostatic environment, we expect the fitting parameter, D_{op}, to be affected by uncertainty in carrier concentration in high mobility samples, with a weaker apparent phonon coupling potentially compensating for underestimation of temperature-dependent carrier concentration, present within all methods of mobility measurement.

Our analytical model, based on scattering by charged impurities and phonons, describes and interrelates the temperature dependences of each of the transport parameters: ρ_{max}, δn and μ. It demonstrates that the resistivity of graphene at low carrier concentrations, $n < \delta n$, which is typically excluded from the data analysis due to the nonlinear $\sigma(n)$, can be analysed using a model based on Fermi-Dirac temperature broadening and impurity-induced broadening of δn.

Chapter 4

Transport in Perturbed Superlattices

4.1 Formation of Moiré Patterns

Moiré patterns form in overlapping hexagonal layers due to angular rotation and/or lattice mismatch in the size of the unit cells. Hexagonal boron nitride (hBN) is often used to protect graphene from the substrate materials (as discussed in chapter 3) or to provide a tunnel barrier [16, 129, 130]. Due to the larger lattice constant of hBN, 1.8% longer than in graphene [131], there exists Moiré patterns even without misalignment, as shown in fig. 4.1a. Rotation of the basal planes in adjacent hexagonal layers can cause further Moiré patterns, as shown in fig. 4.1b for two graphene layers. Twisted bilayer graphene can exhibit rich phenomena such as Mott insulator-like phases and ferromagnetism due to the flattening of bands and opening of band gaps [132, 133]. Superconductivity has even been observed for an angle of misalignment between the two overlapping monolayers of around 1.1°- the 'magic angle' [134].

Periodicity within the arising Moiré patterns forms a superlattice (SL) with a lattice constant which depends on the size difference and angle of rotation between the unit cells in adjacent layers. The wavelength of the Moiré pattern, which describes the spatial extent of this periodicity and the resulting SL lattice constant is [131]

$$\lambda = \frac{(1+\delta)a}{\sqrt{\left(1-\frac{\cos\phi}{1+\delta}\right)^2+\left(\frac{\sin\phi}{1+\delta}\right)^2}} \tag{4.1}$$

where a is the lattice constant of graphene and δ is the ratio of lattice mismatch ($\delta = 0$ for bilayer graphene, $\delta = 0.018$ for graphene on hBN). For large rotation angles, the SL lattice constant becomes small, such that the low energy structure within the individual layers is unchanged and the layers are effectively uncoupled.

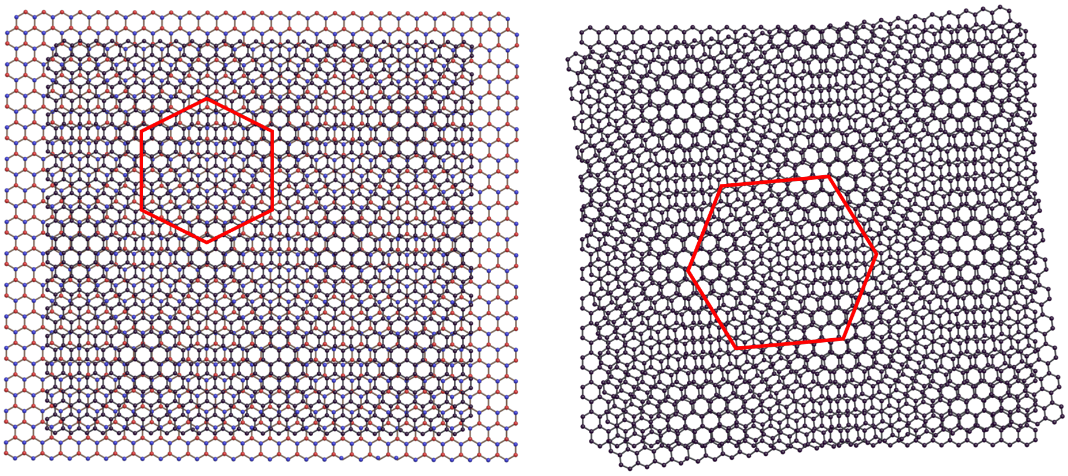
(a) (b)

Figure 4.1: Schematic diagrams showing Moiré patterns in overlapping hexagonal lattices comprising (a) graphene on hBN and (b) twisted bilayer graphene. Lattice mismatch between the hBN and graphene unit cell sizes has been exaggerated in (a) for illustrative purposes.

4.2 The Reciprocal Lattice and Brillouin Zones

The superlattice exhibits the same hexagonal translational symmetry as in graphene, except the lattice constant is larger. This means that the reciprocal lattice vectors are smaller and multiple superlattice Brillouin zones can fit into the 1st Brillouin zone (BZ) of the intrinsic graphene lattice. We denote the 6 reciprocal lattice vectors between neighbouring high symmetry lattice points $\mathbf{G}_n$, each of magnitude $2\pi/a_{SL}$ where a_{SL} denotes the SL constant.

To construct the Brillouin zones, standard geometrical procedures can be used by drawing out the Bragg planes, intersecting the vectors joining reciprocal lattice points. However, it is much more convenient to use the eigenvectors of the superlattice central equation. This will be discussed in section 4.4. Figure 4.2 provides a schematic of the first $\approx$ 24 BZs and one of the reciprocal lattice vectors, $\mathbf{G}_n$, for a reciprocal lattice constant $a_{SL} = 7.5$ nm. We will assume $a_{SL} = 7.5$ nm for the entirety of this chapter.

4.3 The Central Equation

We consider the periodic SL potential, $U(\mathbf{r}+\mathbf{R}) = U(\mathbf{r})$, where $\mathbf{R}$ is a combination of primitive lattice vectors connecting symmetric points of the real space lattice, to perturb the low-energy graphene Hamiltonian, H_0, as given by eq. (1.12), resulting in a new SL Hamiltonian, $H_0 + U(\mathbf{r})$. For a sinusoidal potential, the SL potential can be written as a Fourier series,

$$U(\mathbf{r}) = \sum_{n=1}^{6} U_{\mathbf{G}_n} e^{i\mathbf{G}_n\cdot\mathbf{r}}, \tag{4.2}$$

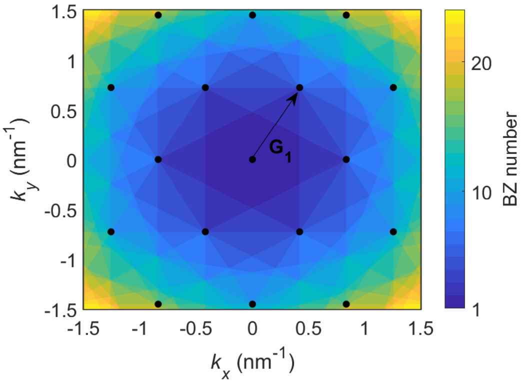

Figure 4.2: Brillouin Zones (BZs) of the superlattice created by Moiré interference with a lattice constant $a_{SL} = 7.5$ nm. The reciprocal lattice points (black dots) have hexagonal symmetry with nearest neighbours connected by the vectors $\mathbf{G}_n$, as shown for $\mathbf{G}_1$.

where $U_{\mathbf{G}_n}$ are the Fourier coefficients at the reciprocal lattice points, $\mathbf{G}_n$. We will assume lattice symmetry such that all SL potential energy Fourier coefficients are the same under translations by each reciprocal lattice vector, $U_{\mathbf{G}_n} = U_G$, corresponding to a spatially isotropic potential. For graphene on hBN, U_G was calculated as $U_G \approx 0.06$ eV using second order perturbation theory on the two coupled layers [131].

The general wavefunction for the perturbed Hamiltonian can be written as a series of plane waves with arbitrary coefficients, $C_{s,\mathbf{k}}$, over both positive and negative energies ($s = \pm 1$),

$$\Psi_{SL}(\mathbf{r}) = \sum_s \sum_{\mathbf{k}} C_{s,\mathbf{k}} e^{i\mathbf{k}\cdot\mathbf{r}}. \tag{4.3}$$

The low-energy eigenstates of graphene are given by eq. (1.14),

$$\Phi_{s,\mathbf{k}} = \frac{1}{\sqrt{2A}} \begin{pmatrix} 1 \\ s e^{i\varphi_{\mathbf{k}}} \end{pmatrix} e^{i\mathbf{k}\cdot\mathbf{r}}, \tag{4.4}$$

around a single K point in SLG. We can calculate the energies of the perturbed SL Hamiltonian directly from the Schrodinger equation,

$$\left(H_0 + \sum_n U_{\mathbf{G}_n} e^{i\mathbf{G}_n\cdot\mathbf{r}} \right) \sum_s \sum_{\mathbf{k}} C_{s,\mathbf{k}} e^{i\mathbf{k}\cdot\mathbf{r}} = \varepsilon \sum_s \sum_{\mathbf{k}} C_{s,\mathbf{k}} e^{i\mathbf{k}\cdot\mathbf{r}}, \tag{4.5}$$

given the coefficients, $C_{s,\mathbf{k}}$. To determine the energy and coefficients, we act both sides of eq. (4.5) on the spinor part of the graphene eigenstate, $\begin{pmatrix} 1 & s e^{i\varphi_k} \end{pmatrix}^{\mathrm{T}}$, and take the overlap with the full graphene eigenstate, $\Phi_{s',\mathbf{k}'}$. This results in a set of simultaneous equations,

$$\left(\varepsilon(s,\mathbf{k}) - \varepsilon_0(s,\mathbf{k}) \right) C_{s,\mathbf{k}} = \sum_{s'} \sum_{n=1}^{6} U_{\mathbf{G}_n} \frac{1}{2} \left[1 + s s' e^{(i(\varphi_{\mathbf{k}-\mathbf{G}_n} - \varphi_{\mathbf{k}}))} \right] C_{s',\mathbf{k}-\mathbf{G}_n}, \tag{4.6}$$

describing the SL energy in terms of the unperturbed graphene energy eigenvalues, $\varepsilon_0(s, \mathbf{k})$, and the eigenstate mixing, $\left\langle \Phi_{s',\mathbf{k}'} \left| U(\mathbf{r}) \right| \Phi_{s,\mathbf{k}} \right\rangle = \sum_n \delta_{\mathbf{k}',\mathbf{k}+\mathbf{G}_n} U_{\mathbf{G}_n} \left[1 + ss' \exp\left(i(\varphi_{\mathbf{k}} - \varphi_{\mathbf{k}'}) \right) \right] / 2$, due to the SL potential. The energies and coefficients are given by the eigenvalues and eigenvectors of the effective SL Hamiltonian:

$$H_{SL} = \left[\begin{array}{cccccc} \ddots & \ddots & \ddots & \ddots & \ddots & \\ & \varepsilon_0(-1, \mathbf{k} - \mathbf{G}) & U_{-1,\mathbf{k}-\mathbf{G},-1,\mathbf{k}} & U_{-1,\mathbf{k}-\mathbf{G},+1,\mathbf{k}} & U_{-1,\mathbf{k}-\mathbf{G},+1,\mathbf{k}-\mathbf{G}} & \\ & U_{-1,\mathbf{k},-1,\mathbf{k}-\mathbf{G}} & \varepsilon_0(-1, \mathbf{k}) & U_{-1,\mathbf{k},+1,\mathbf{k}} & U_{-1,\mathbf{k},+1,\mathbf{k}-\mathbf{G}} & \\ & U_{+1,\mathbf{k},-1,\mathbf{k}-\mathbf{G}} & U_{+1,\mathbf{k},-1,\mathbf{k}} & \varepsilon_0(+1, \mathbf{k}) & U_{+1,\mathbf{k},+1,\mathbf{k}-\mathbf{G}} & \\ & U_{+1,\mathbf{k}-\mathbf{G},-1,\mathbf{k}-\mathbf{G}} & U_{+1,\mathbf{k}-\mathbf{G},-1,\mathbf{k}} & U_{+1,\mathbf{k}-\mathbf{G},+1,\mathbf{k}} & \varepsilon_0(+1, \mathbf{k} - \mathbf{G}) & \\ & \ddots & \ddots & \ddots & \ddots & \ddots \end{array} \right], \tag{4.7}$$

where $U_{s',\mathbf{k}',s,\mathbf{k}} = \left\langle \Phi_{s',\mathbf{k}'} \left| U(\mathbf{r}) \right| \Phi_{s,\mathbf{k}} \right\rangle$. The matrix, eq. (4.7), extends over all reciprocal lattice points, $\mathbf{G}$, described by all possible linear combinations of reciprocal lattice vectors, $\mathbf{G}_n$. However, it can be truncated at a maximum number of reciprocal lattice points to accurately evaluate the energy. Typically, to model the energy landscape within a given BZ, it is only necessary to include the nearest neighbour reciprocal lattice points.

The matrix, eq. (4.7), also provides a fast and efficient way to construct the BZs. Setting all off-diagonal elements, $U_{s',\mathbf{k}',s,\mathbf{k}}$, to 0 simply returns the graphene eigenenergies. We can evaluate the BZ by finding the eigenvalue corresponding to the energy about the central reciprocal lattice point, $\varepsilon_0(+1, \mathbf{k})$. This can easily be located from the corresponding eigenvector, since, for the simple diagonal matrix the eigenvectors will not change. The electronic energy in the n-th BZ corresponds to the n-th energy band when translated back into the 1st BZ. Therefore, for the n-th BZ, the eigenvalue $\varepsilon_0(+1, \mathbf{k})$ will be the n-th smallest of the positive ($s = +1$) eigenvalues.

4.4 Construction of the Energy Bands

Two representations can be used to model the energy subbands of the superlattice: reduced zone and extended zone. The extended zone describes the states over an unconstrained range of wavevectors, $\mathbf{k}$, relative to $\mathbf{k} = 0$. In this representation, the eigenstates in the n-th BZ are given by those corresponding to the n-th smallest eigenenergy. Due to the periodicity and symmetry of the lattice, all physical states can be traced back into the first BZ under translation by reciprocal lattice vectors. Therefore, we can restrict $\mathbf{k}$ to values only within the first BZ. Then, the first 'n' eigenenergies form the first 'n' subbands. This is the reduced zone representation.

The carrier density, n, is calculated numerically by summing over the occupancy of

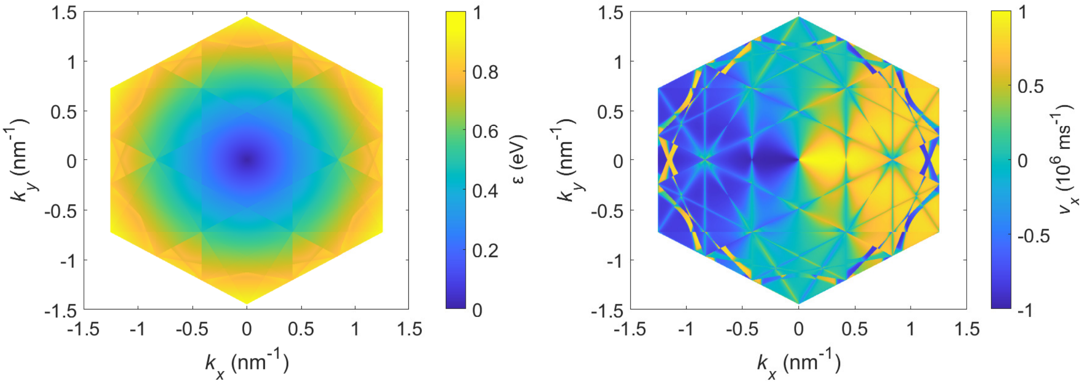

(a) (b)

Figure 4.3: (a) Energy band structure, ε, and (b) group velocity in the x direction, v_x, in the extended zone representation of momentum space. Results shown in both (a) and (b) are taken from the conduction band ($\varepsilon > 0$). The superlattice potential is $U_G = 0.05$ eV.

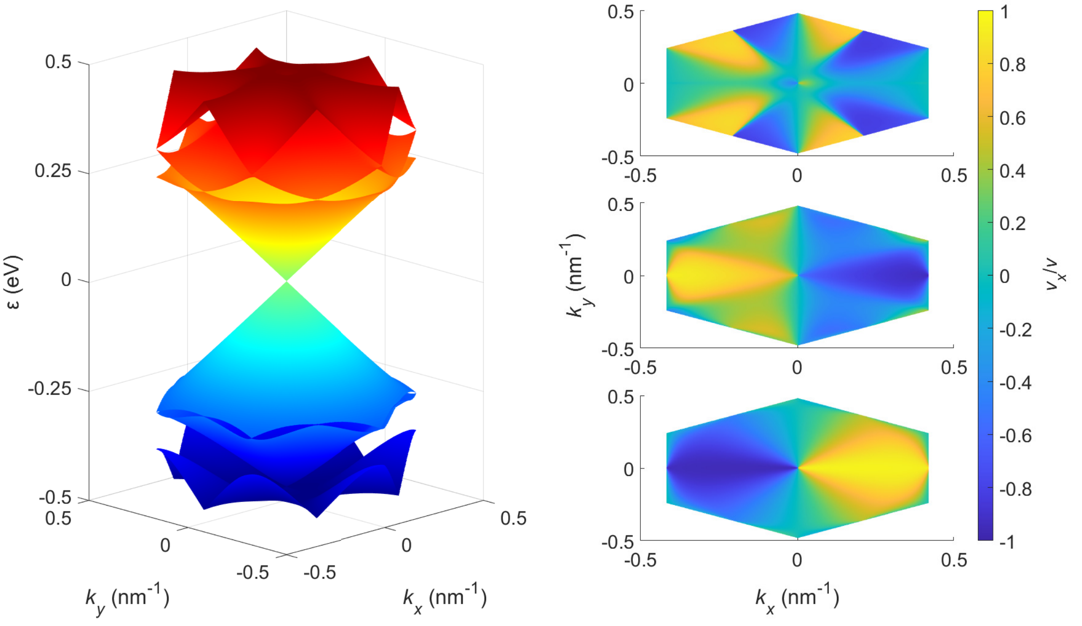

(a) (b)

Figure 4.4: (a) Energy band structure, ε, and (b) group velocity in the x direction, v_x, in the reduced zone representation of momentum space. Results shown in (b) are taken from the first three subbands of the conduction band ($\varepsilon > 0$), with the bottom axes showing the first (lowest energy) subband. The superlattice potential is $U_G = 0.05$ eV.

all k states, discretised into cells, α,

$$n = \frac{4}{(2\pi)^2}\sum_{\alpha} f(\varepsilon_{\mathbf{k}_\alpha})\Omega_\alpha \tag{4.8}$$

as in eq. (2.91), where Ω_α is the area of cell α in k space.

Since the effective SL Hamiltonian, eq. (4.7), is Hermitian, the group velocity in the x-direction is

$$v_x(s,\mathbf{k}) = \frac{1}{\hbar}\left\langle s,\mathbf{k}\left|\frac{\partial}{\partial k_x}H_{SL}\right|s,\mathbf{k}\right\rangle, \tag{4.9}$$

given the eigenstate $|s,\mathbf{k}\rangle$ of the matrix (4.7).

Figure 4.3 shows the energy band structure and velocities in the conduction band ($s = +1$) within the extended zone representation. Figure 4.4a shows the first 3 subbands in both the conduction ($s = +1$) and valence ($s = -1$) bands, and fig. 4.4b shows the corresponding velocities in the first 3 conduction subbands. The SL potential opens band gaps between the subbands, with the largest gap between the 1st and 2nd conduction subbands appearing at the K points on the SL Brillouin zone. At the M points, $\mathbf{k} = \mathbf{G}_n/2$, the gap closes, forming secondary Dirac points. In the SL potential, electrons have to tunnel through the energy gaps between subbands in order to accelerate up the conduction/valence bands. Also, flattening of the bands towards the subband gaps causes the initially relativistic electrons to gain an effective mass. This results in a reduced group velocity, as shown in fig. 4.4b.

At the BZ edges, where the bands are most deformed, the density of states (DoS) is perturbed relative to that of SLG. Flattening of the subbands towards the band gaps causes initial peaks in the DoS with dips in between due to the energy gaps, as shown in fig. 4.5a. Figure 4.5b shows the effect that this has on the carrier density for varying chemical potential. The carrier density is increased with increasing SL potential, U_G, over the range of chemical potentials considered, due to the flattening of the bands into a lower energy range, and there exists plateaus at chemical potentials corresponding to the dips in the density of states.

4.5 Diffusive Transport

To model diffusive transport within the SL band structure, we will adapt the MC method (section 2.5.1) for electron acceleration through the SL subbands with a single source of electron scattering. We will use the reduced zone representation, which allows us to easily Umklapp scatter electrons within the first BZ and move them up or down the bands at given tunnelling points.

4.5.1 Momentum Relaxing Scattering

Before we discuss the details specific to modelling transport through the SL subbands, we first characterise the scattering. For now, we are mostly concerned with the effects of

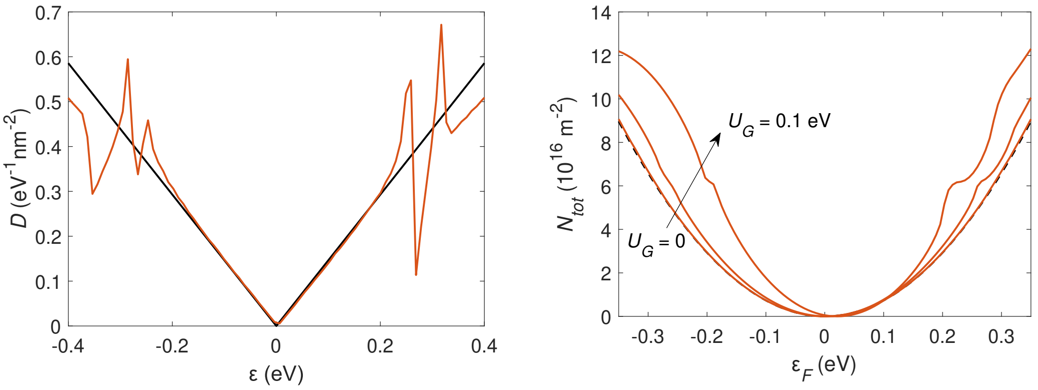

(a) (b)

Figure 4.5: (a) Energy density of states, $D(\varepsilon)$, for a superlattice potential $U_G = 0.05$ eV. (b) Total carrier density, $N_{tot} = n + p$, calculated as a function chemical potential, ε_F, for varying superlattice potentials, $U_G = 0$, 0.01, 0.05 and 0.1 eV.

the SL perturbations. Therefore, we want to use the simplest form of scattering possible. We use an energy-independent scattering rate given by $\Gamma = 1/\tau$, as in section 3.2. Since we do not directly include any inelastic scattering, we relax the electron energy to a k-state from the initial Fermi-Dirac distribution upon scattering to avoid uncontrolled Joule heating of the electron distribution. This replicates the momentum relaxation time approximation [30],

$$\left(\frac{\partial f(t,\mathbf{k})}{\partial t}\right)_{coll} \approx -\frac{f(t,\mathbf{k}) - f(t=0,\mathbf{k})}{\tau} \tag{4.10}$$

made in the linearised Boltzmann (LB) equation of conductivity, eq. (1.53).

4.5.2 Umklapp Scattering

Umklapp scattering describes the translation of the electron wavevector by one reciprocal lattice vector. Each k-state on the BZ edge is equivalent to a k-state on the opposing edge, connected by a reciprocal lattice vector, where the reciprocal space distance between them is $2\pi/a$, as shown in fig. 4.6. The electron wavevector, $\mathbf{k}'$, after Umklapp scattering from a state $\mathbf{k}$ on the BZ boundary is

$$\mathbf{k}' = \mathbf{k} - 2\mathbf{K}_{\Gamma\mathrm{M}} \tag{4.11}$$

where $\mathbf{K}_{\Gamma\mathrm{M}}$ is the vector between the Γ point and the closest M point.

Due to the lattice symmetry, an electron accelerated continuously through k-space without Umklapp scattering experiences the same changes in energy and velocity as if it is continuously accelerated up to the edge of the first BZ and Umklapp scattered back. Therefore, all of the physical properties can be considered within just the first BZ.

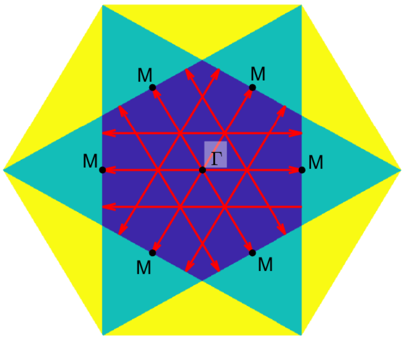

Figure 4.6: Schematic showing Umklapp scattering (red arrows) across the 1st Brillouin zone (purple) by the reciprocal lattice vector $2\mathbf{K}_{\Gamma\mathrm{M}}$ where $\mathbf{K}_{\Gamma\mathrm{M}}$ connects the closest M point to the Γ point. Black dots show the positions of the M and Γ points, as labelled. Turquoise and yellow zones show the second and third Brillouin zones, respectively.

4.5.3 Monte Carlo for a Multi-Band Superlattice

Here, we describe the adaptations made to algorithm outlined in section 2.5.1 to model transport through the subbands.

As described in section 2.5.1, the grid of cells used to quantify electron occupation should be shifted along with the particles under the uniform, field-induced acceleration in order to ensure that the PEP is obeyed. We will call this the ‘floating grid’. To avoid solving eq. (4.7) at each time step and for each particle, we initialise all parameters (energy, velocity, BZ edges, subband energy gaps) on a ‘static grid’, equal to the floating grid at $t = 0$. When the floating grid cells have shifted by more than half the cell length from their initial positions, the grid is ‘re-calibrated’ i.e. moved back by one cell length. This process ensures that the floating grid cells remain centered on their corresponding position relative to the static grid, which crucially tells us where the electrons are with respect to the BZ edges. To reduce temporal noise in the measurable parameters, such as velocity, a third static grid can be used with increased resolution, allowing electrons within a given floating cell to have different velocities.

To ensure that the floating grid does not deviate too far from the static grid, the time step of acceleration, Δt_{acc}, used should be constrained to

$$\Delta t_{acc} \leq \frac{\hbar \Delta k_x}{2eE}, \tag{4.12}$$

where Δk_x is the cell size in the x direction (the direction of the applied electric field, E). Therefore, it may be necessary to use two time steps: one for scattering, typically $\Delta t_s = 0.2\tau$, and one for acceleration, Δt_{acc}. The time step of acceleration, Δt_{acc}, is chosen as the largest possible value which satisfies both eq. (4.12) and $\Delta t_s = n_{acc}\Delta t_{acc}$, where n_{acc} is an integer. All physical parameters are calculated at each scattering time step.

At any acceleration time step for which the floating grid is re-calibrated, any elec-

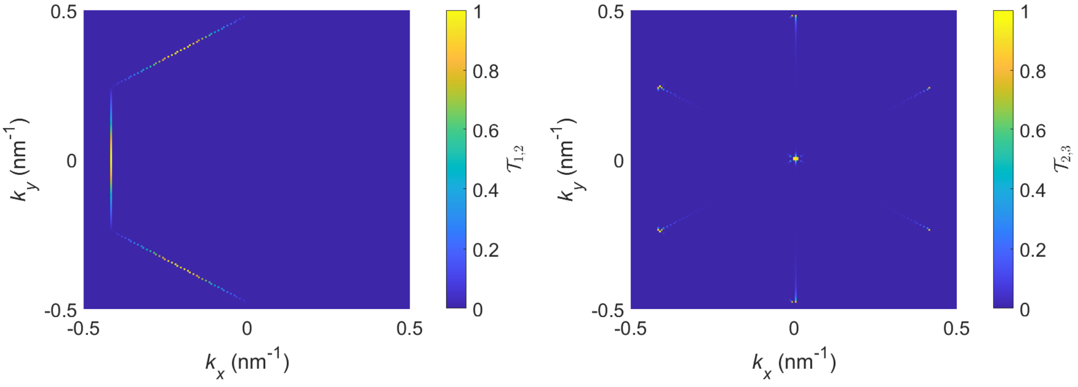

(a) (b)

Figure 4.7: Tunnel points in momentum (k) space used in the Monte Carlo simulations for tunnelling between (a) the first and second subband and (b) the second and third subband. The colour bars show the probability of tunnelling, $\mathcal{T}$, at each tunnel point for an SL potential $U_G = 0.01$ eV.

trons that pass into a cell outside of the BZ are Umklapp scattered back into the BZ, according to eq. (4.11).

As the electrons accelerate through the bands, they can also tunnel into adjacent bands. Typically, this occurs at the points of minimum energy gap. We define such points as ‘tunnel points’. They lie at the points in k-space where the eigenstate of eq. (4.7) with $U_G = 0$, corresponding to the energy within the subband, change. This corresponds to the points at the edges of the BZs in the extended zone representation. Care should be taken when locating the tunnel points to ensure that they are chosen only at the point where the eigenstates change in the direction of the applied field. This ensures that the direction of electron acceleration through bands is satisfied. At each acceleration time step for which the floating grid is re-calibrated, electrons within a cell corresponding to a tunnel point are moved up or down the subbands based on the following process: if $\varrho < \mathcal{T} = \mathcal{T}_{ZK}(\delta\varepsilon)$, where $0 \leq \varrho \leq 1$ is a uniformly selected random number, $\mathcal{T}_{ZK} = \exp\left(-\pi\delta\varepsilon^2/(4\hbar veE)\right)$ is the Zener-Klein tunnel probability and $\delta\varepsilon$ is the minimum energy difference between bands within the cells of the tunnel points, then the electron is moved between subbands. The transmission probability, $\mathcal{T}$, at all tunnel points between the first and second and second and third subbands in the conduction band are shown in fig. 4.7 for $U_G = 0.01$ eV. The transmission probability is highest at the points of smallest band gap: the M points between subbands 1 and 2 and the K and Γ points between subbands 2 and 3. The energy gap $\delta\varepsilon$ is found with increased resolution around the tunnel points, ensuring that $\mathcal{T} \approx 1$ at all tunnel points for $U_G = 0$.

4.5.4 Diffusive Results

Figure 4.8a shows the initial distribution of simulated particles for a SL potential $U_G = 0.05$ eV, arranged in accordance with the Fermi-Dirac distribution at $T = 10$ K. We

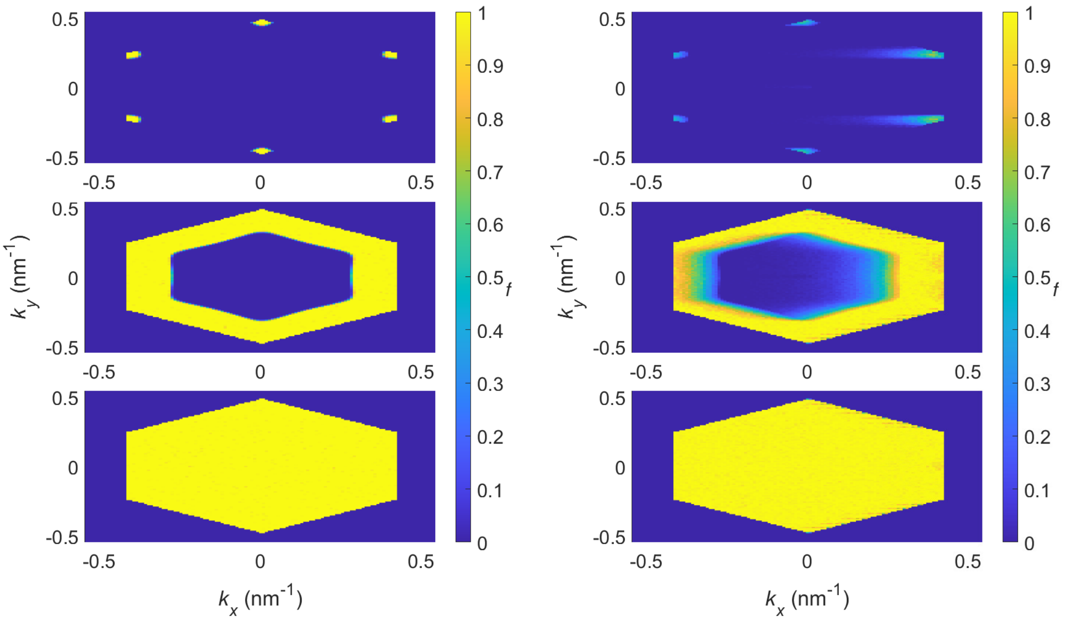

(a) (b)

Figure 4.8: Simulated electron momentum distribution, $f(\mathbf{k})$, over the first three conduction subbands (bottom to top) for (a) $t = 0$ i.e. the initial Fermi-Dirac distribution and (b) $t \to \infty$ i.e. the steady-state distribution. Results are obtained from the Monte Carlo simulation for diffusive scattering with a momentum relaxation time, $\tau = 1$ ps. The SL potential is $U_G = 0.05$ eV and applied electric field strength is $E = 5 \times 10^4$ V/m.

have used this small finite temperature to ensure continuity over the discretised grid. The usual Fermi circle is distorted by the perturbed energy bands, resulting in the flat edges seen in the second band. Figure 4.8b shows the steady-state distribution under an applied field, $E = 5 \times 10^4$ V/m, with a scattering rate of $\tau = 1$ ps. The distribution is shifted in the negative k_x direction by the applied field, with Umklapp scattering at the BZ edges and tunnelling between subbands, most noticeable at the K points in the third subband in this example.

Figure 4.9 shows the results of conductivity for varying chemical potential obtained from the MC simulation and compared to the results of the low-field LB approximation, eq. (1.53), for SLG (i.e. $U_G = 0$):

$$\sigma = \frac{e^2 \varepsilon_F \tau}{\pi \hbar^2}. \tag{4.13}$$

If the chemical potential is such that the extent of the initial distribution is close to the BZ boundary, then Umklapp scattering can suppress the bulk acceleration of the electron distribution when the subband gaps are large: electrons Bloch oscillate, confined within the first subband. Coupled with the reduction in electron velocity around the edge of the 1st BZ, this results in large dips in the conductivity around energies corresponding to the M points, as shown in fig. 4.9. As U_G increases, the

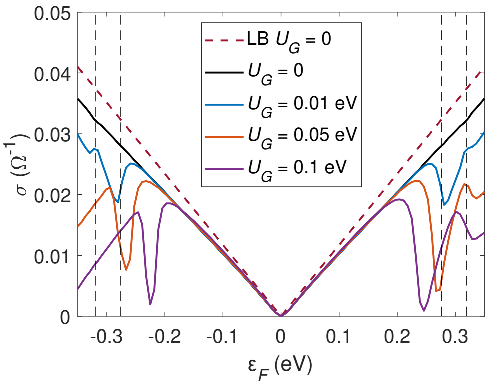

Figure 4.9: Conductivity, σ, calculated as a function chemical potential, ε_F, for varying superlattice potentials, U_G. Results are obtained from the Monte Carlo simulation for diffusive scattering with a momentum relaxation time, $\tau = 1$ ps, and acceleration under an applied electric field of strength $E = 1 \times 10^4$ V/m. The dashed red line shows the results of the linearised Boltzmann conductivity, eq. (1.53), for graphene (i.e. $U_G = 0$). The vertical dashed black lines show the energy at the M and K points in the SL, assuming $\varepsilon \approx \hbar v k$, where $k_M = 0.42$ nm^{-1} and $k_K = 0.48$ nm^{-1}.

position of the BZ boundary (i.e. M and K points) in energy space is decreased due to the flattening of the bands, resulting in a shift in the conductivity dip with respect to ε_F. Since only carriers on the fringe of the distribution contribute to the drift velocity, the conductivity increases again as the chemical potential is increased past the first BZ. As the SL potential, U_G, is increased, the effect of subband confinement and reduced group velocity causes larger suppression of conductivity at the BZ edge.

4.6 Ballistic Transport

To calculate the conductivity in the limit of no electronic scattering, we use the Landauer equation (3.50) and numerically integrate over a cartesian grid in k-space. Assuming an applied electric field, E, in the x direction, momentum in the y direction is conserved. Electrons tunnelling between any two subbands will be required to tunnel through an energy gap, unless directly at the monolayer Dirac point ($k_y = 0$) or any of the secondary SL Dirac points. For a given k_y, we define the minimum energy gap between neighbouring bands $\Delta(k_y)$. Then, the Zener-Klein transmission coefficient between any two bands/subbands is

$$\mathcal{T}_{ZK}(k_y) = \exp\left(-\frac{\pi\Delta(k_y)^2}{4\hbar v e E}\right). \tag{4.14}$$

To perform a continuous integral over k_x and k_y, we use the extended zone representation. This also means that constraint on conservation of momentum, $\hbar k_y$, can be easily implemented without the need to Umklapp transform the crystal momentum, $\hbar\mathbf{k}$. Usually, the Landauer integral is restricted to $k_x > 0$ i.e. only right going carriers, in

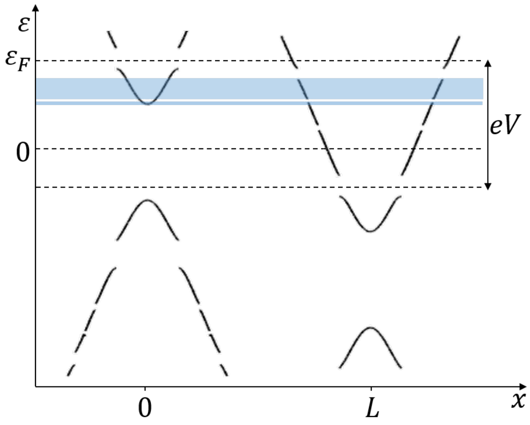

Figure 4.10: Energy, ε, band structure taken as a cross-section through the K point of the SL Brillouin zone ($k_y = 0.24$ nm^{-1}) with a potential difference V applied in the x direction over a length L. The blue bands show the energy bands through which electron transport can be facilitated for the given example chemical potential, ε_F.

the direction of induced transport. In the SL band structure, there can exist right going carriers with $k_x < 0$ due to the curvature at the band edges (see fig. 4.3b). Therefore, we integrate over all k-space, with the imposed condition $v_x > 0$ on included k-states.

We impose a second constraint on k-states to ensure energy conservation. Within each subband, the integral is performed over all energy states, $\varepsilon(k_x, k_y)$, for which there exists a subband with energy, $\varepsilon'(k_y)$, at the same k_y, such that $\varepsilon(k_x, k_y) = \varepsilon'(k_y) - eV$ as shown in fig. 4.10.

The transmission coefficient for a given k-state depends on the position of the energy state $\varepsilon'(k_y)$ within the energy band structure. If ε' and ε are in the same subband then $\mathcal{T} = 1$ and if they are in neighbouring subbands then $\mathcal{T} = \mathcal{T}_{ZK}$. It is possible that the states are separated by more than one subband, as in fig. 4.10, in which case the transmission coefficient is the product of all intermediate probabilities between the two subbands.

The limits of the integral in k_y and k_x can be constrained, depending on the occupancy, $f(k_x, k_y)$. For $T = 0$, only energy states up to the chemical potential, ε_F need to be included for a given k_y. For each k_x, we also need to ensure that all states up to $\varepsilon_F + eV$ are included. This imposes the minimum limits $k_y = \varepsilon_F/\hbar v$ and $k_x = (\varepsilon_F + eV)/\hbar v$ on integration over k_y and k_x, respectively. Here, we consider a range of $\varepsilon_F \leq 0.35$ eV and $V \leq 0.4$ V, encompassing the first 8 BZs.

4.6.1 Ballistic Results

When the chemical potential lies around the subband gaps, the conductivity is suppressed due to the tunnel barriers, the reduced window of energy-conserving states and reduced group velocity. As described in section 4.5.4, the first subband gaps lie around the edge of the first BZ. Figure 4.11 shows the conductivity for varying chemical potential with different SL potential energies, U_G. The first dip in conductivity

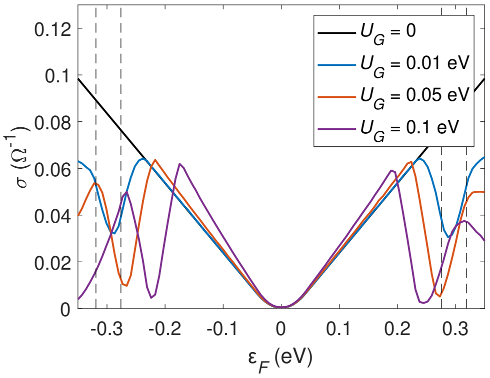

Figure 4.11: Conductivity, σ, calculated as a function chemical potential, ε_F, for varying superlattice potentials, U_G. Results are obtained from the Landauer equation with Zener-Klein limited tunnelling. The potential difference is $V = 0.04$ V, corresponding to an electric field of strength $E = 1 \times 10^4$ V/m over a length $L = 4$ µm. The vertical dashed black lines show the energy at the M and K points in the SL, assuming $\varepsilon \approx \hbar v k$, where $k_M = 0.42$ nm^{-1} and $k_K = 0.48$ nm^{-1}.

occurs between the M and K points in the SLG energy, as found for diffusive scattering (fig. 4.9).

4.7 Differential-Conductance

It is clear that, when the most energetic electrons within the SL exist at the edges of the BZ, there exists a dip in conductivity caused by the SL potential, U_G. This leads to an interesting interplay between the chemical potential, ε_F, and the applied field, E, which can even result in a regime of negative differential conductance (NDC).

Under diffusive acceleration, the electron distribution is shifted by an amount $\delta k \approx eE\tau/\hbar$. Assuming small SL energy perturbations, this corresponds to a shift in the energy at the fringe of the distribution by $\delta\varepsilon_{diff} \approx sevE\tau$. Figure 4.12 shows the variation of conductivity and differential conductivity with both chemical potential and applied field for diffusive limited scattering with relaxation time, $\tau = 1$ ps. The position in energy at which the conductivity starts to dip, deviating from that of SLG, is given by the point at which the fringe of accelerated electrons reaches the BZ edge:

$$\varepsilon_F + sevE\tau \approx s\varepsilon_M, \tag{4.15}$$

where s denotes the conduction/valence band ($s = +1$ for $\varepsilon_F > 0$ and $s = -1$ for $\varepsilon_F < 0$).

For larger relaxation time between scattering events, electrons are accelerated further by the electric field, reducing the extent of the 'SLG-like' zone, as shown in fig. 4.13 for $\tau = 3$ ps.

For ballistic transport, the distribution is not limited by the scattering time, τ, (or

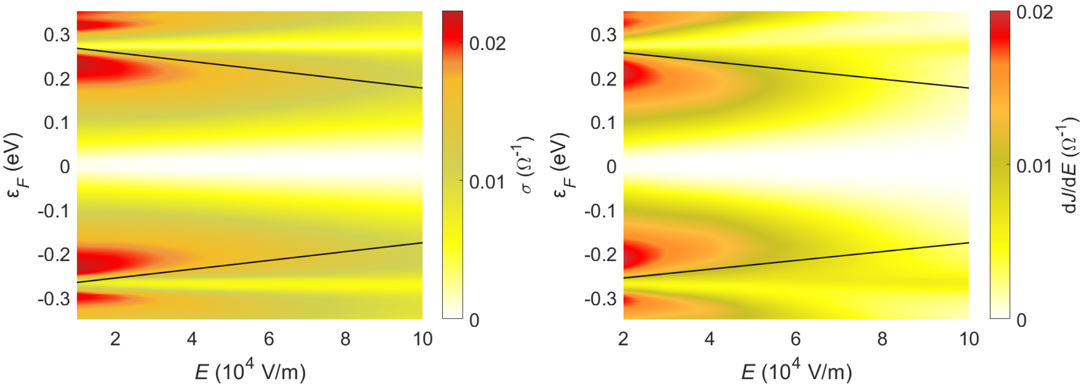

(a) (b)

Figure 4.12: (a) Conductivity, σ, and (b) differential conductivity, $\mathrm{d}J/\mathrm{d}E$, where $J = \sigma E$ is the current density, calculated as a function chemical potential, ε_F, and electric field strength, E. Results are obtained from the Monte Carlo simulation for diffusive scattering with a momentum relaxation time, $\tau = 1$ ps, and a superlattice potential $U_G = 0.05$ eV. The black lines show the estimated chemical potential required for the extent of the charge carrier ensemble momentum distribution to reach the M point of the first Brillouin zone for a given applied field strength.

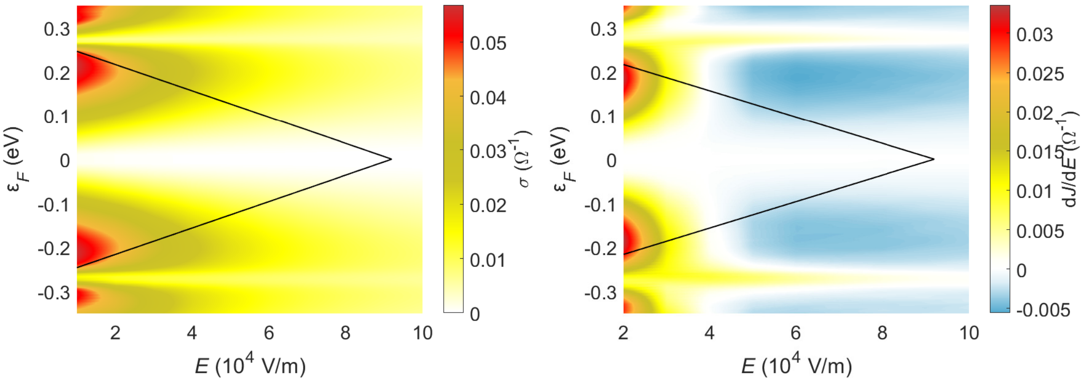

(a) (b)

Figure 4.13: (a) Conductivity, σ, and (b) differential conductivity, $\mathrm{d}J/\mathrm{d}E$, where $J = \sigma E$ is the current density, calculated as a function chemical potential, ε_F, and electric field strength, E. Results are obtained from the Monte Carlo simulation for diffusive scattering with a momentum relaxation time, $\tau = 3$ ps, and a superlattice potential $U_G = 0.05$ eV. The black lines show the estimated chemical potential required for the extent of the charge carrier ensemble momentum distribution to reach the M point of the first Brillouin zone for a given applied field strength.

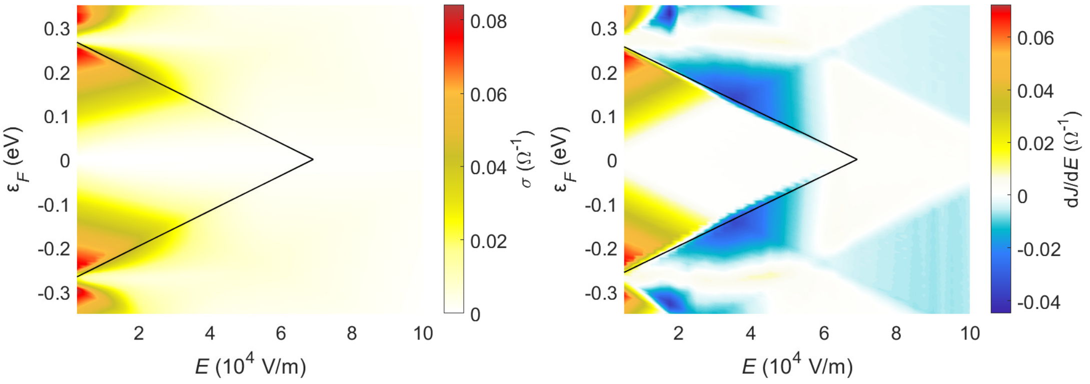

(a) (b)

Figure 4.14: (a) Conductivity, σ, and (b) differential conductivity, $\mathrm{d}J/\mathrm{d}E$, where $J = \sigma E$ is the current density, calculated as a function chemical potential, ε_F, and electric field strength, E. Results are obtained from the Landauer equation with Klein-Zener limited tunnelling and a superlattice potential $U_G = 0.05$ eV. We have assumed that $E = V/L$, where V is the potential difference across the device and $L = 4$ µm is the device length. The black lines show the estimated chemical potential required for the extent of the charge carrier ensemble momentum distribution to reach the M point of the first Brillouin zone for a given applied field strength.

equivalently, the mean free path l_s) but rather the distance between the contacts, L. The shift in the internal electron energy is $\delta\varepsilon_{ball} \approx eEL = eV$. As shown in fig. 4.10, the energy states on the RHS are shifted down by eV. Therefore, for transport within the conduction band, the point at which the conductivity deviates from that of SLG is given by the point at which the chemical potential, ε_F, aligns with the edge of the BZ on the RHS, $\varepsilon_M - eV$. Allowing also for hole transport, $\varepsilon_F < 0$, gives

$$\varepsilon_F + seV \approx s\varepsilon_M, \tag{4.16}$$

as shown in fig. 4.14a.

At the boundary between diffusive and ballistic transport, given by $l_s = L$, where $l_s = v\tau$ is the scattering mean free path and L is the device length, eqs. (4.15) and (4.16) become equivalent. We can reformulate eqs. (4.15) and (4.16) to give the chemical potential at which accelerated electrons reach the SL subband gap over both diffusive and ballistic transport regimes:

$$\varepsilon_F + seE\min(l_s, L) \approx s\varepsilon_M. \tag{4.17}$$

In both the diffusive and ballistic cases, for a given electric field, there is an initial drop in the conductivity at a chemical potential given by eq. (4.17), with a local minimum around $\varepsilon_F \approx s\varepsilon_M$. As the field is increased, the position of the onset of this dip in conductivity decreases, as shown by the black lines in figs. 4.12a, 4.13a and 4.14a. This causes a decrease in the differential conductivity as shown in figs. 4.12b, 4.13b and 4.14b. As the relaxation time decreases, through to the ballistic limit, the position this onset conductivity drop starts to decrease sharply with increasing applied field. This causes a negative differential conductance at low fields, as shown in figs. 4.13b and 4.14b. This interesting phenomenon, where the current decreases with increasing applied electric field, can be explained physically by the increased number of Bloch oscillating carriers. As the field is increased, more carriers are Umklapp scattered across the BZ into states with opposing velocity. It can also be understood, in the ballistic case, by the lowering of available energy states between the drain lead (i.e. RHS of fig. 4.10) and the source lead (i.e. LHS of fig. 4.10) over the transport window ($\varepsilon_F - eV < \varepsilon < \varepsilon_F$) due to acceleration into or from an area with low density of states, effectively 'blocking' the current flow.

Chapter 5

Modelling Conductivity in Deposited Graphene Flakes

5.1 Percolation of Current in Graphene Flake Networks

Additive manufacturing provides promising new methods to manufacture functional devices comprising electrically conducting graphene networks [20, 135]. Generally, liquid-exfoliated graphene flakes are deposited onto a substrate via inkjet. The ink is made up of the graphene flakes, a liquid solvent and additional surfactants to enhance the dispersion of the graphene flakes. Alternatively, graphene oxide flakes are hydrophilic and can be dispersed in water without the need for additional surfactants [136, 137]. After deposition, the resulting structure is post-processed. This usually requires thermal or photonic annealing, to evaporate the solvent [20, 138]. In the case of graphene oxide flakes, UV reduction of the flakes is also required, which can often lead to the presence of atomic defects [139, 140].

Here, we consider the dynamics of current flow through a network of deposited graphene flakes. We will define the microscopic tunnel current and see how flake positioning affects the macroscopic properties of printed graphene electronics. We model the conductive characteristics of the network of flakes by first using Monte Carlo simulations of flake positioning and then analysing the percolation networks between flakes.

5.1.1 Inter-Flake Tunnel Current

We use the Simmons equation [141], derived for tunnelling between two similar metallic electrodes, for the current between two graphene flakes, I_{ff}. In the limit of a small potential difference between flakes, $eV_{ff} \ll \phi_0$, the Simmons equation reduces to

$$I_{ff} \propto A_{ff} e V_{ff} \exp(-\alpha s) \tag{5.1}$$

where A_{ff} is the areal overlap of the two flakes, V_{ff} is the potential difference between flakes, s is the normal distance between flakes, $\alpha = (2/\hbar)\sqrt{2m\phi_0}$ is the tunneling constant, m is the mass of the tunnelling electron and ϕ_0 is the work function. We take m to be the free electron mass and the work function $\phi_0 = 1$ eV. This value of the work function is comparable to that found using Simmons fits for tunnelling between two graphene sheets [142–144]. Note that, for this value of ϕ_0, the approximation of a constant barrier height ($\phi_0 \gg eV_{ff}$) is reasonable because the drain-source potential is $\lesssim 1$ V, and the channel is made up of $> 10{,}000$ flakes (channel length approx. 4000 μm, flake diameter approx. 0.057 μm) for all measurements used in this study [19, 20]. The key exponential dependence on distance, s, in eq. (5.1) results from the WKB approximation for the tunnelling probability [141, 145]. The constant of proportionality in eq. (5.1) could be temperature dependant, as described by the Arrhenius equation for hopping transport, eq. (1.55).

5.1.2 Flake Resistor Network Model

We consider a distribution of parallel flakes, each of volume $\mathcal{V}_f = 50 \times 50 \times 1.95$ nm^3, consistent with the mean area and thickness of flakes used in the inks [19, 20]. We define the packing factor, PF $= \mathcal{V}_{gr}/\mathcal{V}_d$, as the ratio of the total volume occupied by graphene flakes, $\mathcal{V}_{gr} = N\mathcal{V}_f$, where N is the number of flakes, to the total volume of the device, $\mathcal{V}_d$.

Two methods can easily be employed to generate a ‘pseudo-random’ simulated distribution of flakes: randomly dispersed flakes and planes of flakes.

In the case of randomly dispersed flakes, the flakes are inserted into a cuboid space individually with randomly generated positions and a constraint to ensure that no two flakes occupy the same space. Examples of randomly distributed flakes for two different packing factors can be found in figs. 5.2a and 5.2b.

To build the distribution of flakes using planes, we start with a perfectly ordered, close-packed arrangement of flakes where each flake has a fixed separation, $\langle d\rangle$, from all of its 6 neighbours in all directions, x, y and z. For a given printed layer thickness, $\langle d\rangle$ will specify the number of distinct planes that the flakes occupy, or vice versa. Next, we randomize both the overlap area between adjacent flakes on different planes and the distance between individual flakes, d, which is constrained to lie between 0 and $2\langle d\rangle$. The PF can then be reduced by randomly removing flakes. In this representation, the interflake separation is controlled and the gaps are in-plane. Not only does this allow us to achieve more ordered and dense structures, it may also better represent the physical system: where flakes sit and fold tightly on top of one another in the z direction with gaps forming in the x-y plane [135]. Examples of flake distributions for different numbers of planes (i.e. different mean separation distances, $\langle d\rangle$) can be found in figs. 5.2c and 5.2d. Inserting flakes in planes allows us to reach higher values of packing factors, where a certain amount of ordering is required to fit the flakes into a given volume.

We define the tunnelling distance, s, between two flakes as $s = d + d_{vdW}$ where d is the distance between two modelled flakes and $d_{vdW} = 0.335$ nm is the van der Waals

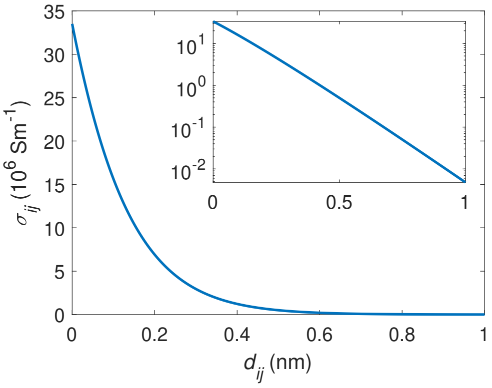

Figure 5.1: Conductivity of tunnel junction, σ_{ij}, between two flakes versus inter-flake separation, d_{ij}.

distance [146, 147]. This ensures that when $\langle d \rangle = 0$, i.e. PF = 1 and the space is completely full of flakes, then the van der Waals distance between contacting flakes is still accounted for.

A hard-core soft shell model is employed to define the adjacency of any two flakes [148, 149]. The hard-core is defined by the physical dimensions of the flakes, whilst the soft-shell protrudes the hard core by a length d_s. Flakes with intersecting shells are considered to be adjacent and a current is allowed to flow between them. This essentially enforces a maximum tunnelling distance of $2d_s$, which should be chosen with care, such that the current between flakes (5.1) is insignificant at distances $d > 2d_s$. Using eq. (5.1), with the computationally enforced soft-shell, the conductance between two flakes i and j is

$$G_{ij} = \begin{cases} e\zeta_0 A_{ij} \exp(-\alpha d_{ij}) & \text{if } d_{ij} < 2d_s \\ 0 & \text{if } d_{ij} \geq 2d_s \end{cases}, \tag{5.2}$$

where the van der Waals distance, d_{vdW}, is included in the constant of proportionality, ζ_0. To calibrate the constant of proportionality, ζ_0, we ensure that the conductivity between flakes, $\sigma_{ij} = G_{ij}(d_{ij} + d_{vdW})/A_{ij}$ is comparable to that of few-layer-graphene (FLG), $\sigma_{FLG} \approx 40 \times 10^6$ Sm^{-1} [150], for flakes in contact ($d_{ij} = 0$). Therefore, we are assuming that, for two FLG flakes in direct contact, the total conductivity is given by that of the flakes, i.e. the contact resistance is negligible. We set $e\zeta_0 = 10^{17}$ Sm^{-2}. The resulting conductivity between flakes is shown in fig. 5.1.

For simplicity, the resistance of each flake will be neglected in the computational calculations. In most cases, this is a reasonable simplification, since the tunnelling resistance typically dominates. For particularly high packing factors, we will use Matthiessen's rule to include the upper-limit of σ_{FLG}, as will be demonstrated in fig. 5.2f.

A current is driven through the simulated device by applying a voltage between the N_s left- and N_d right- most flakes (green shaded regions in figs. 5.2a to 5.2d).

The potential of these ‘contact’ flakes determines the boundary conditions, from which we calculate the potential of the N_p intermediate flakes self-consistently, by ensuring conservation of current through each flake. This equates to solving a system of N_p coupled simultaneous equations,

$$\sum_{i=1}^{N_p} G_{ij}(V_i - V_j) = \sum_{s=1}^{N_s} G_{js}(V_j - V_s) + \sum_{d=1}^{N_d} G_{jd}(V_j - V_d) \tag{5.3}$$

for each flake, j, where V_j is the potential of the j-th flake and the potential of the contact flakes, V_s and V_d, are fixed to the values of the applied source and drain potential respectively.

For the V-independent conductance (5.2), eq. (5.3) can be solved by a simple matrix inversion. If the potential difference between flakes is large, $eV \sim \phi_0$, the full Simmons equation should be used [141], and a Newton-Raphson method can be applied to solve the N_p coupled equations (5.3).

Once eq. (5.3) has been solved to find the potential of each flake, we can calculate the total conductivity, $\sigma = G_{tot}\mathcal{L}/\mathcal{W}\mathcal{T}$ where G_{tot} is the total conductance of the device and $\mathcal{L}$, $\mathcal{W}$ and $\mathcal{T}$ are the device length, width and thickness in the x, y and z directions respectively ($\mathcal{L} \times \mathcal{W} \times \mathcal{T} = \mathcal{V}_d$). The total conductance is given by $G_{tot} = I_{tot}/V_{ds}$, where

$$I_{tot} = \sum_{s=1}^{N_s}\sum_{i=1}^{N_p} G_{is}(V_i - V_s) = \sum_{d=1}^{N_d}\sum_{i=1}^{N_p} G_{id}(V_d - V_i) \tag{5.4}$$

is the total current through the device and $V_{ds} = V_d - V_s$ is the drain-source potential.

Figure 5.2e shows the variation of conductivity, σ, with packing factor, PF, calculated for 4 to 7 planes of flakes per printed layer, i.e. for $\langle d \rangle = 0.05$ nm to $\langle d \rangle = 1.55$ nm, where we have assumed a thickness of 14 nm for each printed layer [19]. Figure 5.2f shows the modified conductivity, $(1/\sigma + 1/\sigma_{FLG})^{-1}$, using Matthiessen’s rule to include the FLG upper limit on the total conductivity. Comparing figs. 5.2e and 5.2f, we find that a potential drop along the flakes should also be accounted for when $\langle d \rangle \lesssim 0.8$ nm, as the effect of the tunnelling resistance is sufficiently reduced due to the closely packed layers.

5.1.3 Percolation Dynamics

Figure 5.3 shows the conductivity for $\langle d \rangle = 0.05$ nm, where there exists a clear insulating phase ($\sigma \approx 0$) and conducting phase ($\sigma \approx \sigma_{FLG}$) with a percolating transition. The nature of the transition around the percolation threshold, $\mathrm{PF_c}$, can be characterised as a continuous phase transition with order parameter given by the conductivity and a critical exponent, $\beta \approx 0.47$, describing the power law onset of conductivity at percolation, $\sigma_{perc} \propto (\mathrm{PF} - \mathrm{PF_c})^{\beta}$.

For bulk materials the conductivity should be independent of the device geometry. However, for randomized percolation networks, we find that the size of the device

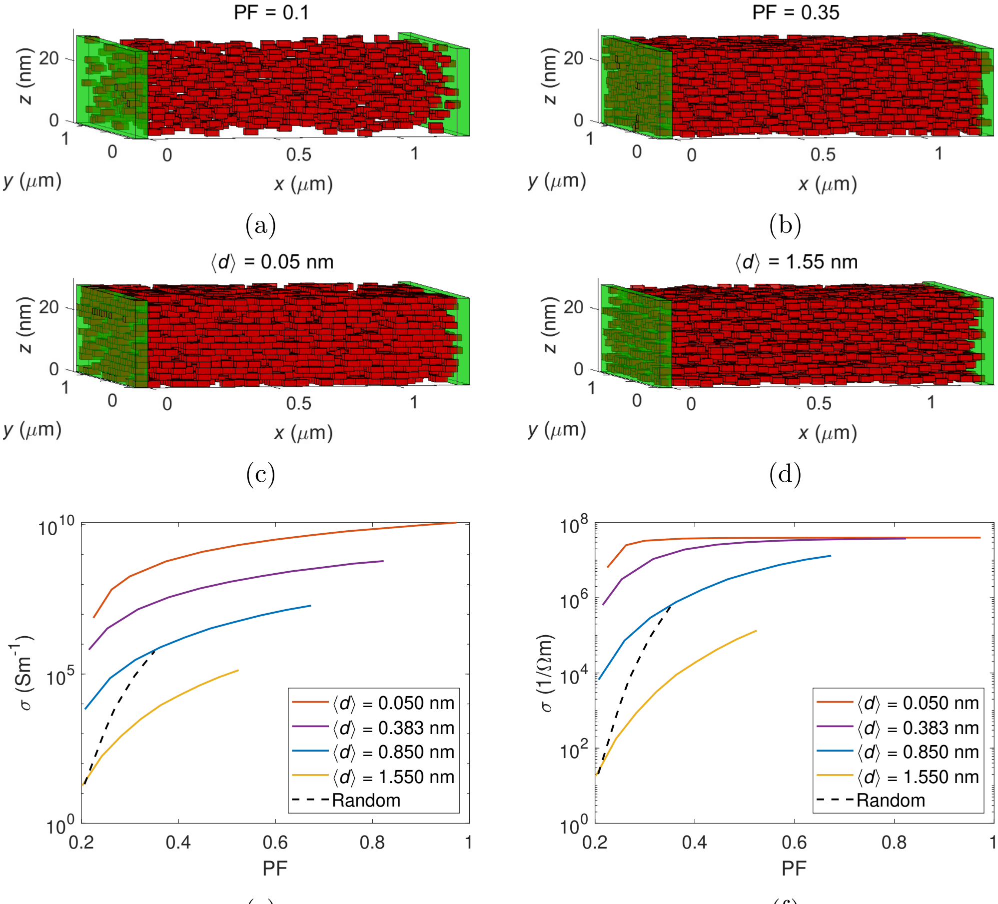

(a) (b)

(c) (d)

(e) (f)

Figure 5.2: (a) Random distribution of flakes with packing factor PF = 0.1. (b) Random distribution of flakes with packing factor PF = 0.35. (c) Distribution of flakes in distinct planes with packing factor PF = 0.35. There are 7 planes of graphene per printed layer (per 14 nm), with a mean separation of $\langle d \rangle = 0.05$ nm between flakes in adjacent planes. (d) Distribution of flakes in distinct planes with packing factor PF = 0.35. There are 4 planes of graphene per printed layer (per 14 nm), with a mean separation of $\langle d \rangle = 1.55$ nm between flakes in adjacent planes. (a)-(d) Red rectangles represent flakes. Green shaded regions represent the source-drain electrodes; any flake within these regions are contact flakes. (e)-(f) Total conductivity calculated for two printed layers ($\mathcal{T} = 28$ nm) over a square region of area $A_s = (1.25\ \mu\text{m})^2$ for varying packing factor using planes of flakes with mean separation $\langle d \rangle$ (solid coloured lines) and random flakes (black dashed line). (e) Initial results, where we have only accounted for the inter-flake resistance. (f) Results after applying Matthiessen's rule with the intra-flake conductivity, $\sigma_{FLG} \approx 40 \times 10^6$ Sm^{-1}.

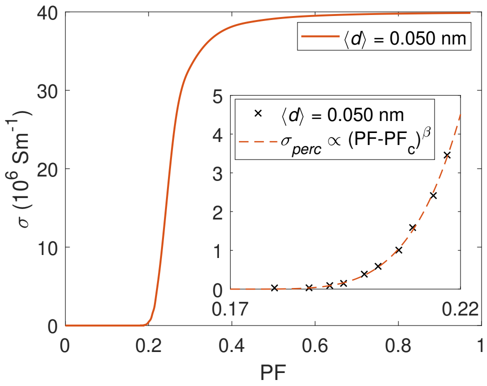

Figure 5.3: Conductivity simulated for two printed layers ($\mathcal{T} = 28$ nm) over a square region of area $A_s = (1.25\mu\text{m})^2$ using planes of flakes with mean separation $\langle d \rangle = 0.05$ nm. The inset shows the results of simulation (black crosses) around the percolation threshold, $\text{PF}_\text{c} \approx 0.17$, and the critical behaviour at percolation (dashed red line) with a critical exponent of $\beta = 0.47$.

can effect the total conductivity. Given the constant resistivity in bulk materials, the resistance, R, of a bulk conductor is inversely proportional to its thickness, $\mathcal{T}$. Experimentally, the conductivity of printed devices is found to decrease with decreasing thickness and the measured conductivity is found to be unstable for particularly thin devices [135, 151]. We consider the effect of increasing the number of printed layers, n, on the conductivity (see left of fig. 5.4a). Figure 5.4a shows the ratio of the mean resistance for one printed layer ($n = 1$, $\mathcal{T} = 14$ nm) to the mean resistance of two printed layers ($n = 2$, $\mathcal{T} = 28$ nm) for different packing factors and a square area of $(1.25\ \mu\text{m})^2$. As the packing factor increases, the behaviour of the disordered flakes tends towards the bulk ratio of $R_1/R_2 = 2$.

As the sheet area, $A_s = \mathcal{W} \times \mathcal{L}$ increases, the conductivity decreases, as shown in figs. 5.4b and 5.4c, due to the increased probability of finding a high resistance junction in any given path from the source to drain. Complete randomisation of flake positions results in a strong decrease of conductivity with length (fig. 5.4c), which converges to a constant value for large sheet areas. However, we find that the conductivity for planes of flakes is much more stable with increasing sheet area (fig. 5.4b). Since the conductivity is found to be approximately independent of the top area of the region probed, A_s, for planes of flakes, this method is thus ideal for reducing the large number of flakes ($\sim 10^9$) in an actual sample to a computationally manageable quantity (typically $\sim 10^4$) in our calculations.

We find that 5 planes of flakes per printed layer ($\langle d \rangle = 0.85$ nm) with a packing factor of PF = 0.26 and a random distribution of flakes with PF = 0.31 results in the sheet conductance $G_s \approx 2.2$ mS for 2 printed layers with the sheet areas considered here (see figs. 5.4b and 5.4c), consistent with that measured for the printed graphene ink in ref. [20].

In both the simulated devices and the experimentally measured data for the ink-jet

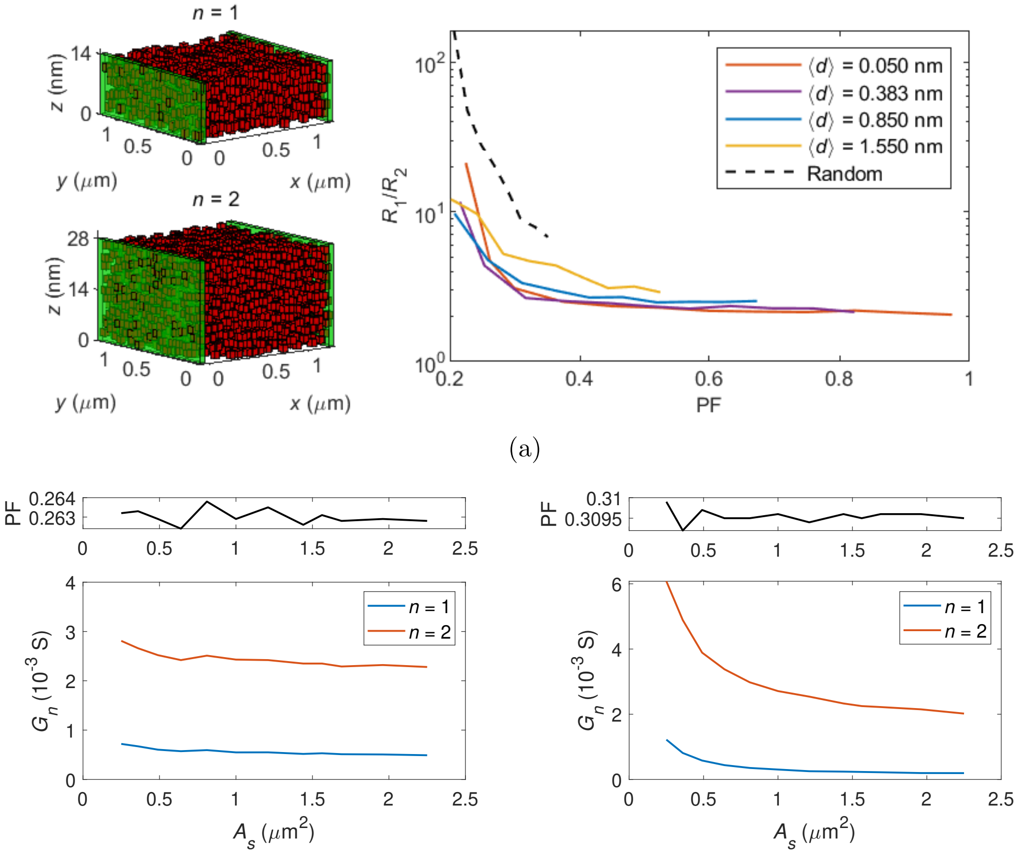

(a)

(b)

(c)

Figure 5.4: (a) Ratio of resistance for one printed layer, $R_n = R_1$, to the resistance of two printed layers, $R_n = R_2$, over a square region of area $A_s = (1.25\ \mu\text{m})^2$ for varying packing factor, using planes of flakes with mean separation $\langle d \rangle$ (solid coloured lines) and random flakes (black dashed line). The left panel shows exemplar flake arrangements for one printed layer, $n = 1$, and two printed layers, $n = 2$. The thickness of each layer is assumed to be 14 nm. (b)-(c) Conductance, G_n, for varying sheet area, A_s, for 1 printed layer, $n = 1$, and two printed layers, $n = 2$. The top plots show the slight changes in packing factor, PF, as we vary the area, A_s, due to the discrete number of flakes that can be used. (b) $\langle d \rangle = 0.85$ nm, PF ≈ 0.26. (c) Random, PF ≈ 0.31.

printed graphene [20, 151], the resistance decreases with increasing thickness (fig. 5.5a), but at a higher rate than expected for a bulk conducting material, where $R \propto 1/\mathcal{T}$, due to increased percolation arising from the randomized positioning of flakes. This percolation effect increases further when the positions of the flakes are completely randomised, rather than randomised about the mean separation $\langle d \rangle$. We also find that the coefficient of variation, measuring the deviation of resistance about the mean, decreases as the thickness increases for the simulated devices (fig. 5.5b), indicating better stability and repeatability of the electrical properties for larger printed samples.

The simulations reveal regions of inhomogeneity in the potential landscape (5.5c) and charge trajectories (fig. 5.5d) due to the randomized positioning of flakes. As the thickness of the conductor decreases, the size of these regions of spatial inhomogeneity become comparable to the device thickness, resulting in the significant variance in the resistance between devices shown in fig. 5.5b. Since the current between two flakes is determined by their areal overlap, the current between flakes with lateral overlap is significantly larger than the current between the edges of adjacent flakes. From the example shown in fig. 5.5d, the two highest current percolation paths (fig. 5.5e), which meander between several layers, require tunnelling in the z direction. Therefore, as the conductor thickness decreases, the probability of these high-conductivity meandering paths existing also decreases, thus explaining the increased resistivity as shown in fig. 5.5a.

5.1.4 Aspect Ratio

Changing the aspect ratio (radius/thickness) of the flakes has been shown to have a large effect on the total conductivity in graphene-based composites [152]. For a completely ordered distribution of flakes with tunnelling only in the z-direction, where the mean inter-flake separation is kept constant, regardless of flake aspect ratio, the total resistivity is proportional to the flake thickness, $\rho \propto T_f$. This can be understood from consideration of the resistor network. For increasing flake thickness, the number of parallel channels in the network decreases, with inverse proportionality. Similarly, the number of parallel channels is also decreased if the width of the flake, W_f, in the direction parallel to the contacts, is increased. However, if the flake length, L_f, in the direction perpendicular to the contacts is increased, the number of resistive junctions in series increases proportionally. Assuming that the flakes are approximately circularly symmetric, such that $W_f \approx L_f$, and the orientation in the x-y plane is randomised, the effects of decreasing parallel junctions and increasing series junctions cancel out with increasing flake area. However, the conductance of the the individual tunnel junctions, eq. (5.2), is proportional to the overlap area. Therefore the overall effect of increasing flake area, A_f, is $\rho \propto 1/A_f$.

To demonstrate the expected behaviour, $\rho \propto T_f$ and $\rho \propto 1/A_f$, for an ordered distribution of flakes with tunnelling in the z-direction, we have used a simplified model with only tunnelling in the z-direction and a shell size equal to the mean interflake

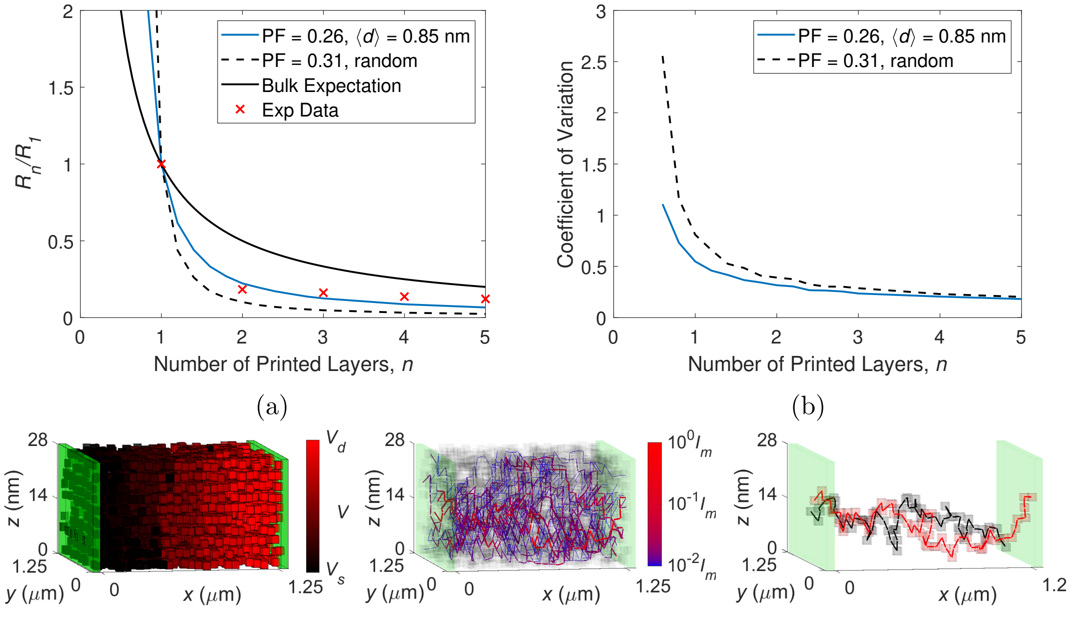

(a) (b)

(c) (d) (e)

Figure 5.5: (a) Ratio of electrical resistance, R_n, calculated for n printed layers to the resistance of one printed layer, R_1, for inkjet graphene with: 5 layers per printed layer (mean interlayer separation $\langle d \rangle = 0.85$ nm) with packing factor 0.26 (solid blue curve); and randomly distributed flakes with packing factor 0.31 (black dashed black curve). The expected dependence for a bulk conductor is shown by the solid black curve, $R_n/R_1 = 1/n$. The thickness of each layer is assumed to be 14 nm. Data points are experimental results from reference [20]. (b) Coefficient of variation of the calculated conductance with varying number of printed layers, n, for 1000 simulated flake distributions. (c) Representative arrangement of flakes used in our Monte Carlo simulation with packing factor PF $= 0.26$ and mean interlayer separation $\langle d \rangle = 0.85$ nm, positioned between electrodes (green cuboids). The colour of each flake represents the value of electrical potential between the source and drain potentials, V_s and V_d (scale right). (d) Current paths between flakes (positions shown grey) with colour-scaled current magnitudes, relative to the highest inter-flake current (scale right). (e) The two highest contributing current paths found by following the path of highest current from the left electrode to right (black) and vice versa (red).

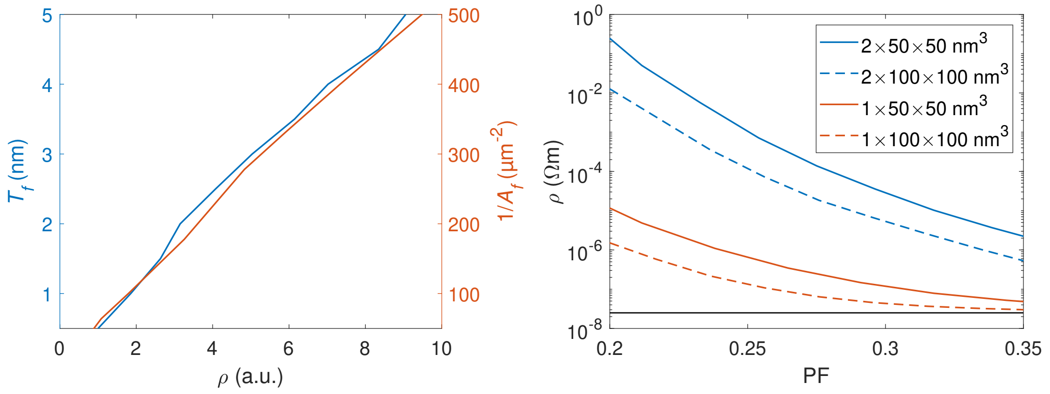

(a) (b)

Figure 5.6: (a) Modelled behaviour of resistivity, ρ, for varying flake dimensions: thickness, T_f, perpendicular to the direction of the applied potential difference, and area, A_f, parallel to the direction of the potential difference. The flake positions are structured in layers with a fixed mean separation, $\langle d \rangle$. Distances between flakes are randomised about the mean separation and some flakes are randomly removed to reduce the packing factor to PF ≈ 0.3. The mean distances and number of removed flakes is constant for all flake dimensions considered. Tunnelling is assumed to be only in the z-direction, i.e. perpendicular to the flakes. We consider only nearest-neighbour tunnelling by setting the shell size, $d_s = 2\langle d \rangle$. (b) Modelled resistivity, ρ, as a function of packing factor, PF, for flakes of varying dimensions, as shown in the legend. Here, the flake positions are randomised and the shell size is kept constant, $d_s = 2$ nm. The solid black line shows the few-layer graphene limit.

distance, $d_s = \langle d \rangle$, such that there only exists nearest neighbour tunnelling. We vary the flake sizes but keep the mean interflake separation, on top of the van der Waals distance, constant, $\langle d \rangle = 0.1$ nm. An array of 25×25 flakes is used with 10 layers of flakes with randomised overlap. The number of randomised 'gaps' (flakes removed) per layer is 444, resulting in a packing factor PF ≈ 0.3. Figure 5.6a shows the resulting resistivity for varying flake thickness and flake area.

For a disordered, percolating network, there exists a higher probability for there to exist a percolating path when there are more parallel channels and fewer series junctions. Therefore, increasing flake thickness leads to a further increase of resistance. This is entirely analogous with the results shown in fig. 5.5a, where the device thickness is varied, rather than the flake thickness.

For a given density (PF) of flakes, the mean interflake separation increases as the flake size increases. Given that the tunnelling in the z-direction contributes the most, changes in the mean interflake distance in the z-direction, d_z, given by

$$\delta d_z^3 + \frac{3}{2} T_f^2 \delta d_z - \frac{T_f^3}{2}\left(\frac{1}{PF} - 1\right) \approx 0 \tag{5.5}$$

for cuboid shaped flakes, causes further increase in resistivity with increasing flake thickness.

A combination of increased percolation, decreased tunnelling distances, and increased next-nearest neighbour connectivity result in a potentially large decrease in resistivity with increasing flake aspect ratio for a given packing factor when flake positions are completely randomised, as shown in fig. 5.6b, beyond the expectation for an ordered resistor array.

5.2 Calculations of Transport Between Individual Graphene Flake Pairs

We now turn our attention to the temperature and chemical potential dependence of the conductivity between any two few-layer graphene flakes. We know that for systems of localised energy states, the hopping conductivity generally follows the Arrhenius conductivity, eq. (1.55). However, in graphene flakes there can exist a distribution of multiple energy states per site covering the energy range $\varepsilon_F \pm k_B T$, depending on the flake size.

5.2.1 Hopping

The transition rate from energy state ε_i at flake i to energy state ε_j at flake j is [38]

$$\Gamma_{ij} = f(\varepsilon_i)\left[1 - f(\varepsilon_j)\right]\gamma_{ij} = \frac{\gamma_{ij}}{4}\frac{\exp\left(\frac{\varepsilon_j - \varepsilon_i}{2k_BT}\right)}{\cosh\left(\frac{\varepsilon_i-\varepsilon_F}{2k_BT}\right)\cosh\left(\frac{\varepsilon_j-\varepsilon_F}{2k_BT}\right)} \tag{5.6}$$

where $f(\varepsilon)$ is the Fermi-Dirac distribution function, ε_F is the chemical potential of the flakes and γ_{ij} is the hopping rate. Using Miller-Abrahams hopping, eq. (1.54), to describe the hopping rate, the transition rate becomes

$$\Gamma_{ij} = \frac{\gamma_0 e^{-\alpha R_{ij}}}{4}\frac{\exp\left(-\frac{|\varepsilon_j - \varepsilon_i|}{2k_BT}\right)}{\cosh\left(\frac{\varepsilon_i-\varepsilon_F}{2k_BT}\right)\cosh\left(\frac{\varepsilon_j-\varepsilon_F}{2k_BT}\right)}. \tag{5.7}$$

A potential difference, V, between the two flakes will drive a current between them. This offsets the energy states at flake j by eV relative to flake i, as shown in fig. 5.7. The net current between the two energy states on the two flakes is given by

$$\begin{aligned} I_{ij} = e\left(\Gamma_{ij} - \Gamma_{ji}\right) &= e\gamma_{ij} f(\varepsilon_i)\left[1 - f(\varepsilon_j + eV)\right] - e\gamma_{ji} f(\varepsilon_j + eV)\left[1 - f(\varepsilon_i)\right] \\ &= \frac{e\gamma_0 e^{-\alpha R_{ij}}}{2}\sinh\left(\frac{eV}{2k_BT}\right)\frac{\exp\left(-\frac{|\varepsilon_j - \varepsilon_i|}{2k_BT}\right)}{\cosh\left(\frac{\varepsilon_i-\varepsilon_F}{2k_BT}\right)\cosh\left(\frac{\varepsilon_j+eV-\varepsilon_F}{2k_BT}\right)}. \end{aligned} \tag{5.8}$$

Assuming that $eV \ll k_BT$ and eV is much smaller than relevant energies, i.e. $eV \ll \varepsilon_F$ or $eV \ll \varepsilon_i$,

$$I_{ij} \approx e^2 V \frac{\gamma_0 e^{-\alpha R_{ij}}}{4k_BT} \frac{\exp\left(-\frac{|\varepsilon_j-\varepsilon_i|}{2k_BT}\right)}{\cosh\left(\frac{\varepsilon_i-\varepsilon_F}{2k_BT}\right)\cosh\left(\frac{\varepsilon_j-\varepsilon_F}{2k_BT}\right)}. \tag{5.9}$$

Further assuming that the chemical potential and temperature are small relative to the state energies, $\varepsilon_F \ll \varepsilon_i, \varepsilon_j$ and $k_BT \ll \varepsilon_i, \varepsilon_j$, we find the the approximate conductance

$$G_{ij} = I_{ij}/V \approx e^2 \frac{\gamma_0 e^{-\alpha R_{ij}}}{k_BT} \exp\left(-\frac{|\varepsilon_j-\varepsilon_F|+|\varepsilon_i-\varepsilon_F|+|\varepsilon_i-\varepsilon_j|}{2k_BT}\right) \tag{5.10}$$

as often seen in the literature [33, 38, 43]. For 2D flakes, we need to sum over all energy states in each flake. Using eq. (5.8), for the current between individual states, and summing over k-states k_i and k_j, the total hopping current between flakes i and j is

$$I_h = \beta_h \sinh\left(\frac{eV}{2k_BT}\right)(g_sg_v)^2 \sum_{s_i=\pm1}\sum_{s_j=\pm1}\sum_{k_i}\sum_{k_j} \frac{\exp\left(-\frac{\left|\varepsilon_{sj,kj}-\varepsilon_{si,ki}-eV\right|}{2k_BT}\right)}{\cosh\left(\frac{\varepsilon_{si,ki}-\varepsilon_F}{2k_BT}\right)\cosh\left(\frac{\varepsilon_{sj,kj}-\varepsilon_F}{2k_BT}\right)}, \tag{5.11}$$

where

$$\beta_h = \frac{e\gamma_0 e^{-\alpha R_{ij}}}{2}, \tag{5.12}$$

g_s and g_v are the spin and valley degeneracies, respectively, $\varepsilon_{si,ki} \equiv \varepsilon(s_i, k_i)$ is the 'internal' energy of electron state k_i in band s_i, as determined by the bandstructure, and we have taken care that the energy of flake j is offset by the potential i.e. $\varepsilon_j = \varepsilon(k_j) - eV$, as shown in fig. 5.7. Assuming the flakes are large such that the energy gaps between states are small around the chemical potential relative to k_BT, we can make the continuum approximation for the summation over individual states,

$$I_h \approx A_iA_j\beta_h \sinh\left(\frac{eV}{2k_BT}\right)\int_{-\infty}^{\infty}\int_{-\infty}^{\infty} \mathrm{d}\varepsilon_{ki}\mathrm{d}\varepsilon_{kj} \frac{D(\varepsilon_{ki})D(\varepsilon_{kj})\exp\left(-\frac{\left|\varepsilon_{kj}-\varepsilon_{ki}-eV\right|}{2k_BT}\right)}{\cosh\left(\frac{\varepsilon_{ki}-\varepsilon_F}{2k_BT}\right)\cosh\left(\frac{\varepsilon_{kj}-\varepsilon_F}{2k_BT}\right)}, \tag{5.13}$$

where $D(\varepsilon)$ is the density of states and A_i is the area flake i. Typically, graphene flakes used in ink-jet printing are of few-layer thickness [20, 135, 136, 153]. Assuming that the flakes, which are exfoliated from bulk graphite, contain strongly interacting layers, the 2D bands of each layer will be parabolic with a constant density of states, given by eq. (1.24). Substituting in the density of states and evaluating the integral, we find the hopping current

$$I_h \approx \frac{\pi^2}{3}A_iA_j\left(\frac{g_sg_vm^*}{2\pi\hbar^2}\right)^2 e\gamma_0 e^{-\alpha R_{ij}} k_BTeV \propto k_BT \tag{5.14}$$

in the limit $k_BT \gg eV$.

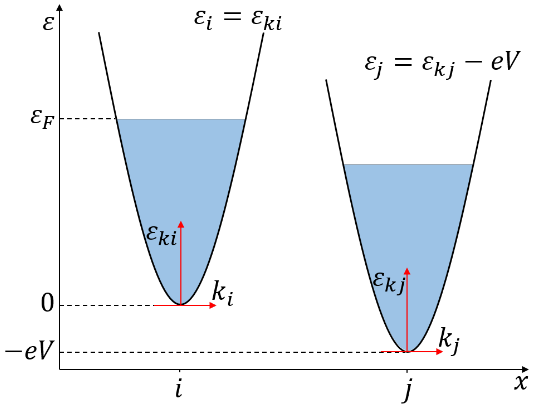

Figure 5.7: Diagram of the energetic band structure in two adjacent flakes, i and j, with a potential difference, V. ε_F denotes the chemical potential. The internal energy is given by the parabolic dispersion, $\varepsilon_k = \hbar^2 k^2/2m^*$. For flake j, this internal energy is shifted by eV relative to that of flake i, as described by the energies ε_i and ε_j.

The allowed k-states in any system are discretised by the boundary conditions imposed at the edges [59]. For a 2D flake, the allowed states are given by

$$(k_x, k_y) = \left(\frac{2\pi l}{L}, \frac{2\pi m}{L}\right), \qquad l, m = 0, \pm 1, \pm 2, \ldots \tag{5.15}$$

where the energy of each state is $\varepsilon_k = \hbar^2 \left(k_x^2 + k_y^2\right) / 2m^*$ and $L = \sqrt{A}$ is the length of the flake. As $L \to \infty$, the gaps between energy states become small and the continuum approximation is valid, however for small sized materials the energy level spacing becomes large. This effect is often exploited, for example in quantum dots where the energy level spacing gives rise to photoluminescence. The flakes in ink-jet printed graphene vary in lateral size and have been reported with average sizes between 50 nm and 530 nm [19, 20, 135, 151, 154], inks containing flakes with average size as large as 36 μm have also been successfully printed [153]. Therefore, we should check the validity of the continuum approximation. Figure 5.8 shows the results of summing over all k-states, as given by eq. (5.11) compared to the approximation of eq. (5.14). From fig. 5.8a, we see that, for $T > 100$ K and $L > 200$ nm, the continuum approximation, eq. (5.14), holds well over a reasonable range of chemical potentials ($|\varepsilon_F| < 0.5$ eV). For smaller sizes, at $T = 100$ K, the hopping current shows significant peaks at chemical potentials corresponding to to the energy values of the discrete k-states. For a given size, the results converge back to eq. (5.14) as temperature is increased due to the thermal broadening of electron energies over many k-states, as shown in fig. 5.8b. For the parabolic band considered here, the size of the energy gaps increases as energy is increased, since $\varepsilon \propto k^2$. Therefore, the effect of the discrete k-states is more significant at large chemical potentials.

For a random distribution of flake sizes, the hopping current between flakes will dephase due to the mismatch of energy level spacing at different junctions. This should

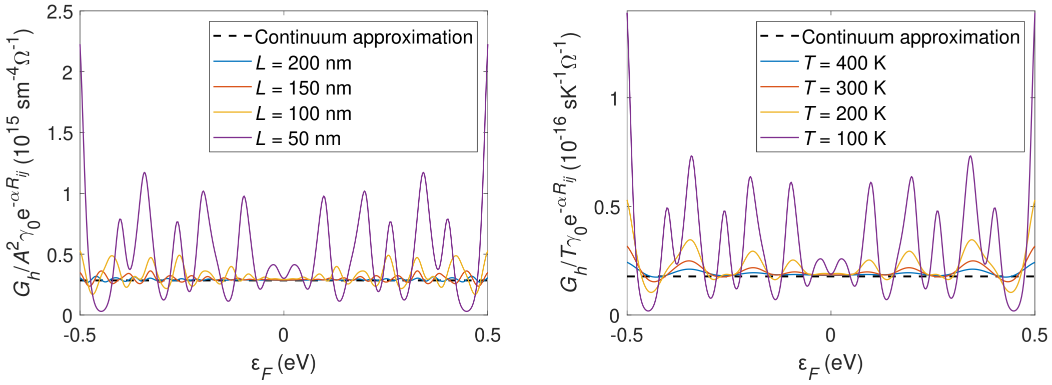

(a) (b)

Figure 5.8: (a) Hopping conductance, $G_h = I_h/V$, between two flakes for varying chemical potential, ε_F, parameterised by the flake area, $A = L^2$, for varying lengths, L. The temperature is $T = 100$ K (b) Hopping conductance, $G_h = I_h/V$, between two flakes for varying chemical potential, ε_F, parameterised by the temperature, T, for varying temperatures. The length is $L = 50$ nm. In both (a) and (b) we have also divided the conductance by unknown/phenomenological parameters: hopping strength, γ_0, and $e^{-\alpha R_{ij}}$ where α is the inverse localisation radius and R_{ij} is the inter-flake distance. The hopping current, I_h, is calculated using eq. (5.11) assuming a small potential, V. Dashed lines show the results of the continuum approximation, eq. (5.14), which becomes exact in the limit $L \to \infty$.

lead to a smoothing out of the current peaks seen in fig. 5.8 for a single junction, when measured over many junctions.

5.2.2 Tunnelling

Assuming a potential applied in the x-direction, the Landauer tunnel current density, eq. (3.50), is

$$J_t = \frac{eg_sg_v}{A}\sum_{s=\pm1}\sum_{k:k_x>0} v_{g,x}e^{-\alpha R}\left(f(\varepsilon_{s,k}) - f(\varepsilon_{s,k}+eV)\right) \tag{5.16}$$

where $v_{g,x}$ is the x-component of the group velocity, which is $v_{g,x} = \hbar k_x/m^*$ for a parabolic band. This is in analogy with the Simmons tunnel current for electrons incident on a barrier [141], i.e. electrons incident on the flake edges. Making the continuum approximation, we find that

$$J_t \approx \frac{eg_sg_v}{2\pi^2}\frac{\sqrt{2m^*}}{\hbar^2}e^{-\alpha R}\int_{-\infty}^{\infty} \mathrm{d}\varepsilon\, |\varepsilon|^{1/2}\left(f(\varepsilon) - f(\varepsilon+eV)\right) \tag{5.17}$$

which, assuming that $\varepsilon_F \gg k_BT$ and $\varepsilon_F \gg eV$, is

$$J_t \approx \frac{eg_sg_v}{2\pi^2}\frac{\sqrt{2m^*}}{\hbar^2}e^{-\alpha R}\varepsilon_F^{1/2}eV. \tag{5.18}$$

Therefore, the total inter-flake conductance is

$$G_{ff} = I_h/V + J_t W/V \approx \frac{e^2 g_s g_v}{2\pi^2} e^{-\alpha R} \left[\frac{\pi^2}{6} \frac{A^2 g_s g_v m^{*2}}{\hbar^4} \gamma_0 k_B T + W \frac{\sqrt{2m^*}}{\hbar^2} \varepsilon_F^{1/2} \right] \tag{5.19}$$

where W is the width of flake overlap and we have assumed that $\varepsilon_F \gg k_B T$, $eV \approx 0$ and $L \to \infty$. Therefore, the total flake-to-flake conductance can be expected to be proportional to temperature and proportional to the square root of the chemical potential independently.

5.2.3 Single Droplet Graphene FET

If the number of flakes within the device is small, the glassy behaviour associated with large-scale disorder can be reduced. In this case, it is possible to observe the field effect resulting from the doping of the graphene flakes, without complications arising from the slow-relaxations present in highly disordered systems, which give rise to the anomalous field effect. Here, we consider a single droplet graphene FET composed of a thermally annealed, drop-cast graphene ink droplet. This single droplet forms the active material in a 5 μm organic field-effect transistor (OFET) with a SiO_2 gate dielectric and silver electrodes.

For percolating resistor networks, the total conductance is described by $G = NG_c$ where N is some characteristic scale of the system and G_c is the critical conductance, defined as the lowest conductance between any two flakes in the highest conductance connected path spanning the full length of the network, i.e. the lowest conductance in the first percolating path [33, 38, 155]. Therefore, if nearest-neighbour hopping applies, we can express the total network conductance as $G \approx NG_{ff,c}$ where $G_{ff,c}$ is the conductance given by eq. (5.19) for the highest resistance junction within a percolating path and N is representative of the total number of independently percolating paths.

Assuming gapless ($\varepsilon_g = 0$) parabolic bands with electron and hole densities, n and p, described by eqs. (1.26) and (1.27), results in a charge density of

$$n - p = \frac{g_s g_v m^*}{2\pi\hbar^2} \varepsilon_F \tag{5.20}$$

for chemical potential, ε_F. An expression describing the dependence of the chemical potential, ε_F, on gate voltage, V_g,

$$\varepsilon_F = \frac{C}{e} \frac{T_f}{\mathcal{T} N_l} \frac{1}{PF} \frac{2\pi\hbar^2}{g_s g_v m^*} (V_g - V_0), \tag{5.21}$$

is found by equating the total charge across all 2D layers, given by eq. (5.20), to the charge induced by the gate voltage over a capacitance, C, where T_f is the flake thickness, $\mathcal{T}$ is the total thickness of flake network, N_l is the number of 2D layers per flake, and V_0 is the offset of gate-induced doping, due to doping by charged impurities for example.

Substituting eq. (5.21) into eq. (5.19), the total current through a percolating flake network can be described by

$$I \approx N\left(c_1\sqrt{V_g - V_0} + c_2 T\right) \tag{5.22}$$

where

$$c_1 = \frac{e^2 V g_s g_v e^{-\alpha R}}{\pi^2 \hbar} W \sqrt{\frac{C}{e}\frac{T_f}{\mathcal{T} N_l}\frac{1}{PF}\frac{\pi}{g_s g_v}} \tag{5.23}$$

and

$$c_2 = \frac{e^2 V g_s g_v e^{-\alpha R}}{\pi^2 \hbar}\frac{\pi^2 A^2 g_s g_v m^{*2}}{12\hbar^3}\gamma_0 k_B. \tag{5.24}$$

Measurements on a single, post processed droplet of the graphene ink on a SiO_2 substrate reveal that the current appears proportional to temperature over a temperature range 100 K $< T <$ 350 K, as shown in fig. 5.9a, and over gate voltages $|V_g - V_0| < 150$ V for a 300 nm SiO_2 gate dielectric (fig. 5.9b). Similar to the analysis of graphene in section 2.3.1, we assume spatial fluctuations of the quasi Fermi level. This means that at charge neutrality, $V_g = V_0$, there exists a net charge carrier population described by V_g^*. We use the same approximation as in eq. (2.25). For gate voltages $|V_g - V_0| > V_g^*$, we assume spatial inhomogeneities to be washed out and the transport characteristics to be dominated by transport calculated at the Fermi level induced by the gate. For gate voltages $|V_g - V_0| < V_g^*$, we assume that the total charge transport is dominated by transport at the quasi Fermi level induced by the spatially varying potential across the structure. Fitting eq. (5.22) to the measurements on the single droplet, as shown in fig. 5.9b, we find that $Nc_1 \approx 0.129$ µAV$^{-1/2}$, $Nc_2 \approx 1.76$ nAK^{-1} and $V_g^* \approx 78.8$ V.

The values of c_1 and c_2 can be used to estimate the hopping strength, γ_0, and the exponent describing the penetration of the wavefunction through the barrier, αR. Evaluating c_1/c_2, we find

$$\frac{A^2\gamma_0}{W} \approx 6.5 \times 10^{-12}\ \mathrm{m^3 s^{-1}}, \tag{5.25}$$

where we have assumed that $C = 1.15 \times 10^{-4}$ Fm^{-2} (300 nm of SiO_2), $m^* \approx 0.03 m_e$ [88], $T_f \approx 2$ nm, $N_l \approx 3$, $\mathcal{T} \approx 2T_f$, $PF \approx 0.5$. Further assuming that $W = \sqrt{A}$ and $A \approx 2500$ nm^2 is the average flake area, then $\gamma_0 \approx 52$ ns^{-1}.

The ink used contains an additive, ethyl cellulose. This acts as a stabalizing polymer. However, it is also expected to further facilitate charge transport upon decomposition in the annealing process [19]. This is due to the carbon residuals formed upon decomposition of the ethyl cellulose, resulting in a network of graphene flakes which are densely packed with aromatic species. Such aromatic species are graphene-like. The smaller size of the aromatic residuals, compared to the graphene flakes, means that there exists a smaller amount of states within a given energy range for transport, as characterised by a smaller area, A, in eq. (5.25). This results in a large uncertainty in the value of γ_0. For example, if we assume transport between a graphene flake of size

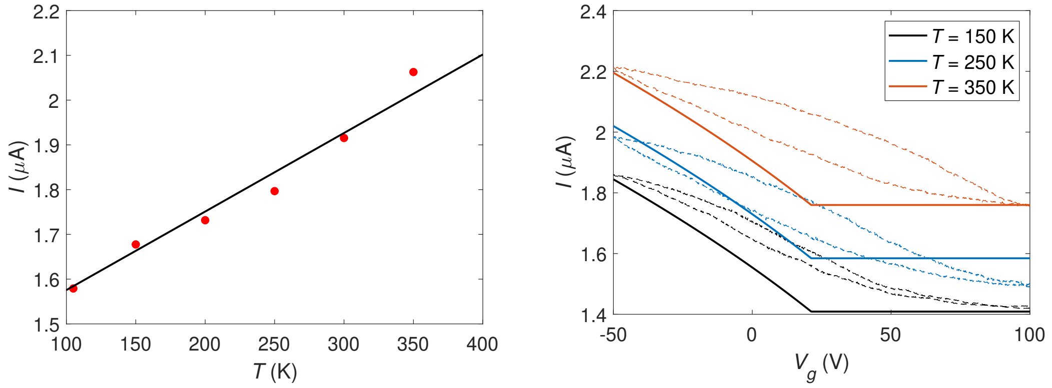

(a) (b)

Figure 5.9: (a) Current, I, measured across a 5 μm thermally annealed graphene ink droplet for varying temperature, T (red data points). The applied potential is 20 mV. Black line shows a linear relationship, $I \propto T$. (b) Current, I, measured across the same device for varying gate voltages, V_g, (dashed lines) for 3 temperatures (shown in the legend). Solid lines show the results of eq. (5.22) where we have used $Nc_1 = 0.129$ μAV$^{-1/2}$, $Nc_2 = 1.76$ nAK^{-1}, $V_0 = 100$ V and we have imposed $V_g^* = 78.8$ V on the minimum value of $|V_g - V_0|$, a fitting parameter which accounts for spatial inhomogeneities in the chemical potential. The measured current (dashed lines) shows a hysteresis over the forward and backward gate voltage sweeps. Similar hysteresis is also observed in CVD graphene and is expected to arise from the gate capacitance or charge transport between the graphene and neighbouring adsorbates or charge trap states in the substrate [156, 157]. We thank Nathan D. Cottam at the University of Nottingham for the fabrication of the single droplet FET and for the measurement and analysis of the data used in figures (a) and (b).

50 nm and a single aromatic ring of size 2.5 Å, then $\gamma_0 \sim 10$ ps^{-1}, comparable to the vibrational frequency of low energy optical phonons in SLG and FLG [67, 158–160].

From the value of c_1, we find that $NWVe^{-\alpha R} \approx 0.1$ nVm. Assuming that $W \sim 10$ nm, $V \sim 1$ mV, [1] and $1 \lesssim N \lesssim 100$, we find

$$\alpha R \sim 1, \tag{5.26}$$

i.e. the distance between flakes, R, is approximately equal to the size of the localization radius, α^{-1}, as may be expected for the highest resistance junction in a percolating path.

---

[1] Applied source-drain voltage is 20 mV. Approximately 100 flakes across channel (50 nm flakes, 5 μm channel). A larger proportion of the potential will be dropped over highest resistance junction.

Chapter 6

Conclusions

We have developed and unified key analytical models of electron transport in graphene and graphene heterostructures. Numerical time-dependent analysis of charge carrier distributions revealed the effects of Joule heating - relevant for graphene with few impurities, where the diffusive acceleration of electrons results in a dilute, energetic electron gas. The properties of a wide range of devices, from high-quality graphene with low carrier density to graphene-based heterostructures, exhibit "universal" behaviour between the mobility and linewidth (FWHM) that can be accurately described within the model of randomly distributed charged impurity scattering. We showed that the "universal" inverse power law depends crucially on behaviour at the Dirac point. Theoretically, charged impurity correlations were found to result in small deviations from the inverse-power law due to smoothing of the electrostatic impurity potential. The lack correlation observed between the type of graphene device and/or dopant density (CVD/Exfoliated, pristine/surface modified) and the resistivity around the Dirac point can be explained by the remarkable stability of the calculated resistivity at charge neutrality despite the varying effects of charged impurities, charge-neutral impurities and the ballistic quantum limit.

A simple relation between graphene's mobility, μ, charge carrier density fluctuations, δn, and the resistivity at the Dirac point, ρ_{max}, is found to apply accurately for all of the graphene layers including both exfoliated and CVD-grown SLG devices with electron mobilities ranging from 0.5 m^2/Vs to > 25 m^2/Vs in the temperature range $4\ \mathrm{K} < T < 400\ \mathrm{K}$. This universal behaviour provides crucial information regarding the carrier densities that contribute most to the measured charge transport characteristics. Overcoming this conundrum, we were able to effectively demonstrate a generalised, analytical temperature dependence of the charge transport properties of graphene due to phonon scattering and thermally excited charge carriers, compatible with experimentally measured values over the entire range of 6 devices presented in this thesis. We demonstrated that the resistivity of graphene at low carrier concentrations, $n < \delta n$, typically excluded from the data analysis due to nonlinear conductivity, can be analysed using a model based on Fermi-Dirac temperature broadening and impurity broadening of δn.

Our calculations combine multiple parameters that affect charge transport in graphene and facilitate the design, accurate ab initio prediction of key transport parameters, and analysis of future electronic and optoelectronic devices based on 2D materials.

Moiré interference potentials formed by overlapping, twisted 2D lattice structures lead to perturbed low-energy band structures. Flattening of the energy bands causes an increase in the energy density of states and, therefore, an increased charged carrier density. However, the band gaps opened by the overlapping 2D bands results in an increased effective mass and increased Bloch oscillations across subbands. This causes a suppression of charge transport. Therefore, the conductivity is reduced for chemical potentials corresponding to the subband edges. Charge carriers can be accelerated up to the the vicinity of the subband edges before further acceleration is suppressed. This causes a dynamic relationship between the applied electric field of acceleration and the initial internal energy of electrons, which can result in a striking negative differential conductance for both ballistic and diffusive transport.

In inkjet-printed devices, composed of conductive flakes, the electronic properties are largely governed by the interflake transport processes. Disorder in flake positioning results in complex current paths leading to percolating networks, as demonstrated by detailed numerical modelling and confirmed by the measured transport characteristics. Disorder, packing density and morphology are all shown to have strong effects on the percolating structures. The highest conductivity is achieved with laterally larger, thinner flakes with a high density. The effects of complex meandering current paths on the percolation dynamics are reduced as flake ordering is increased, allowing for the potential to achieve better stability in the bulk properties for thin printed films.

References

[1] Philip Richard Wallace. The band theory of graphite. *Physical Review*, 71(9): 622, 1947.

[2] DP DiVincenzo and EJ Mele. Self-consistent effective-mass theory for intralayer screening in graphite intercalation compounds. *Physical Review B*, 29(4):1685, 1984.

[3] Kostya S Novoselov, Andre K Geim, Sergei V Morozov, D Jiang, Y Zhang, Sergey V Dubonos, Irina V Grigorieva, and Alexandr A Firsov. Electric field effect in atomically thin carbon films. *Science*, 306(5696):666–669, 2004.

[4] Minzhen Cai, Daniel Thorpe, Douglas H Adamson, and Hannes C Schniepp. Methods of graphite exfoliation. *Journal of Materials Chemistry*, 22(48):24992–25002, 2012.

[5] YI Zhang, Luyao Zhang, and Chongwu Zhou. Review of chemical vapor deposition of graphene and related applications. *Accounts of Chemical Research*, 46 (10):2329–2339, 2013.

[6] Jian-Hao Chen, Chaun Jang, Shudong Xiao, Masa Ishigami, and Michael S Fuhrer. Intrinsic and extrinsic performance limits of graphene devices on SiO_2. *Nature Nanotechnology*, 3(4):206, 2008.

[7] Vincent E Dorgan, Myung-Ho Bae, and Eric Pop. Mobility and saturation velocity in graphene on SiO_2. *Applied Physics Letters*, 97(8):082112, 2010.

[8] Kosuke Nagashio, Tomonori Nishimura, Koji Kita, and Akira Toriumi. Mobility variations in mono-and multi-layer graphene films. *Applied Physics Express*, 2 (2):025003, 2009.

[9] Xu Du, Ivan Skachko, Anthony Barker, and Eva Y Andrei. Approaching ballistic transport in suspended graphene. *Nature Nanotechnology*, 3(8):491–495, 2008.

[10] Alexander S Mayorov, Roman V Gorbachev, Sergey V Morozov, Liam Britnell, Rashid Jalil, Leonid A Ponomarenko, Peter Blake, Kostya S Novoselov, Kenji Watanabe, Takashi Taniguchi, et al. Micrometer-scale ballistic transport in encapsulated graphene at room temperature. *Nano Letters*, 11(6):2396–2399, 2011.

[11] Liam Britnell, Ricardo Mendes Ribeiro, Axel Eckmann, Rashid Jalil, Branson D Belle, Artem Mishchenko, Y-J Kim, Roman V Gorbachev, Thanasis Georgiou, Sergei V Morozov, et al. Strong light-matter interactions in heterostructures of atomically thin films. *Science*, 340(6138):1311–1314, 2013.

[12] Kallol Roy, Medini Padmanabhan, Srijit Goswami, T Phanindra Sai, Gopalakrishnan Ramalingam, Srinivasan Raghavan, and Arindam Ghosh. Graphene–MoS 2 hybrid structures for multifunctional photoresponsive memory devices. *Nature Nanotechnology*, 8(11):826–830, 2013.

[13] Woo Jong Yu, Yuan Liu, Hailong Zhou, Anxiang Yin, Zheng Li, Yu Huang, and Xiangfeng Duan. Highly efficient gate-tunable photocurrent generation in vertical heterostructures of layered materials. *Nature Nanotechnology*, 8(12):952–958, 2013.

[14] Freddie Withers, O Del Pozo-Zamudio, A Mishchenko, AP Rooney, Ali Gholinia, K Watanabe, T Taniguchi, Sarah J Haigh, AK Geim, AI Tartakovskii, et al. Light-emitting diodes by band-structure engineering in van der Waals heterostructures. *Nature Materials*, 14(3):301–306, 2015.

[15] Carmen Palacios-Berraquero. Atomically-thin quantum light emitting diodes. In *Quantum Confined Excitons in 2-Dimensional Materials*, pages 71–89. Springer, 2018.

[16] Liam Britnell, Roman V Gorbachev, Rashid Jalil, Branson D Belle, Fred Schedin, Mikhail I Katsnelson, Laurence Eaves, Sergey V Morozov, Alexander S Mayorov, Nuno MR Peres, et al. Electron tunneling through ultrathin boron nitride crystalline barriers. *Nano Letters*, 12(3):1707–1710, 2012.

[17] Thanasis Georgiou, Rashid Jalil, Branson D Belle, Liam Britnell, Roman V Gorbachev, Sergey V Morozov, Yong-Jin Kim, Ali Gholinia, Sarah J Haigh, Oleg Makarovsky, et al. Vertical field-effect transistor based on graphene–WS_2 heterostructures for flexible and transparent electronics. *Nature Nanotechnology*, 8 (2):100–103, 2013.

[18] Tae-Hee Han, Hobeom Kim, Sung-Joo Kwon, and Tae-Woo Lee. Graphene-based flexible electronic devices. *Materials Science and Engineering: R: Reports*, 118: 1–43, 2017.

[19] Ethan B Secor, Pradyumna L Prabhumirashi, Kanan Puntambekar, Michael L Geier, and Mark C Hersam. Inkjet printing of high conductivity, flexible graphene patterns. *The Journal of Physical Chemistry Letters*, 4(8):1347–1351, 2013.

[20] Feiran Wang, Jonathan H Gosling, Gustavo F Trindade, Graham A Rance, Oleg Makarovsky, Nathan D Cottam, Zakhar Kudrynskyi, Alexander G Balanov,

Mark T Greenaway, Ricky D Wildman, et al. Inter-flake quantum transport of electrons and holes in inkjet-printed graphene devices. *Advanced Functional Materials*, 31(5):2007478, 2021.

[21] Jayasheelan Vaithilingam, Ehab Saleh, Lars Körner, Ricky D Wildman, Richard JM Hague, Richard K Leach, and Christopher J Tuck. 3-Dimensional inkjet printing of macro structures from silver nanoparticles. *Materials & Design*, 139:81–88, 2018.

[22] Marco Simonelli, Nesma Aboulkhair, Mircea Rasa, Mark East, Chris Tuck, Ricky Wildman, Otto Salomons, and Richard Hague. Towards digital metal additive manufacturing via high-temperature drop-on-demand jetting. *Additive Manufacturing*, 30:100930, 2019.

[23] Belen Begines, Ana Alcudia, Raul Aguilera-Velazquez, Guillermo Martinez, Yinfeng He, Gustavo F Trindade, Ricky Wildman, Maria-Jesus Sayagues, Aila Jimenez-Ruiz, and Rafael Prado-Gotor. Design of highly stabilized nanocomposite inks based on biodegradable polymer-matrix and gold nanoparticles for inkjet printing. *Scientific Reports*, 9(1):1–12, 2019.

[24] J Vaithilingam, E Saleh, C Tuck, R Wildman, I Ashcroft, R Hague, and P Dickens. 3D-inkjet printing of flexible and stretchable electronics. In *Proceedings of the 26th Solid Freeform Fabrication Symposium*, pages 10–12, 2015.

[25] Fan Zhang, Christopher Tuck, Richard Hague, Yinfeng He, Ehab Saleh, You Li, Craig Sturgess, and Ricky Wildman. Inkjet printing of polyimide insulators for the 3D printing of dielectric materials for microelectronic applications. *Journal of Applied Polymer Science*, 133(18), 2016.

[26] Joohoon Kang, Vinod K Sangwan, Joshua D Wood, and Mark C Hersam. Solution-based processing of monodisperse two-dimensional nanomaterials. *Accounts of Chemical Research*, 50(4):943–951, 2017.

[27] G Dresselhaus, Saito Riichiro, et al. *Physical properties of carbon nanotubes*. World Scientific, 1998.

[28] Edward McCann. Electronic properties of monolayer and bilayer graphene. In *Graphene Nanoelectronics*, pages 237–275. Springer, 2011.

[29] Yuanbo Zhang, Tsung-Ta Tang, Caglar Girit, Zhao Hao, Michael C Martin, Alex Zettl, Michael F Crommie, Y Ron Shen, and Feng Wang. Direct observation of a widely tunable bandgap in bilayer graphene. *Nature*, 459(7248):820–823, 2009.

[30] Charles M Wolfe, Nick Holonyak Jr, and Gregory E Stillman. *Physical properties of semiconductors*. Prentice-Hall, Inc., 1988.

[31] Thibault Sohier, Matteo Calandra, Cheol-Hwan Park, Nicola Bonini, Nicola Marzari, and Francesco Mauri. Phonon-limited resistivity of graphene by first-principles calculations: Electron-phonon interactions, strain-induced gauge field, and Boltzmann equation. *Physical Review B*, 90(12):125414, 2014.

[32] Allen Miller and Elihu Abrahams. Impurity conduction at low concentrations. *Physical Review*, 120(3):745, 1960.

[33] Nir Tessler, Yevgeni Preezant, Noam Rappaport, and Yohai Roichman. Charge transport in disordered organic materials and its relevance to thin-film devices: a tutorial review. *Advanced Materials*, 21(27):2741–2761, 2009.

[34] Kevin Whitham, Jun Yang, Benjamin H Savitzky, Lena F Kourkoutis, Frank Wise, and Tobias Hanrath. Charge transport and localization in atomically coherent quantum dot solids. *Nature Materials*, 15(5):557–563, 2016.

[35] Rachel H Gilmore, Samuel W Winslow, Elizabeth MY Lee, Matthew Nickol Ashner, Kevin G Yager, Adam P Willard, and William A Tisdale. Inverse temperature dependence of charge carrier hopping in quantum dot solids. *ACS Nano*, 12 (8):7741–7749, 2018.

[36] Willi Aigner, Oliver Bienek, Bruno P Falcão, Safwan U Ahmed, Hartmut Wiggers, Martin Stutzmann, and Rui N Pereira. Intra-and inter-nanocrystal charge transport in nanocrystal films. *Nanoscale*, 10(17):8042–8057, 2018.

[37] NF Mott and EA Davis. Electron processes in non-crystalline materials', in Mott, N. F.(Ed.). *Adv. Phys., Clarendon Press, Oxford*, 50:865–945, 1979.

[38] Vinay Ambegaokar, BI Halperin, and JS Langer. Hopping conductivity in disordered systems. *Physical review B*, 4(8):2612, 1971.

[39] Alton Harold Clark. Electrical and optical properties of amorphous germanium. *Physical Review*, 154(3):750, 1967.

[40] KL Chopra and SK Bahl. Structural, electrical, and optical properties of amorphous germanium films. *Physical Review B*, 1(6):2545, 1970.

[41] L Essaleh, SM Wasim, G Marín, C Rincón, S Amhil, and J Galibert. Mott type variable range hopping conduction and magnetoresistance in p-type $\mathrm{CuIn_3Te_5}$ semiconductor compound. *Journal of Applied Physics*, 122(1):015702, 2017.

[42] CJ Adkins, JD Benjamin, JMD Thomas, JW Gardner, and AJ McGeown. Potential disorder in granular metal systems: the field effect in discontinuous metal films. *Journal of Physics C: Solid State Physics*, 17(26):4633, 1984.

[43] Michael Pollak. Electrons in Anderson–Mott insulators. *The European Physical Journal Special Topics*, 227(15):2221–2240, 2019.

[44] Ariel Amir, Yuval Oreg, and Yoseph Imry. Electron glass dynamics. *Annu. Rev. Condens. Matter Phys.*, 2(1):235–262, 2011.

[45] Gloria Martinez-Arizala, DE Grupp, C Christiansen, AM Mack, N Markovic, Y Seguchi, and Allen M Goldman. Anomalous field effect in ultrathin films of metals near the superconductor-insulator transition. *Physical Review Letters*, 78 (6):1130, 1997.

[46] Thierry Grenet. Symmetrical field effect and slow electron relaxation in granular aluminium. *The European Physical Journal B-Condensed Matter and Complex Systems*, 32(3):275–278, 2003.

[47] Z Ovadyahu. Nonequilibrium transport and electron-glass effects in thin $\mathrm{Ge}_x\mathrm{Te}$ films. *Physical Review B*, 94(15):155151, 2016.

[48] Z Ovadyahu. Slow dynamics of electron glasses: The role of disorder. *Physical Review B*, 95(13):134203, 2017.

[49] A Vaknin, Z Ovadyahu, and M Pollak. Evidence for interactions in nonergodic electronic transport. *Physical Review Letters*, 81(3):669, 1998.

[50] Zvi Ovadyahu and Michael Pollak. Disorder and magnetic field dependence of slow electronic relaxation. *Physical Review Letters*, 79(3):459, 1997.

[51] Han Wang, Allen Hsu, Jing Kong, Dimitri A Antoniadis, and Tomas Palacios. Compact virtual-source current–voltage model for top-and back-gated graphene field-effect transistors. *IEEE Transactions on Electron Devices*, 58(5):1523–1533, 2011.

[52] Mikhail I Katsnelson. *Graphene: carbon in two dimensions.* Cambridge University Press, 2012.

[53] EH Hwang and S Das Sarma. Screening-induced temperature-dependent transport in two-dimensional graphene. *Physical Review B*, 79(16):165404, 2009.

[54] EH Hwang and S Das Sarma. Dielectric function, screening, and plasmons in two-dimensional graphene. *Physical Review B*, 75(20):205418, 2007.

[55] Izrail Solomonovich Gradshteyn and Iosif Moiseevich Ryzhik. *Table of integrals, series, and products.* Academic Press, 2014.

[56] AL Efros, FG Pikus, and VG Burnett. Density of states of a two-dimensional electron gas in a long-range random potential. *Physical Review B*, 47(4):2233, 1993.

[57] Shaffique Adam, EH Hwang, VM Galitski, and S Das Sarma. A self-consistent theory for graphene transport. *Proceedings of the National Academy of Sciences*, 104(47):18392–18397, 2007.

[58] Tsuneya Ando. Screening effect and impurity scattering in monolayer graphene. *Journal of the Physical Society of Japan*, 75(7):074716–074716, 2006.

[59] John H Davies. *The physics of low-dimensional semiconductors: an introduction.* Cambridge University Press, 1998.

[60] TO Wehling, S Yuan, AI Lichtenstein, AK Geim, and MI Katsnelson. Resonant scattering by realistic impurities in graphene. *Physical Review Letters*, 105(5): 056802, 2010.

[61] ZH Ni, LA Ponomarenko, RR Nair, R Yang, S Anissimova, IV Grigorieva, F Schedin, P Blake, ZX Shen, EH Hill, et al. On resonant scatterers as a factor limiting carrier mobility in graphene. *Nano Letters*, 10(10):3868–3872, 2010.

[62] M Monteverde, C Ojeda-Aristizabal, R Weil, K Bennaceur, M Ferrier, S Guéron, C Glattli, H Bouchiat, JN Fuchs, and DL Maslov. Transport and elastic scattering times as probes of the nature of impurity scattering in single-layer and bilayer graphene. *Physical Review Letters*, 104(12):126801, 2010.

[63] John P Robinson, Henning Schomerus, László Oroszlány, and Vladimir I Fal'ko. Adsorbate-limited conductivity of graphene. *Physical Review Letters*, 101(19): 196803, 2008.

[64] TO Wehling, MI Katsnelson, and AI Lichtenstein. Adsorbates on graphene: Impurity states and electron scattering. *Chemical Physics Letters*, 476(4-6):125–134, 2009.

[65] T Stauber, NMR Peres, and F Guinea. Electronic transport in graphene: A semiclassical approach including midgap states. *Physical Review B*, 76(20):205423, 2007.

[66] Dmitri K Efetov and Philip Kim. Controlling electron-phonon interactions in graphene at ultrahigh carrier densities. *Physical Review Letters*, 105(25):256805, 2010.

[67] Kostyantyn M Borysenko, Jeffrey T Mullen, EA Barry, S Paul, Yuriy G Semenov, JM Zavada, M Buongiorno Nardelli, and Ki Wook Kim. First-principles analysis of electron-phonon interactions in graphene. *Physical Review B*, 81(12):121412, 2010.

[68] EH Hwang and S Das Sarma. Acoustic phonon scattering limited carrier mobility in two-dimensional extrinsic graphene. *Physical Review B*, 77(11):115449, 2008.

[69] S Piscanec, M Lazzeri, Francesco Mauri, AC Ferrari, and J Robertson. Kohn anomalies and electron-phonon interactions in graphite. *Physical Review Letters*, 93(18):185503, 2004.

[70] SQ Wang and GD Mahan. Electron scattering from surface excitations. *Physical Review B*, 6(12):4517, 1972.

[71] Jürgen Schiefele, Fernando Sols, and Francisco Guinea. Temperature dependence of the conductivity of graphene on boron nitride. *Physical Review B*, 85(19): 195420, 2012.

[72] P Lugli and DK Ferry. Degeneracy in the ensemble Monte Carlo method for high-field transport in semiconductors. *IEEE Transactions on Electron Devices*, 32(11):2431–2437, 1985.

[73] Vittorio Romano, Armando Majorana, and Marco Coco. DSMC method consistent with the Pauli exclusion principle and comparison with deterministic solutions for charge transport in graphene. *Journal of Computational Physics*, 302: 267–284, 2015.

[74] Mark Lundstrom. *Fundamentals of carrier transport.* Cambridge University Press, 2009.

[75] Sigal Gottlieb and Chi-Wang Shu. Total variation diminishing Runge-Kutta schemes. *Mathematics of Computation*, 67(221):73–85, 1998.

[76] Randall J LeVeque et al. *Finite volume methods for hyperbolic problems*, volume 31. Cambridge University Press, 2002.

[77] Marco Coco, Armando Majorana, and Vittorio Romano. Cross validation of discontinuous Galerkin method and Monte Carlo simulations of charge transport in graphene on substrate. *Ricerche di Matematica*, 66(1):201–220, 2017.

[78] Randall J LeVeque and Randall J Leveque. *Numerical methods for conservation laws*, volume 3. Springer, 1992.

[79] Philip B Allen and Mengkun Liu. Joule heating in Boltzmann theory of metals. *Physical Review B*, 102(16):165134, 2020.

[80] Matthew Yankowitz, Qiong Ma, Pablo Jarillo-Herrero, and Brian J LeRoy. van der Waals heterostructures combining graphene and hexagonal boron nitride. *Nature Reviews Physics*, 1(2):112–125, 2019.

[81] Sang-Hoon Bae, Hyun Kum, Wei Kong, Yunjo Kim, Chanyeol Choi, Byunghun Lee, Peng Lin, Yongmo Park, and Jeehwan Kim. Integration of bulk materials with two-dimensional materials for physical coupling and applications. *Nature Materials*, 18(6):550, 2019.

[82] Daniel Rhodes, Sang Hoon Chae, Rebeca Ribeiro-Palau, and James Hone. Disorder in van der Waals heterostructures of 2D materials. *Nature Materials*, 18 (6):541, 2019.

[83] Jinbing Cheng, Chunlan Wang, Xuming Zou, and Lei Liao. Recent advances in optoelectronic devices based on 2D materials and their heterostructures. *Advanced Optical Materials*, 7(1):1800441, 2019.

[84] MI Katsnelson, KS Novoselov, and AK Geim. Chiral tunnelling and the Klein paradox in graphene. *Nature Physics*, 2(9):620–625, 2006.

[85] Kirill I Bolotin, Kenneth J Sikes, J Hone, HL Stormer, and Ph Kim. Temperature-dependent transport in suspended graphene. *Physical Review Letters*, 101(9): 096802, 2008.

[86] Alexander S Mayorov, Daniel C Elias, Ivan S Mukhin, Sergey V Morozov, Leonid A Ponomarenko, Kostya S Novoselov, AK Geim, and Roman V Gorbachev. How close can one approach the Dirac point in graphene experimentally? *Nano Letters*, 12(9):4629–4634, 2012.

[87] Klaus Ziegler. Minimal conductivity of graphene: Nonuniversal values from the Kubo formula. *Physical Review B*, 75(23):233407, 2007.

[88] S Das Sarma, Shaffique Adam, EH Hwang, and Enrico Rossi. Electronic transport in two-dimensional graphene. *Reviews of Modern Physics*, 83(2):407, 2011.

[89] Exfoliated graphene Hall Bars were provided by Prof. K.S. Novoselov (Manchester University UK). Experimental analysis was performed by Natham Cottam (University of Nottingham UK).

[90] Zakhar R Kudrynskyi, Mahabub A Bhuiyan, Oleg Makarovsky, Jake DG Greener, Evgeny E Vdovin, Zakhar D Kovalyuk, Y Cao, A Mishchenko, KS Novoselov, Peter H Beton, et al. Giant quantum hall plateau in graphene coupled to an InSe van der Waals crystal. *Physical Review Letters*, 119(15):157701, 2017.

[91] Nathan D Cottam, Chengxi Zhang, Lyudmila Turyanska, Laurence Eaves, Zakhar Kudrynskyi, Evgenii E Vdovin, Amalia Patanè, and Oleg Makarovsky. Defect-assisted high photoconductive UV–visible gain in perovskite-decorated graphene transistors. *ACS Applied Electronic Materials*, 2(1):147–154, 2019.

[92] Lyudmila Turyanska, Oleg Makarovsky, Laurence Eaves, Amalia Patanè, and Nobuya Mori. Mobility enhancement of CVD graphene by spatially correlated charges. *2D Materials*, 4(2):025026, 2017.

[93] Kostya S Novoselov, Andre K Geim, Sergei Vladimirovich Morozov, Da Jiang, Michail I Katsnelson, IVa Grigorieva, SVb Dubonos, and AA Firsov. Two-dimensional gas of massless Dirac fermions in graphene. *Nature*, 438(7065):197–200, 2005.

[94] Byung-Sung Kim, Darren CJ Neo, Bo Hou, Jong Bae Park, Yuljae Cho, Nanlin Zhang, John Hong, Sangyeon Pak, Sanghyo Lee, Jung Inn Sohn, et al. High performance PbS quantum dot/graphene hybrid solar cell with efficient charge extraction. *ACS Applied Materials & Interfaces*, 8(22):13902–13908, 2016.

[95] Youngbin Lee, Jeong Kwon, Euyheon Hwang, Chang-Ho Ra, Won Jong Yoo, Jong-Hyun Ahn, Jong Hyeok Park, and Jeong Ho Cho. High-performance perovskite–graphene hybrid photodetector. *Advanced Materials*, 27(1):41–46, 2015.

[96] Garry W Mudd, Simon A Svatek, Lee Hague, Oleg Makarovsky, Zakhar R Kudrynskyi, Christopher J Mellor, Peter H Beton, Laurence Eaves, Kostya S Novoselov, Zakhar D Kovalyuk, et al. High broad-band photoresponsivity of mechanically formed InSe–graphene van der Waals heterostructures. *Advanced Materials*, 27(25):3760–3766, 2015.

[97] FHL Koppens, T Mueller, Ph Avouris, AC Ferrari, MS Vitiello, and M Polini. Photodetectors based on graphene, other two-dimensional materials and hybrid systems. *Nature Nanotechnology*, 9(10):780–793, 2014.

[98] Qiuzi Li, EH Hwang, Enrico Rossi, and S Das Sarma. Theory of 2D transport in graphene for correlated disorder. *Physical Review Letters*, 107(15):156601, 2011.

[99] Oleg Makarovsky, Lyudmila Turyanska, Nobuya Mori, Mark Greenaway, Laurence Eaves, Amalia Patané, Mark Fromhold, Samuel Lara-Avila, Sergey Kubatkin, and Rositsa Yakimova. Enhancing optoelectronic properties of SiC-grown graphene by a surface layer of colloidal quantum dots. *2D Materials*, 4(3):031001, 2017.

[100] Victor W Brar, Régis Decker, Hans-Michael Solowan, Yang Wang, Lorenzo Maserati, Kevin T Chan, Hoonkyung Lee, Çağlar O Girit, Alex Zettl, Steven G Louie, et al. Gate-controlled ionization and screening of cobalt adatoms on a graphene surface. *Nature Physics*, 7(1):43–47, 2011.

[101] S Das Sarma, EH Hwang, S Kodiyalam, LN Pfeiffer, and KW West. Transport in two-dimensional modulation-doped semiconductor structures. *Physical Review B*, 91(20):205304, 2015.

[102] Clemens Heitzinger and Christian Ringhofer. An effective quantum potential for particle–particle interactions in three-dimensional semiconductor device simulations. *Journal of Computational Electronics*, 6(4):401–408, 2007.

[103] J-H Chen, Ci Jang, Shaffique Adam, MS Fuhrer, Ellen D Williams, and Masa Ishigami. Charged-impurity scattering in graphene. *Nature Physics*, 4(5):377–381, 2008.

[104] DS Novikov. Numbers of donors and acceptors from transport measurements in graphene. *Applied Physics Letters*, 91(10):102102, 2007.

[105] AV Kretinin, Y Cao, JS Tu, GL Yu, R Jalil, KS Novoselov, SJ Haigh, A Gholinia, A Mishchenko, M Lozada, et al. Electronic properties of graphene encapsulated with different two-dimensional atomic crystals. *Nano Letters*, 14(6):3270–3276, 2014.

[106] MT Greenaway, R Krishna Kumar, P Kumaravadivel, AK Geim, and L Eaves. Magnetophonon spectroscopy of Dirac fermion scattering by transverse and longitudinal acoustic phonons in graphene. *Physical Review B*, 100(15):155120, 2019.

[107] SV Morozov, KS Novoselov, MI Katsnelson, F Schedin, DC Elias, John A Jaszczak, and AK Geim. Giant intrinsic carrier mobilities in graphene and its bilayer. *Physical Review Letters*, 100(1):016602, 2008.

[108] Bingyan Chen, Huixin Huang, Xiaomeng Ma, Le Huang, Zhiyong Zhang, and Lian-Mao Peng. How good can CVD-grown monolayer graphene be? *Nanoscale*, 6(24):15255–15261, 2014.

[109] J Huang, JA Alexander-Webber, AMR Baker, TJBM Janssen, A Tzalenchuk, V Antonov, T Yager, S Lara-Avila, S Kubatkin, Rositsa Yakimova, et al. Physics of a disordered Dirac point in epitaxial graphene from temperature-dependent magnetotransport measurements. *Physical Review B*, 92(7):075407, 2015.

[110] Wenjuan Zhu, Vasili Perebeinos, Marcus Freitag, and Phaedon Avouris. Carrier scattering, mobilities, and electrostatic potential in monolayer, bilayer, and trilayer graphene. *Physical Review B*, 80(23):235402, 2009.

[111] S Das Sarma and EH Hwang. Density-dependent electrical conductivity in suspended graphene: Approaching the Dirac point in transport. *Physical Review B*, 87(3):035415, 2013.

[112] Y-W Tan, Yuanbo Zhang, Horst L Stormer, and Philip Kim. Temperature dependent electron transport in graphene. *The European Physical Journal Special Topics*, 148(1):15–18, 2007.

[113] DA Abanin, SV Morozov, LA Ponomarenko, RV Gorbachev, AS Mayorov, MI Katsnelson, Kenji Watanabe, Takashi Taniguchi, KS Novoselov, LS Levitov, et al. Giant nonlocality near the Dirac point in graphene. *Science*, 332(6027): 328–330, 2011.

[114] P Kumaravadivel, MT Greenaway, D Perello, A Berdyugin, J Birkbeck, J Wengraf, S Liu, JH Edgar, AK Geim, L Eaves, et al. Strong magnetophonon oscillations in extra-large graphene. *Nature Communications*, 10(1):1–6, 2019.

[115] Kei Kinoshita, Rai Moriya, Momoko Onodera, Yusai Wakafuji, Satoru Masubuchi, Kenji Watanabe, Takashi Taniguchi, and Tomoki Machida. Dry release transfer of graphene and few-layer h-BN by utilizing thermoplasticity of polypropylene carbonate. *NPJ 2D Materials and Applications*, 3(1):1–8, 2019.

[116] Claudia Backes, Amr M Abdelkader, Concepción Alonso, Amandine Andrieux-Ledier, Raul Arenal, Jon Azpeitia, Nilanthy Balakrishnan, Luca Banszerus, Julien Barjon, Ruben Bartali, et al. Production and processing of graphene and related materials. *2D Materials*, 7(2):022001, 2020.

[117] Devices (Exf1, Exf2, Exf3, Exf4, CVD1, CVD2) were fabricated and experimental measurements on the devices were provided by: Oleg Makarovsky and Zakhar Kudrynskyi (School of Physics and Astronomy, University of Nottingham, Nottingham, NG7 2RD, UK); and Sergey V. Morozov, Evgenii E. Vdovin and Yurii N. Khanin (Institute of Microelectronics Technology RAS, Chernogolovka 142432, Russia).

[118] Clarence Zener. A theory of the electrical breakdown of solid dielectrics. *Proceedings of the Royal Society of London. Series A, Containing Papers of a Mathematical and Physical Character*, 145(855):523–529, 1934.

[119] William Vandenberghe, Bart Sorée, Wim Magnus, and Guido Groeseneken. Zener tunneling in semiconductors under nonuniform electric fields. *Journal of Applied Physics*, 107(5):054520, 2010.

[120] AV Andreev. Magnetoconductance of carbon nanotube p- n junctions. *Physical Review Letters*, 99(24):247204, 2007.

[121] L Matthew Zhang and MM Fogler. Nonlinear screening and ballistic transport in a graphene p- n junction. *Physical Review Letters*, 100(11):116804, 2008.

[122] EB Sonin. Effect of Klein tunneling on conductance and shot noise in ballistic graphene. *Physical Review B*, 79(19):195438, 2009.

[123] Niels Vandecasteele, Amelia Barreiro, Michele Lazzeri, Adrian Bachtold, and Francesco Mauri. Current-voltage characteristics of graphene devices: Interplay between Zener-Klein tunneling and defects. *Physical Review B*, 82(4):045416, 2010.

[124] Jakub Tworzydło, Björn Trauzettel, Misha Titov, Adam Rycerz, and Carlo WJ Beenakker. Sub-Poissonian shot noise in graphene. *Physical Review Letters*, 96 (24):246802, 2006.

[125] DA Bandurin, Iacopo Torre, R Krishna Kumar, M Ben Shalom, Andrea Tomadin, A Principi, GH Auton, E Khestanova, KS Novoselov, IV Grigorieva, et al. Negative local resistance caused by viscous electron backflow in graphene. *Science*, 351(6277):1055–1058, 2016.

[126] Zachary J Krebs, Wyatt A Behn, Songci Li, Keenan J Smith, Kenji Watanabe, Takashi Taniguchi, Alex Levchenko, and Victor W Brar. Imaging the breaking of electrostatic dams in graphene for ballistic and viscous fluids. *arXiv preprint arXiv:2106.07212*, 2021.

[127] Andrew Lucas and Kin Chung Fong. Hydrodynamics of electrons in graphene. *Journal of Physics: Condensed Matter*, 30(5):053001, 2018.

[128] Mathias J Boland, Abhishek Sundararajan, M Javad Farrokhi, and Douglas R Strachan. Nonlinear ballistic transport in an atomically thin material. *ACS Nano*, 10(1):1231–1239, 2016.

[129] Kenji Watanabe, Takashi Taniguchi, and Hisao Kanda. Direct-bandgap properties and evidence for ultraviolet lasing of hexagonal boron nitride single crystal. *Nature Materials*, 3(6):404–409, 2004.

[130] Mark T Greenaway, EE Vdovin, Davit Ghazaryan, Abhishek Misra, Artem Mishchenko, Yang Cao, Zihao Wang, JR Wallbank, Matthew Holwill, Yu N Khanin, et al. Tunnel spectroscopy of localised electronic states in hexagonal boron nitride. *Communications Physics*, 1(1):1–7, 2018.

[131] Matthew Yankowitz, Jiamin Xue, Daniel Cormode, Javier D Sanchez-Yamagishi, K Watanabe, T Taniguchi, Pablo Jarillo-Herrero, Philippe Jacquod, and Brian J LeRoy. Emergence of superlattice Dirac points in graphene on hexagonal boron nitride. *Nature Physics*, 8(5):382–386, 2012.

[132] Aaron L Sharpe, Eli J Fox, Arthur W Barnard, Joe Finney, Kenji Watanabe, Takashi Taniguchi, MA Kastner, and David Goldhaber-Gordon. Emergent ferromagnetism near three-quarters filling in twisted bilayer graphene. *Science*, 365 (6453):605–608, 2019.

[133] Yuan Cao, Valla Fatemi, Ahmet Demir, Shiang Fang, Spencer L Tomarken, Jason Y Luo, Javier D Sanchez-Yamagishi, Kenji Watanabe, Takashi Taniguchi, Efthimios Kaxiras, et al. Correlated insulator behaviour at half-filling in magic-angle graphene superlattices. *Nature*, 556(7699):80–84, 2018.

[134] Yuan Cao, Valla Fatemi, Shiang Fang, Kenji Watanabe, Takashi Taniguchi, Efthimios Kaxiras, and Pablo Jarillo-Herrero. Unconventional superconductivity in magic-angle graphene superlattices. *Nature*, 556(7699):43–50, 2018.

[135] Tian Carey, Stefania Cacovich, Giorgio Divitini, Jiesheng Ren, Aida Mansouri, Jong M Kim, Chaoxia Wang, Caterina Ducati, Roman Sordan, and Felice Torrisi. Fully inkjet-printed two-dimensional material field-effect heterojunctions for wearable and textile electronics. *Nature Communications*, 8(1):1–11, 2017.

[136] Minzhen Cai, Daniel Thorpe, Douglas H Adamson, and Hannes C Schniepp. Methods of graphite exfoliation. *Journal of Materials Chemistry*, 22(48):24992–25002, 2012.

[137] Yang Su, Jinhong Du, Dongming Sun, Chang Liu, and Huiming Cheng. Reduced graphene oxide with a highly restored π-conjugated structure for inkjet printing and its use in all-carbon transistors. *Nano Research*, 6(11):842–852, 2013.

[138] Ethan B Secor, Bok Y Ahn, Theodore Z Gao, Jennifer A Lewis, and Mark C Hersam. Rapid and versatile photonic annealing of graphene inks for flexible printed electronics. *Advanced Materials*, 27(42):6683–6688, 2015.

[139] Siegfried Eigler, Christoph Dotzer, and Andreas Hirsch. Visualization of defect densities in reduced graphene oxide. *Carbon*, 50(10):3666–3673, 2012.

[140] B Lesiak, G Trykowski, J Tóth, S Biniak, L Kövér, N Rangam, L Stobinski, and A Malolepszy. Chemical and structural properties of reduced graphene oxide—dependence on the reducing agent. *Journal of Materials Science*, 56(5): 3738–3754, 2021.

[141] John G Simmons. Generalized formula for the electric tunnel effect between similar electrodes separated by a thin insulating film. *Journal of Applied Physics*, 34(6):1793–1803, 1963.

[142] Amedeo Bellunato, Sasha D Vrbica, Carlos Sabater, Erik W de Vos, Remko Fermin, Kirsten N Kanneworff, Federica Galli, Jan M van Ruitenbeek, and Grégory F Schneider. Dynamic tunneling junctions at the atomic intersection of two twisted graphene edges. *Nano Letters*, 18(4):2505–2510, 2018.

[143] CS Lau, JA Mol, JH Warner, and GAD Briggs. Nanoscale control of graphene electrodes. *Physical Chemistry Chemical Physics*, 16(38):20398–20401, 2014.

[144] Konrad Ullmann, Pedro B Coto, Susanne Leitherer, Agustín Molina-Ontoria, Nazario Martín, Michael Thoss, and Heiko B Weber. Single-molecule junctions with epitaxial graphene nanoelectrodes. *Nano Letters*, 15(5):3512–3518, 2015.

[145] Jeff Greensite. *An Introduction to Quantum Theory.* IOP Publishing, 2017.

[146] Joost Wintterlin and M-L Bocquet. Graphene on metal surfaces. *Surface Science*, 603(10-12):1841–1852, 2009.

[147] Matthew Yankowitz, Jeil Jung, Evan Laksono, Nicolas Leconte, Bheema L Chittari, Kenji Watanabe, Takashi Taniguchi, Shaffique Adam, David Graf, and Cory R Dean. Dynamic band-structure tuning of graphene moiré superlattices with pressure. *Nature*, 557(7705):404–408, 2018.

[148] Ashkan Behnam and Ant Ural. Computational study of geometry-dependent resistivity scaling in single-walled carbon nanotube films. *Physical Review B*, 75 (12):125432, 2007.

[149] Irina V Vodolazskaya, Andrei V Eserkepov, Renat K Akhunzhanov, and Yuri Yu Tarasevich. Effect of tunneling on the electrical conductivity of nanowire-based films: Computer simulation within a core–shell model. *Journal of Applied Physics*, 126(24):244903, 2019.

[150] Xiao-Yong Fang, Xiao-Xia Yu, Hong-Mei Zheng, Hai-Bo Jin, Li Wang, and Mao-Sheng Cao. Temperature-and thickness-dependent electrical conductivity of few-layer graphene and graphene nanosheets. *Physics Letters A*, 379(37):2245–2251, 2015.

[151] Felice Torrisi, Tawfique Hasan, Weiping Wu, Zhipei Sun, Antonio Lombardo, Tero S Kulmala, Gen-Wen Hsieh, Sungjune Jung, Francesco Bonaccorso, Philip J Paul, et al. Inkjet-printed graphene electronics. *ACS Nano*, 6(4):2992–3006, 2012.

[152] Ali Tarhini, Ali Tehrani-Bagha, Michel Kazan, and Brian Grady. The effect of graphene flake size on the properties of graphene-based polymer composite films. *Journal of Applied Polymer Science*, 138(6):49821, 2021.

[153] Pei He and Brian Derby. Inkjet printing ultra-large graphene oxide flakes. *2D Materials*, 4(2):021021, 2017.

[154] De Kong, Linh T Le, Yue Li, James L Zunino, and Woo Lee. Temperature-dependent electrical properties of graphene inkjet-printed on flexible materials. *Langmuir*, 28(37):13467–13472, 2012.

[155] MCJM Vissenberg and M Matters. Theory of the field-effect mobility in amorphous organic transistors. *Physical Review B*, 57(20):12964, 1998.

[156] Haomin Wang, Yihong Wu, Chunxiao Cong, Jingzhi Shang, and Ting Yu. Hysteresis of electronic transport in graphene transistors. *ACS Nano*, 4(12):7221–7228, 2010.

[157] Jens Mohrmann, Kenji Watanabe, Takashi Taniguchi, and Romain Danneau. Persistent hysteresis in graphene-mica van der Waals heterostructures. *Nanotechnology*, 26(1):015202, 2014.

[158] Jia-An Yan, WY Ruan, and MY Chou. Phonon dispersions and vibrational properties of monolayer, bilayer, and trilayer graphene: Density-functional perturbation theory. *Physical Review B*, 77(12):125401, 2008.

[159] LJ Karssemeijer and Annalisa Fasolino. Phonons of graphene and graphitic materials derived from the empirical potential LCBOPII. *Surface Science*, 605(17-18): 1611–1615, 2011.

[160] Valentin N Popov and Christian Van Alsenoy. Low-frequency phonons of few-layer graphene within a tight-binding model. *Physical Review B*, 90(24):245429, 2014.

Appendix A

Device Details

All devices presented here were fabricated by those in ref. [117]. Devices details shown below are also provided by those in ref. [117].

In this study, we compared theoretical analysis to the results from 6 different SLG FETs, which can be categorised into 3 groups:

(i) High mobility devices, Exf1 and Exf2, fabricated using dry transfer of single layer graphene exfoliated in a glove box, encapsulated between two hBN layers and dry-transferred onto a Si/SiO$_2$ substrate. Details of the hBN encapsulation and dry-transfer technique can be found in ref. [105].

(ii) Lower mobility exfoliated devices, Exf3 and Exf4, fabricated using conventional wet-transfer of graphene onto Si/SiO$_2$ [116] but without use of additional protective layers of hBN or other materials.

(iii) Lowest mobility devices, CVD1 and CVD2, fabricated using commercial CVD graphene hBN heterostructures mounted on a Si/SiO$_2$ wafer (Graphene Supermarket). The device CVD2 was fabricated by capping roughly half of the graphene layer with a thin (~ 1 μm) layer of exfoliated monocrystalline InSe using the technique described in ref. [90].

All SLG FETs were processed into Hall bars of similar size (fig. A.1, table A.1).

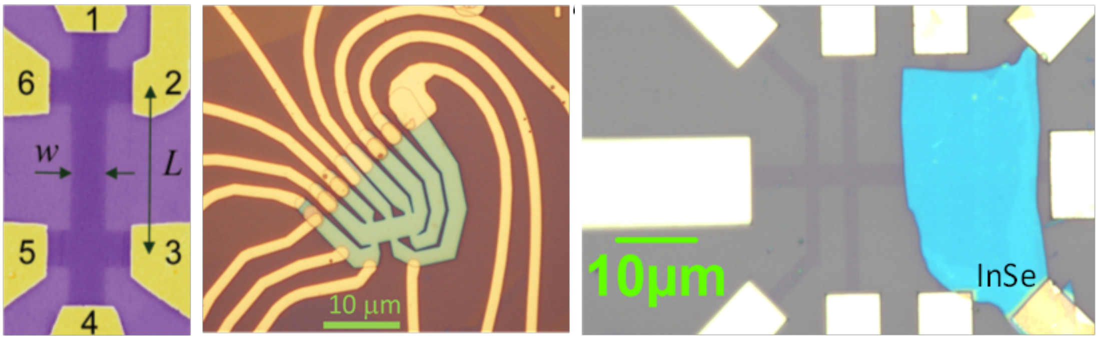

(a) (b) (c)

Figure A.1: Optical images of samples (a) Exf1, (b) Exf2, (c) CVD1, CVD2. Images provided by: [117].

Sample Name	Material used and sample processing techniques	Distance between potential leads, L	Graphene channel width, W	Doping level at $T < 10$ K (m^{-2})	Carrier mobility at $T < 10$ K (m^2/Vs)
Exf1	Dry transferred exfoliated graphene, encapsulated with hBN	4 µm	1 µm	5.6×10^{13}	25
Exf2		4 µm	4 µm	4.1×10^{13}	21
Exf3	Wet transferred exfoliated graphene, on $\mathrm{SiO_2}$	4 µm	1 µm	2.9×10^{14}	1.8
Exf4		4 µm	1 µm	3.0×10^{14}	1.6
CVD1	Commercial CVD graphene	5 µm	3 µm	8.4×10^{15}	0.7
CVD2	Commercial CVD graphene with InSe	5 µm	3 µm	1.1×10^{16}	0.5

Table A.1: Sample details. The doping level is derived from the position of the maximum resistivity relative to gate-induced doping. Data provided by: [117].